POLITECNICO DI MILANO

DEPARTMENT OF BIOENGINNERING

DOCTORAL PROGRAM IN BIOENGINEERING

A new laser self-mixing interferometer system for the assessment of the chest-wall mechanics

Doctoral Dissertation of:

Ilaria Milesi

Tutor: Prof. Antonio Pedotti

Advisor: Prof. Raffaele Dellacà

Supervisor: Prof. Maria Gabriella Signorini, Ph. D.

2011-XXIV Cycle

RINGRAZIAMENTI

Grazie a Raffaele per i suoi preziosi insegnamenti, la sua onestà e la capacità di vedere molto più lontano di me!
Grazie al prof. Pedotti per avermi consentito di portate avanti questo progetto di tesi.
Grazie a tutti i miei colleghi/amici con i quali ho condiviso tre anni intensi di fatica e soddisfazione, in particolare grazie a Ema, Leo, Pasquo, Chiara, Miriam, Ale!
Grazie a Peter Frykholm e al suo gruppo per la generosità ed entusiasmo dimostrati!
Grazie a tutti gli amici che mi sono stati vicini, anche nei momenti di crisi. Come avrei fatto senza i caffè con Stefano, Francesca e Bob!
E infine, ma non in ordine di importanza, grazie alla mia famiglia che mi ha sostenuto nelle mie scelte e ha creduto in me.

SUMMARY

EXTENDED ABSTRACT

The respiratory system is a complex system which accomplishes gas exchange by means of the synergy among functions and structures which have specifically developed at this aim. Processes involved in gas exchange are: 1) ventilation, that is air transport inside and outside the lungs; 2) oxygen and carbon dioxide diffusion among alveoli and blood; 3) oxygen and carbon dioxide delivering for the blood to the cell and finally, 4) ventilation regulation. The respiratory system functionalities are not only reliant on its components, that are a complex branching system of tubing (*airways*), a huge exchange region (*the alveoli*) where gases can diffuse from and into the blood, but its behaviour is deeply influenced also by the respiratory muscles and structures that form a boundary of it, such as the chest-wall and the diaphragm. Impairment at only one of these structure or functions can seriously affect not just the respiratory system but it can yield to a general worsening in the life condition of the subjects due to laboured breathing or asthma attacks, fatigue and difficulty with mobility, heightened sensitivity to ordinary substances and chemicals, and compromised immunity to infection.

In particular ventilation capability, which represents the first step in breathing activity, relies on the mechanical properties of the whole respiratory system: the resistance of the airways, the compliance and elastic recoil of the lung parenchyma, stiffness in chest wall and abdomen, all these components contribute in different and complex ways in the relationship between the pressure generated by active components inside the respiratory chain and the volume of gas introduced.

Diseases affecting the respiratory system, such as ARDS (acute respiratory distress syndrome), restrictive diseases and lung oedema, produce alterations and inhomogeneities in the lung structure and in the chest wall which cause changings in the mechanical properties.

In more details, ARDS is defined as a syndrome of inflammation and increasing permeability that is associated with a constellation of clinical, radiological and physiological abnormalities that cannot be explained by, but may coexist with, left atrial or pulmonary capillary hypertension. The physiological consequences are severe hypoxaemia due to right-to-left shunting of blood and decreased pulmonary compliance due to filling and closure of alveoli. As the airspaces fill with fluid, the gas exchange and mechanical properties of the lung deteriorate.

Restrictive lung diseases are characterized by reduced lung volume, either because of an alteration in lung parenchyma or because of a disease of the pleura, chest wall, or

neuromuscular apparatus. The many disorders that cause reduction or restriction of lung volumes may be divided into two groups based on anatomical structures. The first is intrinsic lung diseases or diseases of the lung parenchyma. The second is extrinsic disorders or extra-parenchymal diseases, which involve the chest wall, pleura, and respiratory muscles, the components of the respiratory pump. Diseases of these structures result in lung restriction, impaired ventilatory function, and respiratory failure (eg, non-muscular diseases of the chest wall, neuromuscular disorders).
Also pulmonary oedema can cause alterations in lung mechanics that directly contribute to clinical morbidity and mortality rates. Both the location of the oedema fluid (interstitital versus alveolar pulmonary oedema) and the aetiology of the pulmonary oedema contribute to the severity and type of abnormalities of lung mechanics observed. The alterations in lung mechanics associated with the adult respiratory distress syndrome may involve the direct effects of released mediators, alterations in pulmonary surfactant, and altered airway reactivity, as well as the direct effects of the oedema fluid.
Up to the present day, the diagnosis and the management of these kinds of pathologies have been carried out mainly by chest radiography, which reveals diffuse opacity according to the stage of the pathology and CT. More specifically ARDS can be detected also by means of measurement of lung endothelial and alveolar epithelial barrier function and BAL (Bronchoalveolar lavage), while restrictive pathology can be detected also by means of some laboratory tests aimed to measure the concentration of well-known markers such as elevated creatine kinase level. Anyway all of them present some intrinsic limitations, indeed they are invasive or required long time to be carried out and thus they can’t be used to monitor in a continuative way the pathology evolution.
On the contrary several published data suggest that global but also local chest wall mechanical properties are parameters that might be useful for the evaluation of structural elasticity and inertia on the overall behaviour of the respiratory system and for estimating the possible impact of both restrictive and obstructive diseases on respiration, thus it could be useful in the assessment of the pathology providing a handy tool for clinicians during the diagnosis but also the therapy of the disease. Although the rich informative content of the chest wall mechanical properties, up to now this parameter has been almost disregarded because of the intrinsic difficulties in its measurement. Therefore a new approach for the detection and the monitoring of these diseases can be based on the measurements of the local and global chest-wall mechanics and the extraction of parameters which are sensitive to pathophysiological alteration. The more promising and inspiring approach has been reported by Dellacà et

al [2002] which suggest the union of FOT (Forced Oscillation Technique) and OEP (Optoelectronic Plethysmography) to estimate the impact of low amplitude pressure stimuli given at the mouth at the level of vibration induced at the chest-wall.

Briefly FOT method is based on the measurements of the response of the respiratory system to small pressure stimuli generated externally and applied during normal breathing. There are two different approaches in studying oscillatory mechanics of the respiratory system: one could study the response of the system by analysing the flow that the pressure stimulus has been able to induce from the mouth or analyse how the stimulus has travelled through the system by measuring the displacement of the external surface of the thorax. The former, widely used in oscillatory mechanics, allows the estimation of the input impedance by combining the measurement of pressure and flow at the airway opening, while the latter allows the estimation of the transfer impedance by combining airway opening and chest wall vibrations.

OEP is a system for motion capture specifically developed to estimate breathing volumes. It is able to measures the three-dimensional coordinates of several passive markers applied to body landmarks on the chest-wall by using several TV cameras which frame the subject by different angles. From these data a dedicated algorithm computes the three-dimensional coordinates of the markers by perspective projection described by the collinearity equations (stereo-photogrammetric methods). Then by means of triangulation on the markers detected or by using the Gauss theorem it is possible to calculate the volume enclosed into the markers surface.

In the past years, most of the published studies were focused on the estimation of the input impedance obtained from the response of the respiratory systems to a pressure stimulus given at the mouth providing information about the average properties of the respiratory system and in particular about the mechanical properties of the airways, on the contrary little is known about the transfer impedance. In the above mentioned study, global transfer impedance and its distribution on the chest wall has been estimated at different frequencies on healthy subjects showing how impedance is not equally distributed on the thoraco-abdominal wall but the ribcage is the predominant component at those frequencies. This study opens interesting insight into the comprehension of chest wall mechanics but it is limited by the complexity in the methodological approach- use of OEP system with 69 markers and cameras which should be carefully calibrated- and costs connected. The already uncovered point in this approach is the measurement of chest wall vibration in a reliable and resolute way by means of low costs and not invasive devices.

The objective of this work is to develop and validate a new method that allow the estimation of the local mechanical properties of the chest-wall based on FOT and optical devices in a non-invasive, low cost and compact way. This new approach will relay on the possibility to have reliable and resolute measurements of the displacement of the chest-wall in order to allow the estimation of impedance map: its knowledge will allow to develop new methodological and technological tools useful for the bed-side assessment of patients affected by pathologies which alter the chest-wall mechanics such as ARDS and restrictive diseases.

To achieve these results new technology, at least for the respiratory system, are needed in particular an optimum candidate is laser self-mixing interferometry which allows the measurement of very little relative displacement (theoretical resolution less than one micrometre).

The work will be presented in four sections whose contents are resumed below.

1 ASSESSMENT OF CHESTWALL KINEMATICS AND MECHANICS:

In this section, the background and the aim of the work are presented. Specifically it is organized in three parts.

In the first one a brief introduction about the respiratory mechanics will be presented together with its assessment by means of the most common techniques used by clinicians. Then a brief look at different pathologies and their classification into obstructive and restrictive diseases is reported focusing on the alterations induced on the mechanics of breathing and in particular in the chest wall mechanics. The main studied pathologies will be ARDS and fibrosis which can be taken as an example of alteration in respiratory mechanics.

The second part deals with non-conventional techniques and technologies which have been proposed in the last years for the measurements of the respiratory mechanics in a non invasive way.

In more details, this section starts with the basics of oscillatory mechanics and the basics of FOT (Forced Oscillation Technique). The FOT represents the current state-of-the art in the assessment of lung function and has reached a high level of sophistication. Here the measurement set up are presented and the main parameters and interpretative models are described and commented

The second technologies described here is OEP which allows the estimation of chest-wall volume variation and its compartmentalization into at least two parts: the rib cage and the abdomen.

The third part of this chapter describes a recent approach that by combining OEP and FOT allows the estimation of the oscillatory mechanics of the chest wall, in this way it is possible to study how a pressure stimulus travels inside the chest wall according to the different structure it finds in its pathway and to build maps which describe how impedance is distributed over chest wall surface. Although this methods give some interesting hints into local properties of the respiratory system, its limits, which are mainly due to methodological issues and to incapacity to reliable measure movements less than 0.5 mm, are underlined. Anyway a strong connection between the measurement of local mechanical properties of the respiratory system and the punctual measurements of point of the chest wall is evidenced. So the measurements of the chest wall mechanics requires the use of new technologies-methodologies which should answer to some fundamental requirements such as spatial and time resolution and reliability, but also at some additional features which make it user friendly such as no need of contact with the skin or no need for calibration. A candidate which has all the wanted property, could be laser self mixing interferometer associated with optical distantiometer.

2 NEW TECHNIQUE TO MEASURE DISPLACEMENT

This chapter will be split into two parts according to the technologies and its validation.

The first part deals with interferometry, which is a well-established technology used to measure relative displacement of target with a very high spatial and time resolution. The main interferometer configurations will be covered starting from the Michelson prototype and coming to the modern self-mixing one. The last one is the most compact and easiest to use, since it doesn’t require the use of any mirror because interference effects take place directly inside the resonant cavity laser and, above all, it allows also the measurement of diffusive target for little measurements. On the contrary, at the state of the art, big displacement (less than one cm) are not carried out because the signal quality is dramatically reduced by the presence of speckles, which are darkness zones due to interference in the light diffuse by rough surface. The very important feature of being suitable also for diffusive target suggests the possibility to use laser self mixing interferometers for measurement directly on the skin of patients and on the chest-wall in order to measure both the little vibrations due to pressure stimuli and the wide movement due to breathing. The introduction of this technology allows fixing the main problem for chest-wall mechanics estimation, that is the measurement of its displacement. The only limitation is the presence of speckles which doesn’t allow using traditional algorithm for processing interferometer signal.

In the following part of this section, the introduction of a new algorithm and methodological approach for measure chest-wall displacement, will be descripted.

The skin behaves as a grey surface diffuser, inducing low back-reflection to the laser diode. In order to analyse the interferometric signal, we propose a new method for estimating the movement direction also in the low-injection regime ,since traditional algorithms, based on fringe counts and extraction of their slope, are not reliable in this

application The developed algorithm was based on two assumptions: 1) the frequency of the fringes is linked to the relative velocity of the target, which must be continuous and 2) each time the target changes its movement direction, the velocity equals zero.
To validate the algorithm in vivo e in vitro measurements have been carried out.
The set-up, protocol, algorithm and results are discussed for the validation on a test object.
Interferometer was carefully aligned with a piston of a linear servo motor and its signal was recorder during the motion of the motor which is controlled to produce a sinusoidal displacement.
Piston velocity, estimated by interferometric signal as described above, was then integrated to obtain displacement. Motor displacement amplitude and the interferometric one were compared; in particular minima and maxima displacement values were detected and used to compute linear regression and to perform the Bland et Altman analysis. A good linearity, r^2=0.99, and the absence of any biased errors demonstrates the algorithm skills to reconstruct displacement from interferometric signals.
In the following part validation of the algorithm when the interfeometer is used directly on skin is reported.
A sinusoidal pressure signal was generated and was applied to the subject through a connecting tube and a mouthpiece. The pressure at the airway opening was measured by a piezo-resistive pressure transducer and the thoraco-abdominal wall velocities in correspondence of the Lewis Angle and approximately 1 cm below the umbilicus were detected using self-mixing interferometer. The interferometer was fixed on a mechanical frame above the subject at a distance of about 60 cm from the subject lying in supine position. Contemporary the scene is surveyed by SMART cameras which are sensitive to interferometer spot, in this way it has been possible to compare displacement measured by interferometer with the one measured by SMART CAMERA
The results obtained were compared. The interferometer displacement shows good agreement with the SMART. In conclusion our data demonstrate that laser interferometry could be used to measure accurately displacements of the chest wall making this technique suitable for all the applications involving the measurement of wide chest wall movement as well as for the detection of very small displacement as those occurring when a pressure wave reaches the chest surface.
Estimation of the phase delay between the pressure signal and the chest-wall vibrations has also be performed using the same set up
Eight normal healthy subjects in supine position during quiet breathing while submitted to a sinusoidal pressure forcing at the mouth with components at 5, 11 and

19 Hz. Displacements of 9 chest wall points along three imaginary lines (nipples lines, left and right, and midline) were measured by laser self mixing interferometers. The phase displacement among these points was estimated by correlation technique between the pressure at the mouth and the velocity of the points measured by the interferometer. The results show spatial inhomogeneities strongly dependent on position and frequency. The results are in good agreement with previous data measured by OEP. In conclusion laser interferometry may be an attractive technique for the assessment of local CW motion.

The basic set up proposed here allows to validate the algorithm and to estimate the phase shift of some points on skin but it can't be proposed to acquire more signal and to generate an impedance maps because of the long time required to move manually the interferometer and because the lack of knowledge about the distances between the points measured.

OPTICAL DISTANTIOMETER FOR MEASUREMENT ON SKIN

Interferometers allow measuring relative displacement but they can't provide information about the absolute position of the points and the direction of the interferometer respects to the skin, for this reason a second optical technology has been sided to interferometry to solve these issues, it is optical distantiometry.

Basic principle behind optical triangulation distantiomer are explained: for distances of a few inches with high accuracy requirements, laser triangulation sensors measure the location of the spot within the field of view of the detecting element and are so named because the sensor enclosure, the emitted laser and the reflected laser light form a triangle. The input-output characteristic of these devices is not linear, so a careful calibration procedure is needed.

The section goes on with a description of the calibration procedure which consists in pointing the distantiometer towards a target which is moved of a known quantity, then the best fitting polynomial waveform is estimated and the calibration coefficients are extracted. A validation protocol has also been carried out; it consists in measuring the distances of a target with distantiometers and contemporary with SMART camera. A model made by three markers placed on the distantiometer and three markers placed on the target, which is a plane surface, has been implemented The distances so measured show a good agreement with the one estimated by OEP with an error less than 0.5 mm.

The last part of this section deals with the description of a method which allows estimating the angle between the optical beam of the distantiometer and a plane, which can be used to correct for not orthogonally of the interferometer. Basically, if the distantiometer is pointing towards a plane and it rotates of a given angle, by measuring the distances between it and the plane before and after the rotation, it is possible to estimate the incidence angle by means of easy trigonometrically equations. An analysis of the sensitivity of this method according to error in measurement estimation is performed. The in vitro validation performed mainly consists in pointing the distantiometer toward a plane with a given inclination and in rotating it by means of a stepper motor, the measured distances are used to perform the estimation of the angle. The results are good although they are strongly dependent on the polynomial degrees of the waveform selected in the calibration procedure.

3 ASSESSMENT OF THE MECHANICAL PROPERTIES OF THE CHESTWALL DURING INDUCTION OF ANAESTHESIA

Once the feasibility of laser interferometer measurements directly on skin has been demonstrated and validated, a new system which allows the measurements of the local mechanical properties of the respiratory system has been proposed. The most innovative aspects are the introduction of new technologies for this context such as interferometry and the synergy between already used technique such as FOT with new technologies such as interferometry and distantiometry.

The realized system has been carefully design to fulfill the design requirements of: 1) high spatial resolution, 2) localizing point on the chest-wall, 3) non-invasiveness, 4) easy methodological approach, 5) short measurement time, 6) contactless, 7) modularity which allows a fast set-up also in clinical environment.

Once a system for scanning the chest-wall and measuring impedance maps is available it is possible to employ it in studying different pathologies or not physiological conditions which are supposed to induce alteration in the chest-wall mechanics.

In particular a protocol for the measurement of mechanical impedance of patients during anesthesia induction has been design and implemented.

This chapter is organized into two sections: the first one deals with the description of the scanning system, while the second one is focused on the protocol.

The realized system has been carefully designed to fulfill the requirements in particular it has been organized in three conceptual blocks, each one with a well-defined function:

The FOT unit provides the pressure stimulus and the measurement of the pressure and flow at the open airways. It can be organized according to the different condition in which the measurement should be performed, i.e. during mechanical ventilation or spontaneous breathing. The FOT approach satisfies the requirement of a non-invasiveness and non-cooperation required to the patients;

The optical scanning unit provides the measurement of velocity and absolute distance of several points (up to five) of the chest-wall by means of interferometers and distantiometers which can be moved to scan the whole chest-wall. Interferometer spatial resolution allows the estimation of the small vibration produced by the pressure stimulus and grants for non-invasive and contactless features

The electronic unit allows: to record all the data, to drive the pressure stimulus generator and finally to move the optical scanning unit.

Then the measurement protocol is described. ARDS, thoracic surgery, and anesthesia are associated with atelectasis, disturbed ventilation-perfusion relationship, and hypoxemia. It has been shown that in these patients the mechanical behavior of the respiratory system is altered, with a reduction in functional residual capacity and compliance. Mechanical ventilation is essential in the treatment of all these patients and, in particular, positive end-expiratory pressure (PEEP) is used to reverse atelectasis and improve lung function. Optimal open lung PEEP may be defined by a mechanical point of view which can be evaluated by measuring input impedance, as proved in previous works, but also taking advantages of the variations in the chest-wall mechanics.

All patients were studied in the supine position while ventilated in pressure support (PS) mode. Just before surgery measurements of oscillatory mechanics were performed at different stages measuring input impedance at 5-11-19 Hz by FOT, local transfer function at 5-11-19 Hz, FRC (Functional Residual Capacity)

The patients were connected to the mechanical ventilator and the laser scanning system has been adopted to measure chest wall movements.

At the end of the chapter results and discussions are reported. Since this group of patients is healthy from the respiratory system point of view, derecruitment is not awaited, while symmetry in the left and right part can be explained as a substantial homogeneity of the respiratory system.

4 CONCLUSION AND DISCUSSIONS

The research activity presented in this work was aimed at proposing s new system and methodology to study local chest wall mechanics by means of oscillatory mechanic which can find an application for the study and the clinical management of patients affected by diseases which induce alterations in the chest wall mechanics. For this purpose new experimental setups and protocols have been designed and used to measure oscillatory mechanics.

Our data demonstrate that laser interferometry could be used to measure accurately displacements of the chest wall as small as 400nm making this technique suitable for all the applications involving the measurement of wide chest wall movement as well as for the detection of very small displacement as those occurring when a pressure wave reach the chest surface.

Phase delay between pressure at the mouth and the chest-wall surface can be estimated by matching FOT and optical devices. Phase delay changes according to the different compartments, and in relation to the chest-wall status.

In conclusion, oscillatory lung mechanics can be considered as a powerful and quantitative tool to measure lung mechanics. This information could be used as a complement of the standard techniques in order to diagnose, treat and monitor in a more specific and effective way pathologies and non-physiological conditions characterized by alteration in chest-wall mechanics

INTRODUCTION

The respiratory system is a complex system which accomplishes gas exchange by means of the synergy among functions and structures which have specifically developed at this aim. Processes involved in gas exchange are: 1) ventilation, that is air transport inside and outside the lungs; 2) oxygen and carbon dioxide diffusion among alveoli and blood; 3) oxygen and carbon dioxide delivering for the blood to the cell and finally, 4) ventilation regulation. The respiratory system functionalities are not only reliant on its components, that are a complex branching system of tubing (*airways*), a huge exchange region (*the alveoli*) where gases can diffuse from and into the blood, but its behavior is deeply influenced also by the respiratory muscles and structures that form a boundary of it, such as the chest-wall and the diaphragm. Impairment at only one of these structure or functions can seriously affect not just the respiratory system but it can yield to a general worsening in the life condition of the subjects due to labored breathing or asthma attacks, fatigue and difficulty with mobility, heightened sensitivity to ordinary substances and chemicals, and compromised immunity to infection.

In particular ventilation capability, which represents the first step in breathing activity, relies on the mechanical properties of the whole respiratory system: the resistance of the airways, the compliance and elastic recoil of the lung parenchyma, stiffness in chest wall and abdomen, all these components contribute in different and complex ways in the relationship between the pressure generated by active components inside the respiratory chain and the volume of gas introduced.

Diseases affecting the respiratory system, such as ARDS (acute respiratory distress syndrome), restrictive diseases and lung edema, produce alterations and inhomogeneities in the lung structure and in the chest wall which cause changings in the mechanical properties.

In more details, ARDS is defined as a syndrome of inflammation and increasing permeability that is associated with a constellation of clinical, radiological and physiological abnormalities that cannot be explained by, but may coexist with, left atrial or pulmonary capillary hypertension. The physiological consequences are severe hypoxaemia due to right-to-left shunting of blood and decreased pulmonary compliance due to filling and closure of alveoli. As the airspaces fill with fluid, the gas exchange and mechanical properties of the lung deteriorate.

Restrictive lung diseases are characterized by reduced lung volume, either because of an alteration in lung parenchyma or because of a disease of the pleura, chest wall, or neuromuscular apparatus. The many disorders that cause reduction or restriction of lung volumes may be divided into two groups based on anatomical structures. The first is intrinsic lung diseases or diseases of the lung parenchyma. The second is extrinsic disorders or extra-parenchymal diseases, which involve the chest wall, pleura, and respiratory muscles, the components of the respiratory pump. Diseases of these structures result in lung restriction, impaired ventilatory function, and respiratory failure (e.g., non-muscular diseases of the chest wall, neuromuscular disorders).

Also pulmonary edema can cause alterations in lung mechanics that directly contribute to clinical morbidity and mortality rates. Both the location of the edema fluid (interstitial versus alveolar pulmonary edema) and the etiology of the pulmonary edema contribute to the severity and type of abnormalities of lung mechanics observed. The alterations in lung mechanics associated with the adult respiratory distress syndrome may involve the direct effects of released mediators, alterations in pulmonary surfactant, and altered airway reactivity, as well as the direct effects of the edema fluid.

Up to the present day, the diagnosis and the management of these kinds of pathologies have been carried out mainly by chest radiography, which reveals diffuse opacity according to the stage of the pathology and CT. More specifically ARDS can be detected also by means of measurement of lung endothelial and alveolar epithelial barrier function and BAL (Bronchoalveolar lavage); while restrictive pathology can be detected also by means of some laboratory tests aimed to measure the concentration of well-known markers such as elevated creatine kinase level. Anyway all of them present some intrinsic limitations, indeed they are invasive or required long time to be carried out and thus they can't be used to monitor in a continuative way the pathology evolution.

On the contrary several published data suggest that global but also local chest wall mechanical properties are parameters that might be useful for the evaluation of structural elasticity and inertia on the overall behavior of the respiratory system and for estimating the possible impact of both restrictive and obstructive diseases on respiration, thus it could be useful in the assessment of the pathology providing a handy tool for clinicians during the diagnosis but also the therapy of the disease. Although the rich informative content of the chest wall mechanical properties, up to now this parameter has been almost disregarded because of the intrinsic difficulties in its measurement. Therefore a new approach for the detection and the monitoring of these diseases can be based on the measurements of the local and global chest-wall mechanics and the extraction of parameters which are sensitive to pathophysiological alteration. The more promising and inspiring approach has been reported by Dellacà et al [2002] which suggest the union of FOT (Forced Oscillation Technique) and OEP (Optoelectronic Plethysmography) to estimate the impact of low amplitude pressure stimuli given at the mouth at the level of vibration induced at the chest-wall.

Briefly FOT method is based on the measurements of the response of the respiratory system to small pressure stimuli generated externally and applied during normal breathing. There are two different approaches in studying oscillatory mechanics of the respiratory system: one could study the response of the system by analyzing the flow that the pressure stimulus has been able to induce from the mouth or analyse how the stimulus has travelled through the system by measuring the displacement of the external surface of the thorax. The former, widely used in oscillatory mechanics, allows the estimation of the input impedance by combining the measurement of pressure and flow at the airway opening, while the latter allows the estimation of the transfer impedance by combining airway opening and chest wall vibrations.

OEP is a system for motion capture specifically developed to estimate breathing volumes. It is able to measures the three-dimensional coordinates of several passive markers applied to body landmarks on the chest-wall by using several TV cameras which frame the subject by different angles. From these data a dedicated algorithm computes the three-dimensional coordinates of the markers by perspective projection described by the collinearity equations (stereo-photogrammetric methods). Then by means of triangulation on the markers detected or by using the Gauss theorem it is possible to calculate the volume enclosed into the markers surface.

In the past years, most of the published studies were focused on the estimation of the input impedance obtained from the response of the respiratory systems to a pressure stimulus given at the mouth providing information about the average properties of the respiratory system and in particular about the mechanical properties of the airways, on the contrary little is known about the transfer impedance. In the above mentioned study, global transfer impedance and its distribution on the chest wall has been estimated at different frequencies on healthy subjects showing how impedance is not equally distributed on the thoraco-abdominal wall but the ribcage is the predominant component at those frequencies. This study opens interesting insight into the comprehension of chest wall mechanics but it is limited by the complexity in the methodological approach- use of OEP system with 69 markers and cameras which should be carefully calibrated- and costs connected. The already uncovered point in this approach is the measurement of chest wall vibration in a reliable and resolute way by means of low costs and not invasive devices.

The objective of this work is to develop and validate a new method that allow the estimation of the local mechanical properties of the chest-wall based on FOT and optical devices in a non-invasive, low cost and compact way. This new approach will relay on the possibility to have reliable and resolute measurements of the displacement of the chest-wall in order to allow the estimation of impedance map: its knowledge will allow to develop new methodological and technological tools useful for the bed-side assessment of patients affected by pathologies which alter the chest-wall mechanics such as ARDS and restrictive diseases.

To achieve these results new technology, at least for the respiratory system, are needed in particular an optimum candidate is laser self-mixing interferometry which allows the measurement of very little relative displacement (theoretical resolution less than one micrometer).

1. ASSESSMENT OF CHESTWALL KINEMATICS AND MECHANICS

The role of respiration is to bring oxygen to tissues and to carry out carbon dioxide, which is reached through four steps: 1) pulmonary ventilation, in order to transport air from the atmosphere to alveoli, 2) diffusion of oxygen and carbon dioxide through alveolar-capillary membrane, 3) transport of oxygen and carbon dioxide from and to cells in blood and liquids, 4) control of ventilation and of other features of respiration.
These vital functions are performed not only by means of its components such as the airways, the lung parenchyma and the pleura, but they rely also on the behavior of the respiratory muscles and on the mechanical properties of the chest-wall, the box which encloses the whole system.

1.1. RESPIRATORY SYSTEM

1.1.1. ANATOMY

The respiratory tract (or system) begins at the nose and ends in the most distal alveolus as reported in Figure 1.1. Thus, the nasal cavity, the posterior pharynx, the glottis and vocal cords, the trachea and all the divisions of the tracheobronchial tree are included in the respiratory system. The *upper airways* consist of all structures from the nose to the vocal cords, including sinuses and the larynx, whereas the *lower airways* consist of the trachea, bronchi and alveoli. The major function of the upper airways is to "condition" inspired air that means to heat it and to humidify it. The nose also acts as a filter, entraps, and clears particles greater than 10 µm in size.
The major structures of the larynx include the epiglottis, arytenoids, and vocal cords. The epiglottis and arytenoids cover the vocal cords during swallowing. Thus, under normal circumstances, they inhibit aspiration into the lower respiratory tract.
The tissue of the lung is called parenchyma, it is very elastic and it can easily distend. It contains elastin and collagen fibers. The collagen fibers normally are folded and they distend during the lung expansion; the elastin fibers stretch when the lung expands. Both fibers, however, exert a force to regain their initial condition. In every healthy human even at the end of the deepest expiration, when the lung contains the minimum amount of air, the fibers of the parenchyma remain always stretched to a certain extent, exerting elastic recoil.

The pleurae are serous, thin, smooth and transparent membranes, covered with mesothelium and forming closed sacks placed between lungs and the internal of thoracic cavity.

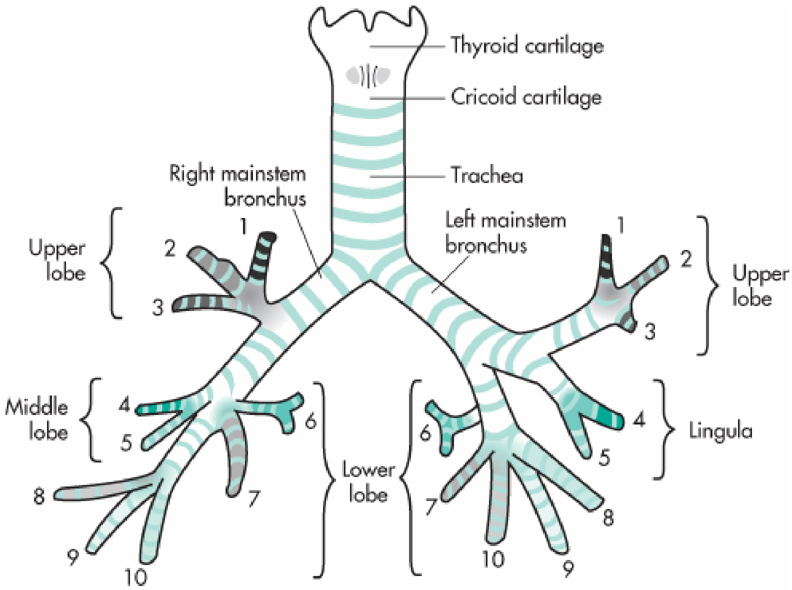

Figure 1.1: Segments: *1,* Apical; *2,* posterior; *3,* anterior; *4,* lateral (superior); *5,* medial (inferior); *6,* inferior; *7,* medial basal; *8,* anterior basal; *9,* lateral basal; *10,* posterior basal. Bronchopulmonary segments, anterior view.

Every pleura consists of two sheets of membranous tissue: *pulmonary pleura*, wrapping the lung, and *parietal pleura* which wrap the inside of the thorax. The space in between these two membranes (*intrapleural cavity*) is filled by a very thin layer of fluid, the *intrapleural fluid*, having excellent lubricating properties. The excess of this fluid is continuously removed through the lymphatic system, in order to maintain a slight suction in the pleural cavity, that is, the pressure of the pleural fluid is sub-atmospheric. The negative intrapleural pressure makes the lung volume to follow closely volume changes of the thoracic cage but, at the same time, thanks to the pleural space and to the pleural fluid, the lung and the thoracic cage are allowed to slide each other. Figure 1.2 shows the relative position of the lungs and the thoracic cage in the resting position, at the end of a quiet expiration, and at the end of the inspiration. We can notice that the lungs slide into the comer of the thoracic cavity, to fill the room left empty when the diaphragm contracts.

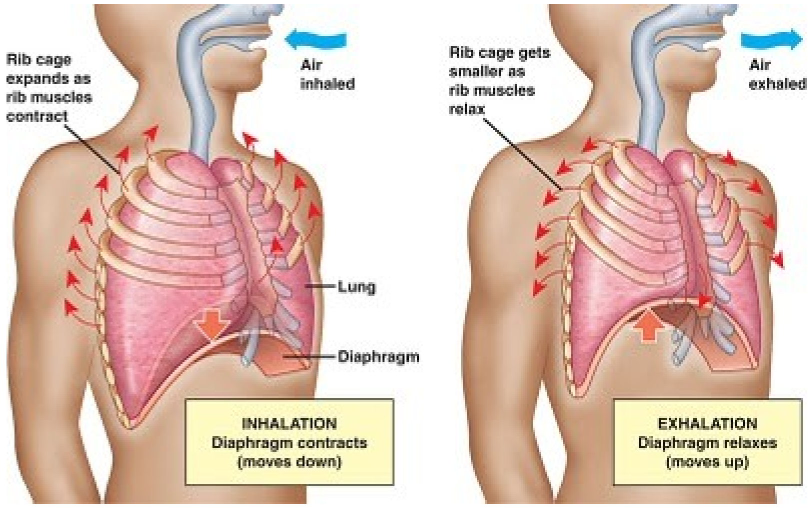

Figure 1.2: Both the lungs and the internal wall of the thoracic cavity are covered by a membranous sheet of tissue called pleura. a. The two pleura are folded in such a way to create two distinct intrapleural cavities (their dimensions are here exaggerated). b. At inspiration, when the diaphragm contracts, the lungs slide along the thoracic cavity to fill the freed space

1.1.2. VENTILATION MECHANICS

The ventilation of the lungs is accomplished alternating phases in which air is flowing into the lungs (inspiration) and phases in which air exits the lungs (expiration). The mechanics of these air movements are strictly related to the peculiar anatomy of the chest.

Inspiration is determined by the contraction of the inspiratory muscles, which are basically the diaphragm and the external intercostal muscles. The diaphragm represents the lower closure of the chest; when relaxed it is dome shaped while when it contracts it moves downward and it flattens.

In this way the bowels are pressed down and the volume of the thoracic cavity increases. During quiet respiration the diaphragm alone is responsible for the 75% of volume expansion of the thoracic cavity.

External intercostal muscles are located in between the ribs, elongated forward and downward, as shown in Figure 1.3. The same figure shows the forces acting on the ribs when they contract, and the moments of these forces around the pivot points at the spinal cord. Accordingly to the third principle of dynamics, each muscle exerts the same force on both ribs it is attached to. The force it exerts on the lower rib, however, has a greater arm than the force acting on the upper rib, due to the physiological leaning of the muscles. The imbalance of the two moments takes the rib to rotate upward. Since ribs normally slant downward, when rotating, they push the sternum in front. This increases the antero-posterior diameter of the thoracic cage and therefore the volume of the thoracic cavity enlarges. The expansion of the thoracic cavity produces negative pressure in the intrapleural space, which induces the lungs to expand. The alveoli, the alveolar ducts and the bronchioles in their turn enlarge, creating a negative pressure (with respect to atmospheric) inside them, which recalls air from the outside.

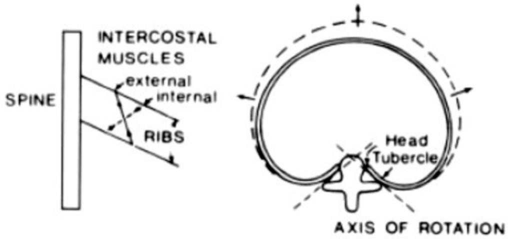

Figure 1.3: When the external intercostal muscles contract, the ribs are pulled upward and forward, and they rotate on an axis joining the tubercle and head of rib. As a result, both the lateral and anteroposterior diameters of the thorax increase. The internal intercostals have opposite action.

Expiration in quiet breathing occurs passively, without the recruitment of any muscle. When the diaphragm and external intercostal muscles stop contracting, the weight of the thoracic cage and its own elasticity bring it to its resting position. At the same time the compressed bowels push back the relaxed diaphragm as well and the volume of the thoracic cavity resumes its smaller dimensions.

If the volume of the lungs decreases, the pressure inside them rises, becoming greater than the atmospheric pressure. This forces the air out, through the airways. When expiration needs to be faster, as during exercise or coughing, the expiratory muscles are recruited to provide greater ventilation. Expiratory muscles are mainly the abdominal muscles and the internal intercostal muscles. When contracting the abdominal muscles squeeze the viscera, which in turn push up the diaphragm. Internal intercostal muscles work similarly to external intercostal muscles (inspiratory muscles); they are also located in between the ribs but they are turned symmetrically, that is the expiratory muscles lean backward and downward.

When these muscles contract, the ribs are pulled down, so that the sternum and the rib cage regain fast their resting position. Expiratory muscles, besides, are able to force the thoracic cavity to a smaller volume than at the end of a passive expiration. Nevertheless, whatever effort is placed in forcing the expiration, it is not possible to empty completely the lungs, which physiologically will always contain some amount of air.

1.1.3. MECHANICAL MODELING OF THE RESPIRATORY SYSTEM

A. ONE COMPARTMENT MODEL

From the anatomical and physiological description given above it is possible to deduce simplified models of the respiratory system, which resume the features that are essential in determining the efficiency of the ventilation. A classical model is represented in Figure 1.4. According to this model the whole respiratory system is subdivided in subsystems and each of them is characterized by one lump parameter. Similar models provide a simplified description of the actual interpretation of the respiration mechanics and also the measurements that are performed for diagnostic purposes are coherent with the same clinical interpretation.

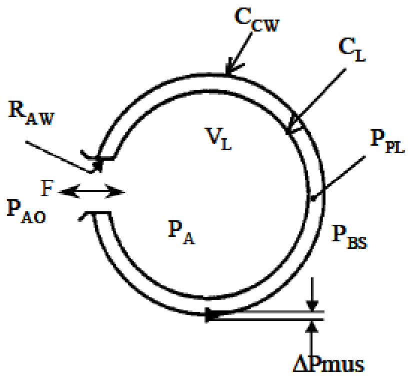

Figure 1.4: A model of the ventilation mechanics. The airways oppose resistance to the air flow; the lungs and the thoracic cage are schematized as elastic bags.

The influence of the airways on the ventilation mechanics is classically described by the resistance they oppose to the air flow. The overall resistance of the airways is determined mainly by the flow conditions in the trachea and in the large bronchi, while the small bronchi and the bronchioles give a small contribution. The upper airways are responsible for the 80-90% of the overall resistance, while the remaining 10-20% is due to the flow condition in the smaller airways. This is explained by two reasons: firstly all the air flow passes through the upper airways where, consequently, air velocity is high and the flow is turbulent. Turbulent flow gives rise to a greater pressure drop; hence it corresponds to a greater resistance than laminar flow. Secondarily, although the terminal airways are very small and for this reason singularly they oppose high resistance to the air flow, the lungs account millions of terminal bronchioles and, considered all together, they add up to a large cross section, which minimally stops the air flow. The effect is similar when in an electrical circuit many large resistors are connected in parallel.

In adults R has an average value of about 3 cm H_2O of pressure drop for 1 l/s of air flow.

B. *ADVANCED MODELING*

In our model the lungs and the chest wall are represented in the form of elastic bags one contained into the other. When a system can be schematically represented in this form, its static behavior is completely described by the relationship connecting the volume inside the elastic bag to the pressure difference between the inside and the outside of the bag. This relationship is determined by the mechanical features of the bag's wall. The curves drawn in Figure 1.5 provide a graphical representation of the volume/pressure relationship for the lungs when they are taken out of the chest wall (P_L) and for the thoracic cage without the lungs inside (P_W).

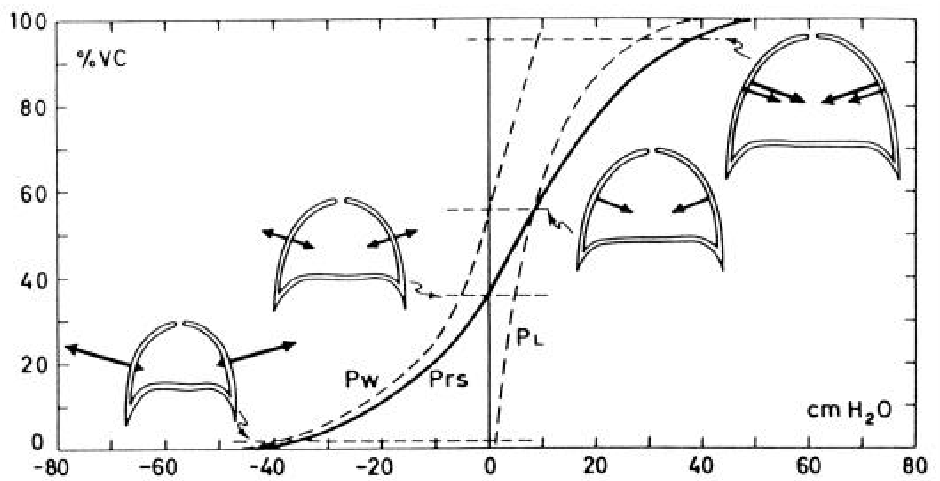

Figure 1.5: Static curves of the lungs (P_L), of the chest wall (P_W) and of the lungs-plus-chest wall (P_{rs}). The slope of these curves is related to the compliance of the systems.

The first curve (P_L) is determined by the characteristics of the parenchyma. The curve of the chest wall alone (P_w) derives from the passive behavior of the tissues that construct the chest and all organs, which somehow interfere with lungs expansion (the bowels for instance are compressed by the diaphragm during inspiration). The third curve represents the whole system lungs-plus-chest wall (P_{rs}); it is the sum of the other two curves.

In order to describe chest wall mechanics during spontaneous breathing in normal subjects, in the past several models have been proposed. The simplest model of chest wall motion was developed by Konno and Mead (1) , who partitioned it into the rib cage and the abdomen. Successively, it was demonstrated that the rib cage cannot be considered as a single compartment and therefore, different two-compartment rib cage models were proposed, in which the part apposed to the lung (pulmonary rib cage) was distinguished from the part apposed to the diaphragm (abdominal rib cage). In Figure 1.6, we reported a detailed mechanical model of respiratory muscle actions on the chest wall, divided into pulmonary rib cage, abdominal rib cage and abdominal wall.

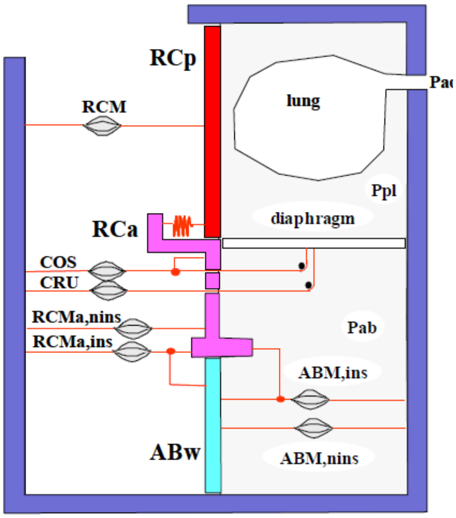

Figure 1.6: Simplified mechanical model of the chest wall incorporating a two-compartment rib cage, i.e. pulmonary (RCp) and abdominal (RCa) rib cage, and abdominal wall (ABw). The respiratory muscles are grouped into: upper rib cage muscles (RCM); lower rib cage muscles (RCMa) divided into insertional (RCMa,ins) and non-insertional (RCMa,nins) on the abdomen; costal and crural diaphragm (COS and CRU, respectively); abdominal muscles (ABM) divided into insertional (ABM,ins) and non-insertional (ABM,nins) on the lower rib cage. Pao, Ppl and Pab represent the airways opening, pleural and intra-abdominal pressures, respectively.

Upper rib cage muscles act on pulmonary rib cage and lower rib cage muscles act on abdominal rib cage. Lower rib cage muscles are divided into insertional and non-insertional on the abdominal wall. The diaphragm is split into its costal and crural parts. The abdominal muscles are divided into insertional and non-insertional on the rib cage. The spring represents the mechanical linkage between pulmonary rib cage and abdominal rib cage and describes the restoring force developed by distortions between the two compartments away from the relaxation configuration.

In conclusion, the partitioning of the pressures differences across different parts of the chest wall and the possibility to measure the volume displacements of the two-compartment rib cage and abdomen have proved major advances in our knowledge of the act of breathing in normal conditions. This is important to better understand the behavior of the chest wall also in different "pathological" conditions.

C. MECHANICAL ELEMENTS

Evaluation of mechanical respiratory system properties consists in studying system cinematic and its dynamic. The first deals with balances configuration that means the positions and the forces acting on the system, while the second deals with the relationship between system movements and the forces which cause them.

The measurements on mechanical system are force and positions, since the respiratory system has a tridimensional geometry, these can be translated into volume, flow (volume variation) and pressure.

Another fundamental aspect is the estimation of passive elements mechanical properties (resistance, elastance and inertance) as reported in Table 1.1 and the estimation of active components action (pressure, work, power) such as the respiratory muscles.

Usually to make easier the comprehension of respiratory system mechanics, an analogue model is used, in particular the respiratory system can be considered as a three dimensional analogue of a mass-spring-damper system.

The respiratory system is usually modeled as an assemblage of just three simple types of primitives passive elements, that are elastance, inertance and resistance; each of them is associated to a different way of handling energy.

In particular the elastance is connected with storage by potential energy, inertance with storage by means of kinetic energy, resistance with dissipation by means of friction.

Table 1.1: Analogue measure for respiratory system, mechanical and electrical models

	Respiratory system	**Mechanical model**	**Electrical model**
State:	Volume: V Flow: $\dot{V} = \frac{dV(t)}{dt}$ Flow variation: $\ddot{V} = \frac{d\dot{V}(t)}{dt}$ Pressure: P	Position: x Velocity v: $\dot{x} = \frac{dx(t)}{dt}$ Acceleration: $a = \ddot{x} = \frac{d\dot{x}(t)}{dt} = \frac{d^2(x(t))}{dt^2}$ Force: F	Charge: q Current: i= $\frac{dq(t)}{dt}$ Current variation: $\dot{i} = \frac{di(t)}{dt}$ Voltage: V
Properties:	Elastance E=P/V Resistance: R= P/ $\dot{V}$ Inertance: I=P/ $\ddot{V}$	Stiffness: K=F/x Friction: B= F/v Mass: M=F/a	Capacity: C=q/v Resistance: R= v/i Inductance: L=v/ $\dot{i}$

Other used components are ideal flow and pressure generators.It is a convention to characterize each element in terms of drop pressure at its terminals and flow passing through it. The relationship between pressure and flow is not necessary linear (Figure 1.7 and 1.1) but to avoid complex non linear characteristics, it is possible to set volume history, lung volume and volumetric flow rate and to consider just little movements around the equilibrium point.

$$\Delta P = P_2 - P_2 = P_{21} = f(\dot{V}) \qquad 1.1$$

Where $f(\dot{V})$ is a function of the volumetric flow rate and P is gas pressure. Rohrer's equation 1.2 for flow resistance is an example of a well-known constitutive relation, where k is a constant and the relation is not linear.

$$\Delta P = k_1 \dot{V} - k_2 \dot{V}|\dot{V}| \qquad 1.2$$

The linearized relationship of pressure difference to volume flow is called an ideal elemental equation.

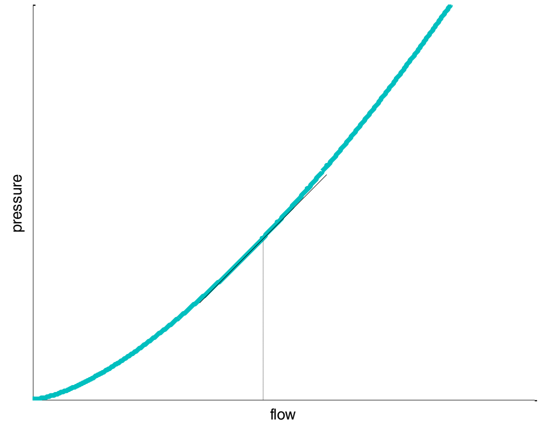

Figure 1.7: Rohrer equation taken as an example of non linear pressure-flow relations linearized for small departure about any given bias flow rate.

According to the analogue circuital model, passive component have positive power consumption.

Elastance (compliance)

An ideal fluid elastance (E) has pressure differences in direct proportion to volume, and it can be also thought as the reciprocal of compliance.

Here the equation 1.3

$$\frac{dP(t)}{dt} = E\dot{V}(t) \qquad 1.3$$

Under static conditions in completely relaxed patients, airway pressure is equal to the elastic recoil pressure of the respiratory system (2). Thus, compliance is measured as the change in lung volume per unit change in applied static pressure (elastic recoil pressure). The units are liters per cmH_2O or milliliters per cmH_2O. Compliance is the mathematical inverse of elastance, the amount of pressure required to change the volume of the lung by a given amount (3). Although both terms are useful, the clinical practice and refers to compliance more frequently than elastance will be followed.

The lung and chest wall are said to be aligned in series, since pressure applied to the airway is first transmitted to the lung. From the lung, a reduced amount of applied pressure is transferred to the chest wall. Because of this series relationship, the pressure to distend the respiratory system is the sum of the pressures required to distend the lung and the chest wall (1.4, 1.5). Thus the elastic of the respiratory system (Ers) is the sum of the lung elastance (E_L) and chest wall elastance (E_{CW}).

$$E_{rs} = E_L + E_{CW} \qquad 1.4$$

$$\frac{1}{C_{rs}} = \frac{1}{C_L} + \frac{1}{C_{CW}} \qquad 1.5$$

The lung and the chest wall display different pressure-volume. The resulting pressure-volume relationship of the respiratory system is sigmoidal in shape, and compliance is greatest in the midvolume range, where breathing normally occurs. At the completely relaxed static equilibrium volume of the respiratory system, elastic recoil of the lung and the chest wall exactly balance each other. Also at this point, compliance of the lung and chest wall is approximately equal in normal subjects. In this midvolume range, the elastic work of breathing and fluctuations in transpulmonary pressure will be minimized (4).

Resistance

An ideal fluid resistance exhibits a pressure drop proportional to flow rate according to the elemental relation reported in the following equation (1.6).

$$P(t) = R\dot{V}(t) \qquad 1.6$$

For steady fully developed laminar flow at low Reynolds number (parabolic velocity profile), in a long straight pipe of length l and cross sectional A, containing fluid viscosity μ, the resistance can be expressed as in the following equation (1.7):

$$R = \frac{8\pi\mu l}{A^2} \qquad 1.7$$

This is the Poiseuille formula for flow resistance.

With fully turbulent flow, the pressure difference is proportional to the square of the gas flow multiplied by another constant (K2), which is related to the density of the gas and is independent of its viscosity (1.8):

$$P(t) = K_2 \dot{V(t)} |\dot{V}| \qquad 1.8$$

In the case of the respiratory system, resistance is rarely linear, and the relationship between pressure and flow is usually expressed by Rohrer's equation (1.9):

$$P(t) = R\dot{V}(t) + K_2 \dot{V(t)} |\dot{V}| \qquad 1.9$$

The customary units of respiratory resistance are cmH_2O/(liter/s). The mathematical inverse of resistance is conductance, but this term is seldom used. The resistance of the respiratory system can itself be subdivided into elements that are in series and hence additive (5). These elements include pulmonary resistance (R_L) and resistance of the chest wall (R_{CW}). Pulmonary resistance is itself further subdivided into airway resistance (Raw) and a lung tissue component. Each of these components is determined by measuring the net pressure required to produce flow of the component .The relationship between driving pressure and airflow depends on whether flow is laminar, turbulent, or a mixture of both (5)

Inertance

An ideal fluid inertance links pressure to first derivate flow as shown in the following equation (1.10):

$$P(t) = I\frac{d(\dot{V}(t))}{dt} \qquad 1.10$$

Where the inertance is the value reported in 1.11:

$$I = \frac{\rho\eta l}{A} \qquad 1.11$$

Fluid inertance increases proportionally with tube length *(l)* and gas density (ρ), but decreases as the reciprocal of the cross section (A).

At frequencies normally encountered during spontaneous and mechanical ventilation, the effects of inertance are usually insignificant and are customarily ignored (6). The pressure generated by inertance is in the opposite direction to that generated by the elastance of the respiratory system. Hence, inertial forces tend to slightly offset the impedance to flow provided by the stiffness of the respiratory system.

The sum of the elastic and inertial forces is referred to as the *reactance* of the respiratory system.(7)

Active elements

There are active elements capable of delivering energy to the system over an extended period that account for sustained respiratory system motions; they may be respiratory system muscles or external loudspeaker or pumps.

Two useful idealized sources are the volume flow (current source) and the pressure source (voltage source); the first can provide a fixed flow independently from the drop pressure at its terminals, while the second can maintain a fixed pressure despite of the flow through it.

The equation of motion

A linear respiratory system model is formulated connecting the passive elements listed above and imposing mass conservation and Newton law.

The mass conservation principle is the equivalent of Kirchhoff's current law in electrical circuits; the second is the principle of compatibility. It applies to pressure drop in the system and guarantees that the net pressure drop taken in a specific direction around any closed path in the system circuit, must be zero, which is the analogous of Kirchhoff's voltage law.

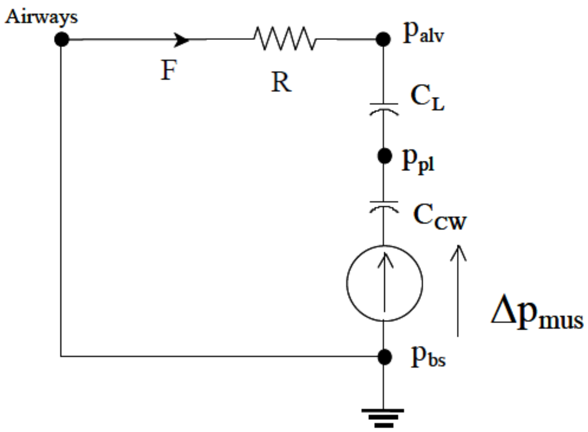

Figure 1.8: An Electrical analogue of the respiratory system. The analogy is between flow and current, volume and charge, pressure and voltage.

The simplest model of respiratory system is represented in Figure 1.8; it is just a RLC series. Applying the continuity and the compatibility principles to the model, the following equation (1.12) can be found:

$$P_{rs} = P_{ao} - P_{bs} \qquad 1.12$$

Substituting the elemental relations into Eq. 1.8 and rearranging the term, then one obtains 1.12 and 1.13:

$$P_{rs} = \Delta P_C + \Delta P_R + \Delta P_I = EV + R\dot{V} + I\ddot{V} \qquad 1.13$$

This is a very important equation known as the motion equation.

1.2. ASSESSMENT OF RESPIRATORY MECHANICS IN CLINICS

As described in the previous paragraph, the mechanical properties of the respiratory system may be express by means of few lumped parameters whose measurement has a diagnostic value in identifying the presence of a disease or in assessing what kind of disease is eventually present but, at the same time, it is time consuming and not easy to perform. Therefore up to now in clinical practice the objectives of measurement procedures are not exactly the airways resistance or the compliance of the lungs or the thoracic cage, but different parameters related to the same conceptual representation of the respiratory mechanics. In particular, the state variables are flow, volume and pressure, here a review of the most significant terms is reported.

1.2.1. LUNG VOLUME DEFINITIONS

The measurement of the lung volumes are normally obtained by means of a spirometer. In Figure 1.9 is shown a typical spirometric track where is depicted the excursion of lung volume during normal breathing and during a maximal inspiration and expiration. The lung volumes depicted are:

1. VT is the tidal volume representing the air volume normally breathed;
2. TLC is the total lung capacity, the lung volume at maximal expansion;
3. RV is the residual volume, the gas volume after a maximal expiration;
4. IRV is the inspiratory residual volume;
5. ERV is the expiratory residual volume;
6. FRC is the functional residual capacity, it is the lung gas volume after a normal expiration;
7. IC is the inspiratory capacity, the maximum gas volume breathed in starting at FRC;
8. VC is the vital capacity, the maximum gas volume breathed in starting at RV.

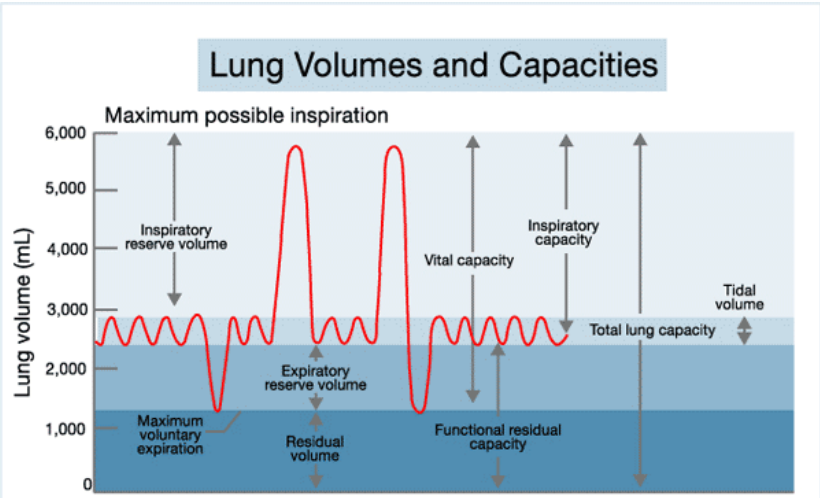

Figure 1.9: Spirometric tracks showing the principle lung volume measurements.

In order to measure breathing volumes, in clinical environment are used two different approaches based on a direct measurement of the volume or on the measurement of the flow, whose integration provides volume.

1.2.2. LUNG VOLUME MEASUREMENTS

The instrumentation commonly operated to measure volumes in testing the pulmonary function can be subdivided into two major categories: volume sensing devices, commonly known as *spirometers,* and flow sensing devices, called *respiratory flowmeters* or *pneumotachometers.* Since the air flow is defined as the volume of air inspired or expired per unit of time, the overall volume moved results from integration of the air flow or, vice versa, knowing the moved volume at every instant of time, we can derive the instantaneous flow just differentiating the volume. For this reason both kinds of devices can theoretically be used to yield to the same results. The measurements of lung volumes and respiratory flow are certainly non-invasive. The measurement devices remain outside of the body and they exploit the fact that the patient naturally moves air in and out of its lungs. This doesn't mean that the measurements can be considered absolutely free of any risk for the patient and for the physician, anyway the main hazards are connected with the risk of cross contamination between patients employing successively the same device or they can be associated to specific situations as pneumothorax, unstable cardiovascular status, in recent surgery.

A. SPIROMETRY

It consists in collecting gas which passes through the opening airways and computing the volume taken in the lung.

The most common spirometer is the bell one, Figure 1.10 which collects air into a sliding bell. By knowing the bell geometry and its movement, it is possible to estimate volume.

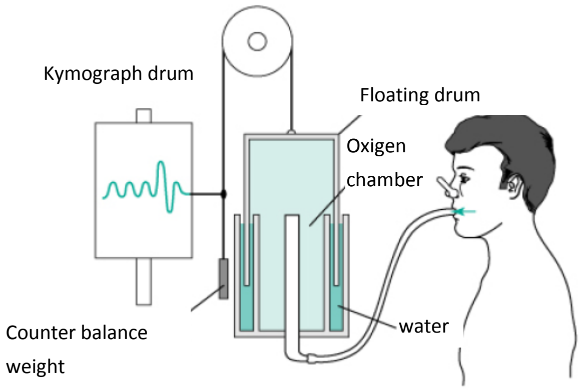

Figure 1.10: A spirometer consists of a floating drum put over a chamber, with the drum counterbalanced by a weight. The drum filled with air or oxygen is connected with the mouth of the patient by a tube. If the patient exhales into the spirometer, the drum rises, by inhaling in the drum falls. On a moving sheet of paper an appropriate recording is made

B. PLETHYSMOGRAPHY

Plethysmography is a general term used to describe all volume measurements, in particular lung volume estimation for respiratory system.

There are numerous types of plethysmograph, but in the clinical practice the total body plethysmograph represents the gold standard.

This method uses Boyle's gas law, which states that pressure × volume, is constant (at a constant temperature). The subject sits in an airtight box and breathes through a mouthpiece that is connected to a flow sensor (Figure 1.11). The subject then makes panting respiratory efforts against a closed mouthpiece. During the expiratory phase of the maneuver, the gas in the lung becomes compressed, the lung volume decreases and the pressure inside the box falls, because the gas volume in the box increases. Knowing the volume of the box and measuring the change in pressure of the box at the mouth, the change in volume of the lung can be calculated.

A. FLOW AND PRESSURE PLETHYSMOGRAPHY

The plethysmographs are divided in flow and pressure plethysmographs. In flow plethysmograph, airway resistance is measured by two maneuvers. The patient first pants while the mouth shutter is open to allow flow changes to be measured. Then, the mouth shutter closes at the patient's end expiratory or FRC level and the patient continues panting while maintaining an open glottis. This provides a measure of the driving pressure used to move air into the lungs.

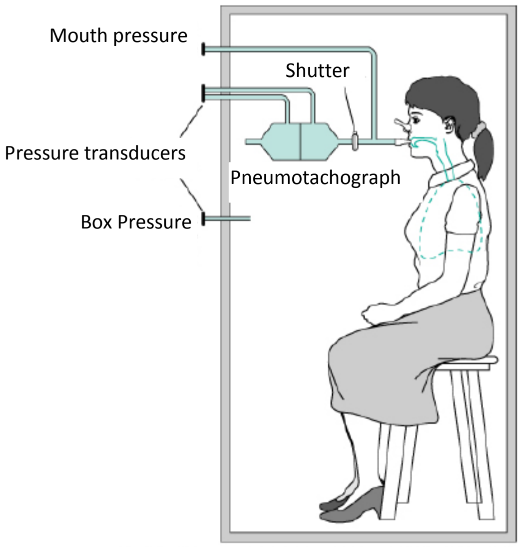

Figure 1.11: Example of a body plethysmography chamber.

Pressure plethysmographs are usually measured at the end-expiratory level and are then equal to FRC. The patient sits in the box, which has the pressure transducer in the wall of the device, and breathes through a mouthpiece connected to a device that contains an electronic shutter and a differential pressure pneumotachograph. The mouth pressure and box pressure changes that are measured during tidal breathing and panting maneuvers which are performed during the test by the patient at the end of expiration are sent to a microprocessor unit that calculates thoracic gas volume.

RESPIRATORY INDUCTIVE PLETHYSMOGRAPHY

This technique has become widely accepted method of measuring ventilation noninvasively. The original respiratory-inductive plethysmograph consisted of insulated wire stitched in a zigzag pattern, of about 2-cm pitch, into a vest consisting of elastic material. The vest encompassed the complete torso from upper chest to pubis, and there were eight continuous complete turns of the wire. Later this device was modified to two separate coils and remains the basis of the currently employed system.
The transducers of the respiratory inductive plethysmograph consist of two coils of Teflon-insulated wire sewn in a zigzag pattern onto elastic-fabricated bands.
One band is positioned to encircle the ribcage, at the level of the sternum, whereas the other band is worn midway between the lower ribs and the iliac crests (Figure 1.12). Modeling experiments with the respiratory-inductive plethysmograph have shown that an increase in the circumference of the coil associated with a reduction in the enclosed cross-sectional area causes a negative deflection in the output signal. Thus, the device measures the average of an infinite number of cross-sectional areas over its complete height rather than the circumference of the enclosed part. When the respiratory-inductive plethysmograph was placed around an expandable cylindrical form, a linear relationship was observed between oscillator output frequency and change in volume of the cylinder.

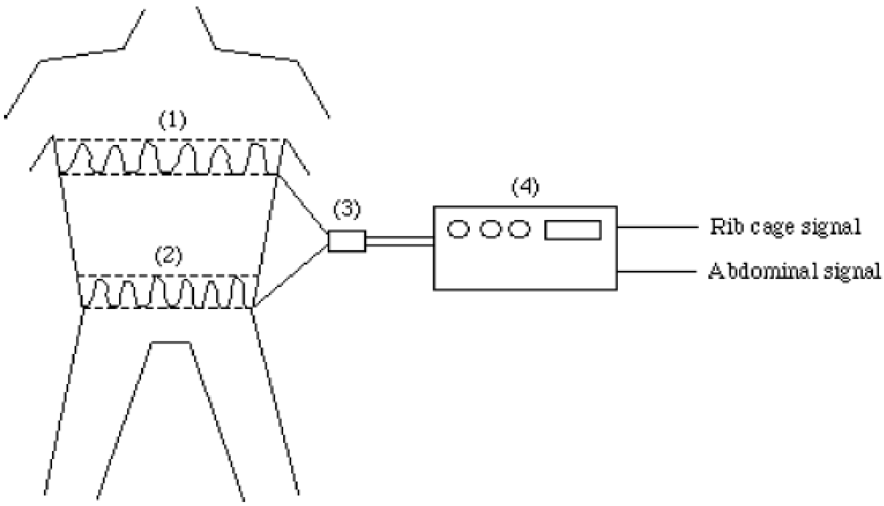

Figure 1.12: Respiratory Inductive Plethysmograph. (1) and (2): bands wrapped around the rib cage (RC) and abdominal (AB) compartments, (3) connecting cables, (4) electronic unit.

Calibration of the respiratory-inductive plethysmograph is based on the assumption that the respiratory system possesses two degrees of freedom, ribcage and abdominal motion. The ribcage and abdominal calibration factors can be derived by a number of different methods (isovolume manoeuvre, simultaneous equation, least squares, natural breathing, etc.), some of which can be performed by hand and others requiring assistance of a computer.

1.2.3. PRESSURE DEFINITIONS

By using the models described in the previous paragraphs it is possible to define the pressure in different sites of the respiratory system as shown Here the most important pressures are shown. They are:

1. P_A is the alveoli pressure;
2. P_{pl} is the pleural liquid pressure, in physiological condition it is negative respect the atmosphere pressure
3. P_L is the lung pressure. It is also: $P_L = P_A - P_{pl}$
4. P_{bs} (body surface) is the pressure measured on the thorax-abdomen surface. In physiological condition it equals the atmosphere pressure;
5. P_W(wall) is the drop pressure across the thorax-abdominal surface.
   It is expressed as: $P_W = P_{pl} - P_{bs}$;
6. P_{rs}(respiratory system) is the pressure of all the respiratory system

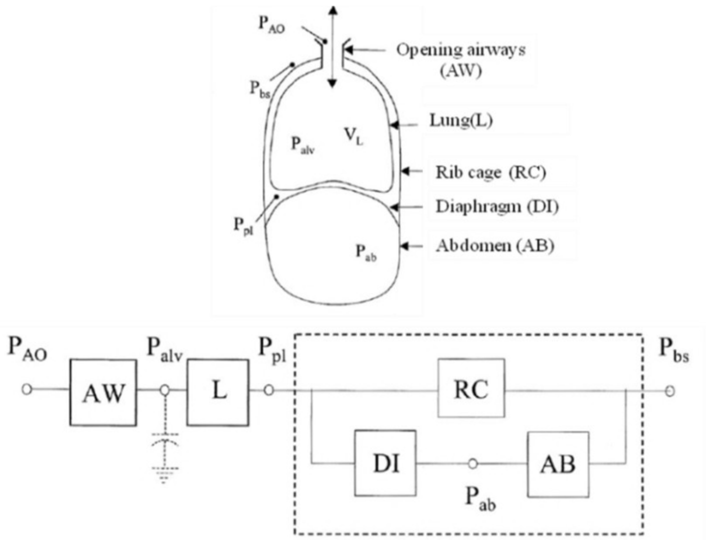

Figure 1.13 : a) a schematic morphology respiratory system representation, b) a simplified model showing the involved pressures

1.3. PATHOLOGICAL CONDITIONS

Lung diseases can be shared into two categories: restrictive and obstructive pathologies.
Restrictive lung diseases are characterized by reduced lung volume, either because of an alteration in lung parenchyma or because of a disease of the pleura, chest wall, or neuromuscular apparatus. In physiological terms, restrictive lung diseases are characterized by reduced total lung capacity (TLC), vital capacity, or resting lung volume. Accompanying characteristics are preserved airflow and normal airway resistance, which are measured as the functional residual capacity (FRC). If caused by parenchymal lung disease, restrictive lung disorders are accompanied by reduced gas transfer, which may be marked clinically by desaturation after exercise.
The obstructive pulmonary diseases are characterized by gas entrapment and FRC rise due to the increased airway resistance, the consequence is hyperinflation and reduction of vital capacity.

1.3.1. ASSESSMENT OF PATHOLOGICAL CONDITIONS

A. FEV1, FVC FEV1/FVC

These indexes are obtained by spirometric measurements.
In detail, FVC represents the vital capacity, while FEV1 represents the forced expiratory volume after one second from FVC Figure 1.14.

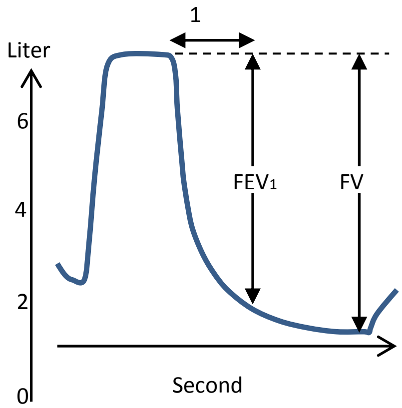

Figure 1.14: A spyrometric track showing FEV_1 and FVC.

FVC usually decreases in every lung pathologies, a more descriptive index is FEV_1/FVC ratio. If the pathology is obstructive, the FEV_1 decreases terribly with respect to a normal subject, consequently the FEV1/FVC ratio decreases too, on the other hand in restrictive pathology the FEV_1 is almost the same of a normal subject, for this reason the FEV_1/FVC slightly increases (Figure 1.15).

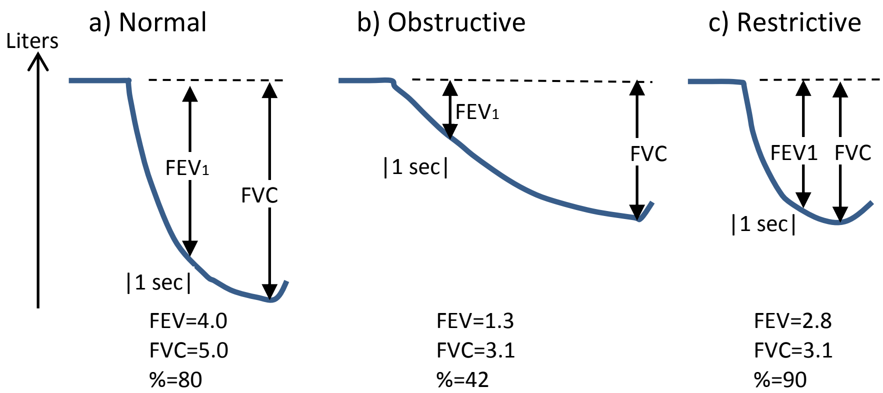

Figure 1.15: FEV1 and FVC ratio for normal subjects, obstructive and restrictive patients

From the spirometry it is possible to derive the flow, which is the first volume derivate. Important flow parameter is the $FEF_{25\%-75\%}$, which is estimated by imposing to the subject a forced maneuver and computing the slope of the line passing through the point of 75% volume and the point of 25% volume (Figure 1.9) [10].

If the pathology is obstructive, the slope decreases because the air undergoes a major resistance when it passes throw the airways, while in the restrictive one this parameter increases.

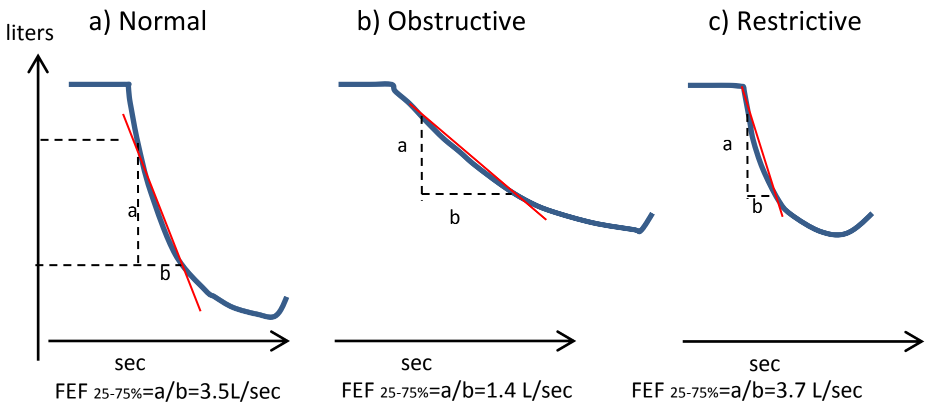

Figure 1.16: FEF 25%-75% for normal subjects, obstructive and restrictive patients

B. FLOW- VOLUME LOOP AND PEF

The Flow-volume loop is obtained by recording the instantaneous flow rate versus volume both during exhalation (expiratory flow-volume loop) and during inspiration (inspiratory flow-volume loop). The result is reported in Figure 1.10.

The flow-volume curve during a normal inspiration and expiration ('tidal loop'), and subsequently recorded during forced in- and expiration allows demonstrating the considerable ventilatory reserves available for a healthy subject. Compared to resting ventilation, inspiratory and expiratory flows can still be considerably increased. From this loop it is possible to derive also other parameters: 1) the peak expiratory flow rate (PEFR) which is the greatest flow rate achieved during the maneuver peak expiratory flow rate (PEFR), 2) maximal inspiratory flow at 50% of FVC (MIF 50% FVC) and 3)maximal expiratory flow at 50% of FVC (MEF 50% FVC)(8) .

The maximum flow is reduced in obstructed patients. Loop area is the same both during forced expiration both during normal breathing, thus this patient can't increase the expiratory flow.

In restricted patients volumes are lower than for normal subjects, but expiratory flow is higher than normal subjects for a fixed volume.

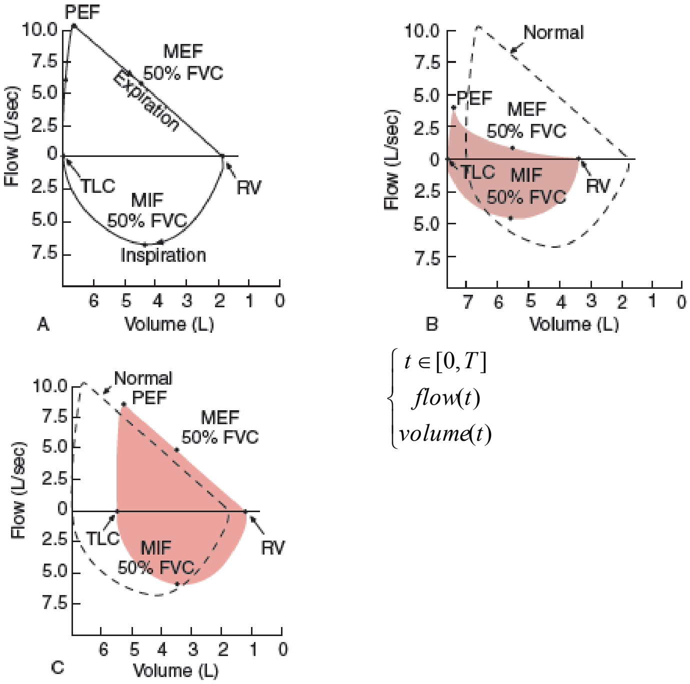

$$\begin{cases} t \in [0, T] \\ flow(t) \\ volume(t) \end{cases}$$

Figure 1.1.17: a) Normal subjects. Inspiratory limb of loop is symmetric and convex. Expiratory limb is linear, b) Obstructive patients, c) Restrictive patients.

C. VOLUME –PRESSURE CURVE

This curve is built by reporting in abscissa translung pressure in cmH_20 and in ordinate the percentage vital capacity volume.

The curve represents the system compliance. A high slope means the system is distensible, while a low slope means the system is rigid. The slope is maximal for physiological breathing volume (35%-45% FVC); therefore the respiratory action is easier.

Pathologies change this curve (Figure 1.12); in particular part of the gas is entrapped into the lung for obstructive diseases, thus the curves move on. On the other hand, restricted patients volume is reduced because of tissue thickening increases rigidity, as a consequence the curve goes down.

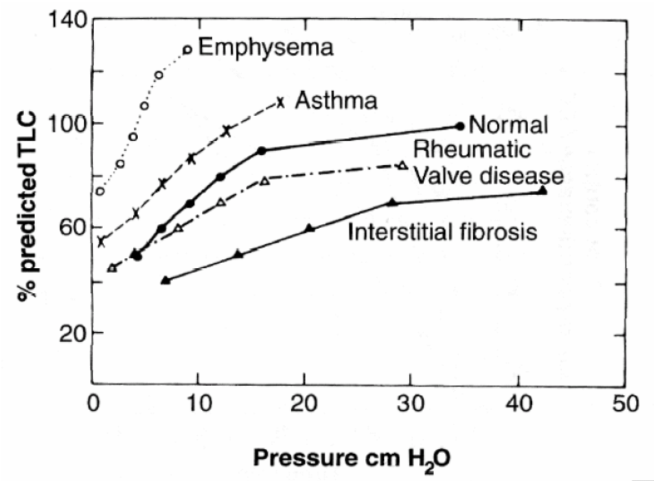

Figure 1.1.18: Volume pressure curves in different diseases

1.3.2. ARDS

Since the 60s some striking symptoms had been notice in patients in ICU who had received ventilation support, this physiological, radiographical and pathological abnormalities distinguished them.

Ashbaugh et al. (9), in a classic article, described 12 patients all had severe dyspnoea, tachypnoea, cyanosis that was refractory to oxygen therapy, decreased respiratory system compliance and diffuse alveolar infiltrates on chest radiography.

Post mortem examination of the lungs of seven of them revealed atelectasis, vascular congestion and haemorrhage, severe pulmonary oedema and hyaline membranes.

Shortly afterwards, Petty and Ashbaugh (10) called this constellation of findings adult respiratory distress syndrome (adult RDS).

After 30 years from this mile stone study, there is disagreement about exactly what adult RDS is, its etiology, frequency and prognosis, because it is just a costellation of sympthoms that nearly always occurs suddenly in the presence of risk factors, such as aspiration, sepsis or multiple blood transfusions. Chest radiographs show widespread alveolar infiltrates caused by pulmonary oedema and atelectasis. The physiological consequences are severe hypoxaemia due to right-to-left shunting of blood and decreased pulmonary compliance due to filling and closure of alveoli.

In 1994 the American –European Consensus (11) classed all these findings in an homogenous and coherent definition, first of all it unified ALI (Acute Lung Injury) to ARDS(Acute Respiratory Distress Syndrome), that were considered as the same pathology albeit at different stages, and they recommended that ALI/ARDS be defined as a syndrome of inflammation and increasing permeability that is associated with a constellation of clinical, radiological and physiological abnormalities that cannot be explained by, but may coexist with, left atrial or pulmonary capillary hypertension as reported in

Table 1.2

Table 1.2: Recommended criteria for diagnosing acute lung injury (ALI) and acute respiratory distress syndrome (ARDS) (12)**.**

	Timing	Oxygenation	Chest radiography	Pulmonary artery occlusion pressure
ALI	Acute onset	Pa, O_2/F_I, O2<39.9 kPa (regardless of PEEP)	Bilateral infiltrates seen on frontal chest radiograph	≤2.4 kPa when measured or on clinical evidence of left atrial hypertension.
ARDS	Acute Onset	Pa, O_2/F_I, O2<26.6 kPa (regardless of PEEP)	Bilateral infiltrates seen on frontal chest radiograph	≤2.4 kPa when measured or on clinical evidence of left atrial hypertension.

Pa, O_2: arterial oxygen tension; F_I, O2: inspiratory oxygen fraction; PEEP: positive end expiratory pressure

The incidence of ARDS remains unknown. It has been difficult to study the incidence of ARDS due to changing definitions causing inaccurate diagnoses, failure to capture complete data and uncertainty about the true population base or denominator, the size of the population with the risk factor.

Several studies have complemented knowledge of the frequency of ARDS and ALI by determining the prevalence of these syndromes in the critically ill. Two recently published studies reported that 16–18% of the ventilated ICU population suffer from ARDS and 4–5% from ALI (13, 14). The annual incidence of acute respiratory failure (ARF; mechanically ventilated for 24 h) ranged from 50–100 cases per 100,000, ARDS from 7–32 cases per 100,000 and ALI 17.9 cases per 100,000(15)

A. CAUSES

ARDS can be caused by any major swelling (inflammation) or injury to the lung. Some common causes include: breathing vomit into the lungs (aspiration), inhaling chemical, pneumonia, septic shock, and trauma.

ARDS leads to a buildup of fluid in the air sacs. This fluid prevents enough oxygen from passing into the bloodstream.

The fluid buildup also makes the lungs heavy and stiff, and decreases the lungs' ability to expand. The level of oxygen in the blood can stay dangerously low, even if the person receives oxygen from a breathing machine (mechanical ventilator) through a breathing tube (endotracheal tube).

ARDS often occurs along with the failure of other organ systems, such as the liver or the kidneys. Cigarette smoking and heavy alcohol use may be risk factors.

In more details, Fowler *et al.* (16) and Pepe *et al.* (17) suggest that the common conditions with the highest incidence of ARDS include severe sepsis or sepsis syndrome (43%), multiple emergency transfusions (40%), severe trauma (23%) and aspiration of gastric contents (20%). Secondary factors associated with an increased risk of ARDS include an elevated APACHE II score in patients with sepsis, and increased APACHE II and injury severity scores in trauma victims (Table 1.3). Mortality was three-fold higher in those succumbing to ARDS (62%) than among patients with clinical risk who did not develop ARDS (19%). The difference in mortality if ARDS developed was particularly striking in patients with trauma (56% versus 13%), but less in those with sepsis (69% versus 49%).

Table 1.3: Clinical condition and incidence of acute respiratory distress syndrome in two large single-center studies (12).

	University of Colorado	University of Washington		
	Single risk	Single risk	Multiple risk	Total %
Sepsis				
Bacteraemia	9/239			
Sepsis syndrome		39/94	15/31	43
Pneumonia in ICU	10/84			
Aspiration of gastric contents	16/45	6/62	15/45	20
Drug overdose in ICU		8/76	7/18	16
Fractures	2/18	5/52	18/48	23
Multiple transfusions				
10 units 24 h^{-1}	9/197			
…15 units 24 h^{-1}		18/53	18/36	40
Pulmonary contusion		13/72	23/65	26
Cardiopulmonary bypass	4/237			
Burns	2/87			
DIC	2/9			
Near drowning		3/6	4/6	58
Head Injury		6/100	8/28	11
Total	68/993	98/520	58/138	156/658

Data are presented as n (%) unless otherwise stated. DIC: disseminated intravascular coagulation.

B. DIAGNOSIS

The development of physiological indices for the accurate diagnosis of ARDS has been essential for epidemiological studies and the standardization of entry criteria into clinical studies. Because there is no practical "gold standard" for the diagnosis of lung injury, the only aspect of the definition of lung injury that can be studied is its reliability. Reliability (reproducibility of findings between observers) is essential to ensure that similar patients are identified for clinical research and, when effective treatments are found, for clinicians to identify patients similar to those enrolled in the trial.

Listening to the chest with a stethoscope (auscultation) reveals abnormal breath sounds, such as crackles that suggest fluid in the lungs. Often the blood pressure is low. Cyanosis (blue skin, lips, and nails caused by lack of oxygen to the tissues) is often seen.

Tests used to diagnose ARDS include:

1. Chest x-ray and CT
2. Arterial blood gas
3. Bronchoscopy
4. CBC and blood chemistries
5. Sputum cultures and analysis
6. Tests for possible infections

Occasionally an echocardiogram or Swan-Ganz catheterization may need to be done to rule out congestive heart failure, which can look similar to ARDS on a chest x-ray.

Chest X ray

The plain chest radiograph is an important investigation in critically ill patients. Despite known disadvantages, the conventional radiograph is performed as daily routine in many intensive care units (ICUs). Although chest radiography may give normal results for hours after the precipitating event, diffuse bilateral alveolar infiltrates usually appear 4–24 h after the first abnormal radiographic signs.

As reviewed by Desai *et al,* (18) *b*roadly, three histopathological stages are recognized in ARDS (19, 20). In the first 24 h (acute exudative stage), there is sloughing of the alveolar epithelium and the capillary endothelium. Interstitial involvement is limited and there is little, if any, intraalveolar oedema. Predictably, the chest radiograph is usually normal although septal lines may be seen occasionally, presumably reflecting early interstitial edema (21). In the next 36 h (subacute proliferative stage), there is progressive exudation of inflammatory fluid into the interstitium and, eventually, the air spaces. Pulmonary atelectasis becomes more prominent and, on macroscopic examination, the lungs appear densely consolidated. Early in this phase, the chest radiograph demonstrates round glass opacification (denoting interstitial and alveolar oedema) in which there is increased lung density, likened to a "veil", which obscures vascular markings (22), Figure 1.19.

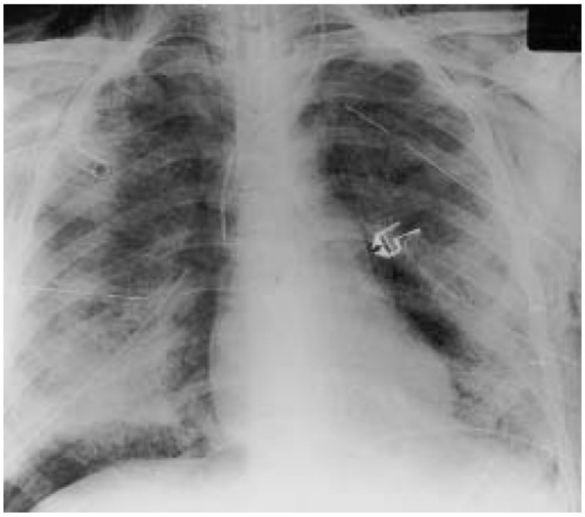

Figure 1.19: Chest radiograph in a patient with acute respiratory distress syndrome following abdominal surgery. There is bilateral symmetrical ground-glass opacification in which lung parenchymal density is increased and bronchovascular markings are obscured. There are bilateral pneumothoraces (22)**.**

Later, there is apparently homogeneous air space opacification and air bronchograms may be seen (23) Figure 1.20. As a general rule, the radiographic changes of "uncomplicated" RDS plateau at this stage and remain unchanged for a variable time thereafter. Therefore, any significant change in serial radiographic appearances (particularly more focal air space opacification) may be the first radiographic sign of incipient nosocomial pneumonia (24).

Figure 1.20: Acute respiratory distress syndrome after a road-traffic accident. The chest radiograph shows asymmetrical dense air-space opacification; air bronchograms are clearly seen in both upper lobes (23)

The final (chronic fibrotic) phase is dominated by lung repair with parenchymal fibrosis and hyperplasia of type II pneumocytes.

CT in ARDS

Because the contrast resolution of CT exceeds that of plain radiography, it has been possible to evaluate the morphological changes of ARDS with greater accuracy, both during the acute stages and in survivors. Furthermore, CT overcomes the problem of anatomical superimposition, a major constraint on the interpretation of plain chest radiographs.

Computed tomography (CT) often reveals patchy infiltrates interspersed with lung of normal appearance, indicating that ARDS is not a global process but a regional disease (25, 26) as can be seen in Figure 1.21. The degree of lung involvement on CT correlates with exchange and lung compliance (27) and can reveal barotrauma, localized infection or pleural effusion not evident on plain films (28). CT also gives an indication of the cause of loss of lower lobe volume, differentiating between inflammatory (preserved lung volume due to alveolar filling) and mechanical atelectasis (reduced lung volume owing to compression) (29).

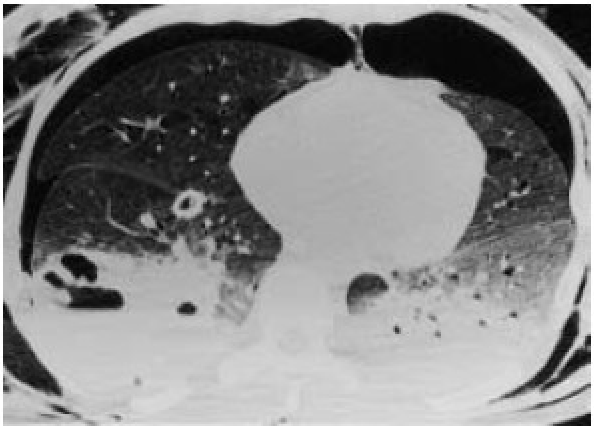

Figure 1.21: "Typical" computed tomography appearances in acute respiratory distress syndrome (ARDS) following abdominal surgery. There is dense parenchymal opacification in dependent lung and ground-glass opacification in nondependent regions. The cavity in right lower lobe developed in the third week of intensive care (after the onset of ARDS) and was secondary to nosocomial (Staphylococcal) pneumonia (30).

C. CHESTWALL MECHANICS IN ARDS

In patients with ARDS, the range of volume excursion is reduced because of the reduction in the number of ventilating units. Therefore we may aspect a reduction in the slope of the V/P curve. In mechanically ventilated patients, the initial part of the V/P curve, at very low lung volume, is remarkably flatter than the rest of the curve, indicating the amount of pressure required to open collapsed peripheral airways and/or alveoli. Following this initial portion, the curve presents a linear section in which the open alveoli are ventilated. Following this, the V/P curve flattens again at values of V_T lower than those observed in normal subjects, indicating that stretching and overdistension, of at least some alveolar structures, start to occur [(31). The following parameters have been identified on the V/P curve (Figure 1.22) and can be used to assess the status and progress of ARDS and to set the ventilator:

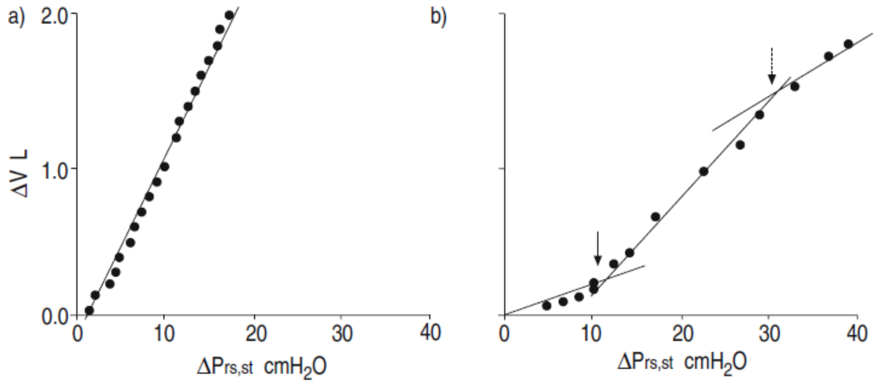

Figure 1.22: Static volume/pressure (V/P) relationship in a) a subject undergoing minor orthopaedic surgery and in b) patients with acute respiratory distress syndrome (ARDS). DV: changes in lung volume relative to end expiratory lung volume; DPrs, st: static end-inspiratory pressure of the respiratory system; solid arrow: lower inflection point (LIP); dashed arrow: upper inflection point (UIP). Note that in the ARDS patient the LIP and the UIP occur within a range of lung volume at which the V/P relationship of a normal subject is linear.

- Lower inflection point. Inflation of an excised lung requires that a critical opening pressure be applied in order to re-expand the collapsed alveoli (32). This critical pressure appears on the V/P curve as the pressure corresponding to the sudden change in slope of the V/P curve after the initial inflation. The pressure corresponding to the LIP should therefore represent the minimal level of PEEP that should be applied in order to have tidal inflation within an open lung (33) .
- Upper inflection point. In normal subjects, the upper inflection point (UIP) of the V/P curve is obtained at a lung volumey85–90% of total lung capacity (32), (34). In patients with ARDS, flattening of the V/P curve occurs at a much lower volume than in normal patients, as reported in some early studies of acute lung injury (ALI) (35). Any further increase of pressure above the UIP (via augmentation of VT or PEEP, or both) provides less increase in volume, indicating that maximal stretching of at least some alveolar structures has been reached, thus, exposing them to overdistension.

Recent data showed that in patients with ARDS not associated with major surgery (medical ARDS), the V/P curves of the chest wall and the abdomen were essentially superimposable with the curves observed in patients during general anesthesia for cardiac surgery, while in those patients in whom ARDS was secondary to major abdominal surgery (surgical ARDS), a rightward shift of the thoracic and abdominal V/P curves was observed. These data seem to suggest that the flattening of the V/P curves of the respiratory system and lung observed in some ARDS patients may, in part, be due to the increase in chest wall elastance related to abdominal distension (36). Gattinoni et al. (37) expanded these observations suggesting that the worsening of the elastic properties of the respiratory system is due primarily to alteration of the lung only in patients in whom ARDS is caused by pulmonary disease ("primary" ARDS). On the other hand, a severe alteration of chest wall mechanics may be responsible for the alteration of respiratory mechanics in patients in whom ARDS is caused by extrapulmonary causes ("secondary" ARDS).

The increase in abdominal pressure has been suggested as the underlying mechanism responsible for the alteration of chest wall mechanics observed in some patients with ARDS (37). Although the diaphragm forms the caudal boundary of the chest cavity, the diaphragm is mechanically coupled to the abdominal wall and contents. Hence, abdominal distension may impact directly on chest wall mechanics by affecting chest wall configuration, and/or causing inhomogeneity in the displacement among different parts of the chest wall (38). Any increase in abdominal pressure may also affect lung mechanics by increasing the propensity for the development of atelectasis and by decreasing FRC, which may also indirectly alter chest wall mechanics by shifting the V/P curve of the chest wall to a lower lung volume (38).

1.3.3. RESTRICTIVE DISEASES

Restrictive lung diseases are characterized by reduced lung volume, either because of an alteration in lung parenchyma or because of a disease of the pleura, chest wall, or neuromuscular apparatus. In physiological terms, restrictive lung diseases are characterized by reduced total lung capacity (TLC), vital capacity, or resting lung volume. Accompanying characteristics are preserved airflow and normal airway resistance, which are measured as the functional residual capacity (FRC). If caused by parenchymal lung disease, restrictive lung disorders are accompanied by reduced gas transfer, which may be marked clinically by desaturation after exercise (Figure 1.23).

The many disorders that cause reduction or restriction of lung volumes may be divided into 2 groups based on anatomical structures.

The first is intrinsic lung diseases or diseases of the lung parenchyma. The diseases cause inflammation or scarring of the lung tissue (interstitial lung disease) or result in filling of the air spaces with exudate and debris (pneumonitis). These diseases can be characterized according to etiological factors. They include idiopathic fibrotic diseases, connective-tissue diseases, drug-induced lung disease, and primary diseases of the lungs (including sarcoidosis).

The second is extrinsic disorders or extraparenchymal diseases. The chest wall, pleura, and respiratory muscles are the components of the respiratory pump, and they need to function normally for effective ventilation. Diseases of these structures result in lung restriction, impaired ventilatory function, and respiratory failure (eg, nonmuscular diseases of the chest wall, neuromuscular disorders).

In cases of intrinsic lung disease, the physiological effects of diffuse parenchymal disorders reduce all lung volumes by the excessive elastic recoil of the lungs, in comparison to the outward recoil forces of the chest wall. Expiratory airflow is reduced in proportion to lung volume.

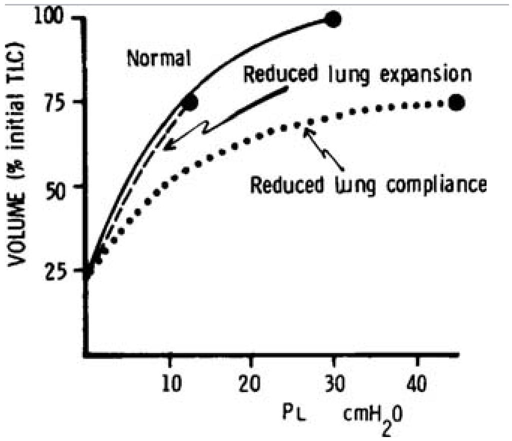

Figure 1.23: Mechanisms of restrictive lung disease. In practice when reduced lung expansion is chronic it is usually accompanied by reduced compliance (displacement of pressure-volume curve to right). Pl, transpulmonary pressure; TLC, total lung capacity.

Arterial hypoxemia in these disorders is primarily caused by ventilation-perfusion mismatching, with further contribution from an intrapulmonary shunt. The diffusion of oxygen is impaired, which contributes a little towards hypoxemia at rest but is primarily the mechanism of exercise-induced desaturation.

Hyperventilation at rest and exercise is caused by the reflexes arising from the lungs and the need to maintain minute ventilation by reducing tidal volume and increasing respiratory frequency.

In cases of extrinsic disorders of the pleura and thoracic cage, the total compliance by the respiratory system is reduced, and, hence, lung volumes are reduced. As a result of atelectasis, gas distribution becomes nonuniform, resulting in ventilation-perfusion mismatch and hypoxemia. In kyphoscoliosis, lateral curvature, anteroposterior angulation, kyphosis, or several of these conditions are present. The Cobb angle, an angle formed by 2 limbs of a convex prime curvature of the spine, is an indication of the severity of disease. An angle greater than 100° is usually associated with respiratory failure.

Neuromuscular disorders affect an integral part of the respiratory system, a vital pump. The respiratory pump can be impaired at the level of the central nervous system, spinal cord, peripheral nervous system, neuromuscular junction, or respiratory muscle. The pattern of ventilatory impairment is highly dependent on the specific neuromuscular disease.

Up to know the diagnosis of restrictive disease may be performed with several technique and tools:

- Laboratory studies
- Imaging studies
- Bronco-alveolar lavage;
- Lung functionalities test

Laboratory studies

The tests changes according to the origin of the disorders. If it is intrinsic routine laboratory evaluations often fail to reveal positive findings. However, anemia can indicate vasculitis, polycythemia can indicate hypoxemia in advanced disease, and leukocytosis can suggest acute hypersensitivity pneumonitis. Antinuclear antibodies and rheumatoid factor should be measured to screen for collagen vascular disorders.

In the other case for extrinsic disorders the most significative index may be an elevated creatine kinase level which may indicate myositis, the cause of muscle weakness and restrictive lung disease.

Imaging studies

Typically chest radiograph and CT, also for these techniques there's a deep difference according to the nature of the disease.

Extrinsic disease, such as kyphoscoliosis, may be appreciated in radiography (Figure 1.24, Panel a)), while intrinsic disorders may be evidenced by opacity and a reticular pattern, nodular, reticulonodular, or mixed patterns, such as alveolar filling (ie, ground-glass appearance) as reported in Figure 1.24, Panel b).

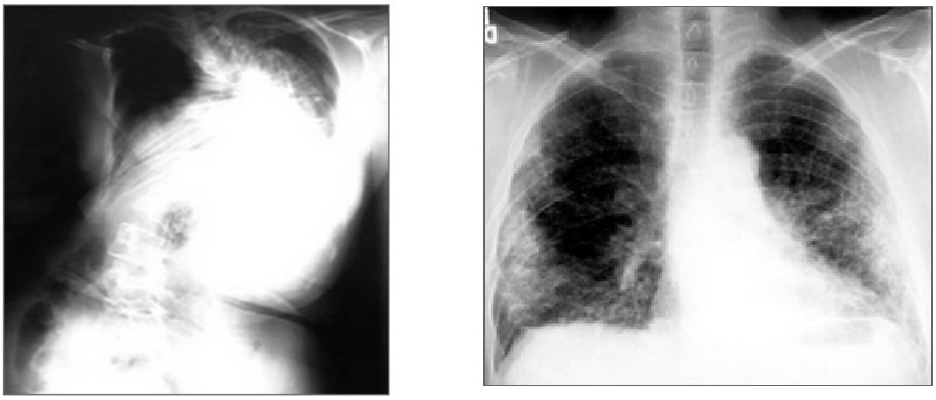

Figure 1.24: Panel a) Chest radiograph from a 39-year-old woman with severe kyphoscoliosis who developed hypercapnic respiratory failure b) Chest radiograph of a 67-year-old man diagnosed with idiopathic pulmonary fibrosis, based on open lung biopsy findings. Extensive bilateral reticulonodular opacities are seen in both lower lobes.

Interstitial lung disease can be diagnosed clinically based on the typical clinical features and CT scan findings without the need for lung biopsy. Bibasilar peripheral lung zone involvement is seen in patients with IPF, asbestosis, connective-tissue disease, or eosinophilia pneumonia (Figure 1.25).

Central disease along bronchovascular bundles is indicative of sarcoidosis or lymphangitic carcinoma.

Upper-zone predominance is observed in patients with sarcoidosis, eosinophilic granuloma, or chronic hypersensitivity pneumonitis. Lower-zone predominance is seen in patients with IPF, asbestosis, or rheumatoid arthritis.

Lower-zone and peripheral infiltration is ordinarily seen in patients with IPF or asbestosis.

The presence of bilateral cysts and nodules, with preservation of lung volumes, may suggest a diagnosis of LAM or histiocytosis X.

Bibasilar reticular fibrosis with coexisting retraction bronchiectasis indicates end-stage irreversible disease, and ground-glass attenuation may result from changes in the interstitium, air spaces, or redistribution of capillary blood flow.(39)

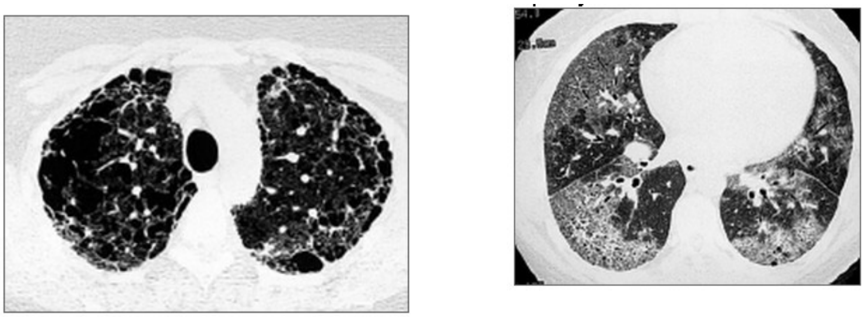

Figure 1.25: Panel a) A CT scan image from a 59-year-old woman shows advanced pulmonary fibrosis. Extensive honeycombing and traction bronchiectasis are present; b) High-resolution CT scan of the same patient in the image below demonstrates peripheral honeycombing and several areas of ground-glass attenuation. Ground-glass opacification may correlate with active alveolitis and a favorable response to therapy.

Lung functionality test

Complete lung function testing includes spirometry, lung volume, diffusing capacity, and arterial blood gas measurements. Pulmonary function test findings do not indicate a specific diagnosis or help distinguish alveolitis from fibrosis. Findings from sequential tests are invaluable for monitoring the course of the disease and assessing the response to therapy.

All disorders are associated with a restrictive defect with a reduction in TLC, FRC, and residual volume (RV).

While a reduction in the forced expiratory volume in one second (FEV_1) and the forced vital capacity (FVC) with a normal or increased FEV_1 -to-FVC ratio suggests a restrictive pattern, the diagnosis of restriction is based on a decreased TLC. The assessment of the severity of restriction is also based on TLC.

An obstructive airflow limitation may be observed in patients with sarcoidosis, LAM, hypersensitivity pneumonitis, and pulmonary fibrosis with concomitant chronic obstructive pulmonary disease.

1.4. ALTERNATIVE TECHNIQUE TO MEASURE MECHANICAL PROPERTIES

1.4.1. OSCILLATORY MECHANICS AND FOT

Oscillatory mechanics is the study of structural and mechanical properties of the respiratory system as deduced from its mechanical responses to small time-varying forces. The method used in this approach is the construction of computational models of the respiratory system and their parameters are some combinations of those seen in the previous paragraphs. There are many models used to describe the respiratory system, some are simple like the RLC series model and the T-network model, some others are more complex. The estimation of parameters is possible by means of the transfer function. It is a linear relationship between the input (forcing signal) and the output of the examined system (7).

To extract information of oscillatory mechanics the main technique is FOT, Forced Oscillation Technique. FOT is a measurement approach which can provide specific and reliable insight on the mechanical properties and important mechanisms that contribute to breathing .It was introduced in 1956 by Dubois and co-workers (40) as a simple, minimally invasive approach to measure the mechanical impedance of the lung or respiratory system. However, up until about ten years ago the impact of the approach was confined to gross clinical categorization with little physiological or anatomical resolution. Substantial advances in technology, signal processing, and modeling have recently resulted in the potential to use of forced oscillations to extract far more specific insight on lung and chest wall mechanical alterations during disease than any other existing measurement of pulmonary mechanics.

D. COMPLEX IMPEDANCE

The main concept behind FOT is to study the response of the respiratory system to a pressure stimulus applied at one of its ports in terms of the flow produced. In order to

discard contribution given to spontaneous breathing activities, the pressure stimulus should be at higher frequency, that is more than 4 Hz (7, 40).
If the stimulus is a sinus, it is possible to express it and the generated flow in terms of phasors, as report in the equation below (1.14,1.15).

$$P(t) = \boldsymbol{P}(\omega)e^{i(\omega t+\Phi_{rs})} \quad 1.14$$

$$\dot{V}(t) = \dot{\boldsymbol{V}}(\omega)e^{i(\omega t)} \quad 1.15$$

Where Φ_{rs}accounts for any phase shift of the pressure wave relative to flow.
Now it is possible to quantify the response of the system by means of its mechanical transfer function that is define as the complex ratio between the pressure and the flow (**1.16**).

$$Z(\omega) = \frac{\boldsymbol{P}(\omega)e^{i(\omega t+\Phi_{rs})}}{\dot{\boldsymbol{V}}(\omega)e^{i(\omega t)}} = \frac{P(\omega)}{\dot{V}(\omega)}e^{i(\Phi_{rs})} = |\boldsymbol{Z}|e^{i(\Phi_{rs})} \quad 1.16$$

That is the impedance is given by two parts: the magnitude, indicating the amplitude of the pressure difference relative to the flow and a phase angle, indicating the phase shift of pressure differences relative to flow.
Introducing impedance allows representing the respiratory system into two models, called one-port system and two pot system.

E. REMARKS ABOUT STIMULUS

The respiratory system is made by visco-elastic structures with mechanical properties that are frequency dependent. Therefore, to evaluate the impact of the alterations induced by the disease on the mechanic of breathing, mechanical impedance should be evaluated around the breathing frequencies. However, during spontaneous breathing it is very difficult to isolate the response of the system to the stimulus from the activity of the respiratory muscles. The application of a pseudo-random signal during a short apnoea period (41)) has been proposed as a solution to measure oscillatory impedance between 0.25 to 5 Hz. A second solution proposed consisted on the application of a broadband signal designed to both sustain the ventilation and stimulate in the range of 0.1-4 Hz with the subject fully relaxed(i.e. Optimal Ventilation Waveform). The phase of each frequency is optimized to produce a waveform that maximizes volume delivered while minimizing peak-to-peak airway opening pressure (42). Although both these methods gave good results, they are not easy to perform in diseased patients.
Moreover, several problems arise when stimulating the respiratory system with a broadband frequency stimulus. Even if healthy lungs behave like a first-order linear system, several phenomena can occur during disease that would make the respiratory system markedly non linear. This is an important concept to keep in mind in the design of the stimulation waveform. Indeed, in a non linear system, harmonic distortion and crosstalk

between the frequencies of the input signal will introduce spurious components into the response of the system that will bias the estimation of the transfer function (43, 44).
The simpler approach to estimate the impedance of the system would consist in stimulating by using single frequency waves and evaluating the response at the same frequency. This approach will maximize S/N and eliminate the influence of crosstalk and harmonic distortion but it will require several measurements to characterize the frequency spectrum making the technique time demanding. Moreover every single frequency component of the spectrum will be estimated in different times, introducing errors in the estimation of the whole spectrum. Suki and Lutchen (79;81) have demonstrated that the impact of crosstalk and harmonic distortion can be reduced by using a stimulus whose frequency components are not integer multiples or linear combination of other components. They demonstrated that such a signal is able to completely eliminate the bias introduced by a system describe by a second order equation and therefore called this family of waves Non-Sum-Non-Difference of order 2 (NSND2).

F. INPUT AND TRANSFER IMPEDANCE

If the pressure and flow variations are applied and measured only at the mouth, the respiratory system can be represented schematically as a black box with a single set of terminals. The only system functions relevant to a one port system become input admittance and its reciprocal, input impedance (Figure 1.26, panel a)).

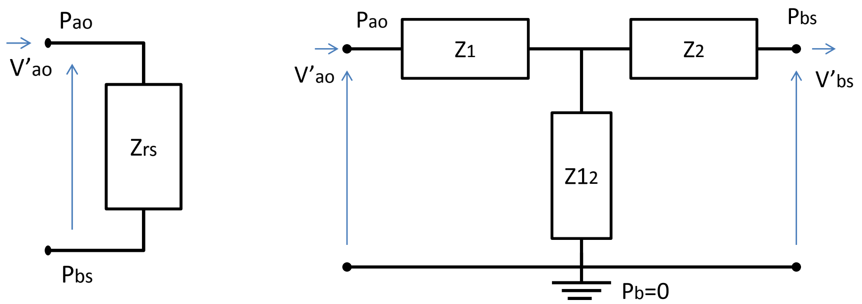

Figure 1.26: Panel a) one port system, b) two port system where the variable state systems are evidenced.

The impedance measured at the airway opening, called respiratory system impedance, can be divided into its real and imaginary components.
Although the single equivalent impedance may be applied to any linear ones port system regardless of complexity, the components of the impedance Z_{rs} may take on special physical meaning when the system in question actually comprises a serial distribution of elements. In this situation the real part of impedance will correspond to the resistance of the system, while the imaginary part will represent the sum of compliance and inertance, that is the reactance of the system.

If the actual system may be decribed by a single compartment as reported in paragraph A, then it possible to create a direct correspondence from the impedance and the physical elements of the respiratory system, in more details, the real part of this impedance, $R(\omega)$, is equal to a constant, R, for all values of ω. In fact, $R(\omega)$ is called resistance for this reason. The imaginary part, $X(\omega)$, is called reactance and for the single-compartment model is a negative hyperbolic function of ω. When oscillation frequencies exceed those of normal breathing, the pressures required to accelerate structures in the lung begin to become important (Figure 1.27). The principle contributor to this phenomenon is the mass of the gas in the central airways. To account for this effect, an inertive term can be added to the equation of the single-compartment model I is usually rather small because air does not have much mass, so the inertive contribution to $Z(\omega)$ only becomes significant at high frequencies when accelerations are large.

The equation which described this model is 1.17

$$Z(\omega) = R + j(\omega I - \frac{jE}{\omega}) \tag{1.17}$$

Accordingly, at low ω the magnitude of E/ω is much larger than the magnitude of ωI, so $X(\omega)$ is negative. As ω increases, however, the term containing I becomes progressively larger, while the magnitude of the term containing E decreases. Eventually, the term containing I will dominate. $X(\omega)$ is zero when E/ω and ωI are equal. The value of ω at which this occurs is called the resonant frequency, ω_{re}

Theoretically it is possible to represent any system as a one port system, also if its elements are arranged into parallel configuration, but in this case the estimated parameters don't have a physical correspondence.

If the mouth is viewed as one port and the body surface as a second port, then during measurement of pressure and flow at each port, the respiratory system may be viewed as a black box with two sets of terminals, or a generalized two-port system (Figure 1.26, panel b)).

If the mouth is viewed as one port and the body surface as a second port, then during measurement of pressure and flow at each port, the respiratory system may be viewed as a black box with two sets of terminals, or a generalized two-port system (Figure 1.26, panel b)).

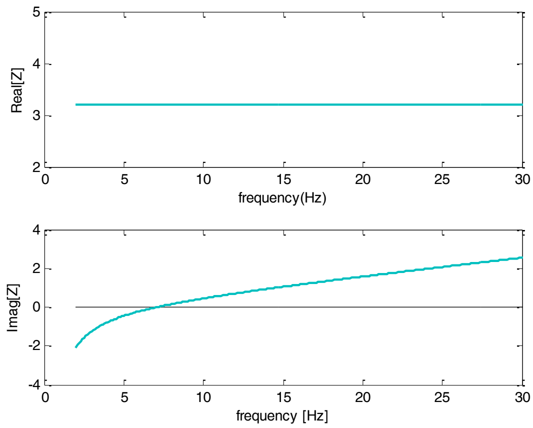

Figure 1.27: Resistance (R) and reactance (X) of the singlecompartment linear model of the lung as a function of angular frequency (ω).

In such a system the input impedance, transfer impedance and transfer function are relevant. Even if alveolar pressure and/or body surface motions are spatially non uniform, one may regard the body surface as a single port by summing displacement as in a body plethismograph. Although we are using the entire respiratory system as an example, two-port analysis could be applied individually to airways, lung, lung tissure and/or chest-wall. A well accepted phisycal model for a two port system is reported in Figure 1.28.

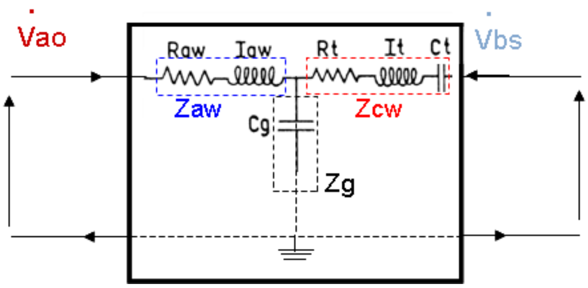

Figure 1.28: Six elements lumped parameter model of the respiratory system.

A direct consequence of the model above is that, even if the mechanical system does not change, measurements of Z_{in} or Z_{tr} give different information by emphasizing different components of the system. Therefore, when measuring Z_{in}, Z_t and Z_g result in parallel, and the input impedance can be expressed as 1.18:

$$Z_{in} = Z_{aw} + \frac{Z_g Z_t}{Z_g + Z_t} \qquad 1.18$$

For frequencies less than 20 Hz, the influence of Z_g on Z_{in} can be considered negligible since it is in parallel with the tissue compartment that has larger compliance and smaller inertance. Therefore, input impedance is composed by the series of airways and tissues impedances as reported in 1.16.

Differently from Z_{in}, Z_g has some influence on Z_{tr}. In fact, by stimulating at the chest wall and recording mouth flow, the gas compartment is in parallel with the airways and both in series with the tissues as in 1.19:

$$Z_{tr} = Z_{aw} + Z_t + \frac{Z_{aw} Z_t}{Z_g} \tag{1.19}$$

Input impedance and its clinical impact

Most of the published studies of oscillatory mechanics have been focused on the measurements of Z_{in} during normal breathing ((45, 46)) using the setup shown inFigure 1.29 (40)(47)(48)(26;29-32). Forcing signal is generated by a loudspeaker and applied to the airway opening of the subject were flow and pressure are measured. Although this setup is very simple, it has the inconvenience of being affected by the adverse effect of the movement of the cheeks and extrathoracic airways that, resulting mechanically in parallel with the intrathoracic respiratory system, constitute a shunt pathway that influence the measure of Z_{in}.

To reduce the effect of the shunt the subject is asked to hold his cheeks with his hands. This procedure results in an increase of the impedance of the upper airways and therefore a decrease of its influence on Z_{in} (49)

As already mentioned Z_{in} allows separating the real almost frequency-constant component that is the respiratory system reactance from the reactance.

In literature we can find numerous studies ((50),(51, 52, 52-60)) that use FOT approach in clinical application based on the measurements of Z_{rs} measured on a wide range of frequency and averaged on the whole breath, showing that this parameter is very sensitive to obstruction of the airways, while another interesting approach consists in study the reactance alterations during breathing at a very well defined frequency and evaluating it during the breathing phases ((49, 61-65)) . The information we can get from this last approach are very sensitive also to alveolar recruitment as will be shown lather.

As exhaustively reported in the review of Oostveen *et al.* (66), FOT data, especially those measured at the lower frequencies, are sensitive to airway and Forced oscillation technique is a reliable method in the assessment of bronchial hyperresponsiveness in adults and children. Moreover, in contrast with spirometry where a deep inspiration is needed, forced oscillation technique does not modify the airway smooth muscle tone. Forced oscillation technique has been shown to be as sensitive as spirometry in detecting impairments of lung function due to smoking or exposure to occupational hazards. Together with the minimal requirement for the subjects' cooperation, this makes forced oscillation technique an ideal lung function test for epidemiological and field studies obstruction, but do not discriminate between obstructive and restrictive lung disorders.

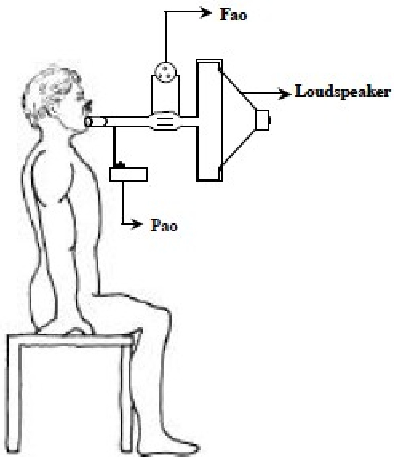

Figure 1.29: Measurement configuration for input impedance

The pattern of change in Z_{rs} in various pulmonary function abnormalities consists of an increase in R_{rs}, especially in the lower frequency range, and a decrease in X_{rs}, associated with an increase in f_{res}. Cle´Ment et al. (50) shown that conventional FOT was a sensitive tool to separate healthy subjects from patients with respiratory complaints (both with and without a reduced forced expiratory volume in one second (FEV_1)). In a later study, the same investigators showed that the sensitivity to detect symptomatic people was similar for FOT and spirometry (51).

In adult patients with intrapulmonary airway obstruction, R_{rs} is increased at the lower frequencies and falls with increasing f. The negative frequency-dependence of R_{rs} is explained on the basis of mechanical inhomogeneities of the lungs (40). Van Noord et al. (52), (67) studied the discriminative power of conventional lung function parameters and FOT in three groups of patients suffering from asthma, chronic bronchitis or emphysema with a similar reduction in FEV_1. A discriminant analysis showed that the FOT parameters were among the best lung function indices in discriminating between the three groups. Wesseling and Wouters (59) found abnormal Z_{rs} data in 70% of the subjects with chronic bronchitis in the presence of normal spirometry. The negative frequency dependence of R_{rs}, which is characteristic of patients with bronchial obstruction, has also been observed in adult patients with upper airway obstruction but without any sign of intrapulmonary disease (57). This finding can readily be explained by the shunt effect of the upper airway walls on the elevated distal impedance. Although the FOT may fail in distinguishing between intra and extrapulmonary obstruction, it may be very useful for the noninvasive diagnosis and follow-up of patients at risk for tracheostenosis (68). In this study, FOT indices proved to be much more closely related to the tracheal dimensions than spirometric indices, thus suggesting that FOT is more sensitive in disclosing the upper airway stenosis.

Surprisingly, no distinctive patterns in Z_{rs} have been observed in restrictive lung disorders: the changes in Z_{rs} are similar to those of moderate obstructive lung disease. Greater negative frequency dependence and higher values of R_{rs} and decreases in X_{rs} were measured in patients with restrictive disorders, such as fibrosing alveolitis (58) and kyphoscoliosis or ankylosing spondylitis (57). Again, this observation can be explained on the basis of the upper airway shunt impedance, which may mask the differences between the alterations in pulmonary mechanics resulting from various respiratory disorders. Obese subjects exhibit an increased R_{rs} resulting from a reduction in lung volume (60).

In conclusion, in patients with various diseases associated with pulmonary function abnormalities, an increase in R_{rs}, especially in the lower frequency range, and a decrease in X_{rs} with a concomitant increase in f_{res}, are observed. However, the standard FOT does not offer the distinction between the underlying restrictive and obstructive changes, or intra and extrapulmonary disorders.

In evaluating the development of pulmonary disease, the long-term monitoring of therapeutic efficiency and the staging of respiratory function decline during aging, FOT provides a convenient follow-up technique (69). However, for longitudinal follow-up of chronic obstructive pulmonary disease (COPD) patients, changes in R_{rs} up to 26% may result from spontaneous variation in resistance (70).

In an early study, use of FOT alone failed to clearly separate smokers from nonsmokers (71). Coe et al. (72) analysed R_{rs} and its frequency dependence in healthy neversmokers and in smokers. There was a strong trend for R_{rs} (especially at lower frequencies) and the frequency dependence of R_{rs} to elevate with increasing age in the smokers. A study on the additional effects of smoking habits on the activity of miners showed that, although FOT provided sensitive indices of the effect of occupational exposure on central airways, it did not detect the additional effect of smoking (73).

The information offered by FOT on respiratory impairment is in every way as significant as spirometry and FOT does not require active cooperation. Feasibility in various epidemiological surveys and field studies has been excellent (56). FOT has proved as sensitive as spirometry in the detection of impairment in ventilatory function in workers exposed to occupational dangers (54, 55). The performance of FOT in the assessment of bronchial hyper responsiveness (BHR) (55) shows a 65% increase in $R_{0.}$

The second approach is lightly different. After a modelization of the respiratory system as a two compartments model proposed by Mead(74), Dellacà et al, (62) find that as soon as R_{pa}, the peripheral resistance, increases the shunt pathway due to the airway walls compliance affects the total input impedance by reducing X_{rs} (Figure 1.30, panel a)).

a) b)

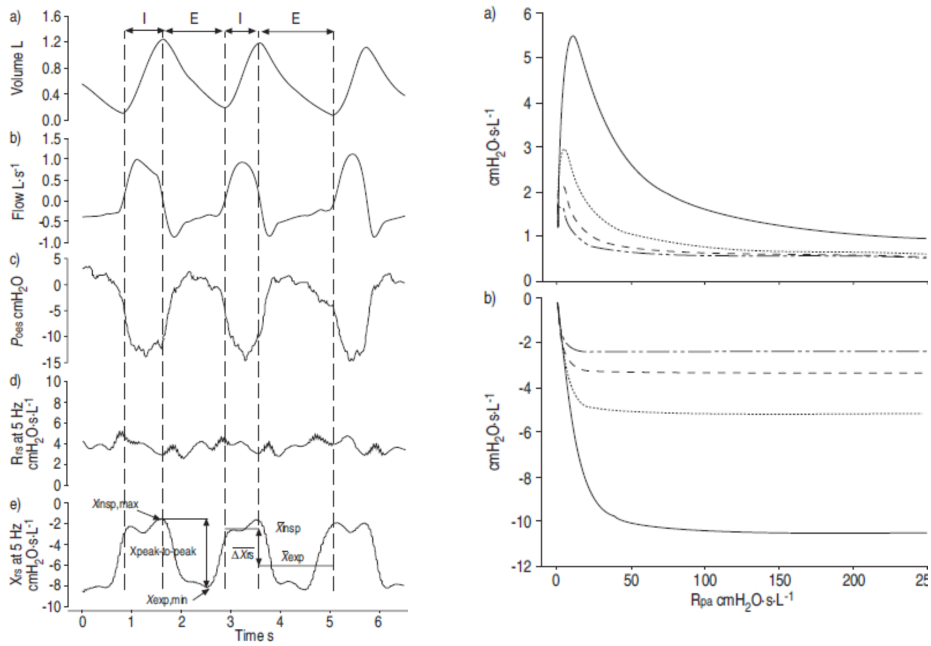

Figure 1.30: Panel a) Experimental tracing from a representative flow-limited patient and definition of the indices used to characterize the respiratory system reactance (X_{rs}) time course during a single breath; Panel b) Simulated real and imaginary part of the input impedance at 5 (––), 10 (.....), 15 (-) and 20 (–...) Hz of a lumped parameter model of the respiratory system that includes airway wall shunting.

Even when this reduction is present at all the frequencies, the greatest difference is seen at the lowest frequency. Therefore, to obtain larger X_{rs} swings from inspiration to expiration when expiration is flow-limited (and thus increasing the sensitivity of the indices), the lowest possible frequency was chosen. Since the quiet breathing signal can interfere with the estimation of Z_{in} at frequencies below 5Hz, 5Hz was used as forcing frequency in this study.

To use 5 Hz stimulus allows a time resolution of 0.2 seconds, moreover, thanks to a LSM approach in finding the impedance, it is possible to estimate the impedance pattern during breathing as shown in (Figure 1.30, panel b).

This approach has been applied to numerous patho-physiological conditions, showing a high sensitivity, although a low specificity. In more details in their first study on expiratory flow limitation, Dellacà et al (62) concluded that in summary, their data indicate that the measurement of expiratory reactance during tidal breathing can reliably detect breaths that are flow-limited and potentially the time at which flow limitation begins. A further useful feature of this method is its ability to identify periods in which total respiratory input resistance no longer reflects the mechanical properties of the respiratory system due to the presence of expiratory flow limitation.

The same approach has been also used on animal models to detect interstitial edema (64) and lung de-recruitment in an ARDS model (61). In the last experiments, ARDS has been induced on a group of six piglets which were undergone to a recruitment maneuver (PEEP increase from 0 to 24 cmH_20 at step of 2 cmH_20 and decrease from 24 to 0 cmH_20 at step of 4 cmH_20), at each step of the maneuver FOT data and CT are contemporary measured. Then the percentage volume of tissue not aerated, $V_{tissNA\%}$, estimated by CT at each PEEP step, has been compared to the parameter defined by the author as $\frac{1}{C_5}$ that is the reactance at 5 Hz.

As can be seen in Figure 1.31 , the comparison between CT data and FOT, reported only for some stage of the protocol, shows a very good agreement.

In this study the authors found that the measurements of C_{X5} before and after an intervention, that is mainly affecting lung volume recruitment with a negligible effect on I_{rs} and chest wall compliance, are an accurate and specific quantification of recruitment and de-recruitment. This hypothesis is confirmed not only by the linear relationship found between C_{X5} and $V_{tissNA\%}$ pooling together data from all pigs and conditions, but also by the even greater determination coefficients obtained by considering each single pig separately even if the limited number of experimental conditions undoubtedly makes individual analysis less statistically powerful in comparison to the pooled data. All these results suggest that even if a single measurement of C_{X5} in a given patient is not highly specific to lung volume recruitment, its changes between before and after an intervention could carry important information on the amount of recruited or derecruited lung volume.

Although the very rich informative content of the input impedance the model applied can failed in presence of dis-homogeneity of the tissue, providing a negative resistance. Moreover as can be seen from 1.18 it is more sensitive to airways mechanical properties than to the parenchyma properties.

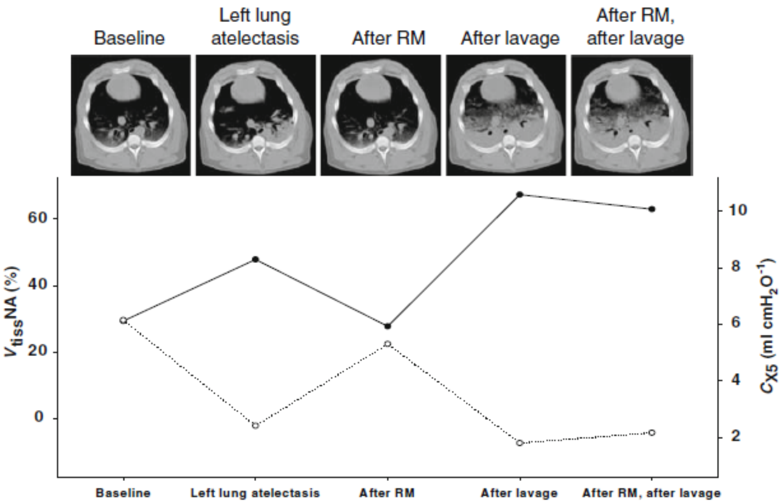

Figure 1.31: Upper panel CT scans of a representative animal: at baseline, during left lung atelectasis induced by 10 min of single-lung ventilation at 100% oxygen, alter a RM, post broncho-alveolar lavage and after RM after broncho-alveolar lavage. Lower panel corresponding non-aerated tissue volume (VtissNA%, closed symbols, solid line) and C_{X5} (open symbols, dotted line)

Transfer impedance and its clinical application

When pressure and flow are measured at different ports, the impedance is called transfer impedance (Z_{tr}). If pressure is measured at the body surface and flow at the mouth, $Z_{tr,bs}$ = P_{bs}/V_{ao} is obtained, whereas if pressure is measuredat the mouth and flow at the body surface $Z_{tr,ao}$ = P_{ao}/V_{bs} is determined. When the forcing signals are small enough to keep the respiratory system behaving as linear, the two transfer impedances are identical by reciprocity.

To measure transfer impedance two different configurations are possible. In the most widely used a pressure forcing signal is applied to the body surface by a modified partial body plethysmograph (with two or more loudspeakers mounted on its walls), and the flow is measured at the mouth by a pneumotachograph, obtaining $Z_{tr,bs}$ = P_{bs}/V_{ao} The T-network model is thus connected as shown in Figure 1.32, panel b) and $Z_{tr,bs}$ can be expressed as in 1.19.

Another approach (Figure 1.32, Panel b)) is to apply the forcing signal to the airway opening and to use a body plethysmograph to measure body surface flow [3] to compute $Z_{tr,ao}$ = P_{ao}/V_{bs}. In the assumption of linear behavior, $Z_{tr,ao}$ and $Z_{tr,bs}$ are both defined by the same equation.

However, there are differences in these two approaches. In the assessment of $Z_{tr,bs}$ it is difficult to obtain homogeneous pressure fields all over the subject's body, especially at high frequencies (greater than 15-20 Hz). Moreover, with this approach it is impossible to obtain the simultaneous estimation of Z_{in}. The estimation of $Z_{tr,ao}$ allows the simultaneous assessment of Z_{in} and Z_{tr}, but the measurement of the body surface flow is critical. In fact the frequency response of the body plethysmograph must be accurately determined for each measurement as it depends upon the gas into the body box and consequently the measurement requires a subject-specific calibration and the flow data must be corrected. Very few studies have been performed using this method (75-77).

Whatever is the approach, the measurement of Z_{tr} always requires the use of a total or partial body plethysmograph. For this reason, there are very few reports of Z, measurements in health and disease [6]. In fact the plethysmographic chamber limits the access to the subject under analysis, is cumbersome, and only applicable to ambulatory patients in a seated posture. Even the use of a partial body plethysmographs (with only the trunk and the arms inside the box, while the head and the legs are kept outside), which has the advantage of having a smaller internal volume, does not significantly improve the applicability of the technique.

Anyway, it is important to underline that the measurement of Z_{tr} performed by plethysmographic chamber, in particular in the configuration reported in Figure 1.32, panel b), just puts in relationship the pressure produced by the stimulus with the volume variation of the chest-wall disregarding the presences of in-homogeneities and heterogeneities in its different compartment. For these reasons some authors suggest a new approach to the estimation of impedance which is based on estimation of local mechanical properties to account for different mechanical behavior due to different compartment and to pathologies.

As already said very few reports about Z_{tr} exist, anyway we should propose a short review of the miles-stone studies in literature.

Peslin et al (75, 76) studied the frequency response of the respiratory system in the range from 3 to 70 Hz in 1 normal subject by applying sinusoidal pressure variations around the chest and measuring gas flow at the mouth and they tried to fit the results with T- models of increasing orders.

They found that the best model for a frequency range of 3-20 Hz was the 3-th one, which neglect the inertance of the tissue and of the airways, while a higher order can be used in order to describe a higher frequency range.

Their main assumptions were: linearity, absence of mechanical coupling, lumped properties, frequency independences of the coefficients, monoalveolar structure.

Some notes should be added about the monoalveolar hypothesis, even in normal subjects, small regional differences in the physical properties of the tissue or of the conducting airways are very likely to occur, due to the structure or t environmental factor like gravity moreover the value found for the compliance of the tissue (2.349-2.49cmH_2O at the different frequencies) seems to be lower than expected.

a)

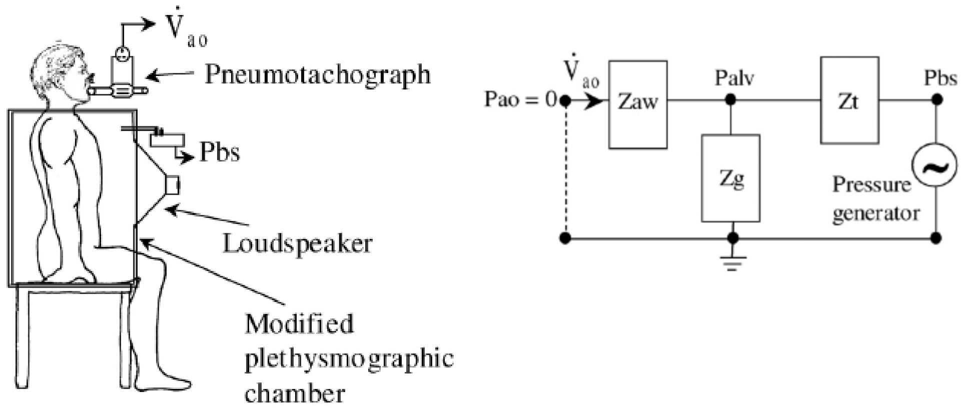

b)

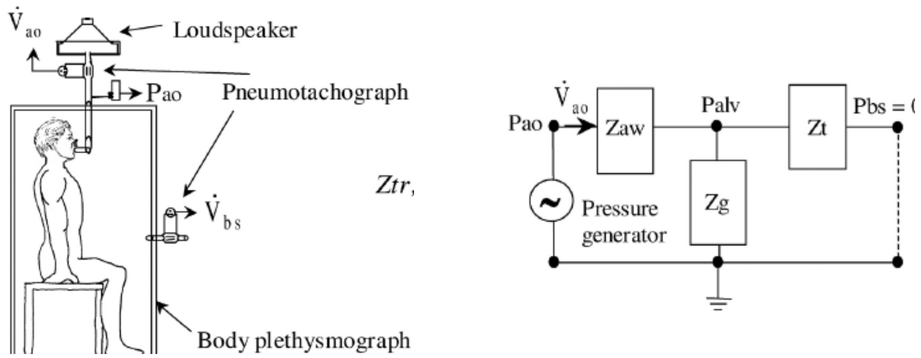

Figure 1.32: Experimental set-up (left) and connections of the T-network model or transfer impedance forcing at the chest (Panel a) or forcing at the mouth (Panel b) are measured. In the T-network models the pressure generator connected to one port is usually constituted by a loudspeaker, while the other port is left open to atmosphere and, therefore, short-circuited to ground (dashed lines).

Although these remarks, the authors concludes that, given the very high quality of the fitting between system and model, the regional differences are too small to influence the behavior of the system or that several factors compensate each other and they argued that a more complicated model, which takes into account the possibility of regional differences in chest wall lung and airways properties would not be useful since the mono-alveolar model is supposed to explain the whole information.

The set up required to measure the $Z_{tr\ is}$ quite bulky and complex, for these reasons there are very few study that use this approach in clinical environment (78, 79)

Lutchen et at. (78) evaluated the clinical utility of Z_{tr} from 1–80 Hz for assessing the degree and type of impaired lung function. Spirometry and Z_{tr} measurements were made on 37 individuals: 11 healthy subjects and 26 patients with lung disease including chronic obstructive pulmonary disease (COPD), asthma, lung cancer, and sarcoidosis. Over the entire patient group, 12 were also smokers.

The COPD and smokers groups showed significant differences in portions of their Ztr spectra from that of the healthy group. They do not expect that Ztr data shows high specificity to the explicit pathophysiology of lung disease. Most notable, COPD is not a specific disease, but a syndrome to reflect several patients, often with variable pathophysiology (e.g., emphysema, chronic bronchitis, and asthma). Nevertheless, with our COPD subjects, the Z_{tr} data fell within rather tight bounds (Figure 1.33) such that this group was completely distinguishable from the healthy Z_{tr} group. Also, the variability in the COPD spectra was similar to that of the spectra in healthy subjects.

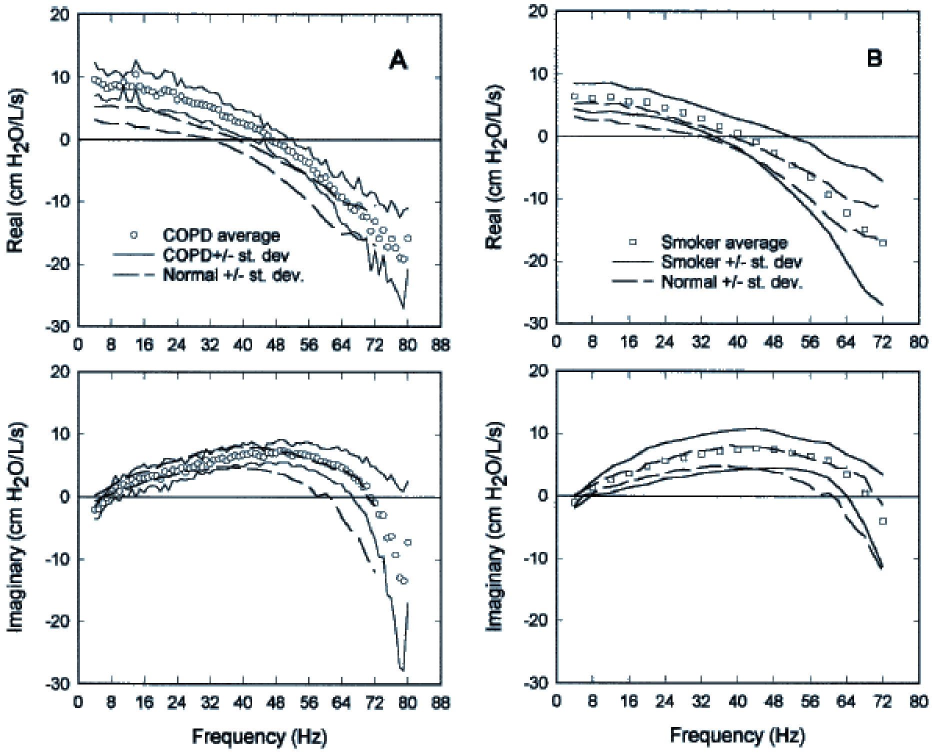

Figure 1.33: Mean (*open symbols*) and *6* SD (*solid line*) Ztr bounds for COPD (*A*), and smoker (*B*) subjects (78)**.**

1.4.2. OPTOELCTRONIC PLETHYSMOGRAPHY

Optoelectronic plethysmography is based on automatic motion analysis using passive 6 or 10 mm diameter markers. Each marker consists of a thin film of retro-reflective paper on a plastic hemisphere. The markers are fixed to the skin by means of biadhesive hypoallergenic tape. Specially designed TV cameras (solid state CCDs) and infrared scene lighting provide the best possible contrast between the marker images and the surrounding environment (Figure 1.34).

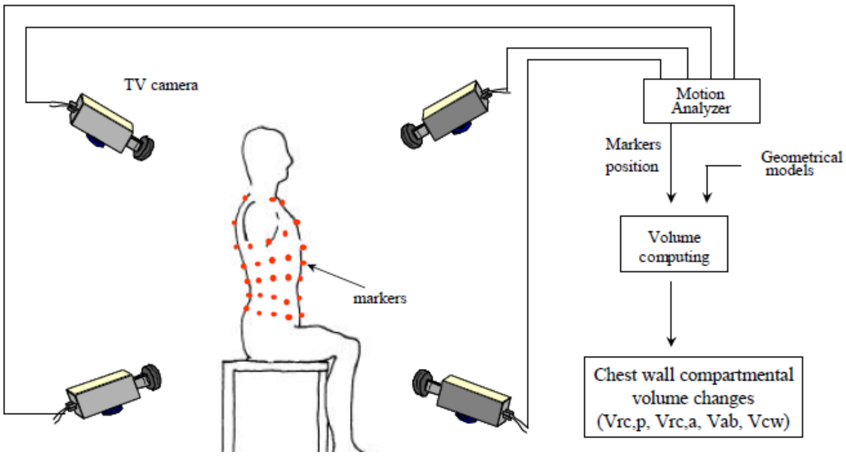

Figure 1.34: Experimental setup for OEP analysis in the seated position

A dedicated processor recognizes and calculates the positions of the markers recorded by the different cameras in real time. System calibration, consisting of camera calibration and spatial camera location, allows 3D reconstruction of the different markers. Special algorithms used for marker detection provide the very high accuracy required for measuring the micro-movements involved in respiration (80).

Once the 3D co-ordinates of the points belonging to the chest wall surface have been acquired, the next step is to calculate the volume of the closed surface obtained by connecting the points to form triangles.

The connections between the points define the geometrical models that describe the whole surface or a part thereof. Closed surfaces are usually described by also considering some 'virtual' markers whose coordinates are defined from the coordinates of the real markers through mathematical relationships (mean value, translation or a combination of both).

In the case of standing and seated positions, i.e. when the whole trunk is visible 'all round', was found (81) that the best marker arrangement consists of 86 markers on the chest wall (42 anterior, 34 posterior and 10 lateral) and virtual markers are used to close the surface at the top and bottom (Figure 1.35).

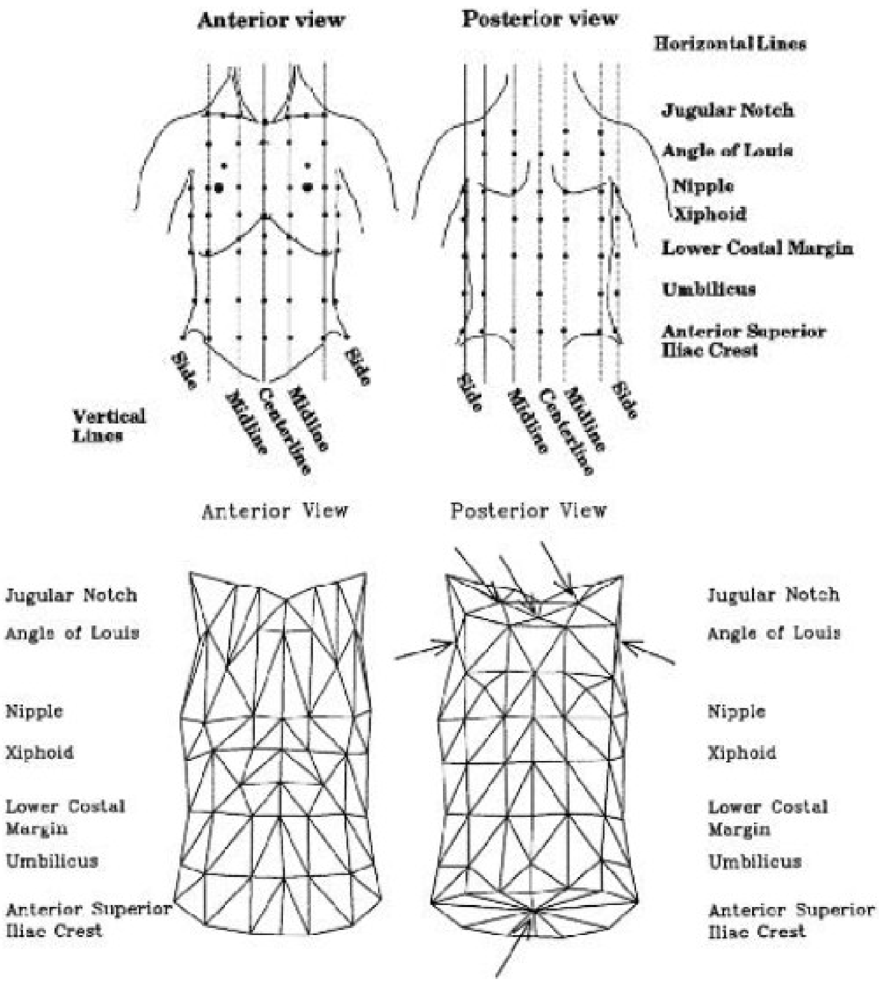

Figure 1.35: Upper panel Placement of infra-red reflective markers on the chest wall: 42 anterior, 34 posterior, and 10laterally between clavicles and anterior superior iliac crest for erect subjects.

The geometrical definition of the model allows the enclosed volume and its changes due to movement to be calculated by surface integration using Gauss's theorem to obtain a volume integral. In detail, the analytical expression of the theorem is (1.20):

$$\int_S \vec{F}\,\vec{n}\,dS = \int_V \nabla\vec{F}\,dV \tag{1.20}$$

where:

S is the surface considered;

V is the volume enclosed by S;

$\vec{F}$ is an arbitrary vector;

$\vec{n}$ is the normal unitary vector at the various points on S;

∇ is the divergence operator;

If we choose an arbitrary vector with unitary divergence, equation 1.20 becomes:

$$\int_S \vec{F}\,\vec{n}\,dS = \int_V dV = V \tag{1.21}$$

and the volume integral is calculated by means of a simpler surface integral.
Passing from a continuous to discrete form, equation (1.21) becomes:

$$\sum_{i=1}^{K} \vec{F}\vec{n}_i A_i = V \tag{1.22}$$

where:
K is the total number of triangles;
A_i is the area of the i-th triangle;
$\vec{n}_i$is the normal unitary vector of the i-th triangle.
By considering the geometric model of the whole trunk surface, it is therefore possible to calculate total chest wall volume changes, whereas by considering only part thereof, the contributions of the different compartments to total volume changes can also be calculated.
This technique is completely non-invasive and allows estimating both volume and movements of single points on the chestwall.
It has been also used in ICU, intensive care unit, (82) on 13 ALI/ARDS patients and the results were compared with spirometry.
The first result was that optoelectronic plethysmography is as feasible for these patients as it is for normal subjects.

1.5. MEASUREMENT OF LOCAL PROPERTIES

Although Peslin (83) postulated that was not necessary to consider a more complex than a one compartment model in order to describe the mechanical behavior of the chest wall, in literature we can find other experiences (40, 84-86) where the authors performed measurements on different compartment of the chest-wall by means of different technique. Here we report just few experiment were different techniques have been used, from the very hand-made set-up proposed by Dubois to the refined method proposed by Dellacà, based on OEP, nevertheless in literature it is possible to find also other instrumentation such as magnetometers directly placed on the chest-wall of the subjects.(87). In any case all the authors find a different behavior of rib cage compared to abdomen, in particulat $Z_{rc}<Z_{ab}$, although the whole impedance reflects the behavior of the ribcage since the parallel arrangement of the two compartments.

1.5.1. REGIONAL IMPEDANCE

The first experiments who try to define the mechanical differences of the rib cage and abdominal districts by means of FOT has been carried out by Dubois *et al.* (40), they produces a sinusoidal pressure stimulus at the mouth and measured the displacement of two points one on the ribcage and the other on the abdomen and compare them.

G. MEASUREMENTS OF RIBCAGE AND ABDOMEN COMPARTMENTS

In more details in this method a transthoracic pressure is generated by a pump and measured by a capacitance manometer, the force of the respiratory muscles is made as small as possible by voluntary relaxation at the end of expiration.
Motion of the chestwall was measured by a light weight, flexible balsa wood shaft, was held against the chest with slight pressure, as reported in Figure 1.36

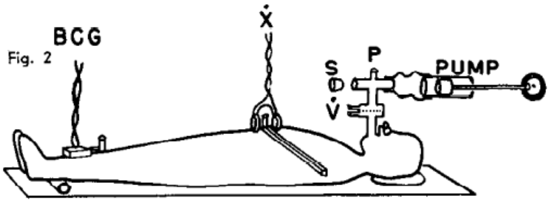

Figure 1.36: set up for measurement of mechanical motion in response to a small pump at the mouth

The records from these transducers were made at a series of different pump frequencies and read for frequency, amplitude and phase difference between simultaneously recorded waves.
The results are shown in Figure 1.37.
These data seems reproducible although the behavior of the chest and of the abdomen, presents fair differences in phase and amplitude, which show different spectral trends.
Then the authors tried to fit the results on a monoalveolar model, but they found that C, the capacitance of the chest, is much less than values in the literature, exactly like (46, 75) this may be an indication that chest exhibits a non homogenous response at higher frequencies. Further evidence for this is added from the measurements of surface of other points of the chest. It seems quite probable that the abdomen responds at lower frequencies and that the chest responds at higher frequency due to their inherent characteristic of mass and elasticity.

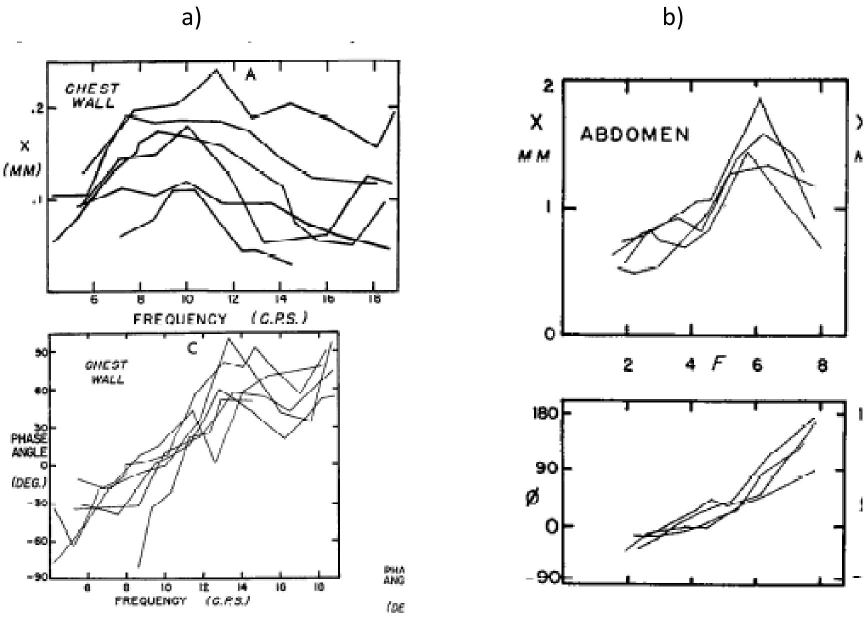

Figure 1.37: Panel a) chest displacement and phase at different frequencies, b) abdomen displacement and phase at different frequencies.

Another interesting study based on compartmentalization has been performed by Barnas *et al* (84), they partitioned the chestwall impedance into the impedance of its two major compartments, the rib cage and the diaphragm abdomen, then they calculated the impedance of the pathways from chest-wall driving pressure, measured with esophageal balloon and gastric balloon , to rib cage and abdominal wall surface displacement, measured with inductance plethysmographic belts.

They reference model is represented in Figure 1.38.

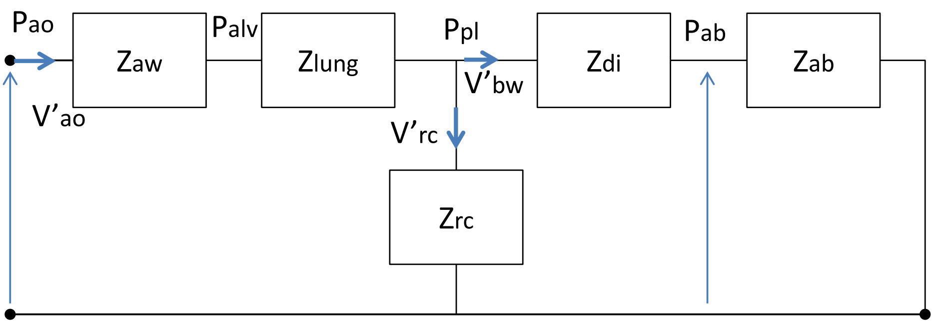

Figure 1.38: Model of the respiratory system where rib-cage and abdomen are considered as two separated compartments.

The impedance is estimated as reported in the Table 1.4.

Volume displacements of the total chest wall surface, measured by summing the rib cage and abdominal signals, approximated measurements using volume-displacement, body plethysmography over the entire frequency range. Resistance (R) and elastance (E) of the diaphragm-abdomen pathway were several times greater than those of the rib cage pathway, except at the highest frequencies where diaphragm-abdominal E was small. R and E of the diaphragm-abdomen pathway and of the rib cage pathway showed the same frequency dependencies as that of the total chest wall: R decreased markedly as frequency increased, and E (especially in the diaphragm-abdomen) decreased at the highest frequencies. These results suggest that the chest wall can be reasonably modeled, over the frequency range studied, as a system with two major pathways for displacement. Each pathway seems to exhibit behavior that reflects nonlinear, rate independent dissipation as well as viscoelastic properties.

Table 1.4: Definition of impedance as reported by Barnas.

Complex ratios measured	Resistance	Elastance	Comments
$Z_{rc,path} = \Delta P_{pl} / \dot{V}_{rc}$	R_{rc}	E_{rc}	Rib cage pathway impedance
$Z_{d-a,path} = \Delta P_{pl} / \dot{V}_{bw}$	R_{d-a}	E_{d-a}	"Pathway impedance" of diaphragm-abdomen
$Z_{bw+} = \Delta P_{ab} / \dot{V}_{bw}$	R_{bw+}	E_{bw}	"+" represents impedance of abdominal contents between belly wall and gastric balloon.

Impedances of these pathways are useful indexes of changes in chest wall mechanical behavior in different situations.

H. IMPEDANCE MAP BY OEP AND FOT

The optoelectronic plethysmography (OEP) has proven capable of measuring volume variations of the chest wall accurately by noninvasive measurements of the displacements of passive markers placed on the external surface of the chest wall over selected reference points (88). It has been shown that using this technique it is possible to track flow excursions of the chest wall while imposing pressure oscillations at the airway opening (85). Considering different subsets of optical markers placed on the thorax, it is possible to partition the Z_{tr} by measuring the contribution of distinct components of the chest wall to the total Z_{tr}. Regardless of which method is used, the interpretation of Z_{tr} often requires fitting the data with a simple lumped element model in which a single airway compartment is partitioned from a single tissue compartment by a shunt gas-compression compliance for the air in the lung. The tissue compartment represents the combined effects of lung parenchyma and chest wall.

The study of regional pleural expansion during high frequency ventilation (HFV) at 15 and 30 Hz of excised lungs using synchronized stroboscopic photography(89) shows that, while at low frequency (1 Hz) the expansion of the lung was nearly synchronous, the lung expanded asynchronously. These nonuniformities suggest marked inter-regional airflow and elastic wave propagation in the parenchyma when a high-frequency pressure forcing is applied to the airway opening. Also, during typical breathing conditions it is commonly accepted that the chest wall has at least two and perhaps more independent mechanical components (as lung-apposed and diaphragm-apposed rib cage and abdomen), all of which have disparate mechanical properties. Evidence for such disparate behavior between the abdomen and rib cage has been published over the frequency range from 0 to 4 Hz by Barnas and co-workers (87).

The current study made up by Dellacà et al. is concerned about how local variations in chest wall and lung properties (measured as local transfer impedance) and elastic wave propagation might or might not impact measures of total Z_{tr} over a frequency range from 4 to 12 Hz.

The hypothesis is that local heterogeneities as well as surface wave propagation, mainly at higher frequencies, are not sufficiently distinct to justify interpretation of Z_{tr} with more than one lumped tissue compartment for the whole respiratory system. On the other hand, a technique that allows the estimation of the distribution of Z_{tr} over the chest wall surface could be useful to study, evaluate, and quantify changes in respiratory mechanics induced by restrictive chest wall diseases or to study heterogeneity in airways obstruction or during bronchial challenge.

Thus, using OEP it is developed a new method to measure the degree of heterogeneity in Z_{tr} with higher spatial resolution and the propagation of pressure waves along the chest wall during pressure oscillations imposed at the mouth.

The experimental setup is composed by: a computer-controlled loudspeaker to apply a sinusoidal forcing pressure at the mouth mounted on a rigid box of $\sim$ 3 l of internal volume. A single sinusoid waveform was used in order to maximize the signal-to-noise ratio. To obtain the frequency dependence of the response, we repeated the measurements on the same subject changing the forcing frequency. Three different forcing frequencies were used in this study for movement analysis (4, 8 and 12 Hz), while for studying regional transfer impedance six frequencies (2, 4, 6, 8, 10 and 12 Hz) were used.

Chest wall kinematics were measured in the supine posture by an automatic optoelectronic motion analyzer able to measure with high accuracy and high temporal resolution (100 Hz) the three-dimensional (3D) coordinates of passive markers placed on the body surface, that are precisely 68 positioned with a high number of markers placed on the abdomen.

Briefly, the protocol used requires a training period on the oscillation system to accustom the subject, lying in a bed, to relax the respiratory muscles during the pressure forcing. During this training period, airway pressure and flow were monitored and the adaptation lasted until the signals became constant in amplitude.

After a few breaths, the subject exhaled passively to functional residual capacity (FRC), placed the mouth tightly around the mouthpiece while an operator firmly supported the cheeks. The subject then stayed relaxed for 13 s holding his breath while pressure and 3D marker position were recorded. Each test was repeated at the different frequencies, with a peak-to-peak pressure value of about 4 cmH_2O.

The accurate measurement of 3D marker coordinates during oscillations allowed two different types of analysis:

Motion analysis: it is calculated the amplitude of marker displacements and the craniocaudal phase shifts of these amplitudes.

The relative displacement at time t of the ith marker [$s_i(t)$], whose position was identified by the 3D coordinates $x_i(t)$, $y_i(t)$, $z_i(t)$, is computed as follows (1.23):

$$s_i(t) = \sqrt{[y_i(t)] - [y_i(0)]^2 + [z_i(t)] - [z_i(0)]^2}, \qquad 1.23$$

where instant 0 identifies the time of the first acquired image frame. We considered only displacements in the anteroposterior (z axis) and laterolateral (y axis) directions, because preliminary analysis revealed that craniocaudal movements along the x axis were not related to the stimulus and, if considered, the signal-to-noise ratio decreased.

The phase shift $\Delta\phi_{1,i}$ is estimated as the phase angle of the transfer function between the displacement of the reference marker [$s_1(t)$] and the other nine markers [$s_i(t)$, with I=2 to 10].

Regional transfer impedance: the chest wall surface is approximated by 110 triangles connecting the markers; from the displacement of each triangle during oscillations are estimated ''local'' volume variations and finally, the transfer functions between the local flow and P_{ao} (local transfer impedance, Z_{el}) describes the spatial distribution of respiratory system transfer impedance.

The phase values become inhomogeneously distributed at the higher frequencies, mainly in the abdominal region, while at 4 Hz they are similar all over the chest wall surface, at 8 and 12 Hz the lower-central subumbilical part of the abdominal wall showed the highest phase shifts, which decreased with distance. This regional differences in phase (and presumably in regional abdominal pressure) show that considering the abdomen as a unique compartment classically modeled as a liquid-filled elastic container, imply excessive simplification, especially during fast maneuvers, as suggested by Decramer et al(90). This phenomenon is particularly important during forced oscillations, where more sophisticated models than a single lumped resistance-inertance-elastance are necessary to describe the mouth pressure-abdominal volume relationship at frequencies equal to or higher than 8 Hz and the definition of these new models requires specific measurements of local chest wall mechanics.

Indeed, the use of optoelectronic plethysmography to measure the transfer impedance of the chest wall partitioned into three compartments (pulmonary rib cage, abdominal rib cage, and abdomen) permits to find that their percentage contribution to total Ztr modulus changed from 33%, 13%, and 54% at 1 Hz to 72%, 13%, and 15% at 24 Hz, respectively as shown in Figure 1.39.

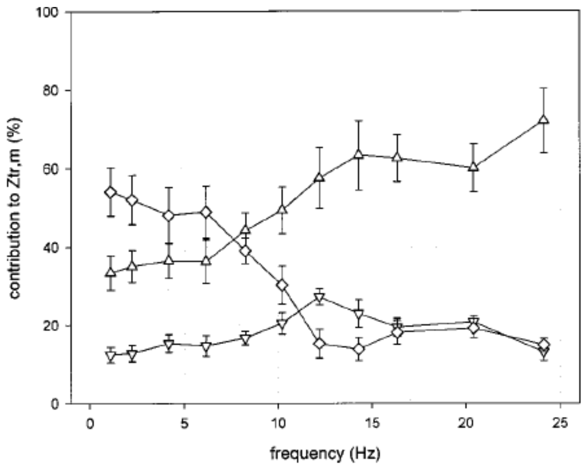

Figure 1.39: Percentage contribution of the different chest wall compartments to total transfer impedance ($Z_{tr,m}$): pulmonary rib cage (Δ), abdominal rib cage (∇), and abdomen (◊).

Optoelectronic plethysmography is a potentially ideal technique to be combined with forced oscillation technique (FOT) because, in principle, it allows the accurate volume measurement of any chest wall compartment one wishes to measure at high sampling rate and without introducing any dynamical effect on the measured volumes. The volume computation procedure for OEP explained before allows the measurement of volume changes due to the motion of very small chest wall surface elements. This procedure is the applied to five healthy subjects to computeZ_{tr} for each local pathway, as the complex ratio between P_{ao} and the small element flow.

Averaged transfer impedance maps have been plotted as specific modulus (modulus divided by element surface) and phase color-scale two-dimensional (2D) graphs. These maps, reported in Figure 1.40, clearly show that Z_{tr} is much more homogeneous in the upper rib cage than in the abdomen. Moreover, when the frequency increased, the amplitude of the abdominal motion rapidly reduced, mainly in the central part of the compartment. Consequently, the abdominal Z_{tr} modulus increased with frequency.

Phase angles reached very high values in the lower-central part of the abdomen, markedly exceeding 180°, probably due to the high inertance of the abdominal contents. All these results confirm that chest wall mechanical properties are characterized by a strongly heterogeneous spatial distribution.

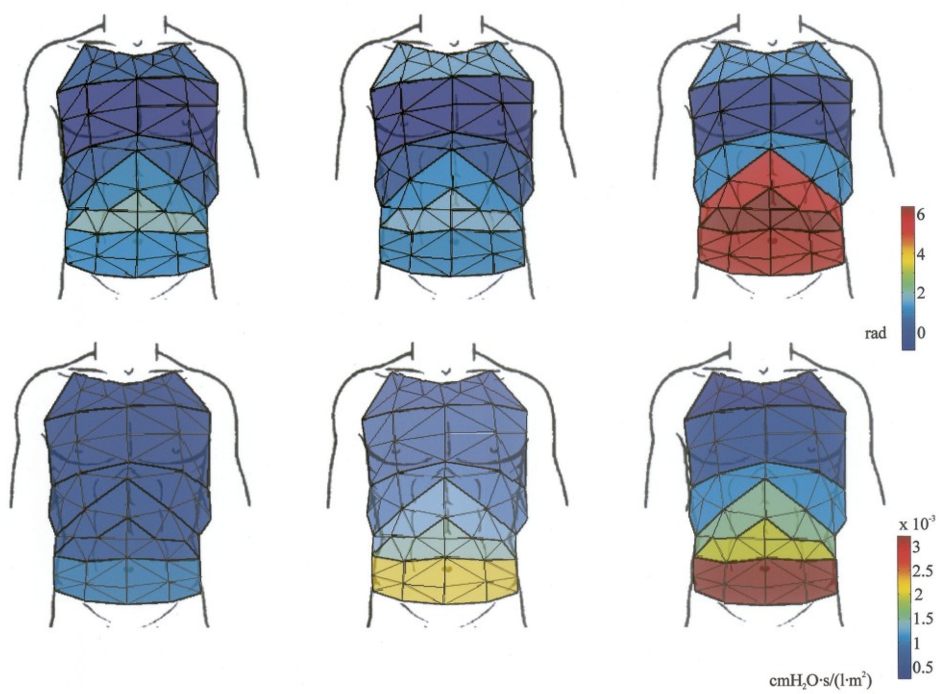

Figure 1.40: Average modulus, upper panels and phase angle, lower panels, local transfer impedance colored maps obtained considering the chest wall as divided in six regions. The forcing frequencies were 4 (left), 8 (center), and 12 Hz (right).

1.6. REMARKS

In conclusion, from literature we can state that the mechanical behavior of the chest-wall is an important parameter to define the state of the respiratory system in healthy and pathological conditions.

Different approaches have been tried to estimate the mechanics and to define quantitatively parameters, the most encouraging are based on the forced oscillation in addition to any system to measure the chest-wall volume variations or chest-wall displacements since it provides information on lung tissue parenchyma.

In the reported studied, where a compartmentalization in at least two regions, rib cage and abdomen, has been carried out, some evident heterogeneities stand up between the two compartments. In fact the ribcage is much more rigid and less inertive than the abdomen; Dellacà *et al*. clearly show that while the pulmonary rib cage behaves homogeneously up to at least 12 Hz, the lower part of the chest wall (abdominal rib cage and abdomen) becomes less homogeneous with increasing frequency, in particular the abdomen cannot be described by a single degree of freedom for a frequency above 6 Hz.

Although these differences are evident in a local analysis they seems to be regardless in studied where the whole Z_{tr} has been measured since the two compartments are in parallel, so the ribcage, which has a lower resistance, covers completely the behavior of abdomen.
Therefore, local analysis of chest-wall mechanics in healthy subjects, presents evident heterogeneity although is well accepted that the lungs in this typology of subject is uniform; as a consequence, we may aspect that pathologies such as ARDS, edema and fibrosis which are featured by lung density, local infiltration, bones deformity, affect heavily and locally the mechanics of the chest-wall requiring local measurements.
To perform these kind of measurements we need tools that allow to detect with a very high spatial resolution the chest wall displacement; the last technique based on the use of an optoelectronic movement tracker system seems to be the more promising in term of richness of information, but it has some practical limitations due to the complex methodological aspects involved and to the spatial resolution.
Thus we are looking for devices that can overcome these limitations such as optical ones, which provide high spatial resolution, no contact with the patients and reduced costs.

1.7. REFERENCES

1. Konno K, Mead J. Measurement of the separate volume changes of rib cage and abdomen during breathing. J Appl Physiol. 1967;22(3):407-22.

2. Rahn H, Otis AB, Chadwick LE, Fenn WO. The pressure-volume diagram of the thorax and lung. American Journal of Physiology--Legacy Content. 1946;146(2):161.

3. Mead J, Milic-Emili J. Theory and methodology in respiratory mechanics with glossary of symbols. Handbook of Physiology.Respiration. 1964:363-76.

4. Otis AB. The work of breathing. Physiol Rev. 1954;34(3):449.

5. Nunn JF, Vitkun SA. Applied respiratory physiology. Anesthesiology. 1994;81(1):275.

6. Mead J. Measurement of inertia of the lungs at increased ambient pressure. J Appl Physiol. 1956;9(2):208-12.

7. Peslin R, Fredberg JJ. Oscillation mechanics of the respiratory system. Comprehensive Physiology. 1986.

8. Fry DL. Theoretical considerations of the bronchial pressure-flow-volume relationships with particular reference to the maximum expiratory flow volume curve. Phys Med Biol. 1958;3:174.

9. Ashbaugh DG, Boyd Bigelow D, Petty TL, Levine BE. Acute respiratory distress in adults. The Lancet. 1967;290(7511):319-23.

10. Petty TL, Ashbaugh DG. The adult respiratory distress syndrome. Chest. 1971;60(3):233-9.

11. Bernard GR, Artigas A, Brigham KL, Carlet J, Falke K, Hudson L, et al. The american-european consensus conference on ARDS. definitions, mechanisms, relevant outcomes, and clinical trial coordination. American journal of respiratory and critical care medicine. 1994;149(3):818.

12. Artigas A. Epidemiology and prognosis of acute respiratory distress syndrome. EUROPEAN RESPIRATORY MONOGRAPH. 2002;7:1-21.

13. Luhr OR, Antonsen K, Karlsson M, Aardal S, Thorsteinsson A, FROSTELL CG, et al. Incidence and mortality after acute respiratory failure and acute respiratory distress syndrome in sweden, denmark, and iceland. American journal of respiratory and critical care medicine. 1999;159(6):1849.

14. Roupie E, Lepage E, Wysocki M, Fagon JY, Chastre J, Dreyfuss D, et al. Prevalence, etiologies and outcome of the acute respiratory distress syndrome among hypoxemic ventilated patients. Intensive Care Med. 1999;25(9):920-9.

15. Reynolds HN, McCunn M, Borg U, Habashi N, Cottingham C, Bar-Lavi Y. Acute respiratory distress syndrome: Estimated incidence and mortality rate in a 5 million-person population base. Critical Care. 1998;2(1):29-34.

16. Fowler A, Hamman R, Good J, Benson K, Baird M, Eberle D, et al. Adult respiratory distress syndrome: Risk with common predispositions. Ann Intern Med. 1983;98(5 Pt 1):593.

17. Pepe PE, Potkin RT, Reus DH, Hudson LD, Carrico CJ. Clinical predictors of the adult respiratory distress syndrome. The American Journal of Surgery. 1982;144(1):124-30.

18. Desai S, Hansell D. Imaging in acute respiratory distress syndrome. EUROPEAN RESPIRATORY MONOGRAPH. 2002;7:105-18.

19. Katzenstein A, Bloor CM, Leibow AA. Diffuse alveolar damage--the role of oxygen, shock, and related factors. A review. The American journal of pathology. 1976;85(1):209.

20. Pratt P, Vollmer R, Shelburne J, Crapo J. Pulmonary morphology in a multihospital collaborative extracorporeal membrane oxygenation project. I. light microscopy. The American journal of pathology. 1979;95(1):191.

21. Ostendorf P, Birzle H, Vogel W, Mittermayer C. Pulmonary radiographic abnormalities in shock. Radiology. 1975;115(2):257.

22. Austin J, Müller N, Friedman PJ, Hansell DM, Naidich DP, Remy-Jardin M, et al. Glossary of terms for CT of the lungs: Recommendations of the nomenclature committee of the fleischner society. Radiology. 1996;200(2):327-31.

23. Milne E, Pistolesi M, Miniati M, Giuntini C. The radiologic distinction of cardiogenic and noncardiogenic edema. Am J Roentgenol. 1985;144(5):879-94.

24. Winer-Muram H, Rubin S, Ellis J, Jennings S, Arheart K, Wunderink R, et al. Pneumonia and ARDS in patients receiving mechanical ventilation: Diagnostic accuracy of chest radiography. Radiology. 1993;188(2):479-85.

25. Gattinoni L, Presenti A, Torresin A, Baglioni S, Rivolta M, Rossi F, et al. Adult respiratory distress syndrome profiles by computed tomography. J Thorac Imaging. 1986;1(3):25.

26. Maunder RJ, Shuman WP, McHugh JW, Marglin SI, Butler J. Preservation of normal lung regions in the adult respiratory distress syndrome. JAMA: the journal of the American Medical Association. 1986;255(18):2463.

27. Gattinoni L, Pesenti A, Bombino M, Baglioni S, Rivolta M, Rossi F, et al. Relationships between lung computed tomographic density, gas exchange, and PEEP in acute respiratory failure. Anesthesiology. 1988;69(6):824.

28. Tocino I, Miller M, Frederick P, Bahr A, Thomas F. CT detection of occult pneumothorax in head trauma. Am J Roentgenol. 1984;143(5):987-90.

29. MEADE MO, COOK RJ, GUYATT GH, GROLL R, KACHURA JR, BEDARD M, et al. Interobserver variation in interpreting chest radiographs for the diagnosis of acute respiratory distress syndrome. American journal of respiratory and critical care medicine. 2000;161(1):85.

30. Howling S, Evans T, Hansell D. The significance of bronchial dilatation on CT in patients with adult respiratory distress syndrome. Clin Radiol. 1998;53(2):105-9.

31. Matamis D, Lemaire F, Harf A, Brun-Buisson C, Ansquer J, Atlan G. Total respiratory pressure-volume curves in the adult respiratory distress syndrome. Chest. 1984;86(1):58-66.

32. Radford E. Static mechanical properties of mammalian lungs. Handbook of Physiology.Section. 1964;3:429-49.

33. Mancebo J. PEEP, ARDS, and alveolar recruitment. Intensive Care Med. 1992;18(7):383-5.

34. Knudson RJ, Clark DF, Kennedy TC, Knudson DE. Effect of aging alone on mechanical properties of the normal adult human lung. J Appl Physiol. 1977;43(6):1054-62.

35. Suter P, Fairley HB, Isenberg M. Effect of tidal volume and positive end-expiratory pressure on compliance during mechanical ventilation. Chest. 1978;73(2):158-62.

36. Ranieri V, Brienza N, Santostasi S, Puntillo F, Mascia L, Vitale N, et al. Impairment of lung and chest wall mechanics in patients with acute respiratory distress syndrome. role of abdominal distension. American journal of respiratory and critical care medicine. 1997;156(4):1082.

37. Gattinoni L, Pelosi P, Suter PM, Pedoto A, Vercesi P, Lissoni A. Acute respiratory distress syndrome caused by pulmonary and extrapulmonary disease. different syndromes? American journal of respiratory and critical care medicine. 1998;158(1):3.

38. Gilroy Jr RJ, Lavietes MH, Loring SH, Mangura BT, Mead J. Respiratory mechanical effects of abdominal distension. J Appl Physiol. 1985;58(6):1997-2003.

39. Restrictive lung disease workup [Internet].; 2009. Available from: http://emedicine.medscape.com/article/301760-workup#a0720.

40. DuBois AB, Brody AW, Lewis DH, Burgess BF. Oscillation mechanics of lungs and chest in man. J Appl Physiol. 1956;8(6):587-94.

41. Hantos Z, Daroczy B, Suki B, Galgoczy G, Csendes T. Forced oscillatory impedance of the respiratory system at low frequencies. J Appl Physiol. 1986;60(1):123-32.

42. Lutchen KR, Yang K, Kaczka DW, Suki B. Optimal ventilation waveforms for estimating low-frequency respiratory impedance. J Appl Physiol. 1993;75(1):478-88.

43. Maki BE. Interpretation of the coherence function when using pseudorandom inputs to identify nonlinear systems. Biomedical Engineering, IEEE Transactions on. 1986(8):775-9.

44. Suki B, Lutchen K. Pseudorandom signals to estimate apparent transfer and coherence functions of nonlinear systems: Applications to respiratory mechanics. Biomedical Engineering, IEEE Transactions on. 1992;39(11):1142-51.

45. Van Noord J, Clement J, Van de Woestijne K, Demedts M. Total respiratory resistance and reactance as a measurement of response to bronchial challenge with histamine. American Journal of Respiratory and Critical Care Medicine. 1989;139(4):921.

46. Peslin R, Duvivier C, Didelon J, Gallina C. Respiratory impedance measured with head generator to minimize upper airway shunt. J Appl Physiol. 1985;59(6):1790-5.

47. Nagels J, Landser F, Van der Linden L, Clement J, Van de Woestijne K. Mechanical properties of lungs and chest wall during spontaneous breathing. J Appl Physiol. 1980;49(3):408-16.

48. Michaelson ED, Grassman ED, Peters WR. Pulmonary mechanics by spectral analysis of forced random noise. J Clin Invest. 1975;56(5):1210.

49. Dellaca R, Santus P, Aliverti A, Stevenson N, Centanni S, Macklem P, et al. Detection of expiratory flow limitation in COPD using the forced oscillation technique. European Respiratory Journal. 2004;23(2):232-40.

50. Clement J, Landser F, Van de Woestijne K. Total resistance and reactance in patients with respiratory complaints with and without airways obstruction. Chest. 1983;83(2):215-20.

51. Pasker H, Schepers R, Clément J, Van de Woestijne K. Total respiratory impedance measured by means of the forced oscillation technique in subjects with and without respiratory complaints. European Respiratory Journal. 1996;9(1):131-9.

52. Van Noord J, Clément J, Van de Woestijne K, Demedts M. Total respiratory resistance and reactance in patients with asthma, chronic bronchitis, and emphysema. American Journal of Respiratory and Critical Care Medicine. 1991;143(5 Pt 1):922.

53. Ducharme FM, Davis GM. Respiratory resistance in the emergency department. Chest. 1998;113(6):1566-72.

54. Pasker H, Peeters M, Genet P, Clement J, Nemery B, Van de Woestijne K. Short-term ventilatory effects in workers exposed to fumes containing zinc oxide: Comparison of forced oscillation technique with spirometry. European Respiratory Journal. 1997;10(7):1523-9.

55. Pairon J, Iwatsubo Y, Hubert C, Lorino H, Nouaigui H, Gharbi R, et al. Measurement of bronchial responsiveness by forced oscillation technique in occupational epidemiology. European Respiratory Journal. 1994;7(3):484.

56. Pham Q, Bourgkard E, Chau N, Willim G, Megherbi S, Teculescu D, et al. Forced oscillation technique (FOT): A new tool for epidemiology of occupational lung diseases? European Respiratory Journal. 1995;8(8):1307-13.

57. Van Noord J, Cauberghs M, Van de Woestijne K, Demedts M. Total respiratory resistance and reactance in ankylosing spondylitis and kyphoscoliosis. European Respiratory Journal. 1991;4(8):945-51.

58. Van Noord J, Clément J, Cauberghs M, Mertens I, Van de Woestijne K, Demedts M. Total respiratory resistance and reactance in patients with diffuse interstitial lung disease. European Respiratory Journal. 1989;2(9):846-52.

59. Wesseling G, Wouters E. Analysis of respiratory impedance characteristics in chronic bronchitis. Respiration. 1992;59(2):81-8.

60. Zerah F, Harf A, Perlemuter L, Lorino H, Lorino A, Atlan G. Effects of obesity on respiratory resistance. Chest. 1993;103(5):1470-6.

61. Dellaca RL, Andersson Olerud M, Zannin E, Kostic P, Pompilio PP, Hedenstierna G, et al. Lung recruitment assessed by total respiratory system input reactance. Intensive Care Med. 2009;35(12):2164-72.

62. Dellacà RL, Duffy N, Pompilio PP, Aliverti A, Koulouris NG, Pedotti A, et al. Expiratory flow limitation detected by forced oscillation and negative expiratory pressure. European Respiratory Journal. 2007;29(2):363.

63. Dellacà RL, Zannin E, Kostic P, Andersson Olerud M, Pompilio PP, Hedenstierna G, et al. Optimisation of positive end-expiratory pressure by forced oscillation technique in a lavage model of acute lung injury. Intensive Care Med. 2011:1-10.

64. Dellacà RL, Zannin E, Sancini G, Rivolta I, Leone BE, Pedotti A, et al. Changes in the mechanical properties of the respiratory system during the development of interstitial lung edema. Respir Res. 2008;9:51.

65. Dellaca R, Rotger M, Aliverti A, Navajas D, Pedotti A, Farre R. Noninvasive detection of expiratory flow limitation in COPD patients during nasal CPAP. European Respiratory Journal. 2006;27(5):983.

66. Oostveen E, MacLeod D, Lorino H, Farre R, Hantos Z, Desager K, et al. The forced oscillation technique in clinical practice: Methodology, recommendations and future developments. European respiratory journal. 2003;22(6):1026-41.

67. Govaerts E, Demedts M, Van de Woestijne K. Total respiratory impedance and early emphysema. European Respiratory Journal. 1993;6(8):1181-5.

68. Horan T, Mateus S, Beraldo P, Araújo L, Urschel J, Urmenyi E, et al. Forced oscillation technique to evaluate tracheostenosis in patients with neurologic injury*. Chest. 2001;120(1):69-73.

69. Carvalhaes-Neto N, Lorino H, Gallinari C, Escolano S, Mallet A, Zerah F, et al. Cognitive function and assessment of lung function in the elderly. American journal of respiratory and critical care medicine. 1995;152(5):1611.

70. Gimeno F, Van Der Weele L, Koeter G, De Monchy J, van Altena R. Variability of forced oscillation (siemens siregnost FD5) measurements of total respiratory resistance in patients and healthy subjects. Ann Allergy. 1993;71(1):56-60.

71. Landser F, Clément J, Van de Woestijne K. Normal values of total respiratory resistance and reactance determined by forced oscillations: Influence of smoking. Chest. 1982;81(5):586-91.

72. Coe CI, Watson A, Joyce H, Pride NB. Effects of smoking on changes in respiratory resistance with increasing age. Clin Sci (Lond). 1989 May;76(5):487-94.

73. Peslin R, Pham QT, Teculescu D, Gallina C, Duvivier C. Comparative value of respiratory input and transfer impedances in field studies. Bull Eur Physiopathol Respir. 1987 Jan-Feb;23(1):37-42.

74. Mead J. Contribution of compliance of airways to frequency-dependent behavior of lungs. J Appl Physiol. 1969;26(5):670.

75. Peslin R, Duvivier C, Gallina C. Total respiratory input and transfer impedances in humans. J Appl Physiol. 1985;59(2):492-501.

76. Peslin R, Gallina C, Duvivier C. Respiratory transfer impedances with pressure input at the mouth and chest. J Appl Physiol. 1986;61(1):81-6.

77. Tomalak W, Peslin R, Duvivier C. Variations in airways impedance during respiratory cycle derived from combined measurements of input and transfer impedances. European Respiratory Journal. 1998;12(6):1436-41.

78. Lutchen KR, Sullivan A, Arbogast FT, Celli BR, Jackson AC. Use of transfer impedance measurements for clinical assessment of lung mechanics. American journal of respiratory and critical care medicine. 1998;157(2):435.

79. Van Noord J, Demedts M, Clement J, Cauberghs M, Van de Woestijne K. Effect of rib cage and abdominal restriction on total respiratory resistance and reactance. J Appl Physiol. 1986;61(5):1736-40.

80. Ferrigno G, Pedotti A. ELITE: A digital dedicated hardware system for movement analysis via real-time TV signal processing. Biomedical Engineering, IEEE Transactions on. 1985(11):943-50.

81. Cala S, Kenyon C, Ferrigno G, Carnevali P, Aliverti A, Pedotti A, et al. Chest wall and lung volume estimation by optical reflectance motion analysis. J Appl Physiol. 1996;81(6):2680.

82. Aliverti A, Dellaca R, Pelosi P, Chiumello D, Pedotti A, Gattinoni L. Optoelectronic plethysmography in intensive care patients. American Journal of Respiratory and Critical Care Medicine. 2000;161(5):1546.

83. Peslin R, Papon J, Duviver C, Richalet J. Frequency response of the chest: Modeling and parameter estimation. J Appl Physiol. 1975;39(4):523-34.

84. Barnas G, Yoshino K, Stamenovic D, Kikuchi Y, Loring S, Mead J. Chest wall impedance partitioned into rib cage and diaphragm-abdominal pathways. J Appl Physiol. 1989;66(1):350-9.

85. Aliverti A, Dellaca R, Pedotti A. Transfer impedance of the respiratory system by forced oscillation technique and optoelectronic plethysmography. Ann Biomed Eng. 2001;29(1):71-82.

86. Dellaca R, Aliverti A, Lutchen K, Pedotti A. Spatial distribution of human respiratory system transfer impedance. Ann Biomed Eng. 2003;31(2):121-31.

87. Barnas GM, Yoshino K, Loring SH, Mead J. Impedance and relative displacements of relaxed chest wall up to 4 hz. J Appl Physiol. 1987;62(1):71-81.

88. Aliverti A, Dellacà R, Pelosi P, Chiumello D, Gattinoni L, Pedotti A. Compartmental analysis of breathing in the supine and prone positions by optoelectronic plethysmography. Ann Biomed Eng. 2001;29(1):60-70.

89. Jackson AC, Lutchen KR. Physiological basis for resonant frequencies in respiratory system impedances in dogs. J Appl Physiol. 1991;70(3):1051-8.

90. Decramer M, De Troyer A, Kelly S, Zocchi L, Macklem P. Regional differences in abdominal pressure swings in dogs. J Appl Physiol. 1984;57(6):1682-7.

2. CONTACTLESS TECHNOLOGIES FOR DISPLACEMENT MEASUREMENTS

From the previous chapter, one can infer that the assessment of the mechanical properties of chest-wall requires an accurate measurement of its displacement which can be carried out by means of laser interferometry and optical distantiometer, two optical technologies with complementary features.
In this chapter preliminary tests to assess displacements in vivo and in vitro are presented.

2.1. MICHELSON CONFIGURATION

“Optical interferometer is an instrument for making precise measurements for beams of light of such factors as length, surface irregularities, and index of refraction. It divides a beam of light into a number of beams that travel unequal paths and whose intensities, when reunited, add or subtract (interfere with each other). This interference appears as a pattern of light and dark bands called interference fringes. Information derived from fringe measurements is used for precise wavelength determinations, measurement of very small distances and thicknesses, the study of spectrum lines, and determination of refractive indices of transparent materials. In astronomy, interferometers are used to measure the between stars and the diameters of stars (1) ”.
Laser interferometer can successful be applied at the measurement of relative displacement of a target with a very high spatial resolution (less than 1 micrometer) and time resolution.
The first interferometer was proposed by Michelson and Morley in 1886 (2), who suggested a homodyne configuration. It is set up by a laser source, a beam splitter a reference mirror, a cube corner as a target and a detector (Figure 2.1).
The coherent light produced by the laser is split by the beam splitter. The first beam goes towards the reference mirror which reflects it; the second one reached the cube corner, which reflects it too. The two reflected beams recombine (they interfere) at the level of the beam splitter and their sum is detected by a suitable detector such as a photodiode.

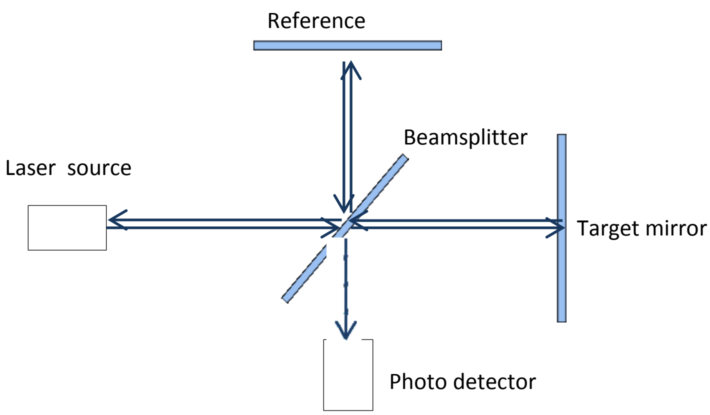

Figure 2.1: Michelson interferometer configuration.

Since the reference path length is constant while the target path changes according to the position of the target, the interference will change providing infinite combinations. Anyway the opposite are:

1) The target beam and the reference beam are completely out of phase, as a consequence their sum equals zero;
2) They are completely in phase and their sum will be the maximum optical power.

If the target is moving always in the same direction it is possible to appreciate a transition from darkness to light in the photo-detected light, which is named fringe each time the target moves of half a wavelength of the laser.

A more detailed analysis leads to the following equations to describe the photo-detected light.

$$I_{ph} = \sigma|\boldsymbol{E_m} + \boldsymbol{E_{mr}}|^2 = \sigma\left\{E_m^2 + E_r^2 + 2E_mE_r \cdot Re\left[e^{i(\varphi_m-\varphi_r)}\right]\right\} \qquad 2.1$$

Where:

$\boldsymbol{E_m}$is electric field related to the measurement path. It has E_m amplitude and φ_m phase;

$\boldsymbol{E_r}$is electric field related to the reference path. It has E_r amplitude and φ_r phase;

From the equation above 2.1 is it possible to find the photodiode current, which results to be:

$$I_{ph} = I_m + I_r + 2\sqrt{I_mI_r}\cos(\varphi_m - \varphi_r) \cdot \qquad 2.2$$

Since the phase is related to the displacement by the following equation:

$$\varphi = 2\frac{2\pi}{\lambda}s \cdot \qquad 2.3$$

Where:

λ is laser wavelength;

s is the target displacement.

It is possible to estimate the target movement from the photodiode signal for less than the direction, which is not defined, in fact at each fringe, transition from darkness to light (or vice versa), corresponds a displacement s of the target of $\lambda/2$.

Anyway since the direction of target displacement is essential in many application, new approaches have been explored to calculate it, based on Michelson interferometer.

Michelson interferometer relies on the information provided by the real part of the electric field; a quadrature signal is required to recover information on direction.

This can be obtained in different ways; here two of them will be discussed. They are the two beams interferometer and the heterodyne interferometer.

2.1.1. TWO BEAMS INTERFEROMETER

The two beams interferometer approach requires: 1)the adding of a second plate which is $\lambda/_8$ deep and which has a slope of 45°, 2) a second detector and 3) a laser light polarized at 45°. This configuration yields to two beams with two different polarizations which follow the same optical path, but with a phase shift of $\pi/2$ due to the second plate which shifts only one of them (Figure 2.2).

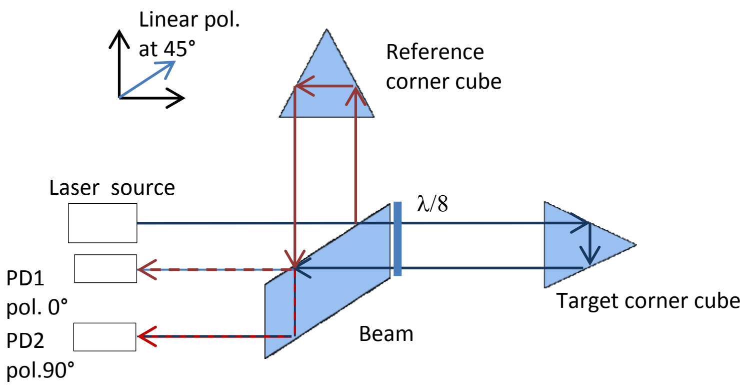

Figure 2.2: two beams interferometer configuration.

Estimation of photodiodes current by electric fields, leads to the equations reported below.

$$I_{ph1} \propto I_m\{1 + \cos[sk(s_m - s_r)]\} \qquad 2.4$$

$$I_{ph2} \propto I_m\{1 + \sin[sk(s_m - s_r)]\} \qquad 2.5$$

Where:

$k = \frac{2\pi}{\lambda}$=wavelength number.

In this way the first signal is a function of cosine shift, while the other one is a function of the sine shift, granting displacement reconstruction without ambiguity.

2.1.2. HETERODYNE LASER SYSTEM

In the heterodyne interferometer configuration (Figure 2.3), the quadrature signal is obtained by the usage of a dual frequency laser source, which contains two polarizations, one with a frequency F1, and the other with frequency F2. The beat frequency between them is F2-F1.

A polarizing beam-splitter reflects the light with frequency F1 into the reference path. Light with frequency F2 passes through the splitter into the measurement path where it strikes the moving reflector causing the frequency of the reflected beam to be Doppler shifted by δF. This reflected beam is then combined with the F1 frequency light at the interferometer, and returned to the laser detector unit with a new beat frequency of F2 – F1 δF.

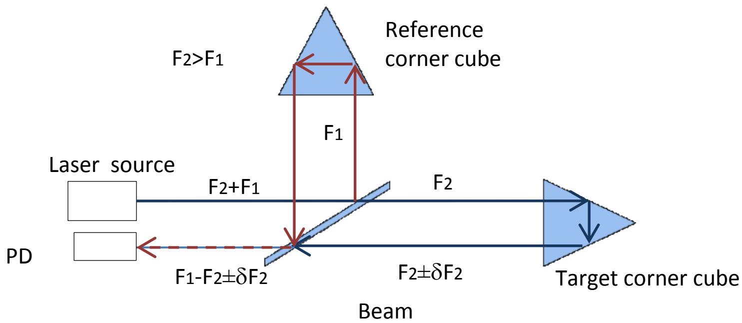

Figure 2.3: heterodyne interferometer configuration.

2.2. *PERFORMANCE AND MEASUREMENTS LIMITS*

Each interferometer, regardless of its configuration, shows some limits in detectable distances, which can be expressed by means of suitable parameters.

2.2.1. DETECTION LIMITS

The most important parameters, which define the laser performances, are listed below:

1) Minimum detectable displacement, which is typically limited by the intrinsic noise or by the downstream electronic resolution;

2) Maximum detectable displacement, which is limited by the maximum laser coherence;

3) Maximum frequency of target displacement which is connected with the electronic downstream bandwidth;

4) Doppler's effect limits, i.e. a slow movement of big amplitude can lead to a high frequency interferometric signal. Suppose a target is moving with a sinusoidal movement

$$s(t) = A\cos(2\pi ft + \varphi) \quad 2.5$$

Its maximum velocity is:

$$v(t)_{max} = \left.\frac{ds(t)}{dt}\right|_{max} = A2\pi f \quad 2.6$$

This is a function of frequency and of amplitude, too.

2.2.2. SPECKLES

Speckles effects are associated with diffusive targets which show a roughness comparable to the laser wavelength.

If a coherent beam is focused on a diffusive surface, the back reflected light assumes a granular bi-dimensional distribution similar to a white noise which is known as speckle pattern (3).

When a coherent light is reflected by a diffusive surface, each point acts as source of radiation, thus the field of a generic point P is given by the sum of several back-reflected fields with a casual phase due to the roughness height Figure 2.4. A speckle is defined as a space region where the field auto correlation is more than 0.5.

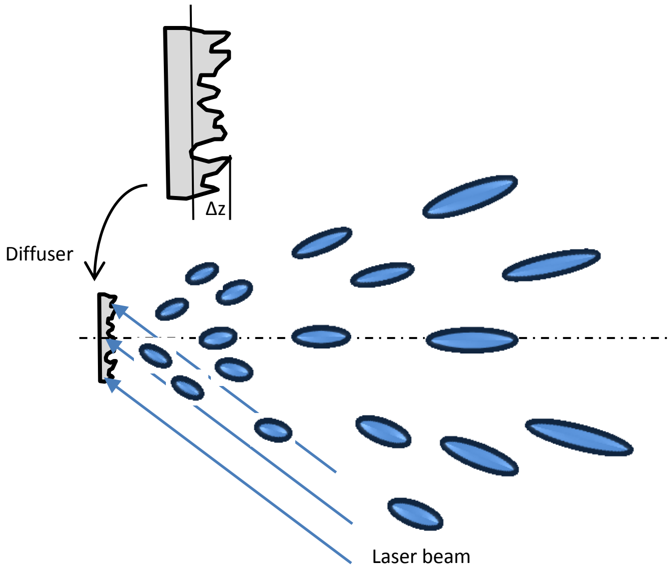

Figure 2.4: speckles generation phenomenon.

A speckle looks like an ellipsoid with the major axes oriented along the line starting from the diffusor center, which dimensions are statistical variables, with the following mean values (4, 5, 5).

$$s_z = \frac{2}{\pi}\lambda\left(\frac{2z}{D}\right)^2 \quad 2.7$$

$$s_{xy} = \frac{4}{\pi}\frac{\lambda z}{D} \qquad 2.8$$

Where:

s_z is the longitudinal dimension along z axes;

s_{xy} is the dimension in the xy plane;

D is the laser spot diameter on the surface;

Speckles patterns should be carefully considered in each measurement, because they can hard affect the back-reflected beam optical power, yielding to a reduction of the signal. In order to control their impact the laser beam should be well focused on the target to increase the dimension of bright speckles.

2.3. SELF MIXING INTERFEROMETRY

Traditional interefometric configurations such as Michelson and MachZender, require mirrors, beam splitter and corner cubes to detect displacement signal but nowadays thanks to technological development a new compact and portable interferometer configuration has been developed: laser self-mixing interferometer.

2.3.1. WORKING PRINCIPLES

Laser self-mixing interferometry, or feedback or induced modulation interferometry, as it has been equivalently called, doesn't need any kind of external mirror or beam splitter because it relies on the concept of back injected light: a fraction of light back-reflected or backscattered by a remote target re-enter the laser cavity, generating a modulation of both amplitude and frequency of the lasing field, thus the laser source acts a sensitive detector for the path length $2ks$ travelled by the light to the target and back(6, 7).

A. THREE-MIRRORS CAVITY MODEL

The self-mixing interferometer configuration can be modeled as a three-mirror cavity model (Figure 2.5), where:

P_0 is the unperturbed light emitted by the laser;

$P_r = \frac{P_0}{A}$ is the power backdiffused or backrefleced by the remote target. A is the power attenuation of the external cavity and A>1.

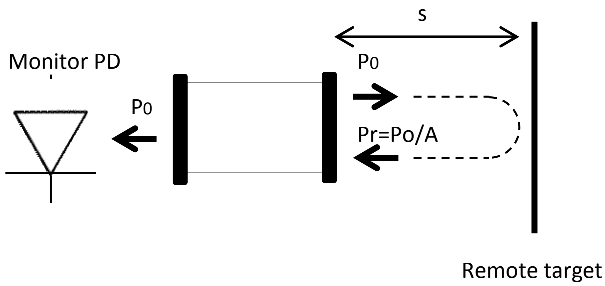

Figure 2.5: three-mirror cavity model for a self-mixing interferometer.

A simple interpretation for injection detection is the following (7), as reported in Figure 2.6: amplitude and frequency modulation interpretation for lasing phasor and reflected phasor: the lasing field phasor $\boldsymbol{E_o}$in the cavity is modulated by the backreflected field phasor $\boldsymbol{E_r}$ which re-enters the cavity and adds to the lasing field. Since the phase of $E_{ris}\varphi(t) = 2ks(t)$, the lasing field amplitude and frequency are modulated by the term$\varphi = 2ks$. Thus the FM term is sin(2ks) and the AM term is cos(2ks). This detection scheme very closely resembles the well-known homodyning at radio frequencies. From the two quadrature signals, the interferometric phase ϕ = 2ks can be recovered without ambiguity, and a measurement of the target displacement is possible (6, 8).

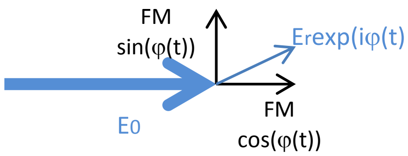

Figure 2.6: amplitude and frequency modulation interpretation for lasing phasor and reflected phasor.

B. THEORY FOR SELF-MIXING IN LASER DIODE

Three-mirror cavities models can be applied only on gas lasers, because of some second order effects that can't be neglected in the case of a single mode Fabry Perot laser diode:

1. the large line width of these source forbids the detection of the frequency modulation term, therefore just one interferometric channel is available, as opposed to conventional external interferometers that provides two in quadrature signals;
2. the intrinsic non-linear nature of the semiconductor active medium makes the amplitude modulation term different from the cosine function.

Finally, the laser diode threshold condition is varied by the phase of the back-reflected light, thus the emitted power changes as the pump current is held constant. The change in the threshold implies a change in the actual LD carrier density; as a consequence, the wavelength emitted by the LD subject to back-reflections is also slightly varied (9).

Thanks to a rigorous mathematical analysis, Lang and Kobayashi (10) first derived an analytic solution to the problem, from which the steady state solution can be found (8, 9, 11).

Steady state solution

The steady state solution allows reaching the following general expression for the power emitted by the laser diode:

$$P(\varphi) = P_o[1 + mF(\varphi)] \cdot \qquad 2.9$$

Where:

P_o is the power emitted by the unperturbed laser diode?

M is the modulation index;

$F(\varphi)$ is a periodic function of the interferometric phase?

The modulation index m and the function $F(\varphi)$ depend on the so called feedback parameter C, as defined by (9), which depends on both the amount of feedback and target distances as can be inferred from the equation below. This parameter is very important because it discriminates among different feedback regime.

$$C = \frac{\kappa s\sqrt{1+\alpha^2}}{L_{las}\eta_{las}} \cdot \qquad 2.10$$

Where:

α is the laser diode line-width enhancement factor?

L_{las} is the laser cavity length;

η_{las} is the cavity refractive index;

κ is a parameter which accounts for the attenuation.

Laser feedback regime according to C.

According to C parameters value, function $F(\varphi)$ and the modulation parameter m assume different morphology.

1. $C \ll 1$ leads to a very weak feedback regime; the function $F(\varphi)$ is a cosine and the modulation index m is inversely proportional to $\sqrt{A}$ (Figure 2.7: self-mixing signal recorder for a sinusoidal displacement of 1.2 um at 675 Hz and C<<1).

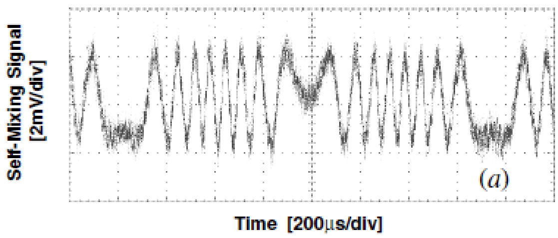

Figure 2.7: self-mixing signal recorder for a sinusoidal displacement of 1.2 um at 675 Hz and C<<1.

2. $0.1 < C < 1$ leads to the weak feedback regime, the function $F(\varphi)$get distorted, showing a non-symmetrical shape and the modulation index m is inversely proportional to $\sqrt{A}$ (Figure 2.8).

a) b)

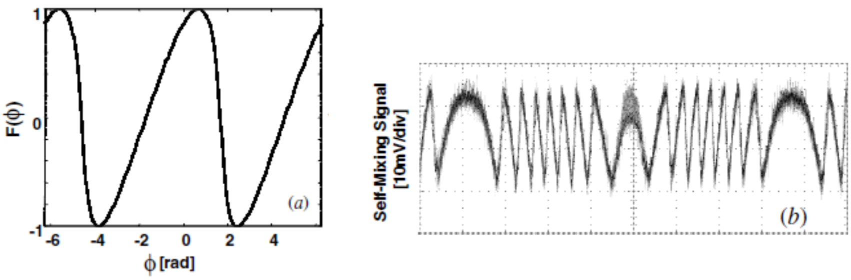

Figure 2.8: Panel a) F(φ) as a funtion of the phase φ, it looks like a distorted cosine function. Panel b) self-mixing signal recorder for a sinusoidal displacement of 1.2 um at 675 Hz and C≈1.

3. $1 < C < 4.6$ leads to the moderate feedback regime, the function $F(\varphi)$ becomes three-valued for certain values of the phase, thus the system is bistable. The modulation index m is not longerinversely proportional to $\sqrt{A}$. The interferometric signal becomes sawtooth-like and exhibits hysteresis (Figure 2.9).

a) b)

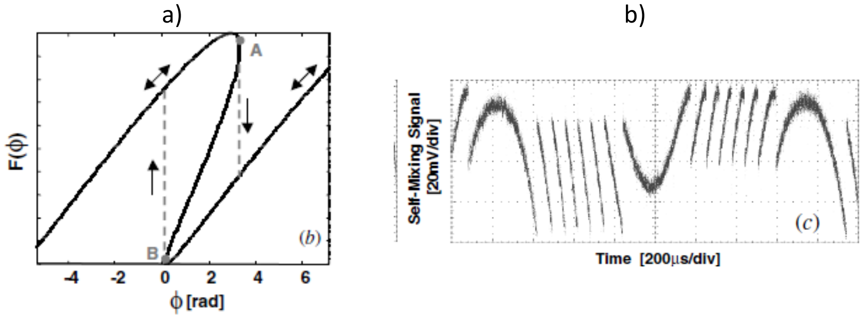

Figure 2.9: Panel a)F(φ) as a function of the phase φ, the segment AB is unstable. Panel b) self-mixing signal recorder for a sinusoidal displacement of 1.2 um at 675 Hz and C>1.

4. $C > 4.6$ leads to the strong feedback regime. the function $F(\varphi)$ becomes five-valued for certain values of the phase, thus the system is unstable. Giuliani observed (6) that not all the specimen of Fabry Perot laser diode remains in the self-mixing regime, some cases they enters the mode-hopping regime avoiding interferometric measurements(Figure 2.10).

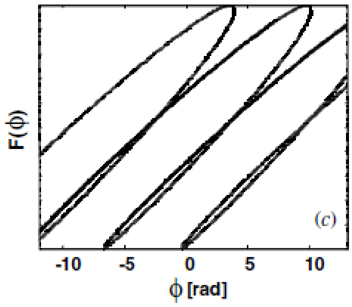

Figure 2.10: F(φ) as a function of the phase φ, this is not a proper function since it is multi values for the same φ.

In the case of moderate feedback, interferometer signal can be easily interpreted: at each fringe corresponds a displacement of $\lambda/2$ and its slope accounts for the direction as will be focused in the next paragraphs.

2.3.2. REMARKS ON SELF-MIXING INTERFEROMETRY

Some important remarks should be highlighted about self-mixing configuration:

1) The asymmetry in the shape of the function $F(\varphi)$, when $C > 0.5$, allows a clear discrimination of the target direction of motion. It is a crucial point: this peculiar characteristic of self-mixing in LDs makes non ambiguous interferometric displacement measurement possible using a single interferometric channel;

2) The modulation coefficient m is such that its value in the moderate feedback regime is in the range 0.5–5%, hence adequate for any kind of subsequent signal processing.

3) The self-mixing signal can be obtained from any type of single-longitudinal mode FP LD for which the side-mode suppression is larger than 7–8 dB Numerous laser diodes have been successfully tested(6) with emission wavelengths ranging from the visible (635 nm) to the third communication window (1550 nm).

2.3.3. OPERATIONS ON DIFFUSIVE TARGETS

Operation of conventional displacement measuring interferometers requires a cooperative target and a really accurate alignment procedure. Typically, the target is a corner-cube mounted on the moving object under test but in some experimental situation this should be a limitation and it would be much better to be able to work directly on a diffuser surface as found in the normal workshop environment, with no invasiveness nor the need to keep optical surfaces clean.

Self-mixing configuration, which is intrinsically self-aligned and effective even for small back reflection can be a good candidate for these measurements, although it is affected by speckles patterns. Especially for the case of target displacements larger than a few mm, the speckle distribution may change randomly, thus causing signal fading (Figure 2.11) and a change in the feedback regime. The saw-tooth like fringe shape can be changed into a sine function; as a consequence, the information about the direction, which is held in the slope of the fringe, is missed.

a) b)

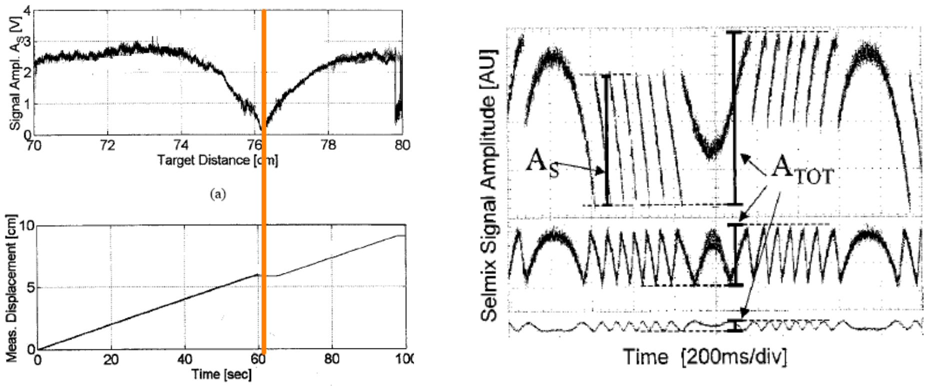

Figure 2.11. Panel a) in the top interferometric signal amplitude, in the bottom the reconstructed displacement. The red line highlights the fading of amplitude due to a dark speckle and the following estimation error in the displacement. Panel b) In the top an interferometric signal in moderate feedback regime and in the bottom an interferometric signal in a weak feedback regime due to dark speckles.

This problem is obviously common also to conventional interferometric techniques, which in turn are faulty and not reliable for these applications.

A more detailed mathematical analysis can help to get a deeper comprehension of the problem. As demonstrated by (5, 12) the interferometer optical power is subjected to speckle regime statistics, and it has the following probability density

$$p(P) = \frac{e^{-\frac{P}{\langle P \rangle}}}{\langle P \rangle}. \qquad 2.11$$

Where:

$\langle P \rangle$ is the average power.

Small amplitude speckles are relative frequent; thus signal can be lost by fading when moving longitudinally the target along speckles.

In a self-mixing interferometer the signal is proportional to the amplitude $|E|$of the field back-injected which can be described as a Rayleigh distribution:

$$p(|E|) = p(\sqrt{P}) = p(P)\frac{dP}{d\sqrt{P}} = 2\sqrt{P}p(P) = \frac{s|E|}{\langle P\rangle}e^{\frac{-|E|^2}{\langle P\rangle}} \qquad 2.12$$

The self-mixing signal amplitude $A_{TOT}$is straightly related to$|E|$, in dependence of C as shown in the equation below.

$$A_{TOT} \propto \begin{cases} |E|, & for\ C \leq 1.4 \\ |E_1| + (|E| - |E_1|) \cdot 0.7, & for\ C > 1.4 \end{cases} \qquad 2.13$$

Where:

$|E_1|$ is the injected electric field that gives C=1.4.

Thanks to this equation the theoretical PDF of the self-mixing amplitude signal A_{TOT} has been calculated for a white paper (2% of surface reflection has been assumed) moving few micrometers at 50 cm distance of from the laser. The theoretical results have also been compared to an experimental experience (13) as shown in the Figure 2.1

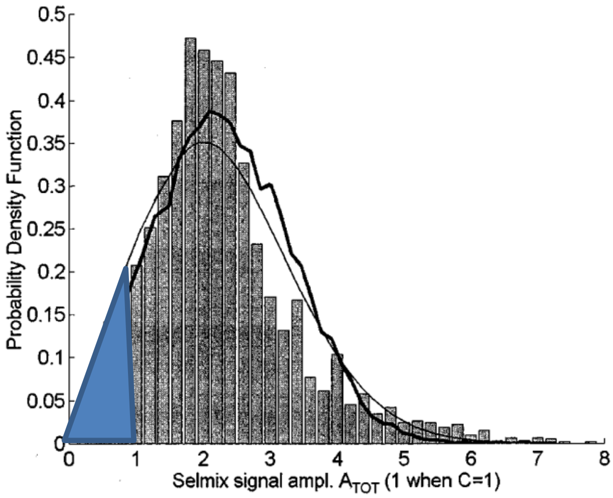

Figure 2.12: PDF of the self-mixing signal amplitude when a spot is focused on a target vibrating 50-cm away from the laser. Bars are experimental data, thin line is the theoretical Rayleigh distribution for ideal diffusive target. Thick line is the result of a numerical simulation assuming 98% diffusion and 2% reflection from the target.

Both experiments and simulation gives a 10% probability (the area of the region highlighted in the Figure 2.12) of C<1, a condition preventing the correct operation of the injection interferometer. As the displacement and the roughness are increased, and the reflectivity is decreased, the probability to obtain C<1 becomes very high.

Norgia et al. (13) suggested an interesting method to reduce speckle effects by means of an optical tracker which moves the laser spot on the target surface, controlled in a closed loop by the amplitude of the inteferometeric signal. The spot movement is obtained by means of a pair of piezo-actuators holding the focusing lens that controls the deflection angle of the laser beam. The piezo-actuators are driven by two square-waves at the same frequency, with a 90. Phase shift, so that the spot position draws a square path on the target, whose extension is set to be much less than the spot size (a few micrometers). This approach shows encouraging results on white paper, but it has not been tested on more tricking surface as skin and moreover, it requires the addition of piezoactuators and a feedback control loop.

2.3.4. DISPLACEMENT RECONSTRUCTION ALGORITHM

A displacement sensor can be set up as reported in Figure 2.13

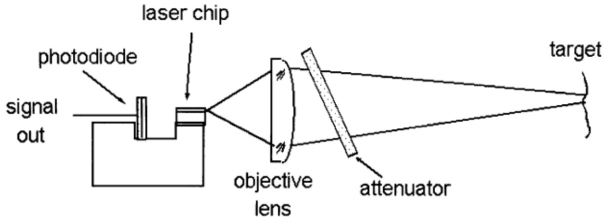

Figure 2.13: laser self-mixing configuration for displacement measurements.

The laser is focused on the target thanks to an objective lens; the beam optical power is controlled by means of an attenuator. The easiest way to build a displacement sensor is to operate the laser diode in the moderate feedback regime (C>1) so that the self-mixing signal is sawtooth-like, i.e. the fringes show a well-defined slope; in this case, the device can retrieve a spatial resolution of$\lambda/2$. An intuitive algorithm used to measure displacement in the case of C>1 is reported in the Figure 2.14

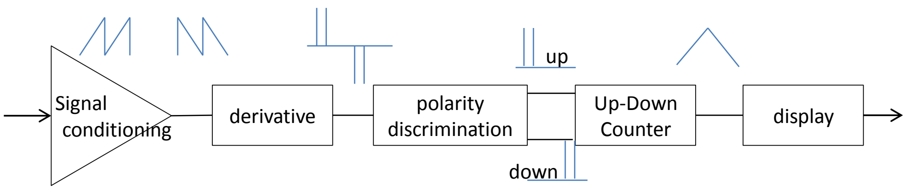

Figure 2.14: flow chart for a displacement reconstruction algorithm when C>1.

The different blocks are:

1) An analogical signal conditioning, realized by means of a trans-Z amplifier, which is used to read the photodiode current;
2) A derivative stage is applied at the saw-tooth like signal. It return a positive peak for a fringe with a positive slope, a negative peak in the opposite case;
3) The polarity discriminator is used to detect the peak polarity;
4) The final displacement is the cumulative sum of the peak scaled by$\lambda/2$.
5) The display block, which is optional, is used to provide the measured displacement on a PC screen or anywhere else.

This scheme has been successfully employed for measuring reflecting target as reported (14, 15).

The maximum target distance is limited by the laser diode coherence length, with a moderate power laser diode with a 780 nm peak; it can reach 7-8 m(16).

Diffusive targets void this approach because of the speckle pattern which produces changes in the feedback regime yielding to a C<1, thus fringes without a well-defined slope and with very variable amplitude. Therefore a new algorithm has been proposed based on Fourier analysis (17, 18). The main concept is that the instantaneous velocity of the target can be related to the instantaneous fringe frequency by the following relationship:

$$v = \frac{\lambda}{2} f \cdot \qquad 2.14$$

The frequency information can be extracted by means of Fourier analysis. In more detailed the first processing of raw measurement data consists of running a window of about 100 points over the acquired signal. Then, the algorithm finds the single tone with the highest amplitude in the windowed signal and returns single-tone frequency f. The "instantaneous" target velocity v (averaged over 100 data points) is obtained from 2.14.

By running the window over the whole set of acquired data, a vector of unsigned velocities is constructed. The velocity vector is the first output of the algorithm. In the case of harmonic or nearly harmonic target movement, the second step consists of computing the parameters of the sine-wave velocity by means of a least squares regression, giving the second output of the algorithm. The phase of this sinusoidal regression is then used to reconstruct the sign of the instantaneous velocity. Last, numerical integration of the signed velocity provides the target displacement (Figure 2.15: Block diagram of the data-handling algorithm for displacement measurement for C<1).

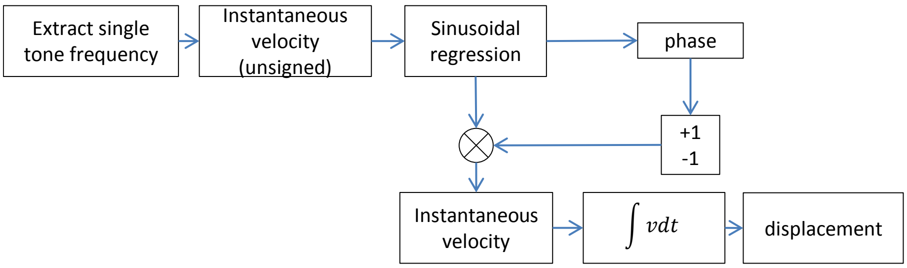

Figure 2.15: Block diagram of the data-handling algorithm for displacement measurement for C<1.

2.4. LASER SELF MIXING INTERFEROMETER FOR MEASUREMENTS ON HUMANS

The assessment of the local mechanical properties of the chest-wall requires the measurement of chest-wall displacement in a reliable and accurate way without interfering with the measured quantity, therefore laser self-mixing interferometer is an ideal candidate to this application, since it is a device which allows to measure relative displacement with a very high spatial and temporal resolution and in a contactless way. The main hurdle to clear is that the already existing reconstruction algorithm are not able to reconstruct large displacement (more than few millimeters) of diffusive target, due to the low injection regime, but in this work of thesis a new algorithm able to overcame these limitations will be described and validate (19).

For the measurement of displacement of the human skin, some custom prototype sensors have been developed by DEI (Dipartimento di Elettronica e Informazione) of Politecnico di Milano. The employed source is a near-infrared laser diode, with wavelength 780 nm and power 15 mW. The laser beam is focussed at about 60 cm of distance, by a collimating plastic lens with 8mm of focal length. The obtained depth of focus is about 20 cm, well adequate for this specific application. The focusing optics creates a beam waist lower than 0.5 mm. In this optical condition, the reflection of the human skin allows reaching a good self-mixing signal, enough for the elaboration described in the next section (Figure 2.16).

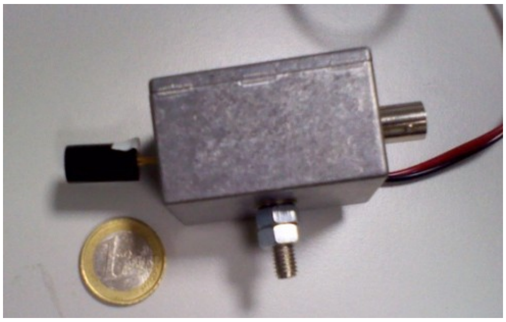

Figure 2.16: Prototype of laser self-mixing interferometer. Comparison with coin evidences its compactness.

For safety reasons, the laser diode power is controlled through the current of the monitor photodiode (PD). The electronic feedback loop keeps constant the emitted power, with a feedback bandwidth limited to 10 Hz. The PD signal component at higher frequency is fed to a trans-impedance amplifier, with 300 kHz bandwidth. The voltage output is the interferometric signal $i(t)$. Particular attention was given to the creation of a well-shielded and compact sensor that can be duplicated for a simultaneous measurement at multiple points.

2.4.1. ALGORITHM FOR LOW INJECTION REGIME

A. ESTIMATION OF THE REQUIRED SAMPLE FREQUENCY

Interferometers allow measuring displacement with very high resolution time and frequency, but they required to use very high frequency sample to catch the fringes dynamic.

To avoid down-sampling and aliasing affects, it is necessary to estimate the required acquisition frequencies.

To estimate the minimum sampling frequency required, we hypothesized to model the movement of the chest-wall during spontaneous breathing as a sinus wave with low frequency (16 acts/minutes) and amplitude of 0.5 cm, whose equation is reported in 2.15

$$s(t) = 0.5 \sin\left(2\pi t \frac{16}{60}\right) [cm] \qquad 2.15$$

The velocity modulus of this point can be estimated by deriving the space (2.16), since we are looking for the worst case, we can maximize the velocities by setting the cosine function to 1.

$$v(t) = \frac{ds(t)}{dt} = 0.5 * 2\pi * \frac{16}{60} \cos(2\pi t \frac{16}{60}) \qquad 2.16$$

It the cosine is 1, the maximum velocity equals 0.0084 m/s, thus, if $\lambda/2$ of the interferometer is 378 nm, the frequency content is 22.800 Hz. Obviously as the sample frequency increases, the discrimination of the fringes improves but this draws a line to the hardware required. After these computations, the chosen sample frequency is 100 kHz.

B. ALGORITHM CONCEPTS

The optical properties of the human skin have been extensively studied in literature (20). The skin behaves as a grey surface diffuser, inducing low back-reflection to the laser diode. In order to analyse the interferometric signal, we propose a new method for estimating the movement direction also in the low-injection regime (C < 1), since traditional algorithms, based on fringe counts and extraction of their slope, are not reliable in this application (14).

In Figure 2.17 is reported an example of the recorded interferometer track during a measurement on skin, in panel a) the amplitude variation of the signal due to the speckles can be appreciated, in panel b) an enlargement of a signal with C>1 where the fringes saw-tooth shape is fairly visible, in panel b) an enlargement of the signal with C<1 where the fringes look like a sinus function; panel a, b, c present all the same scale.

a

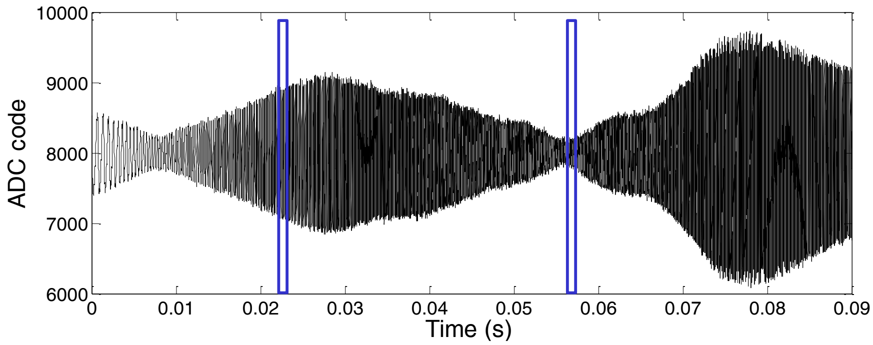

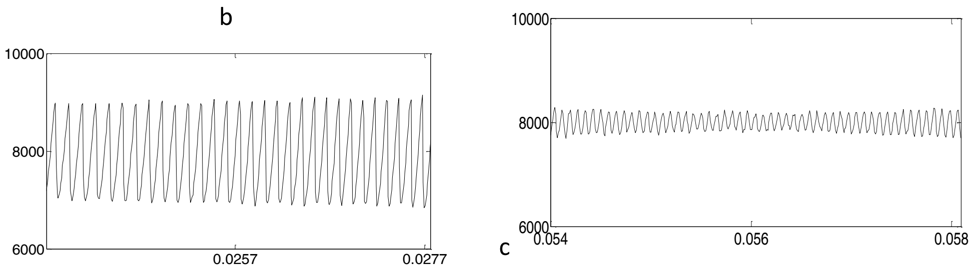

Figure 2.17: Panel a) Interferometer signal expressed in ADC code recorded on skin, b) enlargement of the first evidenced rectangle, c) enlargement of the second evidence rectangle.

The traditional algorithm can't be exploited in every situation in fact as can be seen from Figure 2.18, in the case of moderate feedback injection, the derivative signal presents very well define spikes whose sign is immediately related to the direction of target movements. In fact as can be seen in panel a) the arrow remarks a change in target direction which is fairly visible also in its derivative.

On the other hand, signal in panel c) has been acquired in condition of very low feedback regime in fact the signal has lost its saw tooth like characteristic shape, thus the target direction is unpredictable and its derivative looks like very noisy.

From this example the need for a new algorithm stands out.

The developed algorithm was based on two assumptions (21): 1) the frequency of the fringes is linked to the relative velocity of the target, which must be continuous and 2) each time the target changes its movement direction, the velocity equals zero.

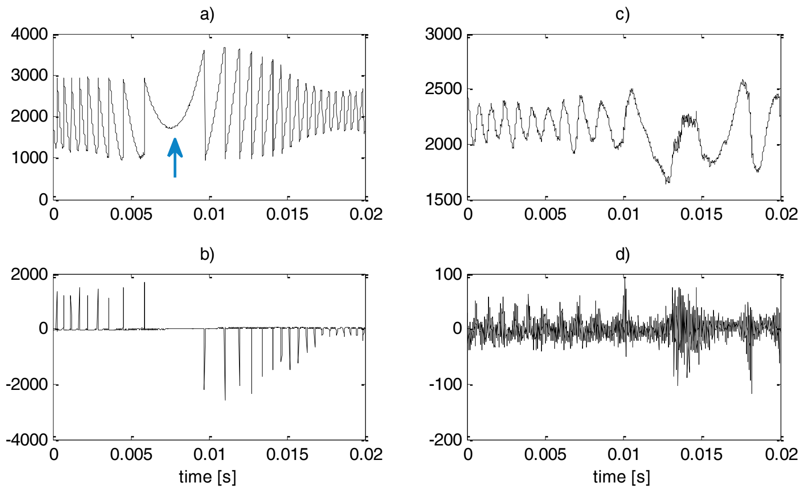

Figure 2.18: Panel a) Part of the interferometric signal in C>1, b) Derivative of signal in panel a), c) Part of the interferometric signal in C<1, d) derivative of the interferometric signal in panel c).

The first assumption relies on an intuitive concept, if the target is moving slowly the interferometric fringes will be far-between, because a fringe appears each time the target moves of λ\2, on the other hand if the target is moving fast, the fringes will be at close range. The intuitive idea of far-between and closed-between can be translated into the mathematical concept of frequency, thus the best and powerful tool to extract the frequency content of a signal is the Fourier Transform.

The algorithm operates on windows of *w* samples from the interferometer signal *i(t)*, which is sampled at very high frequency by an A/D card and processed through two parallel paths as reported in Figure 2.19.

For each window, extraction of single tone is performed by computing the FFT of the interferometric signal *i(t).* The frequency $\bar{f}$ with the highest amplitude is assumed to be the fringe frequency, and the modulus of instantaneous velocity $|v(t)|$ is derived as reported in 2.17

$$|v(t)| = \frac{\lambda}{2}\bar{f} \qquad 2.17$$

Resolution in time versus resolution in frequency is a well-known thread off in signal processing; a possible way to solve it can be use a wavelet approach, which allows obtaining different frequency resolution according to the frequency contents of the signal itself by means of scaled windowing. Anyway we prefer not to implement this heavy computational operation but we prefer to optimize the time-frequency resolution by adjusting the window dimension *w* according to the estimated velocity. Specifically to improve low frequencies resolution, an initial 512 samples long window is processed. If the resulting $\bar{f}$ is zero, then the *w* is doubled until it equals 2048, in this way also low frequency, that means low target velocities, can be discriminated with a higher resolution (Figure 2.20).

Since 100 kHz is much higher than the frequency components of the target displacement, down-sampling has been performed by making the data processing window moving by 50 samples each time. As a result, the sampling frequency of the unsigned velocity is reduced to 2000 Hz, which still largely fulfills the Shannon theorem for the frequency range typically used to probe respiratory system mechanics. When the modulus of the velocity presents some discontinuities a correction realized by imposing continuity between two consecutive velocity points was added (Figure 2.21).

Error in the estimation of velocity may be due to great artifact at very low frequency which can't be removed by de-trending the signal. In more details, when a discontinuity is detected, that is, when the difference between the velocity at time *t* and its previous value at time *t-1* overcomes a threshold, the value of velocity is estimated by looking for the maximum peak in just the part of the spectrum which corresponds to the estimated value of velocity at the previous time.

We choose not to perform the search of the velocities value always near to the previous one, that is not to estimate just part of the spectrum, since this operation is much more computational burdensome than the estimation of all the spectrum because of the impressive efficiency of FFT algorithm.

The sign of the velocity (i.e. the direction of the movement) is determined using a specifically designed sign reconstruction algorithm (lower branch in Figure 2.21) based on the concept that between two zero-velocities points (i.e. within a lobe) the target is moving always in the same direction.

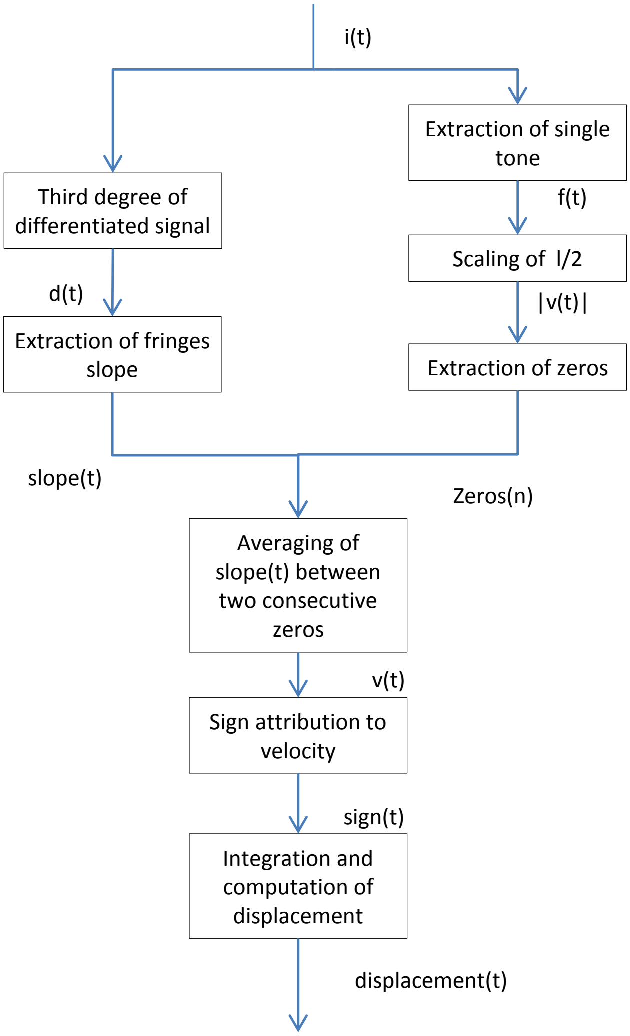

Figure 2.19: Flow chart of the algorithm for the estimation of target relative velocity when C<1. The algorithm develops on two parallel branches: estimation of absolute velocity whit its zeros and extraction of fringes slope.

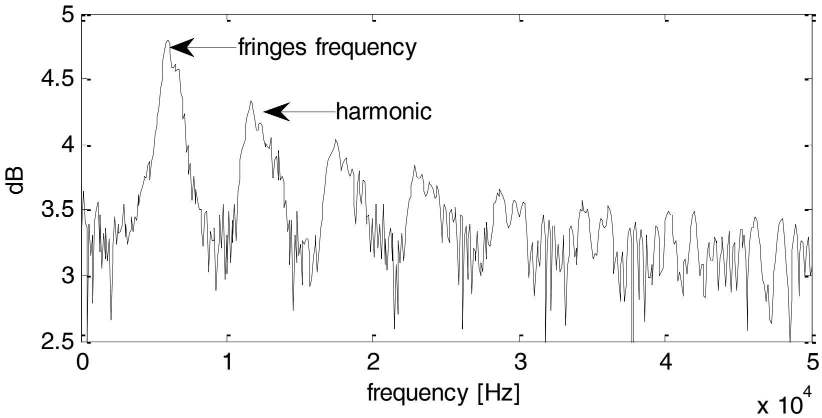

Figure 2.20: FFT of a 512 sample window of the interferometer signal. Arrows highlight the fringes frequency, and the successive harmonics.

Therefore, the fringes of the interferometric signal $i(t)$ corresponding to that part of track will have, on average, the same slope, whose sign correspond to the sign of velocity (21).

To extract fringe slope sign, the third power of the first derivative of the interferometric signal is averaged within the lobe and the sign of the resulting average is attributed to the corresponding velocity lobe (Figure 2.22).

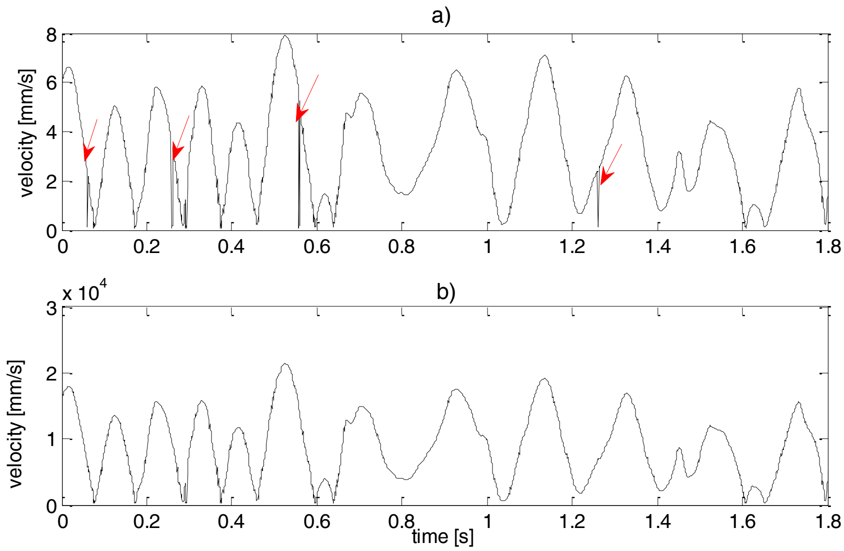

Figure 2.21: Panel a) Unsigned velocity as computed by single tone extraction. Discontinuities are marked by arrows. b) Velocity corrected by the algorithm, artifacts is removed.

In order to enhance the slope and not to be penalizing by the noise, a further improvement has been added.

Since the original signal has been down-sampled, as explain before, we decided to estimate the third power of the first derivative on windows of length equals to the down-sampling factor (50 samples), than on this period, the maxima and minima are searched and the greatest of them, in absolute value, is assigned to the window.

The proposed algorithm has been validated in vivo e in vitro by measuring known displacement or by comparing its results with a well-accepted gold standard.

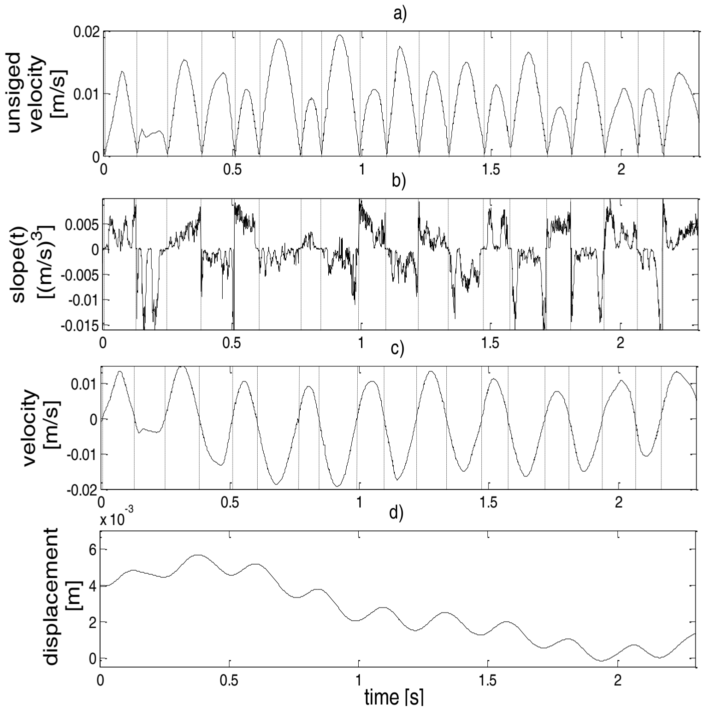

Figure 2.22: Panel a) unsigned velocity reconstructed with single tone algorithm; b) signal used to estimate sign, c) reconstructed signed velocity, d) displacement computed by integrating velocity.

2.4.2. SYSTEM VALIDATION IN VITRO

A. SET UP

To evaluate the performance of the self-mixing interferometer and the new data processing algorithm for very-low optical reflection regime, an in-vitro experimental set-up was developed. A servo-controlled precision linear motor (P01-23X80, 44 N peak force, 280 m/s^2 max acceleration, ±0.1mm position repeatability, Linmot, Spreitenbach, Switzerland) provided with its electronic unit (E100-AT, Linmot, Spreitenbach, Switzerland) was programmed to produce a sinusoidal motion of its shaft characterized by a peak to peak amplitude of 10 mm at 0.1 Hz for 60 seconds while the laser interferometer, aligned to the edge of the shaft and focused on its surface measured its position (Figure 2.23).

The actual piston position was also measured by the internal motor control unit (MCU), sampled at 10 Hz and recorded on a computer simultaneously to the interferometric signal recorded by an AD/DA board (DAQ-CARD 6062E, National Instruments, Austin, TX).

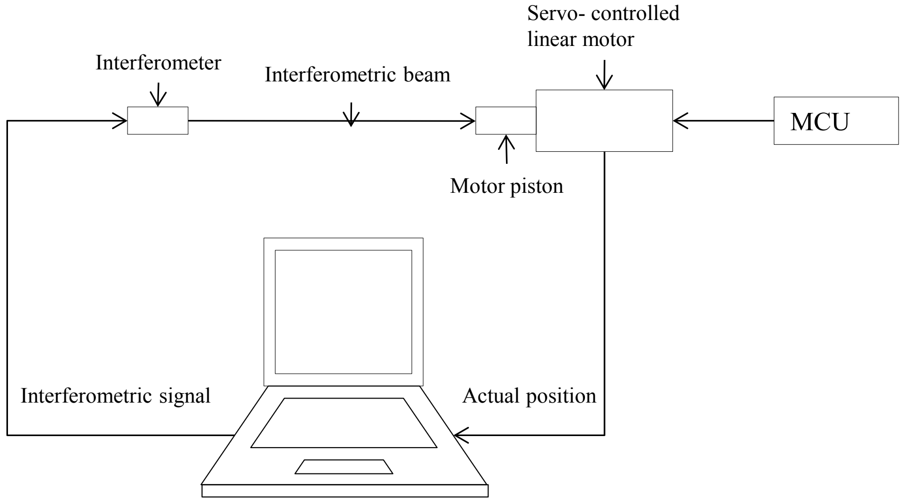

Figure 2.23: In vitro set-up. Interferometer was focused on the motor piston and aligned to it. Actual piston position and inteferometric signal were recorded by the same computer.

Piston velocity, estimated by interferometric signal as described above, was then integrated to obtain displacement. Motor displacement amplitude and the interferometric one were compared, in particular minima and maxima displacement values were detected and used to compute linear regression and to perform the Bland et Altman analysis. We limited the analysis to maxima and minima points because the signal recorded from the electronic unit of the motor driver is internally filtered, leading to a delay between the two traces which increased with the velocity of the motor. As a consequence, if all data points were added, in the Bland Altman plots there were loops opening within zero-velocity points which affect the meaning of the analysis.

B. RESULTS AND DISCUSSION

Piston velocity, estimated by the algorithm described above, is reported in Figure 2.24; steps performed by the linear motor can be appreciated in panel b) as numerous peaks.
Peaks are very short in time and presents a well-defined direction as can be appreciated in panel a) according to the direction of the motor shaft. By integration the resulting displacement has been computed and shown in panel c), it looks like a continuous sinusoidal movement.

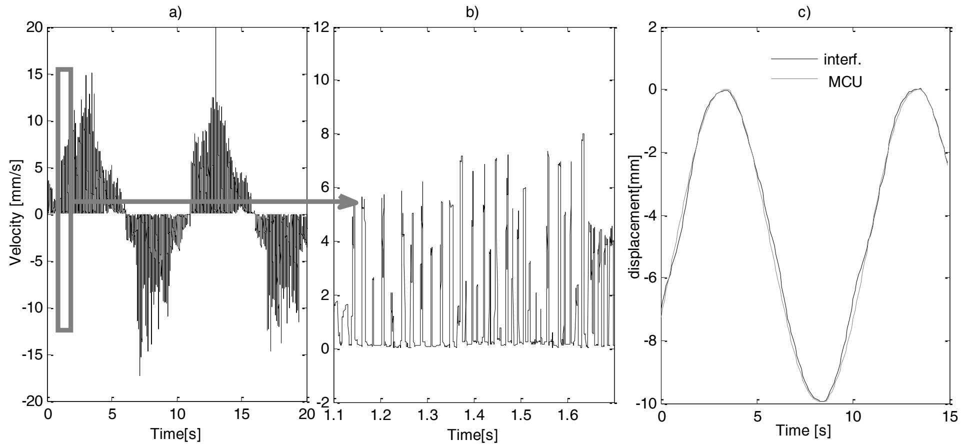

Figure 2.24: Panel a) piston velocity estimated by interferometric signal, b) enlargement to highlight the motor steps, c) displacement measured by MCU and measured by interferometer.

A raw comparison of MCU and interferometric displacement, recorded at the same time, is reported in Figure 2.25, panel c) showing a very good agreement between the two measurement approaches.

The results of the Bland et Altman analisys are reported in Figure 2.25. A good linearity, r^2=0.99, and the absence of any biased errors demonstrates the algorithm skills to reconstruct displacement from interferometric signals.

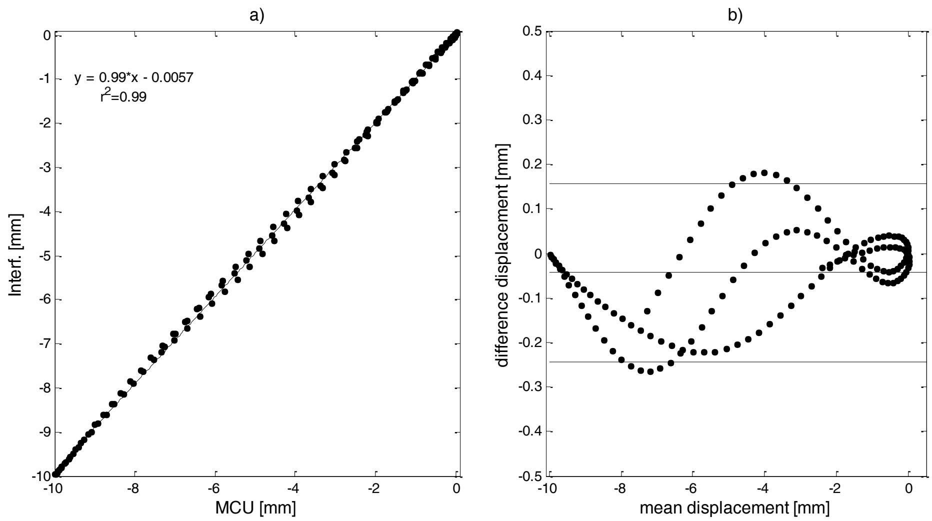

Figure 2.25: Panel a) Displacements measured by interferometer are plotted versus those provided by MCU, b) Bland and Altman plot.

2.4.3. SYSTEM VALIDATION IN VIVO

A. SET UP

Seven healthy male volunteers (age: 29.25±4.85 years, height: 178.2±3.6 cm weight: 74.3±5.4kg) were recruited.

The experimental set up is represented in Figure 2.26, panel a). A sinusoidal pressure signal was generated by an analog-to-digital/digital-to-analog A/D–D/A board (DAQ-CARD 6062E, National Instruments, Austin, TX) and amplified by a power amplifier that drove a 25-cm diameter loudspeaker (model HS250, Ciare, Ancona, Italy). The generated pressure was applied to the subject through a connecting tube and a mouthpiece. The pressure at the airway opening (P_{ao}) was measured by a piezoresistive pressure transducer (model DCXL10DS, Honeywell Sensing and Control, Golden Valley, MN). The respiratory circuit comprised also a high mechanical inertance tube (which was used to provide a low-pass pathway allowing the subjects to breathe room air without major loss of forcing pressure) and a suctioning system providing bias flow of approximately 12 L/min used to reduce the dead-space of the respiratory circuits to the volume of the mouthpiece (22).

Thoraco-abdominal wall velocities (v_{bs}) were detected using self mixing interferometer as described before in more points placed along three imaginary lines: left nipple line, midline and right nipple line (Figure 2.26, panel b)). We decide to sample with more resolution the midline, by acquiring five points instead of only three as in the lateral lines.

The interferometer was fixed on a mechanical frame above the subject at a distance of about 60 cm from the subject lying in supine position and it is moved by hand by an operator who selects the desired points. The laser beam was set as to reach orthogonally the chest-wall surface and its lens has been adjusted to focus on the skin of the subjects.

The subjects were studied in supine position while being oscillated by three different single frequencies pressure sinusoidal waveform at 5, 11 and 19 Hz with peak-to-peak amplitude at the mouth of 2 cmH_2O.

For each frequency, measurements of P_{ao} and v_{bs} were performed while the stimulus was applied at the volunteer during quiet spontaneous breathing for 40 seconds, followed by 5 seconds of breath holding at functional residual capacity (FRC).

To validate the measurements of chest-wall displacement in-vivo, an Optoelectronic Motion Analysis System, OMAS (SMART, BTS, Garbagnate Milanese, IT), was used to monitor the displacements of the laser spot on the skin of the subjects. Briefly, OMAS are systems for motion capture and gait or posture analysis(23). They are able to measures the three-dimensional coordinates of several passive markers applied to body landmarks by using several TV cameras which frame the subject by different angles. The video signal from the cameras is processed in real-time in order to compute the position of the markers in each image. From these data and from a set of parameters computed during a calibration procedure, a dedicated algorithm computes the three-dimensional coordinates of the markers by perspective projection described by the co-linearity equations (stereo-photogrammetric methods). The calibration is performed by surveying a three dimension grid of points and by pivoting a wand of known geometry in the calibration volume.

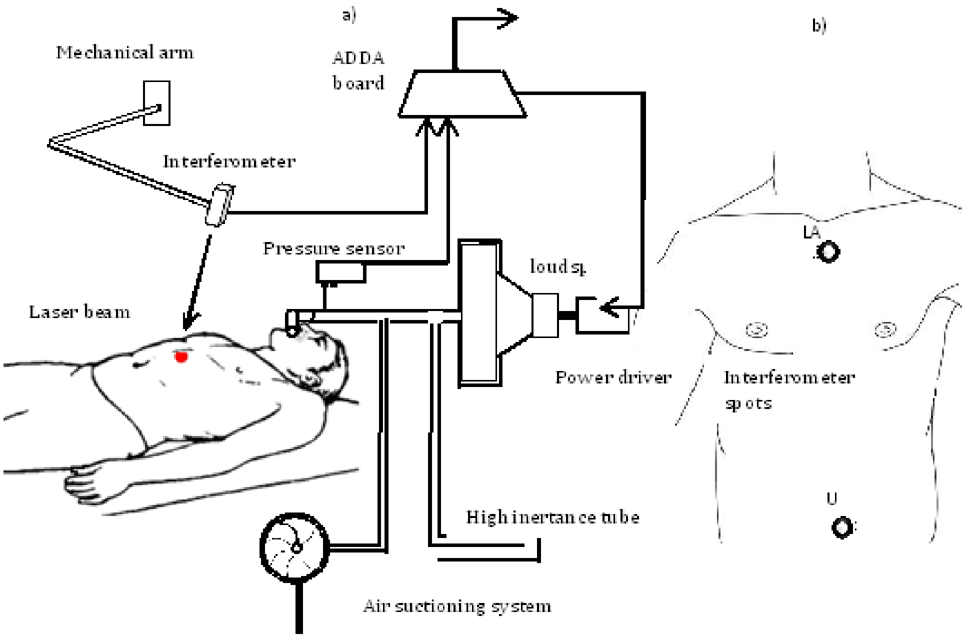

Figure 2.26: Panel a) Set-up for measurement of chest-wall point displacement by means of a self-mixing laser interferometer. A loudspeaker produces a pressure stimulus; a pressure sensor measures the airway opening pressure while a self-mixing laser interferometer is used to measure the thoraco-abdominal displacement, b) Points on which the interferometer has been focused are represented as red spots. Three imaginary lines have been underlined.

In this study, the OMAS was used taking advantage of its ability to recognize the laser spot on the skin as markers, providing its three-dimensional position at a rate of 60 measurements per second.

B. DATA PROCESSING

First of all velocities of each point has been estimated by the interferometric signal as previously described, then the phase delay of the pressure stimulus from airway opening to chest surface during normal breathing was computed as the phase angle of the transfer function (T.F.) between airway opening pressure (P_{ao}) and local velocity (v_{bs}).at the stimulation frequency f_s as reported in 2.18 :

$$\phi_i(f_s) = \measuredangle Z(f_s) = \arctan\frac{p_I v_R - p_R v_I}{p_R v_R + p_I v_I} - \frac{\pi}{2} \quad i = 1,2,..9 \qquad 2.18$$

Where p_I and p_R are the imaginary and real parts of the Fourier transform of P_{ao} respectively, v_I and v_R are the imaginary and real parts of the Fourier transform of v_{bs} and f_s is the stimulus frequency, subscript i represents the point of the chest-wall considered according to the enumeration of Figure 2.26. T.F. was estimated using a Welch approach, with data windowed by a 4096 points Hamming window with 50% of overlap. Values of $\phi(f_s)$ those corresponding coherence was less than 0.97 were excluded from the analysis.

The data from OMAS have been used to compute displacement of the laser spot on the skin.

C. IN VIVO RESULTS AND DISCUSSION

Interferometric velocities of each point were integrated and down-sampled to 60 Hz to allow comparison with OMAS displacement measurements (Figure 2.27, panel a) and b)), simultaneously acquired. OMAS signals resulted significantly noisier when compared to interferometer signals.

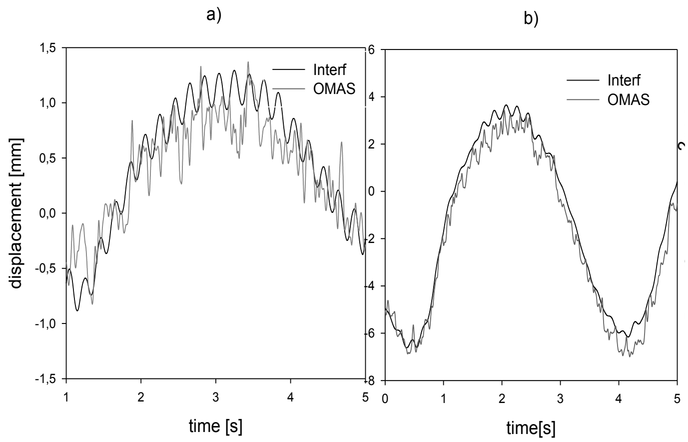

Figure 2.27: Displacement of chest-wall measured with OMAS and interferometer during 5 Hz stimulus of point 4, Lewis angle (panel a) and point 6, umbilicus (panel b).

Comparison between displacement measured by interferometer and OMAS has been also performed as linear regression (Figure 2.28 Panel a)) and by comparing the power spectra of both the signals at 5 Hz (Figure 2.28 Panel b9).

Linear regression (Figure 2.28, Panel a)) confirms the good agreement between the signals with r^2=0.92 which reflects a substantial coincidence between the low frequency components of spontaneous breathing while OMAS has demonstrate a lower spatial resolution which limits the reconstruction of high frequency components. Indeed the low frequency component of spontaneous breathing is clearly visible in both signals reported in Figure 2.29.

Figure 2.28 Panel b), while the high frequency FOT forcing spectral components can be seen only in interferometric signal, with the interferometric spectrum showing a great signal to noise ratio and a narrow peak at 5 Hz.

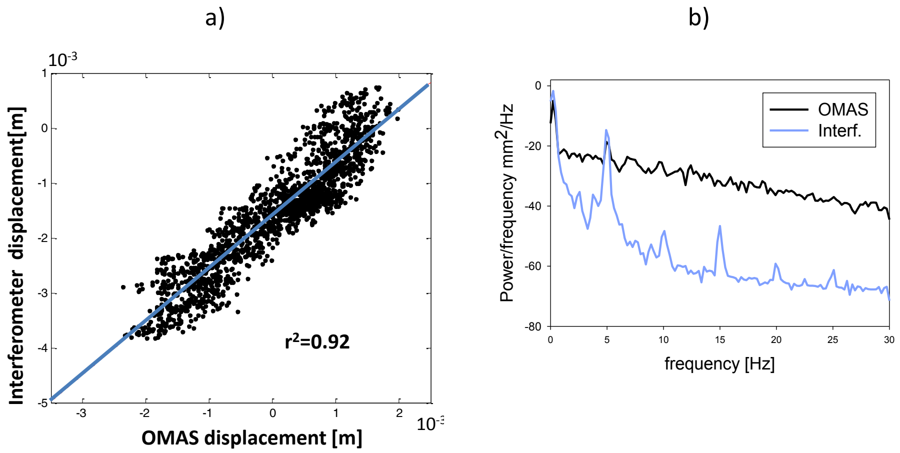

Figure 2.28: Panel a) linear regression between displacement measured by interferometer and OMAS in point 6. Panel b) Power spectra for the displacement measured by interferometer (black) and OMAS (blue).

Finally, the whole v_{bs} signal for Lewis angle points is reported in Figure 2.29. High frequency stimulus is visible in the enlargement. In the lower panels the power spectra of each track are also reported.

Then for each point of the chest-wall the phase delay between P_{ao} and the velocities has been estimated as reported in 2.18. The average phase shifts (ϕ_i) measured during quiet breathing in all subjects are represented in Figure 2.30.

Looking at ϕ_i trend along the nipple lines and midline, we can see that the phase delay increases moving caudally from the head, coherently with an increased distance to cover, and it increased with frequency in each imaginary line.

In particular we can appreciate that right and left nipples lines show high similarity while the mid-line looks different coherently with the presence of different structure inside the chest-wall.

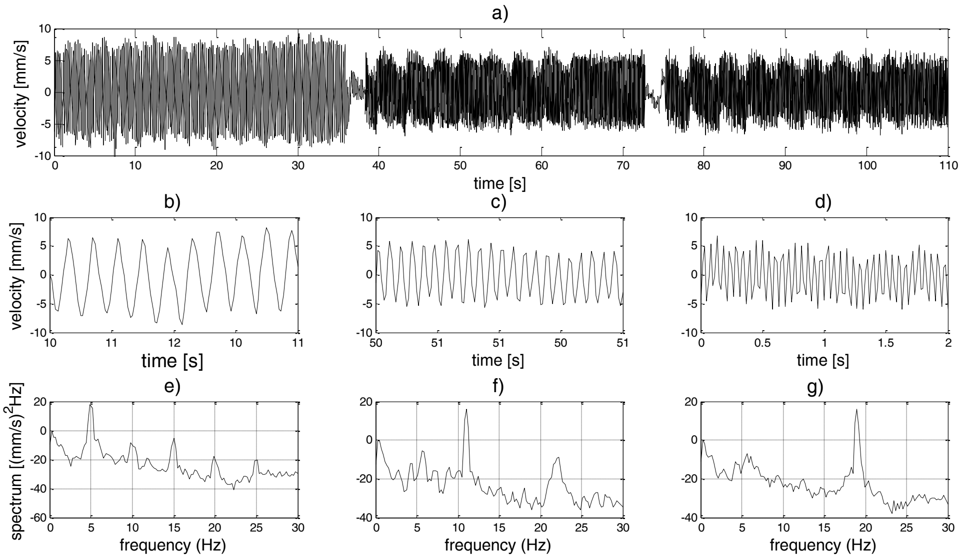

Figure 2.29: Panel a) velocity signal reconstructed by interferometer, b) enlargement on 5 Hz path, c) enlargements on 11 Hz, d) enlargement on 19 Hz, e) spectrum of 5 Hz path stimulation, f) spectrum on 11 Hz path stimulation, g) spectrum of 19 Hz path stimulation.

In particular the different velocities in the chest-wall are emphasized showing an higher velocity in the rib cage than in the abdomen as we may aspect since the rib cage is much stiffer than the abdomen.

Since all the acquisition showed a high coherence (>0.97) all the data were used in computation.

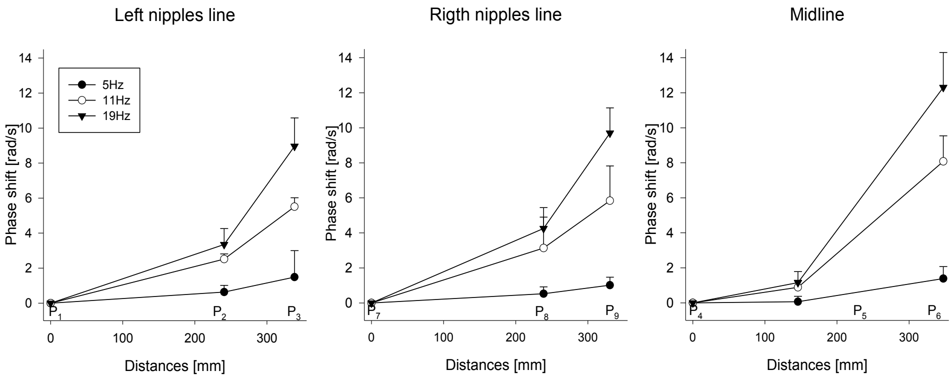

Figure 2.30: each panel shows the phase shift for a different imaginary line measured from the mouth to the points on the chest-wall.

These results are also compared in the same figure with those obtained by using Optoelectronic Plethysmography in a previous study (24) where similar measurements were performed.

Table 2.2: comparison between this study and the previous one

	This study	Dellacà et al. 2002
Forcing frequency [Hz]	5,11,19	4, 8,12
Pressure stimulus amplitude [cmH_2O]	1	2
Subjects	8 male	5 male

Although there were some methodological differences between the two studies and different subjects as underline in the table 2.1, the results estimated for the mid-line show a very good agreement (Fig. 11).

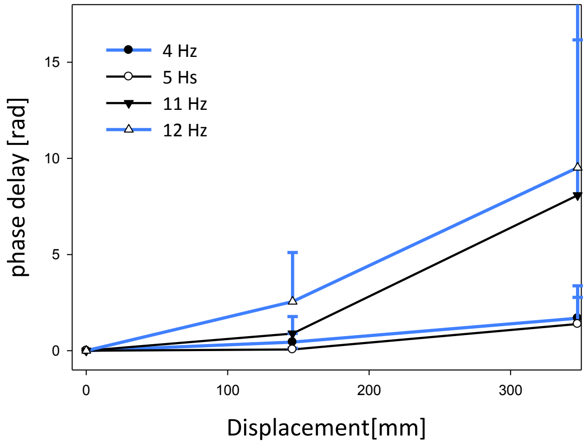

Figure 2.31: Phase shift averaged for all subjects at 5, 11 Hz (black lines). Phase delay measured in a previous study (24) **at 4 and 12 Hz are also reported for comparison (blue lines)**

The midline has been sampled in more sites than the other one, so we can build a more resolved trend for phase shift, which is reported in the Figure 2.32.

In healthy subjects the differences between the two situations, (Figure 2.31,Figure 2.32) look like not meaningful, suggesting that the higher spatial sampling is not necessary.

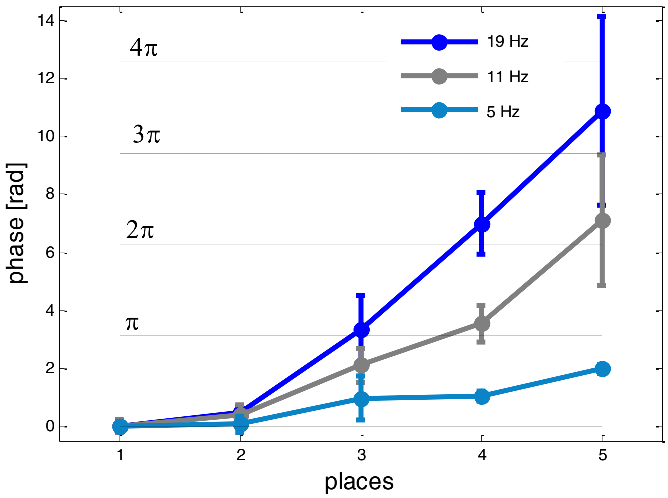

Figure 2.32: Phase shift for the midline at 5 (light blue), 11 (gray), 19 (dark blue) Hz.

2.4.4. CONCLUSION

We demonstrated with our protocol and results the suitability of laser interferometry to measure relative displacements of points of the chest wall. For the direct application of the interferometer on the human body, a specific data-processing algorithm has been realized, in order to analyze very low signals and identify the direction of the movement. The preliminary results showed a good agreement with the previous studies based on Optoelectronic Plethysmograph (24) but offering improved sensitivity and better SNR.

The aim of the present study was to propose and evaluate a novel methodology for an accurate and contactless measurement of chest local displacement.

The data proposed demonstrate that laser interferometry could be used to measure accurately displacements of the chest wall as small as 400nm making this technique suitable for all the applications involving the measurement of wide chest wall movement as well as for the detection of very small displacement as those occurring when a pressure wave reach the chest surface.

This information, together with measurement of mouth pressure, could be used to derive phase delay of an externally applied stimulus between mouth and points over the chest wall under the hypothesis that such quantity would be related to the mechanical properties of the structures the stimulus has traveled through.

Indeed several published data suggest that this parameter might be useful for the evaluation of structural elasticity and inertia on the overall behavior of the respiratory system and for estimating the possible impact of both restrictive and obstructive diseases on respiratory mechanics (25)

At the current stage of development, application of laser interferometry to measure chest wall displacement has still some limitations: motion of the chest surface due to patients' movement or during execution of respiratory maneuvers may change the position of the laser spot over the skin introducing possible artifacts affecting the accuracy of the measurements. Specific measurement protocols aimed at reducing such artifacts need to be designed and evaluated. Thanks to their small size and price, a system composed by multiple interferometers together with algorithms of spatial interpolation can be easily implemented and used to have fast scans of the whole chest wall reducing the impact of motion artifacts.

Being a preliminary study, the evaluation of this technique was performed on a limited number of chest locations and, therefore, the reported results cannot be used to infer any relevant information about the mechanical properties of the underlying structures. Moreover, as in all the gait analysis systems, artifacts related to skin motion still remain and require particular attention when applying this technique in subjects with high BMI. Further studies are needed to suggest and validate interpretative models aimed at improving the current understanding of the relationship between chest movements and properties of the underlying structures. Provided the above limitations, self-mixing interferometers remain an interesting option for the assessment of chest wall vibrations. Indeed, since measurements are performed sending a laser beam to the subject skin and recording the reflected light, no contact with the patient skin is required. As a consequence, the measurements are not affected by the mass of the sensor, area and force of contact. Moreover, the measurement is contactless, preventing any cross-contamination risk between patients without the needs of disposable devices making this technology of potential interest for noninvasive clinical measurement of mechanical properties of the respiratory system.

2.5. PROXIMITY SENSORS

Laser self-mixing interferometers show very high spatial resolution in detecting relative displacement, but they don't allow to measure absolute displacements. Other devices based on different working principles which can overcome these limitations are proximity sensors that allow to measure absolute distances. They can be classified according to the physical principles which rely on. Proximity sensors detect the presence or absence of objects using electromagnetic fields, light, and sound. Various types are available, each suited to specific applications and environments. Some of the most common are as follows: inductive sensors, capacitive sensors, photoelectric sensors, through-beam sensors, retro-reflective sensors, diffuse sensors, and ultrasonic sensors (26). A description of their working principle and the commercial devices which can be found on the market have been reported in literature (27) (28) (29) for each of them.

- Laser proximity sensors: Lasers can be used in various ways to measure distances or displacements without physical contact. In fact they allow for the most sensitive and precise length measurements, for extremely fast recordings (sometimes with a bandwidth of many megahertz), and for the largest measurement ranges, even though these qualities are usually not combined by a single technique. Depending on the specific demands, very different technical approaches can be appropriate. Some of the most important techniques used for laser distance meters are triangulation, time of flight measurements, phase shift methods, frequency modulation (30).
- Infrared (IR) proximity sensors: they work by emitting a beam of IR light, and then computing the distance to any nearby objects from characteristics of the returned signal. There are a number of ways to do this, each with its own advantages and disadvantages: reflected IR strength, modulated IR signal, and triangulation.
- Acoustic proximity sensors: acoustic signals ("pings") are sent out with the time of echo return being a measure of the distance to an obstacle. This does, unfortunately

require a fairly accurate timing circuitry, moreover the velocity of sound depends on the feature of the medium, air which vary with temperature, humidity,

- Capacitive sensor: they sense distance to objects by detecting changes in capacitance around them. When power is applied to the sensor, an electrostatic field is generated and reacts to changes in capacitance cause by the presence of a target. The main disadvantages of this sensor are that its sensitivity relies on the dielectric constant of the target.
- Inductive sensors: another method for sensing distance to objects is through the use of induced magnetic fields. The primary problem with this method is that is largely confined to sensing metallic objects.

2.5.1. LASER SENSORS

As already mentioned, the lasers sensors can be organized into four types (31):

1. Triangulation is a geometric method, useful for distances in the range of ≈ 1 mm to many kilometers. Laser triangulation sensors determine the position of a target by measuring reflected from the target surface Figure 2.33.

Triangulation sensors are either diffuse or specular. The need for two types of sensors arises from differing reflectance characteristics of materials being examined. Smooth surfaces, such as mirrors, are specular; others, such as biological targets, are diffuse. So the selection of sensor type is dictated by the
surface of the object being examined(32).

A 'transmitter' (laser diode) projects a spot of light to the target, and its reflection is focused via an optical lens on a light sensitive device or 'receiver'. If the target changes its position from the reference point the position of the reflected spot of light on the detector changes as well. The signal conditioning electronics of the laser detects the spot position on the receiving element and, following linearization and additional digital or analogue signal conditioning, provides an output signal proportional to target position.

The working principle is explained by means of Figure 2.33. The emitter produces a beam which reaches the target which diffused it according to its optical feature.

Only the diffuse beam of light inside an acceptance range reaches the receiver detector, in particular in the figure the beams which are at a distance *a* from the emitter are accepted. The displacement of the light spot on the detector (*h*) from a reference point is univocally related to the distance *d* at which the target is placed.

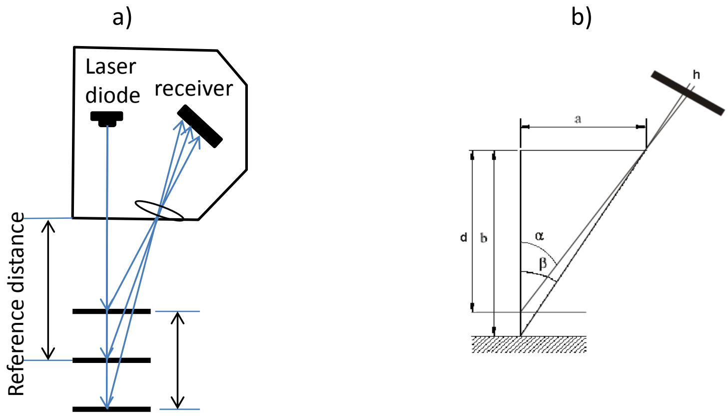

Figure 2.33: Panel a) working principle of a triangulation laser system, b) Geometrical relationship

2. Time-of-flight measurements are based on measuring the time of flight of a laser pulse from the measurement device to some target and back again. Such methods are typically used for large distances such as hundreds of meters or many kilometers Figure 2.34. Using advanced techniques, it is possible to measure the distance between Earth and the Moon with an accuracy of a few centimeters. Typical accuracies of simple devices for short distances are a few millimeters or centimeters.

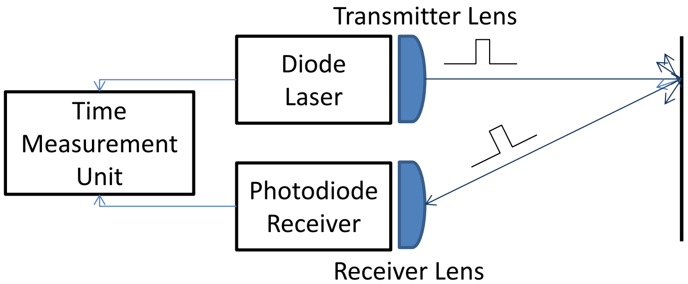

Figure 2.34: Scheme of a time of flight proximity sensors

3. The phase shift method uses an intensity-modulated laser beam. Compared with interferometric techniques, its accuracy is lower, but it allows unambiguous measurements over larger distances and is more suitable for targets with diffuse reflection. Note that the phase shift technique is sometimes also called a time-of-flight technique, as the phase shift is proportional to the time of flight, but the term is more suitable for methods as described above where the time of flight of a light pulse is measured.

4. Frequency modulation methods involve frequency-modulated laser beams, for example with a repetitive linear frequency ramp. The distance to be measured can be translated into a frequency offset, which may be measured via a beat of the send-out and received beam.

2.5.2. INFRARED PROXIMITY SENSORS

A. REFLECTED IR STRENGTH

A simple IR proximity sensor is just an IR LED and an IR photodiode.

An illuminator and compatible detector are provided in a suitable housing, each with its own focusing lens, such that the optic axes of the two converge at a focal point (Figure 2.35). The presence of an object is detected when light is diffusely reflected back towards the detector. A fixed optical geometry defines a sensitive volume from which a return can be received, basically by triangulation. Such a configuration will detect the presence of a surface near the focal point, but if the surface is either closer or further away, no return will be detectable. The distance from sensor to the focal point, the focal distance, can be set by adjusting the convergence angle of the illuminator and detector axes (33).

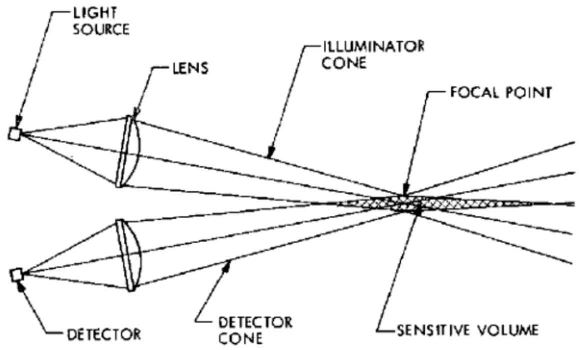

Figure 2.35: The proximity sensor concept

The light returned from the LED source was detected in the presence of normal background illumination both by using an optical filter and by pulsing the light source.

Output profiles are shown in Figure 2.36. The magnitude of the output signal is proportional to the reflectivity of the sensed surface and can be calculated from known geometrical factors.

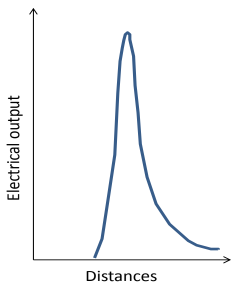

Figure 2.36: Output profile of an IR reflected sensor.

B. TRIANGULATION SENSORS

Triangulation proximity sensors may be used for short distances (from few centimeters to few meters) with high accuracy requirements. These sensors are made by an emitter and a receiver: a pulse of infrared light is emitted by the emitter, this light travels out in the field of view and hits an object and it returns to the detector and creates a triangle between the point of reflection, the emitter, and the detector (Figure 2.37).

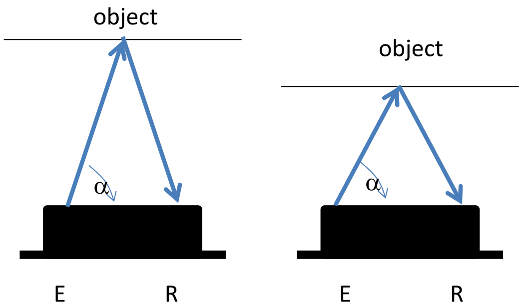

Figure 2.37: Different angles with different distances of the object. E stands for emitter and R stands for receiver.

The angles in this triangle vary based on the distance to the object changing the light that hits the receiver.
This new method of ranging is almost immune to interference from ambient light and offers amazing indifference to the color of object being detected. Detecting a black wall in full sunlight is now possible.
A triangulation sensor can be broken down into three subsystems: transmitter, receiver, and electronic processor.
Transmitter is typically a laser diode or an IR led with beam-shaping optics, projects a beam that illuminates the target object: The optics used to manipulate the light beam creates a small spot at the standoff distance (distance from the sensor housing to the center of the working range), so the size of the spot is dictated by the optical design, and influences the overall system design by setting a target feature size detection limit.
The receiver/detector subsystem gathers the light reflected off the target and images the light onto a detector. The detector then reports the spot position to the processor, which determines the range or height. Of the many types of optical detectors available, two are most commonly used for triangulation sensors: position-sensing detectors (PSDs) and charged- couple devices (CCDs) as reported in Figure 2.38.
PSD are analog devices typically realized by a PIN diode. The light hits the surface and produces a current which is divided on two resistive layers according to the position of the spot. The electronics needed for signal processing of the analog output is quite simple.

A CCD is basically an array of closely spaced MOS diodes. The light is recorded as an electric charge in each diode. Under the application of a proper sequence of clock, voltage pulses the accumulated charges can be transferred to the output of the device.

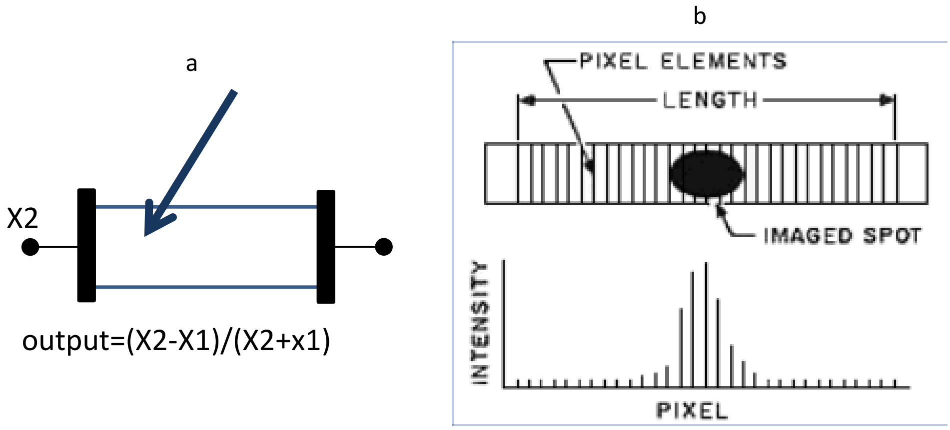

Figure 2.38: Panel a) working principle of a PSD, the output is proportional to the spot position, b)working principle of a CCD, the output is a weighted centroid of the array data

One advantage of PSD-based systems is speed. PSDs are efficient and the processing required to get an answer is simple. Another advantage is that an output will be given regardless of the intensity distribution of the spot. To an extent, this removes the effect of speckle from the system, albeit in a somewhat questionable manner. Speckle is an optical noise effect that limits the ability to determine true spot position. One disadvantage of PSDs is that the centroid of the spot is determined by the detector. If two spots are present the detector will report a single centroid of both spots. Another drawback is that PSD systems are very sensitive to spot intensity. This is inherent in the
Detector and can be accommodated by additional circuitry. The effect of this sensitivity is that if the spot intensity changes while the spot position remains the same, the calculated position of the spot may change (26, 32).

2.5.3. PROXIMITY SENSORS FOR BIOMEDICAL MEASUREMENTS

A. ALGORITHM TO DETECT ANGLES AND TO LOCALIZE MEASURED POINTS ON THE SKIN

Interferometer shows some limitations in the estimation of the mechanical properties, which requires the design of a more complex system of measurement that allows to perform a fast scanning of the chest-wall and to localize the interferometer spot and to estimate the angle of incidence of the interferometer respect to the skin(Figure 2.39).

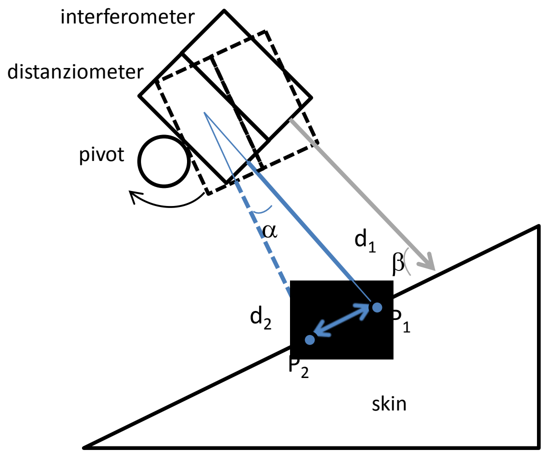

Figure 2.39: Scheme of working of a combined interferometer, distantiometer system to asses geometrical information. The continuous line represents the system at the initial configuration, while the dashed one represents the system in a following configuration.

The system represented in Figure 2.39, it is made of a bar rotated by a stepper motor on which an optical block, constituted by the interferometer and the distanziometer enclosed in the same package, is rigidly anchored.

Albeit interferometer and distantiometer can't be focused on the same point of the skin, if the distance between the two spots on skin is much less than the one between two following measured points, it can be discarded. Thanks to this system one can kwon both the position of the interferometer on the chest-wall, both its inclination as can be explained by the following equations obtained by easy trigonometric relationship.

Let us suppose that the optical block is placed as represented by the continuous lines at the time t_1, in this configuration d_1 represents the distance between the block and the skin and the interferometer acquires the displacement of point P_1. In the time t_2 we are interested in measured a second point P_2 of the chest-wall, thus the optical block is rotated by the stepper motor of a known angle α and the distantiometer outputsd_2.

Under the given hypothesis is easy to estimate d_3 which is the distance between P_1 and $P_2$by means of the Carnot theorem as reported in 2.19.

$$d_3 = \sqrt{{d_1}^2 + {d_2}^2 - 2d_1 d_2 \cos a} \qquad 2.19$$

In the mean time we can also estimate β, the angle of incidence of interferometer, considering the same triangle; it's evident that with the sinus theorem we can calculate the angle between the interferometric beam and the surface:

$$\sin\beta = \frac{D_2}{D_3}\sin\alpha \qquad 2.20$$

$$\beta = \arcsin\left(\frac{D_2}{D_3}\sin\alpha\right) \qquad 2.21$$

In this way the incidence angle and the distances among the measured points depend only on the distances given as output by the distatiometer.

B. REMARKS ABOUT SPATIAL RESOLUTION REQUIRED

Since the distantiometer characteristic is not linear, calibration protocol has been very carefully designed to grant a high accuracy in the estimation of the distances which is a fundamental requirement for the estimation of the angle. Different attempts have been performed to reach the best equation fitting and the right calibration coefficients based on the estimation of the incidence angle in a controlled situation.

To estimate the spatial resolution required for a good estimation of the angle, the following assumptions and computation have been performed.

Suppose the distantiometer is pointing to a surface tilted first to 30°, then 45° and finally 60° and suppose the starting position of the distantiometer is parallel to the ground. The distance between the distantiometer and the surface is chosen to be in the measurement range (40 to 90 cm). At each step of the motor, the distance between the surface and the distantiometer will vary according to the angle of the plane. The spatial resolution required is the minimum difference between two consecutive distances (Figure 2.40).

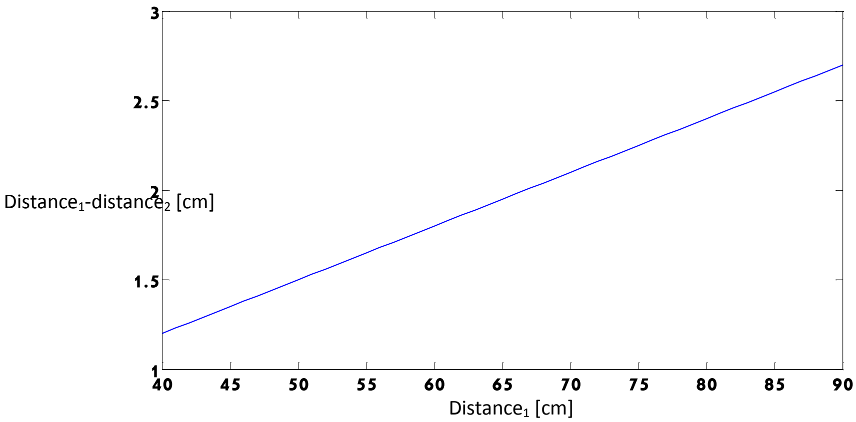

Figure 2.40: simulation of the minimal difference between two consecutive distances. It' a reversely applied the formula for the angle determination to assess the values separating the two consecutive distances measured in the calibration range in order to give the correct angular value.

As shown in Figure 2.40 these differences progressively increase, as the motor covers successive steps from the top to the bottom of the surface so the first distance of each couple is always greater that the other one and obviously changes within the range of interest with a kind of linear pattern, as the angle is constant. In the table below the minimum and maximum value of the distance shifts are reported for the three angles representing suitable samples of the different kind of measurements that we expect to do then on the subjects:

Table 2.3: Maximal and minimal distance shifts within the angle variations.

Angle amplitude (degrees)	Min(d1-d2) (cm)	Max(d1-d2) (cm)
45	1.1996	2.6991
30	2.0462	4.6038
60	0.6934	1.5602

Before dealing with the actual data, we decide to find the best polynomial fitting by simulation using the characteristic curve taken by the datasheet.

The absolute error and percentage are reported according to the polynomial degree used to fit the data.

Table 2.3: Theoretical maximal angular error and percentage accuracy.

Degree	absolute error (cm)	percentage accuracy
3	2.8231	5.98
4	1.1979	2.19
5	0.8286	1.01

It's then evident that the fifth degree polynomial assures a more accurate interpolation of the experimental data, as it's shown in Figure 2.41, assuring an absolute error below 1 cm, which is very important1 A for the proper calculation of the angle with the chest wall surface and a percentage accuracy of the 1%, six times less comparing to the third degree. This last data is also evaluated in out distance range of interest, 30-60 cm, and it get even better using the fifth degree approximation, 0.7%, while increase for the forth and third degree curve respectively reaching the 2.28% and 6.19%.

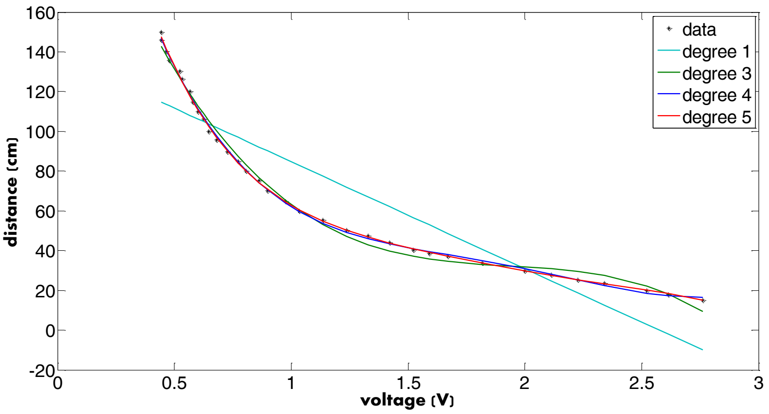

Figure 2.41: Sensitivity curve approximations for several polynomial orders (degree 1 to degree 5).

C. SELECTION OF THE APPROPRIATE DISTANZIOMETER AND REMARKS

The device we are looking for should respect some design requirements, in particular:

1. It shouldn't measure the vibration of the chest-wall due to the FOT, since interferometer does it, but only the low frequency components of the spontaneous breathing that means a low pass system can be accepted.
2. The distance of the system from the patient varies from 50 cm to 80 cm, thus the device should present its maximal sensitivity in that range;
3. The device must be reliant and immune to different light condition and target color.
4. The device should be accurate and reliable on distances measurements.

A device which responds to all the features required is SHARP GP2Y0A02YK0F, a distance measuring sensor unit, composed of an integrated combination of PSD, and an IRED (infrared emitting diode) with λ=850±70 nm and signal processing circuit, as reported in Figure 2.42, indeed its distance measuring range is between 20 to 150 cm, the package size is reduced, so it can side the interferometer, it has a frequency response of 20 Hz and it is not sensitive to environmental light thanks to the modulation circuit.

a) b)

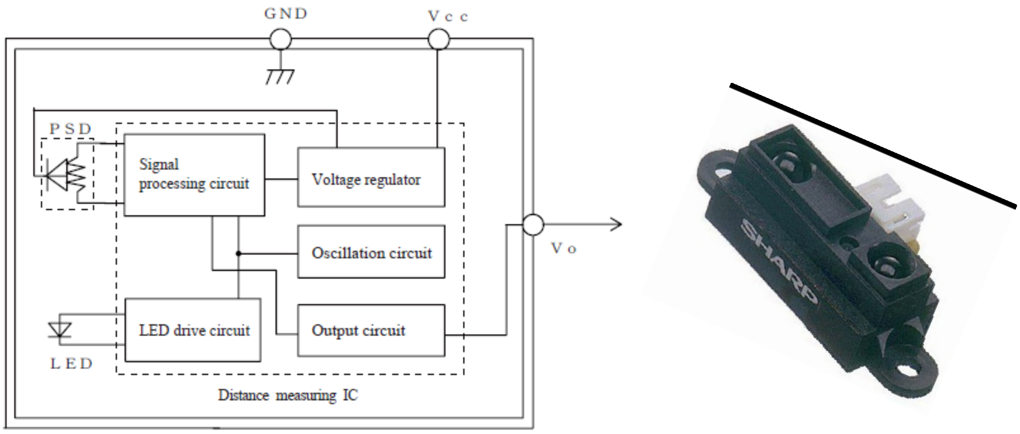

Figure 2.42: Panel a) Block diagram of the distantiometer, b) SHARP GP2Y0A02YK0F sensor.

D. FRONT END BOARD

The distantiometer is acquired by means of a polygraph board described in chapter 3, anyway, it is important to underline by now that the signal should be properly conditioned and digitalized in a way that allow to respect the requirements for the minimal resolution needed.

The schematic of the front end boar is reported, together with the board in Figure 2.43

The schematic results from a compromise between the necessity to make an adequate conditioning and digitalizing of the distantiometer' s signal and the perfect reliability and integration of all the integrated circuits with the optical device. Some initial problems are overcome dealing with the realization of a board which is exactly as the one finally realized, only presented a second order low-pass active filtering which creates some troubles to the distantiometer, so the choice is done in order to the simplify this part while improving the digital conversion with a 16 bit instead of a 12 bit ADC, that will be successively compared.

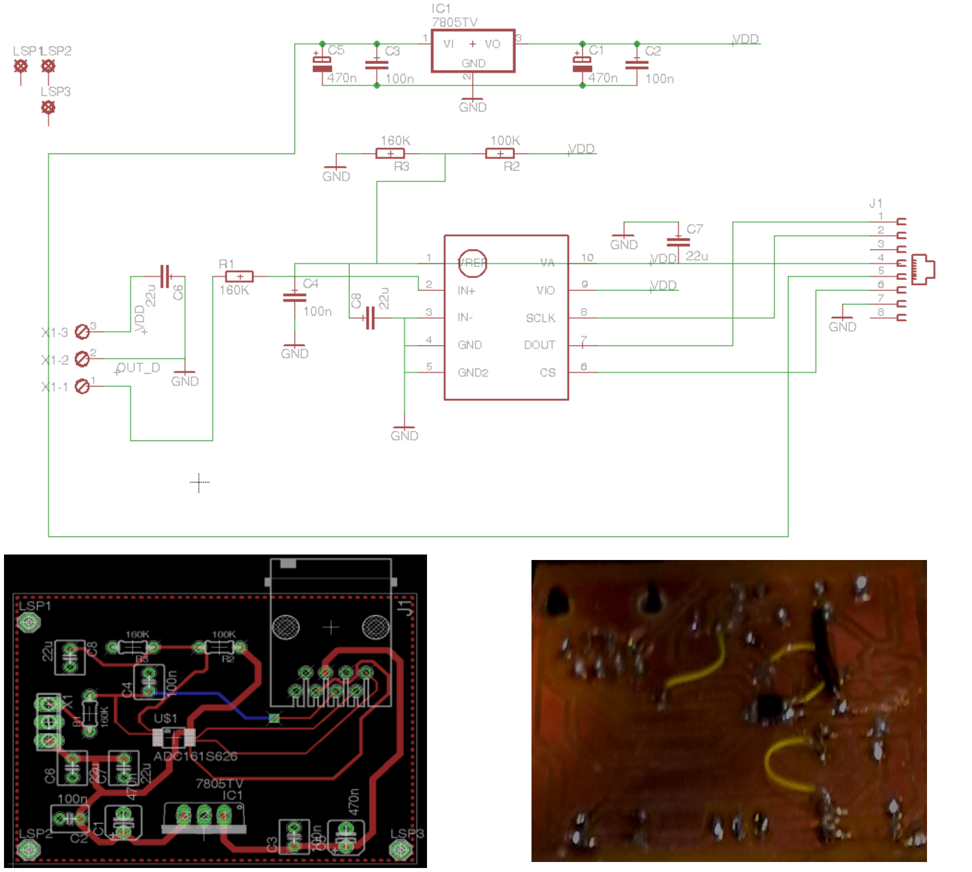

Figure 2.43: Panel a) schematic, b) board, 3) physical board

Just some brief consideration about the ADC, since it is fundamental to obtain reliable measurements.

The ADC161S626 has a differential input (IN+ - IN-) and employs a conventional SAR architecture. In particular it's also important for the purpose of the work that the device supports a serial communication protocol to send the data to the polygraph board as explained later.

The most important features are

- VREF: using a resistance partition, we can diminish the input voltage range of the ADC, increasing this way the resolution, as the LSB size is given by $\frac{VREF}{2^{14.82}}$. In our case VREF

- Differential Nonlinearity (DNL) is specified at +0.8/−0.5 LSB, and Integral Nonlinearity (INL) is offered in ± 0.8 LSB. Botha re almost constant for a wide range of temperatures, sample rate and VREF (from 1 to 5 V);
- Effective Number Of Bits (ENOB): it varies in particular with VREF, in our case it's 14.82, so the LSB size becomes 102.7 µV

The resolution offered by a 12 bit ADC and the one given by this 16 bit ADC is reported in Figure 2.44

The impact of this increment in the resolution is demonstrated below calculating the difference between a determinate value of distance among the ones of the 20-150 cm interval and the same one shifted by the correspondent displacement caused by the maximal resolution. The data obtained from the tension-distance characteristic relation are converted in distance values, following the nonlinear characteristic curve of the distantiometer appropriately approximated, and is recalculated summing the shift of tension corresponding to the maximal resolution. The difference between this two arrays or values is the absolute error, displayed in Figure 2.44 in red color for the 16-bit ADC and blue for the other model.

It's this way evident that the maximal theoretic error that the new device can do is smaller than with a 12 bit, at the lowest sensitivity, so the choice of changing it is justified considering that in the application at the center of the work the distances that we have to measure to reconstruct a FOT map are of about 1-3 cm, so the accuracy and precision of the measurements are necessary requirements.

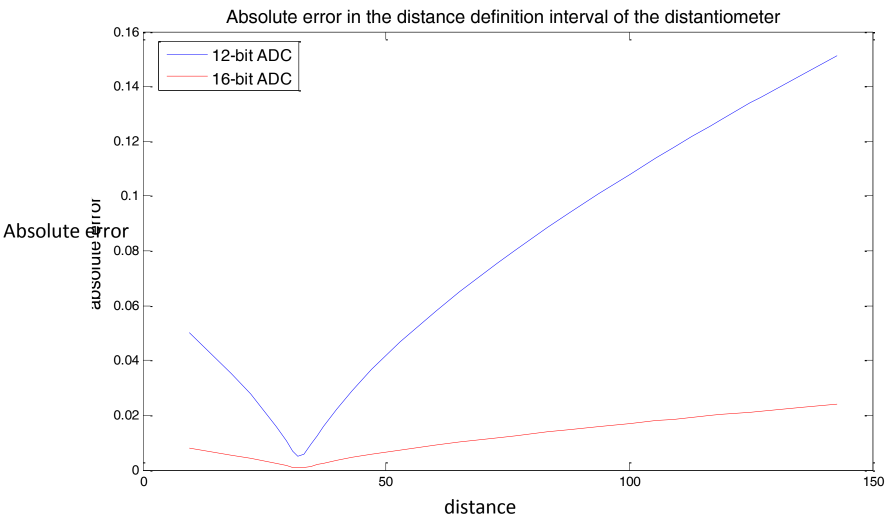

Figure 2.44 Comparison between 12- 16 bit ADC in detecting distances.

E. CALIBRATION PROCEDURE

Calibration procedure and the calibration of the system made by the proximity sensor and its front-end board are very important and critical issue, since the proper estimation of d_3 and β, rely on the accurate measurements of d_1, and d_2, which are complicated by the high non linearity show by the device.

To characterize the system, the following parameters have been evaluated: absolute error, accuracy, precision, resolution, and repeatability.

CALIBRATION PROTOCOL

Distantiometer has been fixed on a frame pointing toward a perpendicular surface, covered with a rough paper to emulate the features of skin that can slide along two rails; it has been moved of a defined displacement, 1 cm/3s, from 40 to 90 cm and from 90 to 40 cm (Figure 2.45).

The selected range represents the interested field of measure. One centimeter has been chosen as step since it represents the minimum distance shift theoretically existing between two consecutive measurements on the chest-wall. The calibration has been performed in both the direction to assure the lack of hysteresis.

Then the extraction of the parameters of a fifth orders polynomial equation has been performed by a LMS algorithm.

To check the repeatability of the procedure, it has been performed ten times, leading to the following results:

1) Maximum error: 4 mm at 46 cm;
2) Worst accuracy: 1.2% at 46 cm.

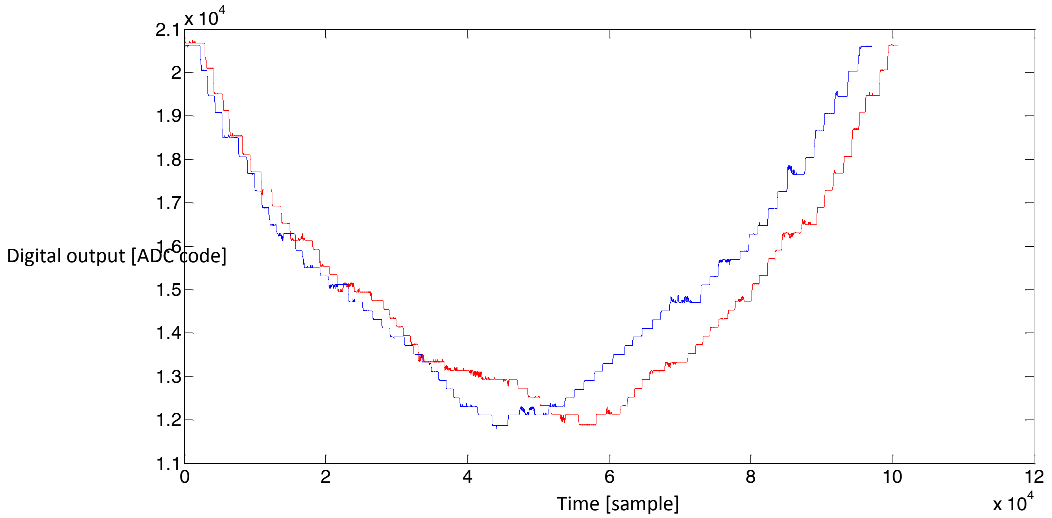

Figure 2.45: Two calibration procedure, the different one centimeters step can be seen.

CALIBRATION VALIDATION

The validation of these results has been carried out by using an optoelectronic system, SMART and repeating the same procedure calibration based on a rigid surface sliding along a rail at known distances, the same distances have been contemporary measured by the distantiometer and the SMART system. Since the distantiometer spot can't be surveyed by the cameras, a more complex approach has been introduces. In more details, the distantiometer plane and the surface plane have been defined by putting three retro-reflective markers on both of them, one marker is placed in correspondence to the sensor emitter. The measured distances has been defines as the distance between the line through the markers on the emitter, belonging to the plane of the distantiometer, and the plane identified by the markers on the test surface.

So it's possible to compare the two different calibrations in the common distance ranges evaluating how much they differs especially in the ADC digital output (Figure 2.45); the length between the distantiometer and the rough calibration surface calculated by the SMART is considered as the gold standard and it has been used to finally establish whether of the curves can be eligible. The biggest difference between the two curves is a shift, which can be actually considered constant for all the distances, so the experimental sensitivity curve determined in the laboratory can be corrected by the correspondent digital value to get the corrected polynomial approximation. The maximal spread between the two experimental graphs obtained with the SMART validation is a distance shift of 0.5 cm that is equal to the minimal difference at which the distantiometer can be sensitive in the desired range, as we can see from the accuracy and absolute error data already showed.

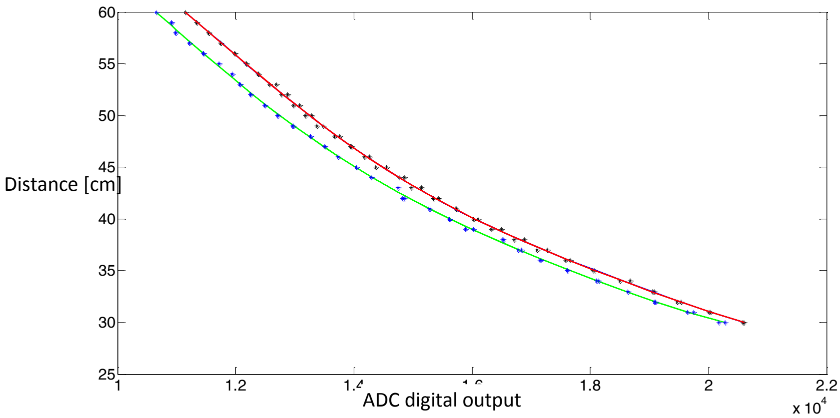

Figure 2.46: Comparison between the different considered calibrations. The calibration performed in laboratory has been reported in red, while the calibration obtained with SMART system is reported in green.

Consequently from these experimental assumptions the calibration procedure constitutes a valid alternative to the ones determined with the OEP measurements of the distances.

F. VALIDATION OF THE ALGORITHM FOR ANGLE ESTIMATION

Finally the evaluation of the distantiometer ability to detect surface angle has been evaluated by in vitro-measurements of a surface at angles of 30°,45° and 60° which span completely different tilting conditions that have an immediate impact on the reflection efficacy.

PROTOCOL

Distanziometer has been fixed on a bar rotated by a stepper motor with an angular resolution of 1.8°C and it has been pointed on a tilted surface. At the beginning of the experimental activity, the plane on which lies the sensor is parallel to the "ground", then the sensor has been rotated of one step each time. To improve the statics the tilted surface has been completely scanned in both the direction for four times.

A sketch of the set-up is reported in Figure 2.47 where are evidenced the angular values measured at different step.

The experimental evaluation has been performed in the same way for three different slopes of the surface: 30°, 45° and 60°.

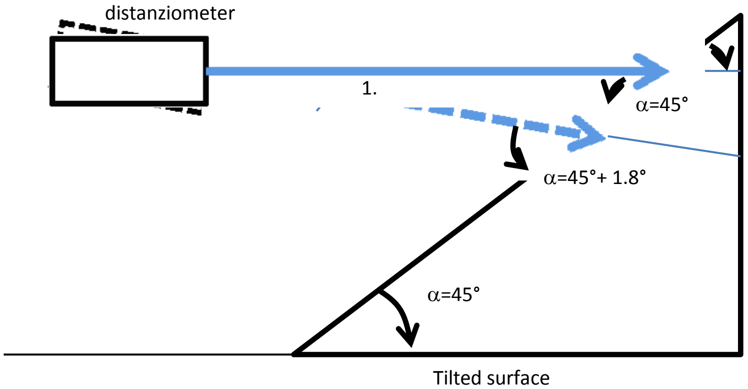

Figure 2.47: Scheme of the set-up used to validate algorithm for the angle estimation. In the picture is shown a surface at angle of 45°

RESULTS

The angle has been estimated by equation 2.21 from the measured consecutive distances d_1 and d_2 for the entire repeated test. In Figure 2.48 the output of the distantiometer for four steps towards and backwards has been reported. It is possible to notice that the four steps show a high repeatability

An easy and immediate way to show if the distantiometer allows estimating the actual surface angle consists in plotting the different measured distances and motor angle on a polar chart, if the distances have been properly acquired, the points would lie on the same line.

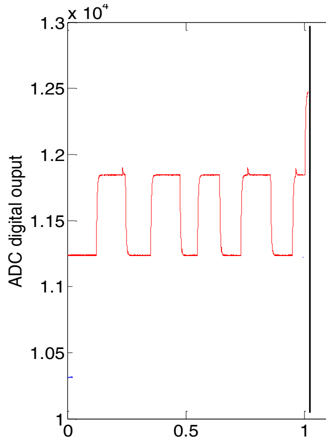

Figure 2.48: ADC output of the distantiometer for four consecutive angular steps forward and backward

This test has been performed and reported in Figure 2.49 for the three angular values of the tilted surface.

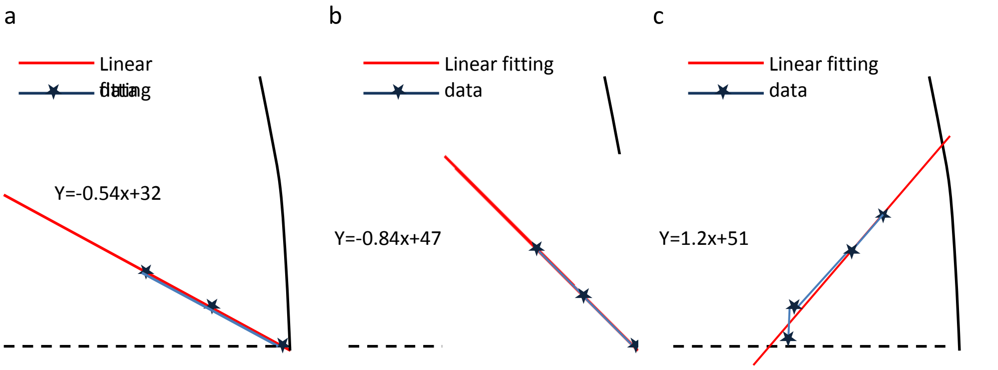

Figure 2.49: Panel a) polar diagram calculated for a plane at an angle of 30°, b) polar diagram for a plane at an angle of 45°, c) polar diagram for a plane at an angle of 60°.

The numerical results are resumed in table 2.4

Table 2.4: estimated angles and errors

Angle	**mean±std**	**Maximum absolute error**	**Maximum percentage error**
30°	30.09±1.39	0.99	4.58
45°	42.54±1.61	2.68	6.44
60°	45.6±1.12	15.42	25.53

Therefore, it is possible to deduce that the distantiometer can well reproduce the considered angle at 30°, and the successive ones following the formula (β-nα), where n is the number of steps performed by the motor, α is the first angle measured and β the second. Good results are obtain also for 45° while for the plane tilted of 60° the obtained error is definitely not acceptable. A possible explanation of this great difference, also considering the not perfect horizontal IR beam that can introduce an error of about 1-3 degrees in the angle calculation, May relies in the very high tilted angle which dramatically affects the reflection of the beam causing a misalignment between the emitter and the detector. The respective beams indeed may not form a planar surface, as the law of reflection establishes, and this may cause a deviation from the correct light spot's shape on the PSD sensor, which becomes a modification of the real distance data as suggested in (34) Definitely, having the distance information, which corresponds to the distance between the distantiometer, which is nearby the same of the interferometer as their beams can be considered parallel, and the tilted surface, and the determined angle formed with it, we have found the vector which gives us the position of the laser devices at every step of the motor. Normalizing this vector we can obtain the surface normal vector and knowing its orientation in the space that will allow, integrating with the interferometer displacement data, to determinate the displacement velocity in the effective direction.

2.6. REFERENCES

1. Optical interferometer [Internet].: Encyclopædia Britannica; 2011. Available from: http://www.britannica.com/EBchecked/topic/430436/optical-interferometer.

2. Michelson A, Sci AJ. 22, 120 (1881). AA michelson and EW morley. Am J Sci. 1887;34:333.

3. Donati S. Electro-optical instrumentation: Sensing and measuring with lasers. Prentice Hall PTR; 2004.

4. Dainty JC. In: Laser speckle and related phenomena. Berlin and new york, springer-verlag (topics in applied physics. volume 9), 1975. 298 p; ; 1975.

5. Goodman J. Statistical properties of laser speckle patterns. Laser speckle and related phenomena. 1975:9-75.

6. Giuliani G, Norgia M, Donati S, Bosch T. Laser diode self-mixing technique for sensing applications. Journal of Optics A: Pure and Applied Optics. 2002;4:S283.

7. Donati S. Photodetectors,devices, circuits and applications. In: Englewood Cliffs: Prentice Hall; 2000.

8. Donati S, Giuliani G, Merlo S. Laser diode feedback interferometer for measurement of displacements without ambiguity. Quantum Electronics, IEEE Journal of. 1995;31(1):113-9.

9. Acket G, Lenstra D, Den Boef A, Verbeek B. The influence of feedback intensity on longitudinal mode properties and optical noise in index-guided semiconductor lasers. Quantum Electronics, IEEE Journal of. 1984;20(10):1163-9.

10. Lang R, Kobayashi K. External optical feedback effects on semiconductor injection laser properties. Quantum Electronics, IEEE Journal of. 1980;16(3):347-55.

11. Wang W, Grattan KTV, Palmer A, Boyle W. Self-mixing interference inside a single-mode diode laser for optical sensing applications. Lightwave Technology, Journal of. 1994;12(9):1577-87.

12. Donati S, Martini G. Speckle-pattern intensity and phase: Second-order conditional statistics. JOSA. 1979;69(12):1690-4.

13. Norgia M, Donati S, D'Alessandro D. Interferometric measurements of displacement on a diffusing target by a speckle tracking technique. Quantum Electronics, IEEE Journal of. 2001;37(6):800-6.

14. Donati S, Falzoni L, Merlo S. A PC-interfaced, compact laser-diode feedback interferometer for displacement measurements. Instrumentation and Measurement, IEEE Transactions on. 1996;45(6):942-7.

15. Norgia M, Donati S. A displacement-measuring instrument utilizing self-mixing interferometry. Instrumentation and Measurement, IEEE Transactions on. 2003;52(6):1765-70.

16. Giuliani G, Norgia M. Laser diode linewidth measurement by means of self-mixing interferometry. Photonics Technology Letters, IEEE. 2000;12(8):1028-30.

17. Wang M. Fourier transform method for self-mixing interference signal analysis. Optics & Laser Technology. 2001;33(6):409-16.

18. Norgia M, Pesatori A, Svelto C. Novel interferometric method for the measurement of laser wavelength/frequency-modulation sensitivity. Instrumentation and Measurement, IEEE Transactions on. 2007;56(4):1373-6.

19. Milesi I, Norgia M, Pompilio PP, Svelto C, Dellacà RL. Measurement of local chest wall displacement by a custom self-mixing laser interferometer. Instrumentation and Measurement, IEEE Transactions on. 2011(99):1-8.

20. V T.
. In:
Tissue Optics: Light Scattering Methods and Instruments for Medical Diagnosis. 2nd Edition ed. SPIE Press Book; 2007.

21. Milesi I, Dellaca R, Norgia M, Svelto C. In: Optical interferometer for measuring forced oscillation on human respiratory system. Instrumentation and measurement technology conference (I2MTC), 2010 IEEE; IEEE; 2010. p. 291-5.

22. Dellaca R, Santus P, Aliverti A, Stevenson N, Centanni S, Macklem P, et al. Detection of expiratory flow limitation in COPD using the forced oscillation technique. European Respiratory Journal. 2004;23(2):232-40.

23. Ferrigno G, Pedotti A. ELITE: A digital dedicated hardware system for movement analysis via real-time TV signal processing. Biomedical Engineering, IEEE Transactions on. 1985(11):943-50.

24. Dellaca R, Aliverti A, Lutchen K, Pedotti A. Spatial distribution of human respiratory system transfer impedance. Ann Biomed Eng. 2003;31(2):121-31.

25. Barnas GM, Mills PJ, Mackenzie CF, Skacel M, Smalley AJ, Watson R, et al. Regional chest wall impedance during nonrespiratory maneuvers. J Appl Physiol. 1991;70(1):92-6.

26. Kinney TA. Proximity sensors: Types and tips. Motion System Design. 2001;43(9):39-44.

27. Volpe R, Ivlev R. In: A survey and experimental evaluation of proximity sensors for space robotics. Robotics and automation, 1994. proceedings., 1994 IEEE international conference on; IEEE; 1994. p. 3466,3473 vol. 4.

28. Schmitz T. Choosing a proximity sensor. Electronic products. 2010;52(11).

29. Loughlin C. Proximity sensors: Close to you. Sens Rev. 1988;8(4):198-202.

30. Distance measurements with lasers [Internet].; 2011. Available from: http://www.rp-photonics.com/distance_measurements_with_lasers.html.

31. Amann MC, Bosch T, Lescure M, Myllylä R, Rioux M. Laser ranging: A critical review of usual techniques for distance measurement. Optical Engineering. 2001;40:10.

32. Kennedy WP. The basics of triangulation sensors. Sensors-the Journal of Applied Sensing Technology. 1998;15(5):76-83.

33. Johnston A. Proximity sensor technology for manipulator end effectors. Mechanism and Machine Theory. 1977;12(1):95-109.

34. Määttä K, Kostamovaara J. In: The effect of measurement spot size on the accuracy of laser radar devices in industrial metrology. Proceedings of SPIE; Citeseer; 1821.

3. VALIDATION OF A NEW SCANNING SYSTEM BASED ON LASER INTERFEROMETRY

The respiratory system status and its behavior is deeply influenced by the mechanical properties of the chest-wall and, on the other hand, pathologies and alterations of the system are reflected in alteration of the mechanical properties as has been stated by Barnas, VanNoord, Lutchen in the already reported studied. Although these important assumptions, the study of the chest-wall mechanics has been deeply influenced and limited by technological aspect that addressed the study towards three main approaches, which are:

1) Behavior of the whole chest-wall by means of plethysmographic chamber and forced oscillations;

2) Behavior of two compartment: abdomen and rib cage by means of inductance plethysmography or magnetometers or balsa wood rib associated with forced oscillations;

3) Behavior of more than two compartments by means of OEP and FOT.

Clearly, the first method required bulky instrumentation, moreover since the compartments are in parallel, the final results is masked by the impedance of the smaller one, indeed the authors found that is not necessary to introduce more than one compartment model for the chest-wall.

The second approach allows to estimate the properties of different compartment, showing a great heterogeneity between abdomen and rib cage, but the used devices interfere with the measurements itself since they are in contact with the skin of the patient and they are not suitable to extend the measurements to more compartments.

The last approach, based on OEP, is the most reliable and theoretically allows studying the behavior of the entire region close to a marker, but, although all these evident advantages, it is methodologically complex and expensive. Moreover the spatial resolution of OEP could represent a limitation for high frequency stimuli which produced small vibrations in the stiffer region such as the rib cage, which can be hardly detected by OEP.

In the previous chapter an alternative approach has been introduced and validated. It is based on optical devices such as laser self-mixing interferometers and IR proximity sensors, two technologies which allow estimating displacements and distances with a different time and spatial resolution. As fully reported in the previous chapter, they provided encouraging results in the first in vivo e in vitro measurements, but they need to be integrated into a system which should respond to the following requirements:

1) Ability to measure low amplitude displacement of the chest–wall;
2) Ability to localize the selected points of the chest-wall;
3) To be non-invasive;
4) To be methodologically easy;
5) To acquire the whole chest-wall mechanics in a few time;
6) To be contactless.

Laser self-mixing interferometers and distantiometers have probed their capability in measuring chest-wall displacement as shown in the previous chapter, but, although the very encouraging results obtained in measuring displacement and in detecting the phase shift between pressure at the mouth and the chest-wall displacement, they still present some limitations which requires to developed a more compact and integrated system to make a scanning of the chest-wall. In particular the improvements are required in granting the acquisition of more points in reasonable time and in an automated way without requiring moving by-hand the interferometers.

3.1. SYSTEM FOR MEASUREMENT OF LOCAL MECHANICAL PROPERTIES OF THE CHEST WALL

In order to solve this problem, a new system has been developed. We can take two different design approaches to realize a system that allow measuring more points in a reduced amount of time.

The first consists in use just one interferometer, whose laser beam can be deflected on the chest-wall by means of two mirrors driven by step motors which can move the interferometer spot along two orthogonal directions (Figure 3.1).

Since the lowest frequency we are interested in is 5 Hz, keeping the laser on the same point for 2 seconds allows capturing ten whole periods of the sinusoid, that can be consider enough in order to have a good spectral estimation.

In this case if we are interested in scanning 20 points, any acquisition will last at least 40 seconds.

Actually more than 2 seconds per point are required, both to insure a good quality of the signal, but also to acquire at least one complete breath and not different phases of breathing, in order to make acquisition on different points comparable. Thus, more realistic 5 seconds for point are required, that brings the total acquisition time to 100 seconds.

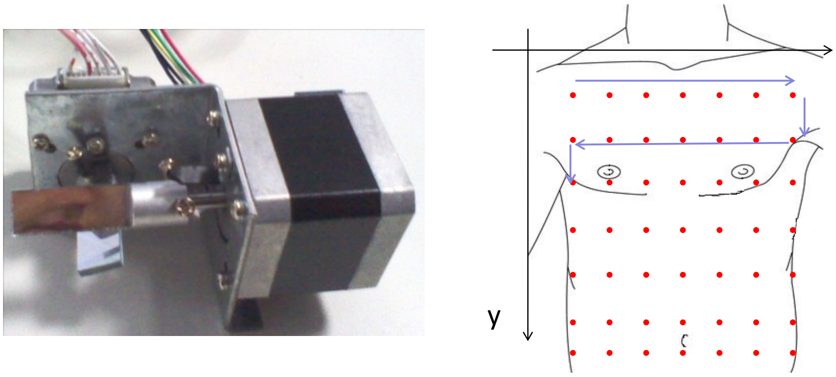

Figure 3.1: Mirrors system with stepper motors, scanning path.

The obvious advantage of this approach is that it allows using only one interferometer for scanning the whole chest-wall, and then other signals such as pressure and flow may be acquired with the same commercial board.

This system has been design and tested, but although the very promising design, it presents some big limitations that lead us to discard this approach, in particular:

1) The interferometer signal quality, that is stated by the C parameter, is not good for all the acquired points, in particular since as the incidence angle between laser beam and the skin is reduced also the quantity of retro injected signal decreases, the signal for peripheral point is too fade, and it doesn't allow to reconstruct velocities.

2) Reconstruction of the selected point and the estimation of the incidence angle are not allowed. It is very difficult to integrate a second device to estimate absolute distances since the presence of mirrors.

For these reasons we need to select a new approach which is based on the use of five interferometers fixed on the same bar and focusing on five aligned points. By rotating this bar it is possible to acquire a more complete row along the cranium-caudal direction.

This configuration allows overcoming limitations encountered with the previous system and the use of five interferometers contemporary allows reducing the total acquisition time, albeit it presents some disadvantages:

1) The need for replicating five times the same block;

2) Five times more data to get;

3) Impossibility to use just a commercial board since the very high required sample frequency, (100 kHz for five interferometers).

The new system proposed is schematically represented in Figure 3.2. The main innovative aspects rely on the introduction of optical technologies, such as laser self-mixing interferometers and IR proximity sensors that have never been used to this field of application. Moreover, the association with forced oscillations allows estimating the mechanical properties in a not invasive way.

The realized system has been carefully design to fulfill the design requirements in particular it has been organized in three conceptual blocks, each one with a well-defined function:

1. The FOT unit provides the pressure stimulus and the measurement of the pressure and flow at the open airways. It can be organized according to the different condition in which the measurement should be performed, i.e. during mechanical ventilation or spontaneous breathing. The FOT approach satisfies the requirement of a non-invasiveness and non-cooperation required to the patients;
2. The optical scanning unit provides the measurement of velocity and absolute distance of several points (up to five) of the chest-wall by means of interferometers and distantiometers which can be moved to scan the whole chest-wall. Interferometer spatial resolution allows the estimation of the small vibration produced by the pressure stimulus and grants for non-invasive and contactless features
3. The electronic unit allows: to record all the data, to drive the pressure stimulus generator and finally to move the optical scanning unit.

For safety reason all the system is powered by a 12 V battery.

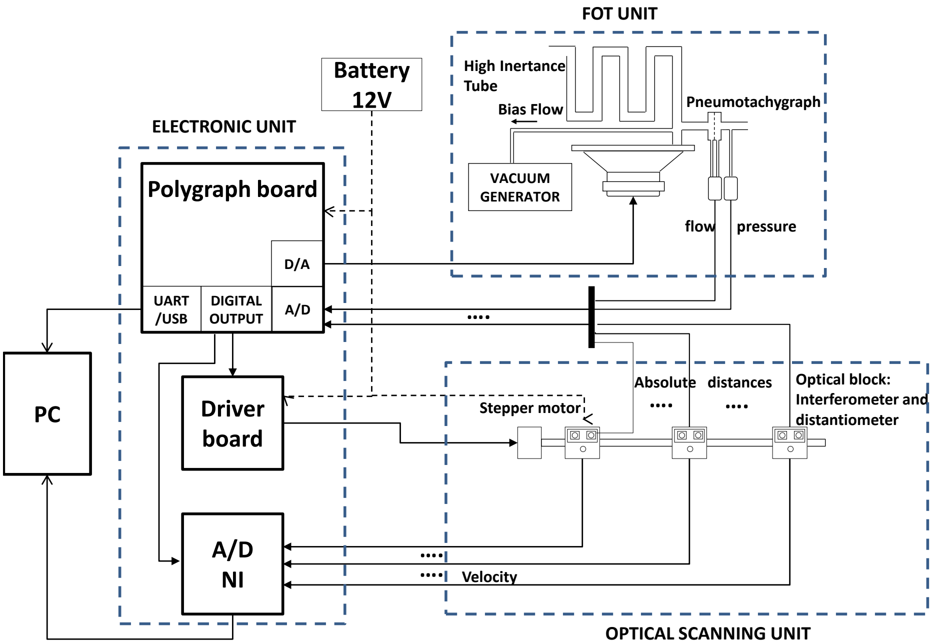

Figure 3.2: schematically description of the system proposed to realize the chest-wall scan.

3.1.1. FOT UNIT

The FOT set-up, that is the part of set-up used to produce the stimulus, can be changed according to the different conditions, in which the measure is performed, awaken subjects, mechanical ventilated subjects…

In particular during mechanical ventilation the FOT set-up used is a little bit different respect to that reported in chapter 2 that has been used on spontaneously breathing healthy subjects, since the loudspeaker should be integrated into the mechanical ventilator circuit.

Briefly, low amplitude sinusoidal pressure may be generated by a loudspeaker connected to the inspiratory line of a conventional mechanical ventilator and applied at the inlet of the endotracheal tube or the laryngeal mask tube. The rear of the loudspeaker was enclosed in a chamber and connected to the inspiratory outlet of the ventilator by a long tub to withstand the positive pressures generated by the ventilator (Figure 3.3).

The forced oscillation generator should meet some requirements:

1) it should not interfere with the ventilation, thus it should have a high impedance at the breathing frequencies;
2) it should be able to withstand the high positive pressures and fast pressure transients delivered by the ventilator during inspiration;
3) it should be able to generate pressure oscillations with a nearly constant amplitude (<2cmH_2O) during the whole respiratory cycle;
4) it should be suitable for the use in an intensive care unit.

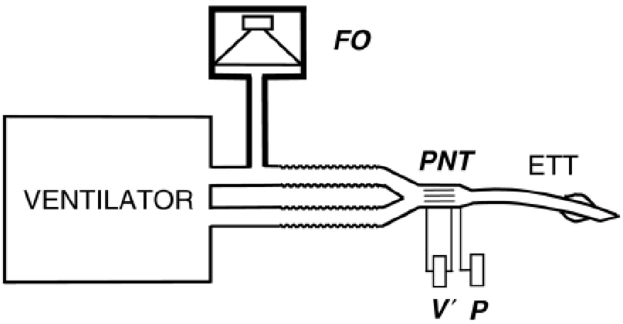

Figure 3.3: Schematic representation of the set-up to apply the forced oscillation technique during mechanical ventilation. A forced oscillation generator (FO) is connected in parallel to the ventilator. Flow (V') and pressure (P) are measured by means of a pneumotachograph (PNT) and a pressure transducer, respectively.

The advantage of this method is that it is very simple and it is able to generate oscillations at almost constant amplitude regardless the subject impedance. The limitation of this solution is that the loudspeaker and the gas enclosed in the box and in the additional tubing represents an additional compliance to the inspiratory line of the ventilator. Anyway, on adult patients, the respiratory frequency is much lower than in a baby, thus the constant of time of the modified circuit can be disregarded.

3.1.2. OPTICAL SCANNING UNIT

The scanning unit is a system design to: 1) provide measurements of little chest-wall movements (few micrometers) and absolute distance of the same point without requiring any contact with the patient and 2) to scan the chest-wall in a short time.
The scanning system is realized by five identical optical blocks which work in parallel in a multi-channel system. Each block is made by an interferometer which may be coupled by a distantiometer in order to fix the requirements for very high spatial-time resolution and absolute measurements which can't be fulfilled by the same sensor. They are enclosed in the same box and carefully aligned to grant the interferometer and the distantiometer are pointed on two much closed points of the chest-wall. The five blocks are fixed on a light aluminum bar equally spaced and oriented towards five points of the patient chest-wall transversally aligned; parallelism reduces acquisition time.
This bar is hanged over the patient bed by means of a mechanical frame and it is rotated by means of a stepper motor with angular resolution of 1.8 ° to allow a very fine resolution on the position which makes the optical blocks scan the chest wall.
An example of this system is reported in Figure 3.4

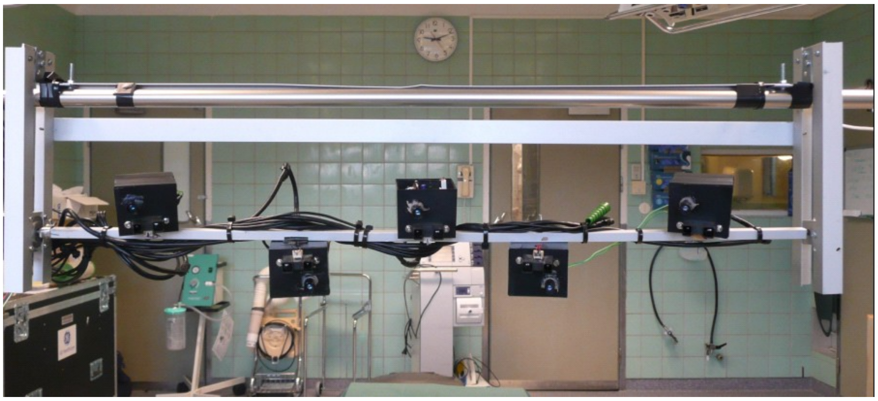

Figure 3.4: Optical unit. Each black box contains an interferometer and a distanziometer.

3.1.3. ELECTRONIC UNIT

The whole system integrates more technologies, more sensors, and actuators which should be handled carefully by means of a customized electronic unit which should control all the primary functions reported in Table 3.1:

Table 3.1: Functions implemented by the electronic unit

Analog signal acquisition	Up to5 interferometers at 100 kHz Up to 5 distanziometers at 200 Hz 1 flow sensor at 200 Hz 1 pressure sensor at 200 Hz
Analog signal generation	5, 11, 19 Hz sinusoidal stimulus sampled at 1000 Hz
Digital signal generation	Control signal to the motor driver Synchronisation signal for the different acquisition unit.
Communication	From the acquisition boards to PC

A scheme of the electronic unit is reported in the Figure 3.5.

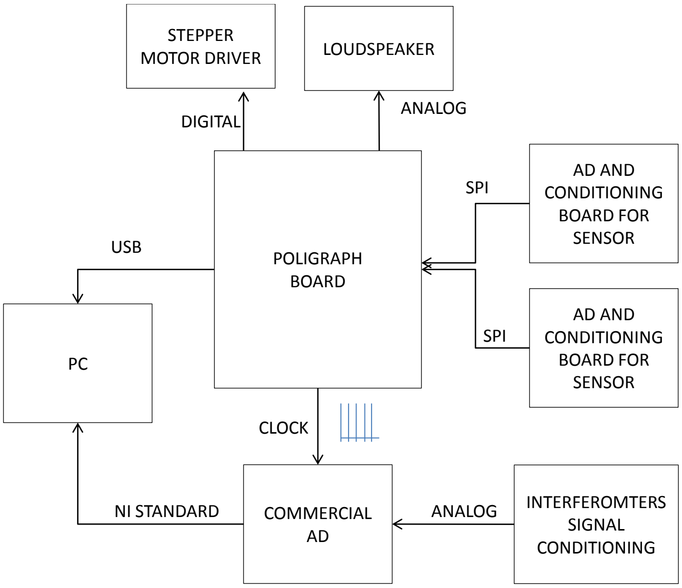

Figure 3.5: Scheme of the electronic unit.

The heart of the system is the polygraph board which manages the acquisition of the sensors sampled at 200 Hz, drives the actuators, synchronizes the acquisition boards and sends data to the PC via USB protocol.

In more details it may acquire signal sampled at 200 Hz up to five distanziometers, from the pressure sensor and the flow one which may be used to estimate the input impedance. Each sensor is integrated on a board which accounts for signal conditioning and digitalization by means of a SAR (successive approximation) ADC, whose control signals are produced by the polygraph board.

All the sensors boards have been carefully designed in order to make them interchangeable and connectable to the polygraph board. Indeed the boards are characterized by:

1) Several sensors;
2) Several conditioning configurations;
3) Several power supply voltages
4) ADC with a resolution of 12 or 16 bits.

This configuration, based on the replication of the conditioning unit, yields to: 1) high flexibility because of each sensor can be interchangeably acquired by any channel, 2) reduction in connection errors, 3) high resistance to electromagnetic noise, since the signal from the sensor to the polygraph has been already digitalized by the on-board ADC.

Once the signals have been digitalized and acquired, they are sent to the PC by means of a USB protocol which has been selected because of its popularity which allows using almost any laptop for the measurements.

The system is powered by an external source, a 12 V battery, because of two reasons which come from different requirements:

1) Safety requirements; indeed the device has been used in a hospital to measure respiratory parameters on humans, thus to avoid any dangers, we decide to not connect the system to the electrical power. Anyway the system is not electrically in contact with the patients.
2) Power management; we know it is possible to power the acquisition system strictly to the USB port of the PC, but the USB port can provide not more than 500 mA, which may be not enough to power the polygraph board and all the whole sensors that we may connect. Therefore we prefer to give the user the possibility to choose if it is better to power the system by the USB port or by the external source provided to allow a higher delivery of power which may be necessary if the system is used to acquire all the distantiometer, which consumes 30 mA each one.

The measurements of the chest-wall displacement, has been performed by means of interferometers, as described in the previous chapter they requires a very high sample frequency compared to the other sensors, up to 100 kHz, thus to acquire 5 of them we prefer to lean on a commercial board (National Instruments 6062E).

Our measurements require to estimate the phase shift from the pressure, which has been acquired by the polygraph board, and the velocity of the chest-wall points which have been derived from the interefometric signals acquired by the commercial board, as a consequence it has been necessary to pay attention to the synchronization of the board to avoid that different time base introduce uncontrolled shift.

For these reasons we don't use the internal clock of the board to drive the acquisition but we prefer to exploit a clock trigger which has been generated directly by the polygraph, thus the time base is the same for all the acquisition units since it has been produced by the same oscillator.
FOT setup requires also the generation of a pressure stimulus, in this experimental activities the pressure stimulus selected is a multi-frequency waveform obtaining by the sum of three sinus function at 5, 11, 19 Hz, which have been selected to obtain a partial frequency transfer function as described in chapter one.
The analogical stimulus is generated by the polygraph board, and then it is magnified by a commercial amplifier to drive the loudspeaker in order to produce a peak to peak signal with amplitude of about 2 cmH_20.
The relative amplitude of each component, can't be decided a priori because of each patient introduce a different load to the system thus the amplitude should be customized and titrated for each specific patient, although we can find an initial configuration. The resulting waveform can be dynamically changed at each measurement and for each condition by the user who can select the amplitude of each component.
Finally the stepper motor has been provided by a power board driven by the control signal produced by the polygraph board, which rotates the bar at fixed interval time of 30 seconds of the desired steps.

A. POLYGRAPH BOARD HARDWARE

The heart of the system, indeed it gets and manages a great quantity and variety of signals of different sources, controls other devices and synchronizes the several data flows is the polygraph, whose schematic is presented in the Figure 3.6
The data acquisition board is actually already made up, so there are analyzed some parts in order to understand its working and then concentrating on the firmware implementation in order to communicate with it and to perform all the necessary functions to allow the computation of all the variables of interest for the assessment of the FOT maps of the chest wall.

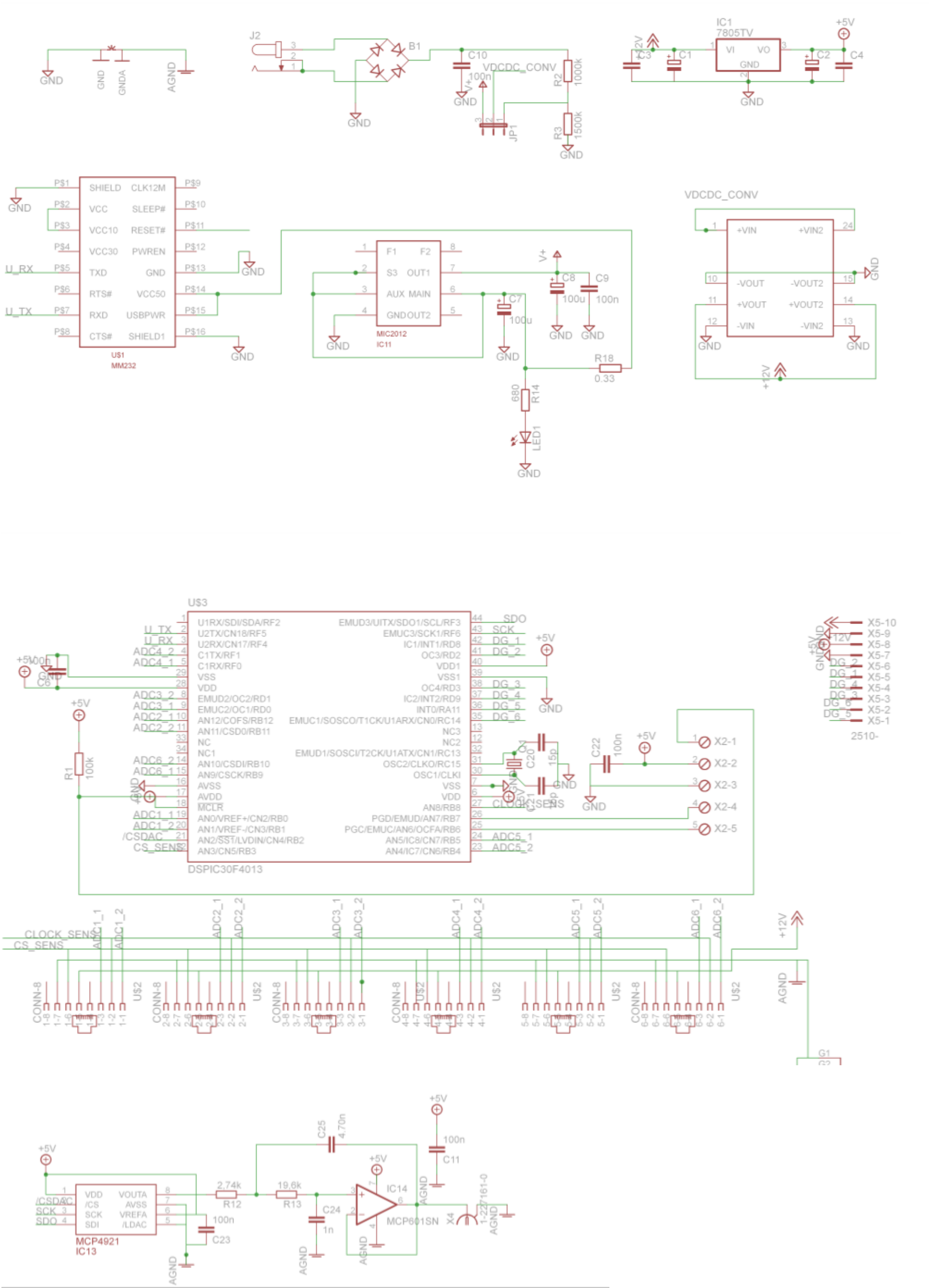

Figure 3.6: Schematic of the board.

DSPIC

The heart of the board is the device that controls all the data flows involved in the measurements of interest, which is the DSPIC30F3014, a processor specialized in managing and elaborating a great quantity of signals.

Power supply circuit

Power supply as we can see in the Figure 3.7 can be delivered by two different sources that can be selected modifying the position of the connections on a jumper:

- An external alimentation;
- The USB PC port.

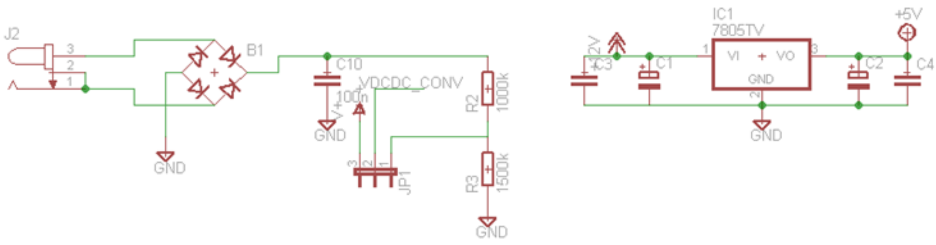

Figure 3.7: Power supply schematic.

Both the power supply path become the input of the DC/DC converter, which is able to receive a 4.5-9 V input and put out a 12 V voltage. This is the signal that is also transmitted to the front-end boards of the distantiometers and of the pressure and flow sensors and supplies all the devices on them, passing through a voltage regulator. This device allows also protecting the downstream circuit from voltage spike up to 1kV that is another protection adopted to minimize any potential electrical danger for the patient.
MIC2012 is a component carefully chosen to preserve the PC USB port to excessive current absorption by the downstream components, when the circuit is USB powered.

USB UART interface module

Communication between the polygraph board and the PC has been implemented by mean of USB protocol, which has been implemented by an external transceiver called MM232R, which is a miniature development module of USB UART interface integrated circuit devices. Briefly, it is a USB to serial UART interface comprising also a fully integrating the external EEPROM, clock circuit and USB resistors onto the device.
We decide not to choose a DS Pic with an internal USB module since the firmware implementation of USB routine is very demanding, limiting the computational capacity of the CPU. On the other hand DSPIC management of the UART module is completely

demanded to the devoted peripheral; moreover the UART module can fully satisfied the requirements of data velocity transfer.

DAC and reconstruction filter

The DAC and reconstruction file has been used to command the loudspeaker that must apply at the airways opening the pressure signal.
The functional structure of this device is characterized by 2.7-5.5V power supply, low DNL and INL, constant for a wide range of temperature and voltage reference, the Power-On Reset (POR) circuit to ensure reliable power-up and it's adopted the SMD package.
The MCP4921 is designed to interface directly with the Serial Peripheral Interface (SPI) port, available on many microcontrollers. To recover the exact frequency content of the digital signal, a reconstructed filter is connected to the DAC output, presenting the same second order Sallen Key low-pass configuration as the anti-aliasing one adopted by the front-end boards.

B. POLYGRAPH BOARD FIRMWARE

The functions described above are implemented by means of the firmware memorized by the DSPIC which is organized into a main function and three interrupts service routines at different priorities which are needed to manage the functionalities required exploiting all the peripheral devices provided by this DSPIC avoiding conflicts.
In more details the algorithm has been implemented as represented in the figures below, which deal with different conceptual blocks.

Main functions

The *main()* functions (Figure 3.8) deals with the initialization of all the peripheral devices used by the DPSPIC, then the waveform composed by the sinusoidal waves at 5,11,19 Hz is computed and saved into an array, the initial amplitudes for each components are chosen according to previous experimental tests on healthy subjects.

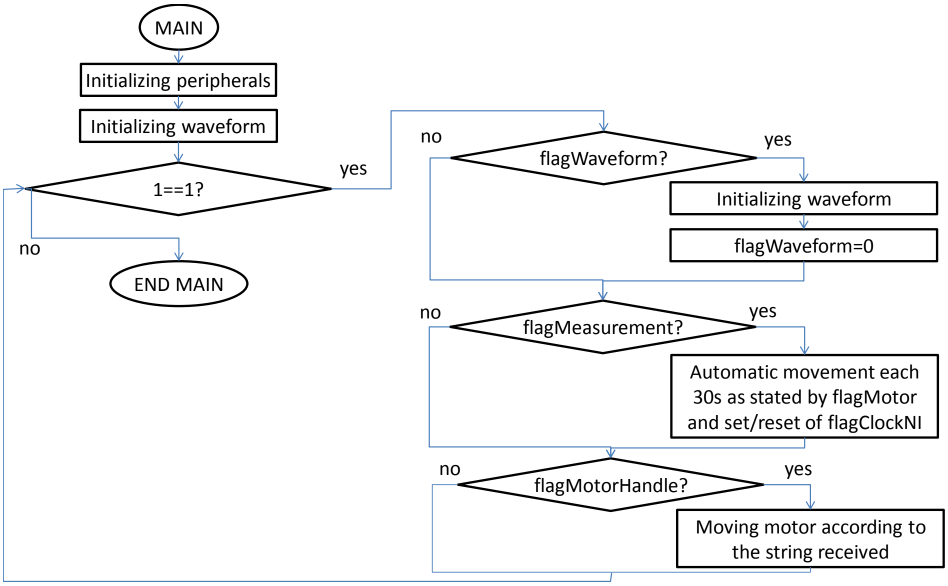

Figure 3.8: ***main*** **function flow chart**

After the initialization the infinite cycle starts, inside it the polling on several flags is performed and the correspondent actions are implemented.

In more details:

- if the waveform flag is set, it means that the DSPIC has received from the PC a string containing the new values for the amplitude of the three components, thus the waveform is computed again and the new array overwrites the old one.
- If the measurement flag is set, it means that the DSPIC has received from the PC a string containing the command of starting the motor movement. The motor will rotate of a pre-determined number of steps each 30 seconds. The time is measured in the ISR _TIMER1 and flagMotor is set when 30 seconds has last to mark the event.

Contemporary at each motor movement, flagClockNI is set, this means that the signal clock which controls the acquisition of data from the commercial NI board can start.

This way the bar with the five interferometers, coupled to the motor, can rotate of a known angular displacement from the beginning, which is the top of the chest wall to the end, which is the abdominal wall covering the wall surface.

ISRTIMER1

The interrupt service routine of the timer1, called *ISRTIMER1,* is generated at a frequency of 200 Hz, that is the one of the data acquisition. At each interrupt the data coming from sensors are acquired by means of an emulated SPI protocol that produces the control signals for the ADCs mounted on the sensor boards and reads the digitalized data coming from the sensors.

If the flagDataSendig has been set by the user, the data are sent to the PC with a frequency of 200 Hz. Each data packet contains a header with a progressive number and an indication about the motor status and the raw that is measured by the system.
In the same routine the clock for the commercial board is turned on and off by activating or deactivating the PWM module according to the status of the flagClockNI which is set into the *main()* functions every time the motor rotates the interferometers from the i^{th} raw to the $i+1^{\ th}$.
The flow chart of the ISRTIMER1 is reported in the Figure 3.9

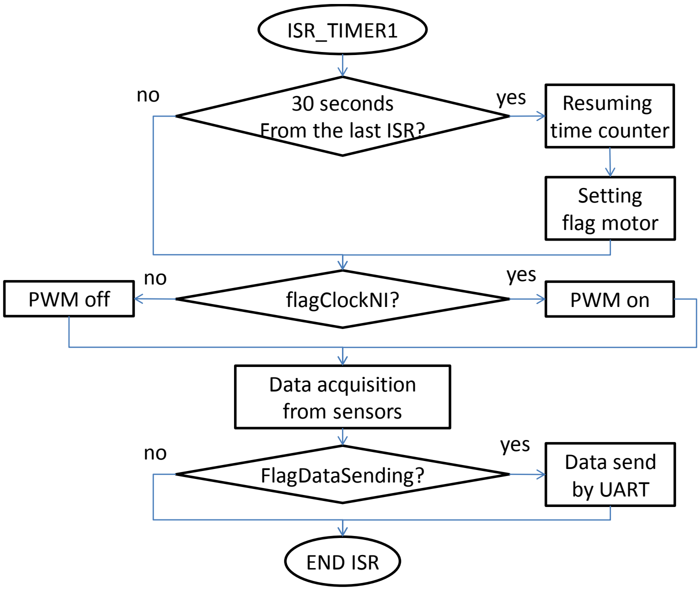

Figure 3.9: flow chart of the ISRTIMER1

ISRTIMER3

The waveform signals is generated by a DAC on chip that is driven by the signal coming from the DSPIC. The protocol used to communicate between the DSPIC and the DAC is the SPI. It has been implemented using the SPI module inside the DSPIC. To grant the transmission of data at the proper frequency, that is 1000 Hz, another timer and ISR has been introduced, it is *IRSTIMER3.* In Figure 3.10 is reported the main action during ISRTIMER3

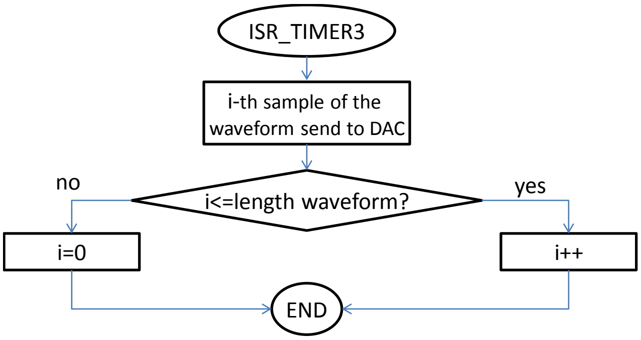

Figure 3.10: Flow chart of the ISRTIMER3

ISR_UART

The UART interrupt is associated with the reception of a character or a control string from the PC. It has the highest priority level.

The string that can be received and the corresponding flag that are set are schematically reported in the Figure 3.11.

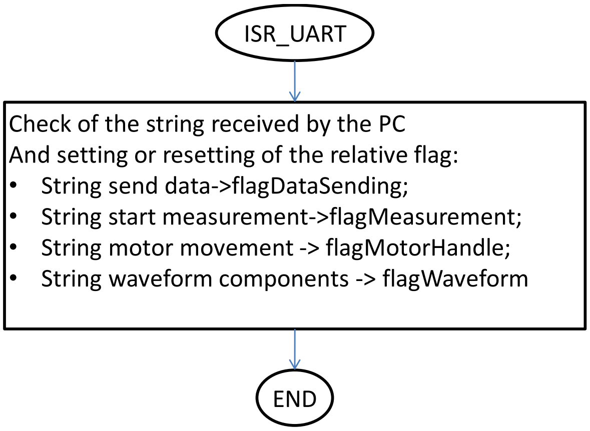

Figure 3.11: Description of the ISRUART

3.1.4. SOFTWARE

Associated to the acquisition system, a LabView application has been developed to allow the communication between the PC and the polygraph board and the data reading from the commercial acquisition board (Figure 3.12).

The architecture of the algorithm consists in two parallel infinite cycles: the first used to acquire data from the commercial board and the second to communicate to the polygraph board.

The two cycles can communicate by means of local variables that inform about several condition and events.

In more detail each time the motor moves from a raw to the following one, the polygraph board codifies the event sending a special character in the packet send to the PC via USB. In the infinite cycle of reading from the USB port, this character is searched and, if it is found, the data coming from the commercial board are saved to a new file identified by the number of the raw acquired.

Since the big quantity of data coming from the commercial board, since the five interferometers are sampled at 100 kHz each one, the data are not saved into a single file, but they are split into a file for each row, which contains the interferometer signal. Each file can be put in relation with the correspondent part of the pressure signal, which has been acquired by the polygraph board, thanks to some special characters send from the polygraph board at the beginning of each new row.

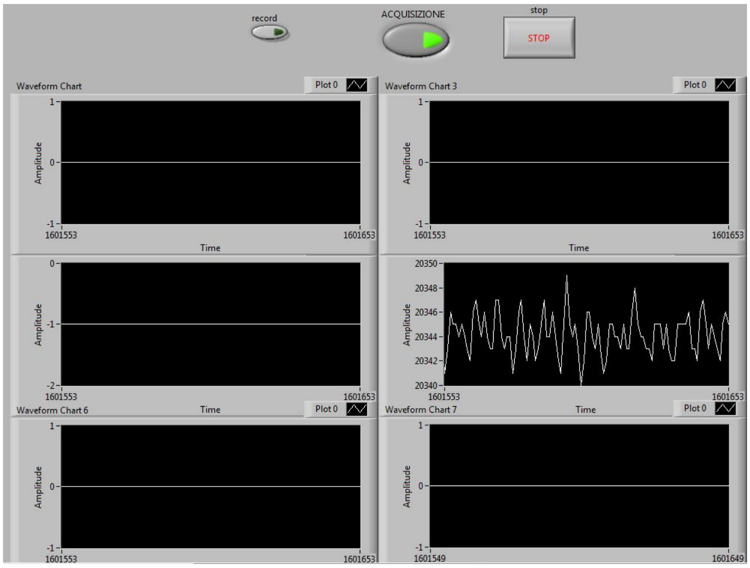

Figure 3.12: GUI of the Labview software

3.2. MEASUREMENTS ON ANESTHETIZED PATIENTS

The scanning system that we have already described in 3.1 allows measuring the velocity of propagation of pressure wave in the chest-wall in any condition, pathological or physiological thanks to its non-invasiveness and flexibility. Anyway it is particular interesting to study situations which present a significant variation in the chest-wall mechanics such as ARDS, edema, restrictive diseases, but also condition like anesthesia which may induce atelectasis and changing in the system condition.

3.2.1. ATELECTASIS IN ANAESTESIA

A. ATELECTASIS DEFINITION

The term atelectasis is derived from the Greek words *ateles* and*ektasis***,** which mean incomplete expansion. Atelectasis is defined as diminished volume affecting all or part of a lung. Pulmonary atelectasis is one of the most commonly encountered abnormalities in chest radiology findings Figure 3.. Atelectasis on a CT scan is defined as pixels with attenuation values of –100 to +100 Hounsfield units (HU) (1).

In Figure 3. panel b) top it is possible to note the absence of dense areas except for the vessels, while in the lower panel the dense areas in the dependent area of the both lungs are evident indicating development of atelectasis.

Several types of atelectasis exist; each has a characteristic radiographic pattern and etiology. Atelectasis is divided physiologically into obstructive and no obstructive causes (2).

Obstructive atelectasis is the most common type and results from reabsorption of gas from the alveoli when communication between the alveoli and the trachea is obstructed. The obstruction can occur at the level of the larger or smaller bronchus. Causes of obstructive atelectasis include foreign body, tumor, and mucous plugging.

Non-obstructive atelectasis can be caused by loss of contact between the parietal and visceral pleurae, compression, loss of surfactant, and replacement of parenchymal tissue by scarring or infiltrative disease.

Relaxation or passive atelectasis results when a pleural effusion or a pneumothorax eliminates contact between the parietal and visceral pleurae. Generally, the uniform elasticity of a normal lung leads to preservation of shape even when volume is decreased.

Compression atelectasis occurs from any space-occupying lesion of the thorax compressing the lung and forcing air out of the alveoli. The mechanism is similar to relaxation atelectasis.

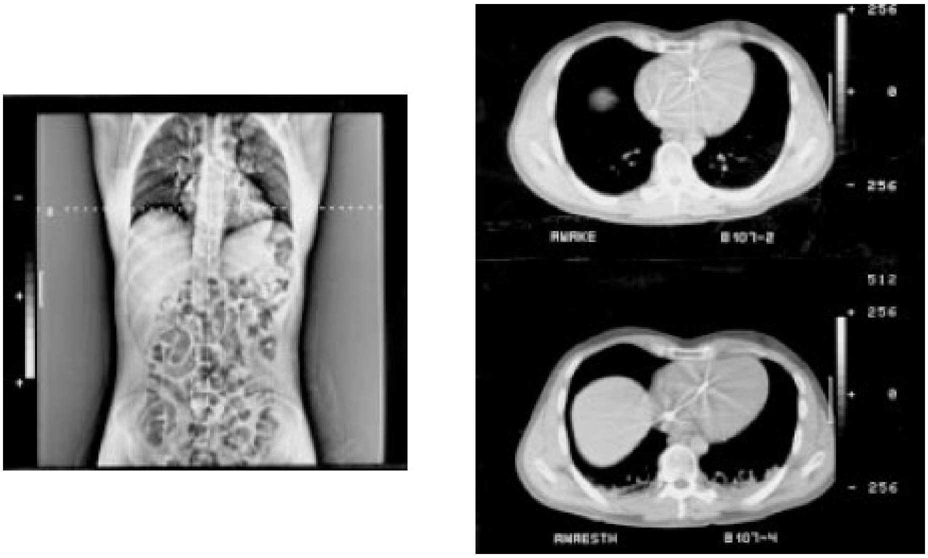

Figure 3.13: Panel a) front view of the chest and the abdomen, b) Transverse CT section in an awaken subject. c) The same subjects as in mid panel, approximately 15 minutes after induction of anesthesia and muscle paralysis. (3)

Adhesive atelectasis results from surfactant deficiency. Surfactant normally reduces the surface tension of the alveoli, thereby decreasing the tendency of these structures to collapse. Decreased production or inactivation of surfactant leads to alveolar instability and collapse. This is observed particularly in (ARDS) and similar disorders.
Cicatrization atelectasis results from diminution of volume as a sequela of severe parenchymal scarring and is usually caused by granulomatous disease or necrotizing pneumonia. Replacement atelectasis occurs when the alveoli of an entire lobe are filled by tumor (e.g., bronchioalveolar cell carcinoma), resulting in loss of volume.

B. ETHIOLOGY

The mechanism of obstructive and non-obstructive atelectasis is quite different and is determined by several factors.
Obstructive atelectasis following obstruction of a bronchus, the circulating blood absorbs the gas in the peripheral alveoli, leading to retraction of the lung and an airless state within a few hours. In the early stages, blood perfuses the airless lung; this results in ventilation-perfusion mismatch and arterial hypoxemia. A filling of the

alveolar spaces with secretions and cells may occur, thereby preventing complete collapse of the atelectatic lung. The uninvolved surrounding lung tissue distends, displacing the surrounding structures. The heart and mediastinum shift toward the atelectatic area, the diaphragm is elevated, and the chest wall flattens.

If the obstruction is removed, any complicating post obstructive infection subsides and the lung returns to its normal state. If the obstruction is persistent and infection continues to be present, fibrosis develops and the lung becomes bronchiectatic.

The loss of contact between the visceral and parietal pleurae is the primary cause of non-obstructive atelectasis. A pleural effusion or pneumothorax causes relaxation or passive atelectasis. Pleural effusions affect the lower lobes more commonly than pneumothorax, which affects the upper lobes. A large pleural-based lung mass may cause compression atelectasis by decreasing lung volumes.

Adhesive atelectasis is caused by a lack of surfactant. The surfactant has phospholipid dipalmitoyl phosphatidylcholine, which prevents lung collapse by reducing the surface tension of the alveoli. Lack of production or inactivation of surfactant causes alveolar instability and collapse; it may occur in ARDS, radiation pneumonitis, and blunt trauma to the lung,

In summary atelectasis mechanisms are three (4):

1) compression;

2) absorption of gas behind occluded airways;

3) loss of surfactant.

Compression atelectasis

The diaphragm separates abdomen from the ribcage compartments which present different pressures, abdomen pressure is more than abdominal one. If the abdomen is not active, the abdominal pressure is transferred into the thoracic cavity, increasing in particular the pleural pressure in dependent regions. Direct support for this theory is delivery by Hedenstierna *et al.* (5) : tensing the diaphragm by phrenic nerve stimulation reduces the amount of anesthesia.

Gas resoprtion

Short periods of breathing 100 % oxygen near residual volume may cause atelectasis. Thus an increased respiratory fraction of oxygen, may promote atelectasis formation if there is a contemporary reduction in FRC (6).

Surfactant

Mechanical ventilation may impede intermittent deep breaths that may results in a decreased content of active form of alveolar surfactant. The lack of active surfactant reduces alveolar stability contributing to liquid bridging in the airway lumen and thereby inducing airways closure.(7-9)

Another important cause of atelectasis is general anesthesia, in fact it affects almost the 90% of the anesthetized patients (10), it is seen during both spontaneous breathing and after muscle paralysis and whether intravenous or inhalational anesthetics are used (11).

Atelectasis due to anesthesia is a phenomenon which affects subject in some unpredictable ways according to the patient's feature.

Strindberg *et al.* (12) and Pelosi *et al.* (13)found a weak correlation between the size of the atelectasis and body weight or body mass index, which is not surprising, but other studies demonstrated that atelectasis is independent of age, children and young people show as much atelectasis as elderly people(10) and that patients with chronic obstructive lung disease(COPD) show less or even no atelectasis during anesthesia(14)

C. ATELECTASIS PREVENTION

The mechanisms that may prevent anesthesia are four: PEEP, maintenance or restoration of respiratory muscle tone, recruitment maneuver and minimization of pulmonary desorption. Typically more than one intervention is performed.

PEEP

The application of a PEEP of 10 cm H_2O has been tested in several studies and will consistently reopen collapsed lung tissue (15). However, some atelectasis persists in most patients. Further increases in PEEP level could re-expand this persistent atelectasis but PEEP may not be ideal. Firstly, shunt is not reduced and the arterial oxygenation is not always improved. Persistent shunt may be explained by the redistribution of blood flow towards the most dependent parts of the lung when intrathoracic pressure is increased, so that residual atelectasis lung receives a larger share of the pulmonary blood flow when PEEP is applied (16). The increased intrathoracic pressure will also impede venous return and reduce cardiac output.

This will decrease venous oxygen tension and augment the impact of shunted blood and perfusion of poorly ventilated regions on arterial oxygenation. Secondly, the lung may re-collapse rapidly after discontinuation of PEEP. Within 1 min after cessation of PEEP the collapse is as large as it was before the application of PEEP. (5). However, PEEP applied immediately after a VCM will completely prevent recurrence of atelectasis, even when 100% oxygen is used (17)

In a 2009 study(10), a recruitment maneuver plus positive end-expiratory pressure (PEEP) reduced atelectasis to 3 ±4%, increased end-expiratory lung volume, and increased the PaO_2/FiO_2 ratio from 266 ±70 mm Hg to 412 ±99 mm Hg. It was found that the PEEP alone did not reduce the amount of atelectasis or improve oxygenation, but a recruitment maneuver followed by PEEP reduced atelectasis and improved oxygenation (18).

Maintenance of muscle tone

The use of an anesthetic which allows maintenance of respiratory muscle tone will prevent formation of atelectasis. Ketamine does not impair muscle tone and does not cause atelectasis. However, if muscle relaxation is required, atelectasis will appear as with other anesthetics (19).

Another attempt is to restore respiratory muscle function which can be achieved, at least partly, by pacing of the diaphragm. This was tested by applying phrenic nerve stimulation which did reduce the atelectatic area (5). This effect, however, was small, and this technique is certainly too complicated to be used as a routine during anesthesia and surgery.

Recruitment maneuver

A VCM (vital capacity maneuver) can completely abolish atelectasis that develops after induction of general anesthesia. Lung inflation to an airway pressure of 20 cm H_2O did not affect atelectasis; an airway pressure of 30 cm H_2O reduced atelectasis; only with a pressure of 40 cm H_2O maintained for 15 s is atelectatic lung tissue fully re-expanded. This pressure is equivalent to inflation to vital capacity, and thus this manoeuvre has been called the VCM. More recently, it has been shown that this manoeuvre needs to be maintained for only 7–8 s in order to re-expand all previously collapsed lung tissue Figure 3.14.

In animal experiments, repeated VCM had no deleterious pulmonary effects as measured by extravascular lung water, pulmonary clearance of ^{99m}Tc-DTPA (which is a marker of the functional integrity of the alveolocapillary barrier) and light microscopy.(20)

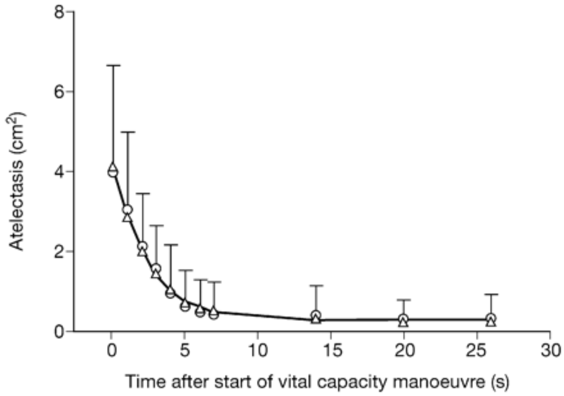

Figure 3.14: Atelectasis before (time=0) and during the vital capacity manoeuvre. Mean values and SD (error bars) are shown. An exponential decay curve is fitted to individual data (from Rothen et al.(20))

Minimizing gas resorption

Ventilation of the lungs with pure oxygen after a vital capacity maneuver that had reopened previously collapsed lung tissue resulted in a rapid reappearance of the atelectasis (21). If, on the other hand, 40% O_2 in nitrogen is used for ventilation of the lungs, atelectasis reappeared slowly, and 40 min after the vital capacity maneuver only 20% of the initial atelectasis had reappeared. Thus, ventilation during anesthesia should be done with a moderate fraction of inspired oxygen (F_IO_2, e.g., 0.3^0.4) and be increased only if arterial oxygenation is compromised. Further, if the lungs are ventilated with high inspiratory fraction of oxygen, the use of PEEP should be considered. As an example, in adults with healthy lungs, 10 cm H_2O of PEEP significantly reduced atelectasis formation after a vital capacity maneuver even if an F_IO_2 of 1.0 was used (17).

3.2.2. PILOT STUDY: AN ANIMAL ARDS MODEL

To assess interferometer capability to detect variation of chest-wall mechanics due to lung atelectasis and de-rectruitment, a pilot study has been performed on an animal model of ARDS. After induction of ALI/ARDS by means of bronco-alveolar lavage, a recruitment maneuver has been performed and the chest-wall mechanics has been measured. The aim of this pilot study was just to assess the feasibility of measurements of mechanical properties by interferometer and to compare the results with a standard like CT.

A. BACKGROUND

Mechanical ventilation is essential in the treatment of patients affected by acute lung injury (ALI) or acute respiratory distress syndrome (ARDS). However, if the ventilatory parameters are not titrated adequately, it may cause volutrauma and atelectrauma as well as worsening of inflammatory processes (22-24). Positive end expiratory pressure (PEEP) improves lung function and may reduce the duration of mechanical ventilation. One goal of a protective ventilatory strategy is to choose a value of PEEP that maximizes recruitment while avoiding over-distension (25). A feasible candidate as optimal PEEP is the one estimated by open lung approach. It is believed that reinflating collapsed lung units also causes lung injury and cytokine release. By stenting the airways open at end expiration, using PEEP, it may be possible to reduce these shearing injuries. There has been a preliminary trial by Amato and colleagues (26), demonstrating the efficacy of this technique.

This group painstakingly constructed pressure volume curves on each patient to determine “Flex” (the lower inflection point on the pressure volume curve), and applied PEEP just above this level. The patients invariably receive a higher than conventional PEEP level, with lower tidal volumes (27).

Critics of this technique have suggested that plotting pressure volume curves is difficult, that Pflex often is impossible to find, and that overdistension of less diseased tissues may occur.

In clinical practice PEEP is usually adjusted according to oxygenation (28), but this may overlook PEEP-induced over-distension and intra-tidal recruitment/derecruitment.

An alternative approach is to set PEEP in order to maximize dynamic compliance (C_{dyn}) (29) or similarly to minimize the elastance (E_{rs}) of the respiratory system ($E_{rs} = 1/C_{dyn}$) (30-32), during a decremental PEEP trial. Even though C_{dyn} has the advantage of being continuously provided by the ventilator, its estimation is strongly affected by non-linearities, which may be relevant in diseased lungs, and by respiratory muscle activity, requiring either deep sedation or the use of an esophageal balloon in the presence of spontaneous breathing.

B. METHODS

We study two anesthetized piglets (weight 26 ± 1.5 kg). Lung injury (ALI/ARDS) was induced by broncho-alveolar lavage and the animals were ventilated in volume control mode with a tidal volume of 6 ml/kg.

Forced oscillations were superimposed on the ventilation waveform for the assessment of respiratory mechanics. PEEP was increased from 0 to 24 cmH_2O in steps of 4 cmH2O and subsequently decreased from 24 to 0 in steps of 2 cmH_2O. Each PEEP step lasted 8 minutes to avoid transient effects.

To generate the waveform stimulus a loudspeaker the ventilator circuit has been modifies and a loudspeaker has been inserted in the inspiratory line.

At each step a stimulus at three different frequencies, 5, 11 and 19 Hz has been administered. The order at whom the frequencies are administered has not been randomized.

A pneumotachograph has been connected to tracheal tube to grant for pressure and flow measurements.

Three interferometers where hanged on a mechanical frame above the piglet and they have been focused on the ribcage of the piglets on the midline and symmetrically respect it at about 10 cm of distances.

Contemporary a CT scan was acquired at each step during an end-expiratory hold.

In more details, as reported in Figure 3.15 we can see the modified ventilator circuit in which a loudspeaker has been introduced to generate the waveform stimulus, the pneumotachograph and the sensor pressure which allows to measure flow and pressure at the mouth for the estimation of input impedance, the CT scan and the interferometers.

Resuming the following parameters have been acquired:

1) Pressure an flow at the airways opening which have been used to estimate the input impedance of the system;
2) Three interferometers signal synchronize to the pressure signal which are used to estimate chest wall mechanics;
3) CT scan used as gold standard to evaluate the actual percentage of aerated vs. not aerated tissue;
4) Blood gas analyses.

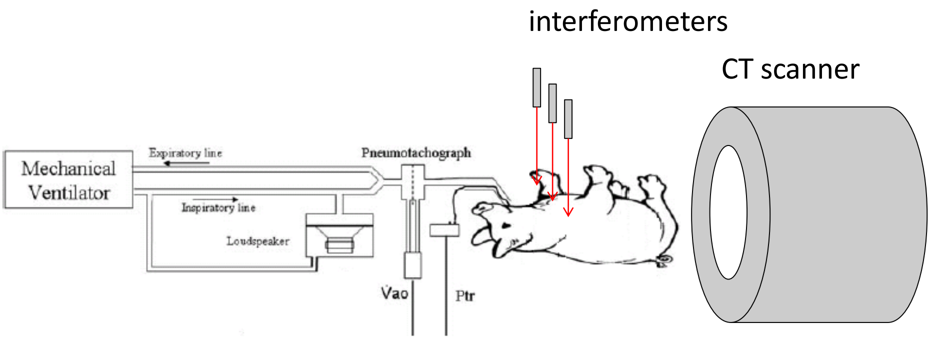

Figure 3.15: Experimental set-up. A piglet is mechanically ventilated while it has been contemporary submitted to FOT. Pressure and flow at the airway opening are measured; Three interferometers are pointed on the chest-wall and a Ct scanner has also been used

C. DATA ANALYSIS

Once the data has been collected, they have been processed to extract data as described below.

Velocity of the three points of the chest-wall has been computed by interferometer signals using the algorithm described in chapter 2. In this way we get for each PEEP step, the velocity of each point of the chest wall which contains the three frequencies of the stimulus and the phase delay between the pressure stimulus at the mouth and the velocity of each point has been estimated at each frequency.

Then the phase delays are estimated by power spectral technique and measurements with coherence less than 0.95 are disregarded.

Resuming the processed information is:

- Phase delay between pressure at the mouth and each point of the chest-wall at 5 Hz for each PEEP steps.
- Phase delay between pressure at the mouth and each point of the chest-wall at 11 Hz for each PEEP steps. Phase delay between pressure at the mouth and each point of the chest-wall at 19 Hz for each PEEP steps.

Then the images were reconstructed with 8-mm slice thickness using a standard body reconstruction filter (B41f, Siemens notation). The images were analyzed using dedicated software (Maluna, Mannheim Lung Analyzing Tool, version 2.02, Mannheim, Germany). The lung contours were manually traced in all the slices to define the regions of interest. The total lung volume was subdivided into overaerated (OA -1,000 to -900 Hounsfield units, HU), normally aerated (-900 to -500 HU), poorly aerated (PA -500 to -100 HU) and nonaerated (NA -100 to RW (33)100 HU) volumes as suggested previously (33, 34). Lung gas (V_{gas}) and tissue (V_{tiss}) volumes were calculated using standard equations (33) for both the whole lung and for each aeration compartment.

In this study the amount of derecruited lung was quantified as the volume of tissue in the nonaerated region and expressed as a percentage of total tissue volume as follows (3.1):

$$V_{tiss}NA\% = \frac{V_{tiss}NA}{V_{tiss}} \cdot 100 \qquad 3.1$$

We chose to express the changes in the recruited lung as changes in non-aerated tissue and not in the total gas volume or in the aerated volume as the latter could also change as a consequence of an increase in alveolar size without changes in the number of recruited alveolar.

D. RESULTS AND DISCUSSIONS

In Figure 3.16 is reported an example of the signals, in more details panel a) show the pressure recorded at the opening airways. The respiratory driver and the PEEP value can be seen. The small FOT oscillation superimposed may be appreciated.

Panel a), b) and c) report the velocities measured by the three interferometers. They represent respectively: velocity acquired on the right side of the piglet (vel_{right}), velocities acquired on the midline ($vel_{midline}$) and the one measured on the left side (vel_{left}.)

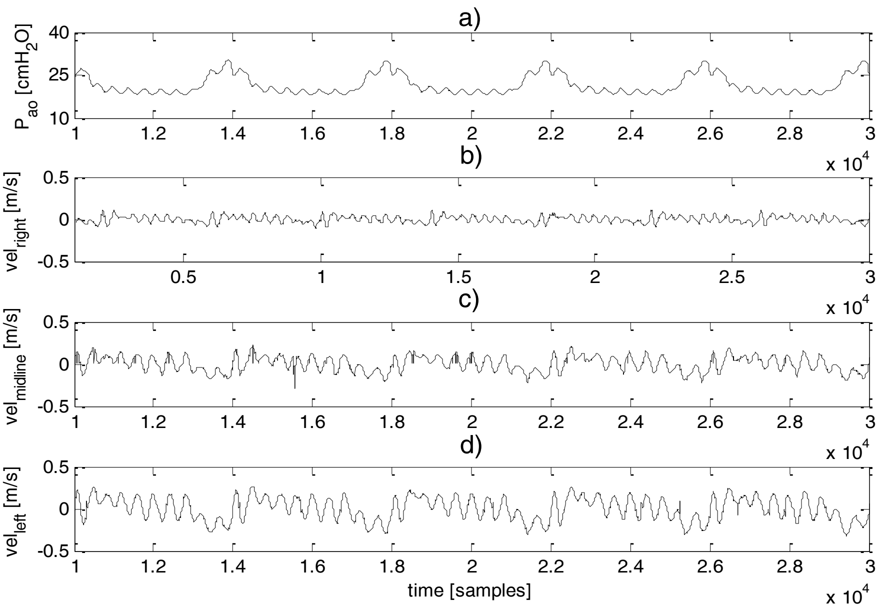

Figure 3.16: Signals of pressure and the three velocities

It is appreciable the quality of the reconstructed signals, although the raw interferometry signals heavily affected by speckles due to the diffusive properties of the piglet skin, the velocities presents almost no artifacts. The velocity signals present a trend which fairly traces out the pressure stimulus, indeed the breathing acts in velocities can be identified in concomitance with the pressure peak administered by the ventilator. In the velocities signals are also evident the superimposed stimulus components.

The phase delay at 5 Hz, 11Hz are reported in Figure 3.17, in an ARDS piglet we may expect an high hysteresis in the phase delay due to recruitment, that is, since the consolidated lung has been re-opened, the mechanical properties should be changed.

In Figure 3.17, we can't find the expected trend, indeed for 5 and 11 Hz the curves seems to be confused, with a lot of crossing in the ascending and descending direction, but they are highly repeatable for the two frequencies and at each position.

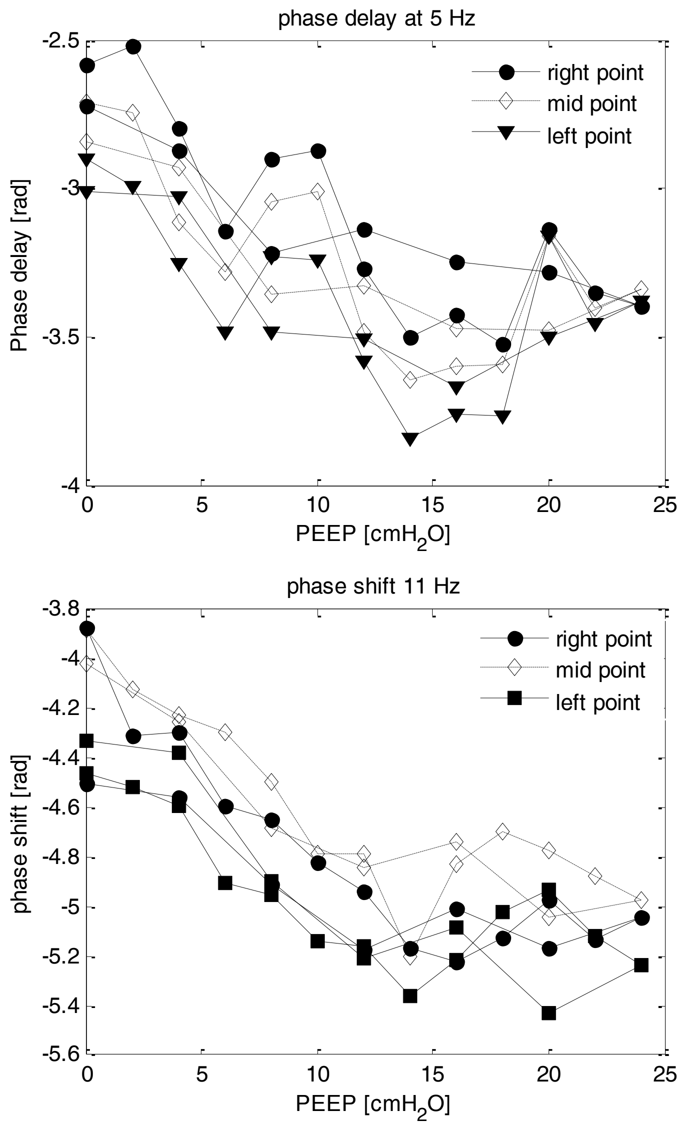

Figure 3.17: upper panel) delay at 5 Hz estimated for right, central and left line, mid panel) delay at 11 Hz estimated for right, central and left line.

There are two possible reasons for this behavior: 1) chest wall mechanics is not sensitive to recruitment, thus phase shift is not representative, 2) the lung lavage has not been properly done and the piglet lung doesn't need recruitment.

In order to find which the best answer is, we refer to the measure X_{c5} and to the CT scan as reported in Figure 3.18. By $V_{tissueNA\%}$ parameter we can infer that the percentage volume of not aerated tissue, show a similar trend with almost absence of hysteresis, that means the quantity of recruited tissue is very poor. X_{c5} seems to

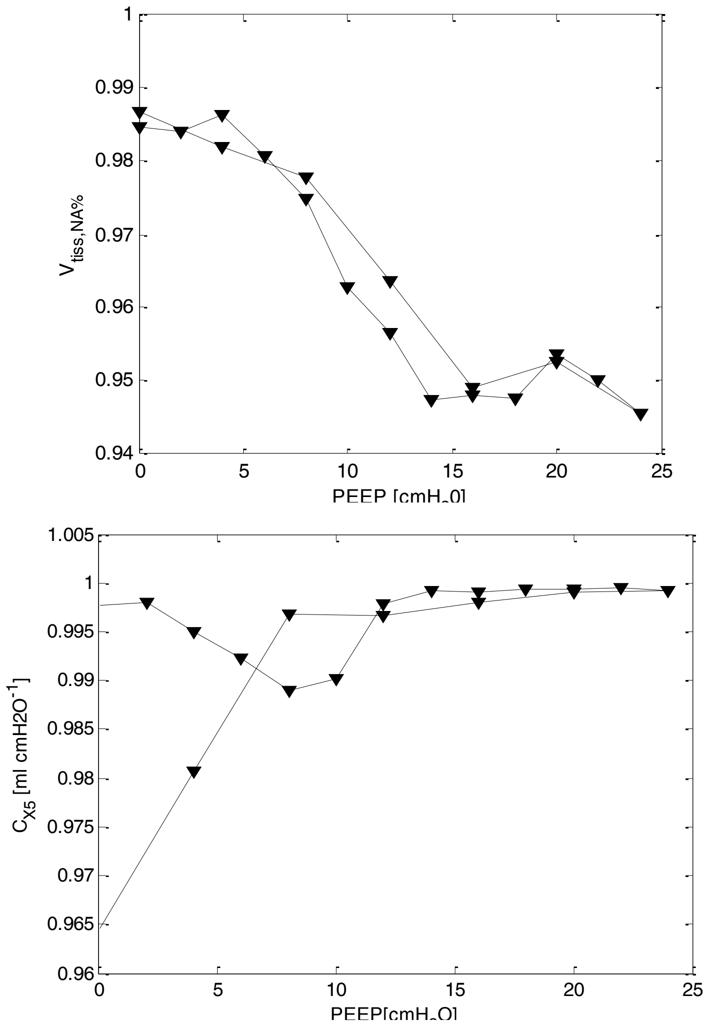

Figure 3.18: upper panel) VtissNA% measured at each PEEP step, lower panel) CX5 estimated by input impedance.

suggest the same result.

Although the piglet seems as the bronco-alveolar lavage has not come to a satisfactory conclusion, we can compare the results of mechanical properties and CT.

Figure 3.19 shows the trend of $V_{tiss}NA\%$ during the descending PEEP administration, as the PEEP decreases the percentage of not aerated tissue decreases too, but it shows a flex point when the open lung PEEP is reached at 14 cmH2O, the same trends can be clearly found also for the phase delay at 11 Hz estimated by interferometer for the mid line and left and right side of the rib cage, which present a minimum for 14 cmH2O PEEP. The trend of the mid line phase is slightly different compared to the sided, maybe due to a different conduction of the pressure stimulus along the sternal bone.

In conclusion, since the trends presented by the phase shift and the CT show good similarity, we can hypothesis that this very preliminary data suggest that the phase delay between pressure and the velocity of points of the chest-wall may be a parameter correlated to the de-rectruitment status of the lung. Moreover since this technique is completely non-invasive it can be proposed also for monitoring.

Anyway, although the results are promising, more data are needed to confirm these hypothesis.

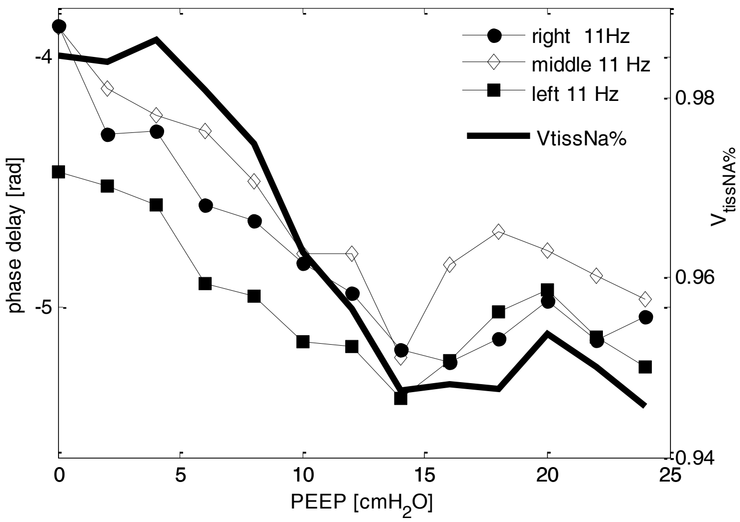

Figure 3.19: Comparison in descending PEEP between 11 Hz phase delay and V_{tiss}NA%

3.2.3. MEASUREMNENT ON HUMANS

A. PROTOCOL

ARDS, thoracic surgery, and anesthesia are associated with atelectasis, disturbed ventilation-perfusion relationship, and hypoxemia. It has been shown that in these patients the mechanical behavior of the respiratory system is altered, with a reduction in functional residual capacity and compliance. Mechanical ventilation is essential in the treatment of all these patients and, in particular, positive end-expiratory pressure (PEEP) is used to reverse atelectasis and improve lung function.

Since we have design and implemented a system to measure the mechanical properties of the respiratory system in terms of phase delay in the pressure propagation, we are interested in validate this method by studying the chest-wall condition on patients during anesthesia induction.

The aim of the study is therefore to check the efficacy of our instruments in detecting variation in the chest-wall condition by comparing the results with other technique which have been already proven to reveal the status of the respiratory system.

All the measurements have been taken to the Uppsala University Hospital.

Up to know the measurements have been applied to five patients who should undergo any kind of surgery none connected with the lung system.

The patients are four women (1.68 ± 3.4 m of height, 65 ± 2.6 kg of weight, 53± 6.5 years old) and a man (1.83 m of height, 77kg, 37 years old).

The protocol stages are reported below:

1. One day before surgery patients has been called for a visit and the baseline pulmonary function was assessed by spirometry.

2. Just before surgery measurements of oscillatory mechanics has been performed at the following stages:

- Awake through a mouthpiece, it will be indicated as SB (Spontaneous Breathing)
- After sedation through a full face mask, it will be indicated as S(Sedation)
- After paralysis with tracheal tube in place at PEEP equals to 0 cmH_20, it will be indicated as PEEP0;
- After paralysis with tracheal tube in place at PEEP equals to 5 cmH_20, it will be indicated as PEEP5d;
- After paralysis with tracheal tube in place during a recruitment manoeuvre at 15 cmH_20 it will be indicated as RM.
- After the recruitment manoeuvre a PEEP a15 cmH_20 again.

During sedation the patients are ventilated in pressure support modality, while during paralysis they received a pressured controlled ventilation with a pressure inspiratory peak (P_{insp}) of 15 cmH_20 and a Tinsp:Tesp (inspiratory time : expiratory time) ratio time of 1:2.

Measurements

For each protocol step the following parameters will be recorded at the end of the stabilization period, except for RM since it should not last more than 2 minutes, not to damage the health of the patient.

- Input impedance at 5-11-19 Hz by FOT
- Chest-wall displacement in 20 point arranged in four lines at 5-11-19 Hz

- FRC measurements estimated by a commercial ventilator (General Elelctric Engström Carestation)

Laser interferometry

The movement of the points of the chest wall will be measured by a self-mixing interferometer as described in detailed below. The measurement points will be chosen along vertical lines (the midline the nipple lines and the two parasternal lines) and will be equally distributed from the clavicles to the anterior superior iliac spines. The chest wall movement will be measured in response to a composite waveform including 5, 11 and 19 Hz. The pick-to-pick amplitude of the stimulus will be ~ 2 cmH_2O.

Figure 3.20: set-up for measurements of chest-wall mechanics

FOT measurements

Respiratory system impedance will be computed from the flow and pressure signals measured at the inlet of the tracheal tube. A composite waveform including 5, 11 and 19 Hz will be used as a stimulating signal.

FRC measurement

This measurement will be performed by means of a commercial mechanical ventilator, (Engstrom Carestation), which can provide FRC by Wash-in and Wash-out method which provide two separates estimations. At the end of the measurement, if the two estimations are similar, a mean value is provided.

Experimental set-up

The patients will be connected to the mechanical ventilator, the circuit of which will be modified for delivering the pressure stimuli for the measurements of oscillatory mechanics.
For the experiments, we use the scanning system described in the first part of the chapter that is made by five interferometers that can be moved by a stepper motor to cover the chest-wall surface.

B. DATA ANALYSIS

Once the data have been acquired they have analyzed, in particular for each patient, the following analysis have been carried out:

- Input impedance, Z_{in}: Z_{in} has been estimated for each condition, (SB, S, PEEP0, PEEP5u, RM,PEEP5d) at the three different frequencies of the stimulus, 5, 11, 19 Hz by spectral technique, then the real and imaginary part has been computed. Thanks to coherence it has been possible to discard not reliable values that are those with coherence less than 0.95.

Data during paralysis, when the patient breaths through the tracheal tube have been corrected by subtracting the impedance of the tube estimated by the same set-up and during forced oscillation.

- Chest-wall mechanics: at each condition a map of the pressure wave propagation velocities has been estimated. For each acquired point the velocity has been extracted and the phase delay between the pressure of the mouth, at 5, 11 and 19 Hz has been estimated as phase of the transfer function between pressure and velocities computed by spectral methods.

Since we have four rows in the cranial-caudal directions, and five interferometer signals , distributed side to side, for each patient condition, three 4X5 matrix has been obtain, each position of the map corresponds to a spot of the interferometer on the chest-wall, and each map is representative of a different frequency of stimulus.
Data with coherence less than 0.95 has been discarded. As a consequence there were some "holes" in the matrix which have been reconstructed by interpolation with the other contiguous points.

C. RESULTS AND DISCUSSIONS

Several parameters have been acquired during the protocol, some of them are conventional and well-accepted one like spirometry and FRC measurements, while others such as Z_{in} are very promising although not completely established; finally the phase shift maps which are the ones we are interested in proven the sensitivity.

Spirometry

Each patient has been subject to a spirometry test to assess its respiratory status by conventional test lung methods. As can be seen in the Table 3.2, patients 1,2and 4 seem to be healthy, since their actual values are higher than the predicted ones. But also 3 and 4 can been considered healthy and the low value respect to the predicted may be interpreted as an evidence of performing properly furcated maneuver in not-trained subjects.

Table 3.2: Spirometry test

PATIENT	FVC(L)	FEV1(L)	%PREDICTED FVC	%PREDICTED FRC
1	4,63	3,79	118	130
2	4,98	5,25	103	100
3	3.19	2.48	86	92
4	3,32	2,65	100	109
5	4,87	3,79	84	88

FRC measurement

During each stage of the protocol, except for the recruitment maneuver, a measurement of FRC has been performed, since it has been shown by Hedenstierna et al (3), that FRC is a parameter that is influenced by sedation and paralysis and then it could be used a flag for the status of the mechanical balance between the lung parenchyma and the chest-wall.

The averaged trend on all the patients is shown in Figure 3.21 along the x axes the anesthesia stages are reported. As expected after sedation induction there is a decrease in the FRC measurements, which goes from 3389 ± 1473 mL to 2392 ± 1234 mL, a percentage redaction of almost 30%.

Then when the patient is mechanical ventilated, the tidal volume increases and also the FRC increases a little, but the most evident variation can be appreciated after the recruitment maneuver, indeed the FRC comes back almost to the spontaneous breathing recorded value(3347±1577mL).

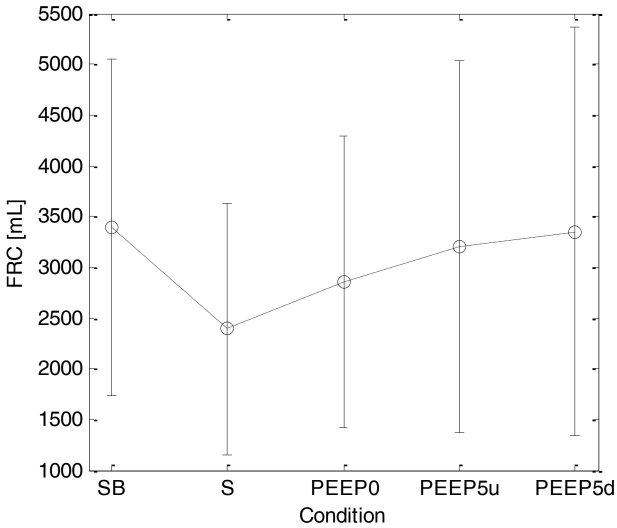

Figure 3.21: FRC averaged trend during the different anesthesia stages.

Input impedance

The real and imaginary part of input impedance has been estimated for each frequency, and for each anesthesia stage, and then they have been averaged on all the patients.

As recently proven ((35)), input impedance is a parameter very sensitive to lung de-rectruitment, thus it could be used an index of atelectasis presence.

Zin at baseline, during spontaneous breathing could be used to assess again the healthy state of the respiratory system of these subjects, since at 5 Hz they show a resistance of 5.4 $cmH20Ls^{-1}$ we can confirm they respect the inclusion criteria, but the most interesting trend is represented by eventual changes during recruitment maneuver, which should indicate the actual recruitment of the collapsed lung.

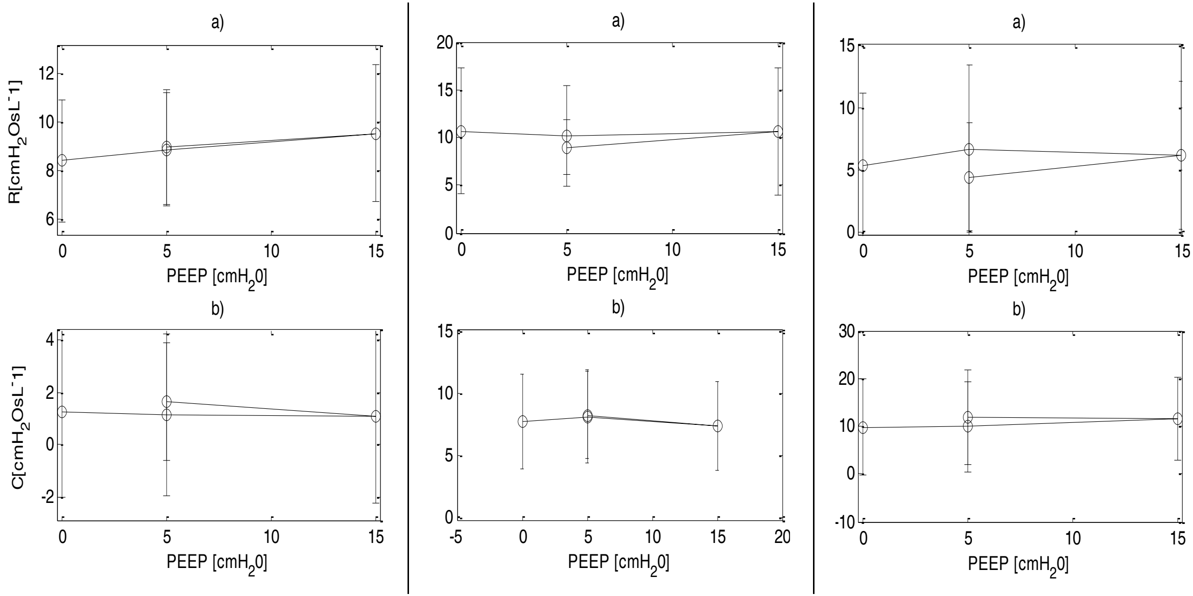

Figure 3.22: Upper panel, R and X measured at 5 Hz, mid panel R and X measured at 11 Hz, lower panel R and X measured at 19 Hz

Figure 3. shows the input impedance parameter at 5, 11 and 19 Hz, plotted versus the PEEP. As can be seen, they present a homogeneous behavior as the frequency changes, since all of them present almost a flat trend. In particular the behavior of the reactance at 5 Hz, that is an indicator of the alveolar units which take part in the breathing correlates very well with the amount of de-recruited tissue, but as can be seen, varying the PEEP, X5 doesn't changes, suggesting that these patients are not de-recruited.

Chest-wall measurement by interferometer

Interferometer has been used to measure in a very accurate way the displacement of each point of the chest-wall to estimate the phase shift between pressure and the velocities. In the velocity signal the frequency content of the stimulus are evidenced compared to the displacement signal.

In Figure 3.23 are reported some "raw" tracks, the first two show pressure and flow at the mouth which have been used to estimate Z_{in}, the third one represent the velocities, here the 5 Hz components are evident, and finally the displacement of the same point estimated by integrating the velocity signal, its value at t=0 is arbitrary since interferometer doesn't provide absolute position

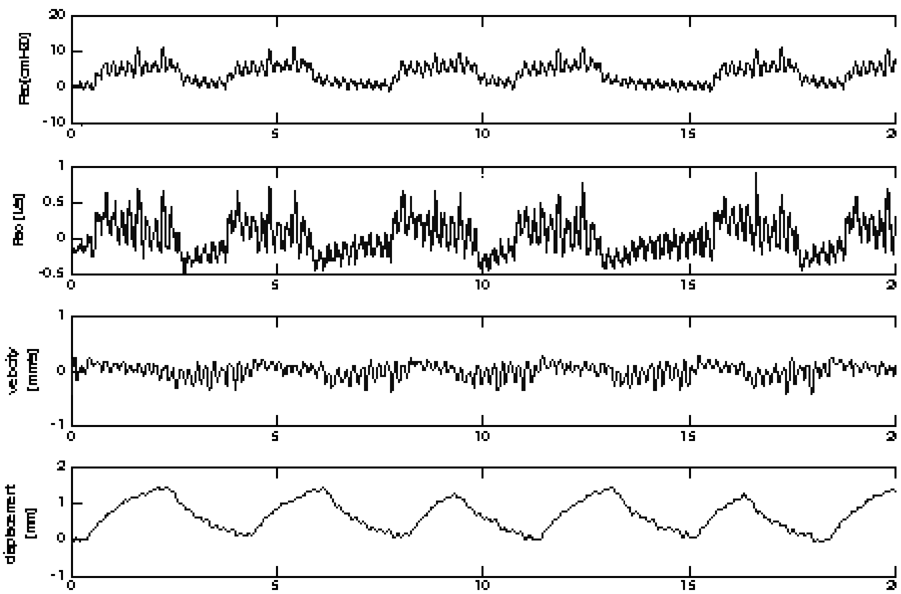

Figure 3.23: Pressure at the airways opening, flow at the airways opening, velocity the left lower ribcage, displacement for the same point.

From each pressure and velocity the phases has been estimated and plotted to produce a map.

The first two rows are respectively on the upper rib cage and lower ribcage, while the last two belong to the abdomen, the third is in the upper abdomen while the fourth is around the umbilicus line.

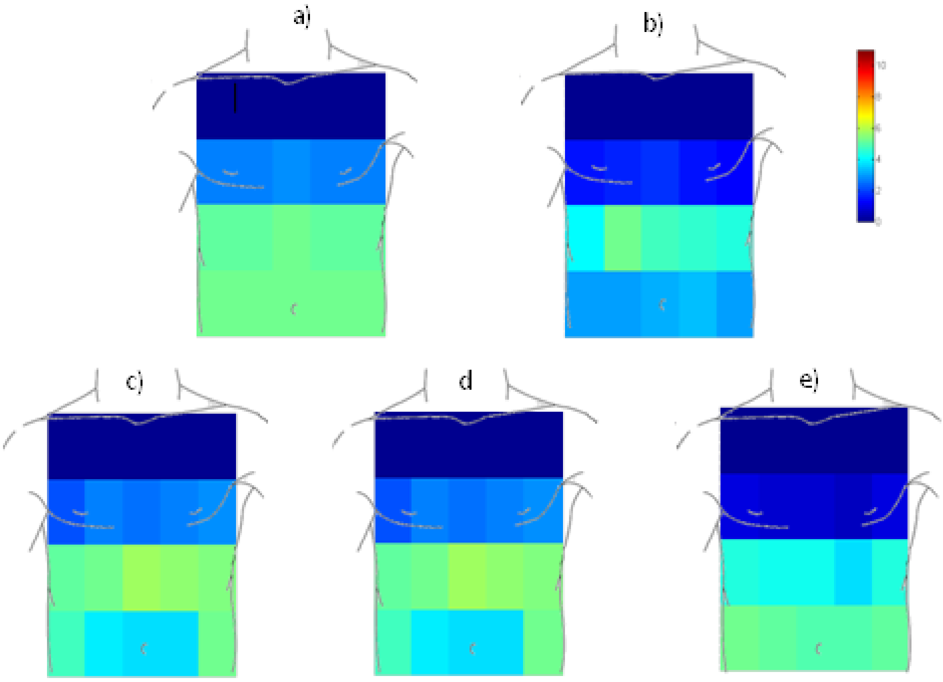

Figure 3.24: Phase shift at 5 Hz during a) spontaneous breathing, b) sedation, c) paralysis at ZEEP, d) paralysis at PEEP 5 before RM, e)paralysis PEEP 5 after RM

Figure 3.24 shows map of phase shift at 5 Hz during different condition, all the conditions show, at first sight, a high similarity, with the chest-wall split into upper and lower abdomen. The same raw trends can be traced also by plotting the mean of each row for each condition, as in Figure 3.25. The phase shift presents an increasing trend as the distance from the mouth is increased, and the maximum value is lower than 2π. The lower ribcage is the point that shows a different trend in the different conditions, assuming values from 0.81±0.36 rad to 2.68±2.34 rad. This point presents a high variability among subjects because it is closed to the costal margin.

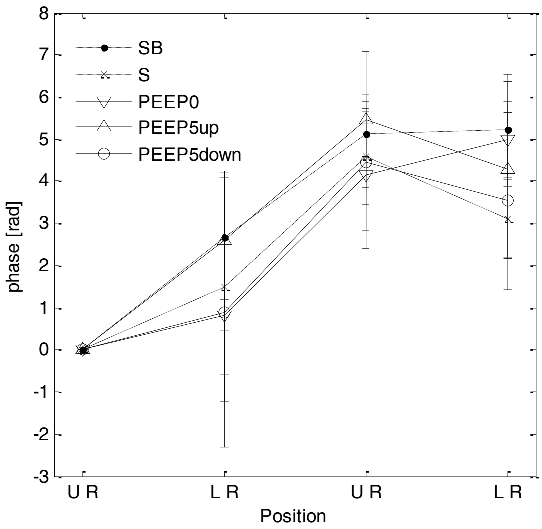

Figure 3.25: averaged phase shift from the upper ribcage (UR) to the lower abdomen (LA) at 5 Hz for the different conditions at 5 Hz

The same evaluations have been done also for 11 and 19 HZ (Figure 3.26, Figure 3.27).

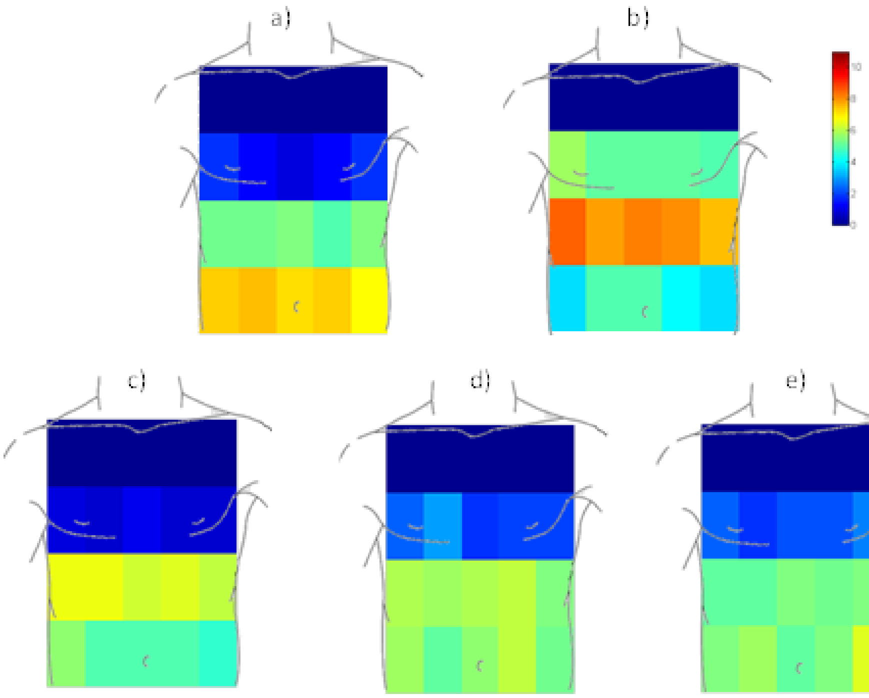

Figure 3.26: : Phase shift at 11 Hz during a) spontaneous breathing, b) sedation, c) paralysis at ZEEP, d) paralysis at PEEP 5 before RM, e)paralysis PEEP 5 after RM

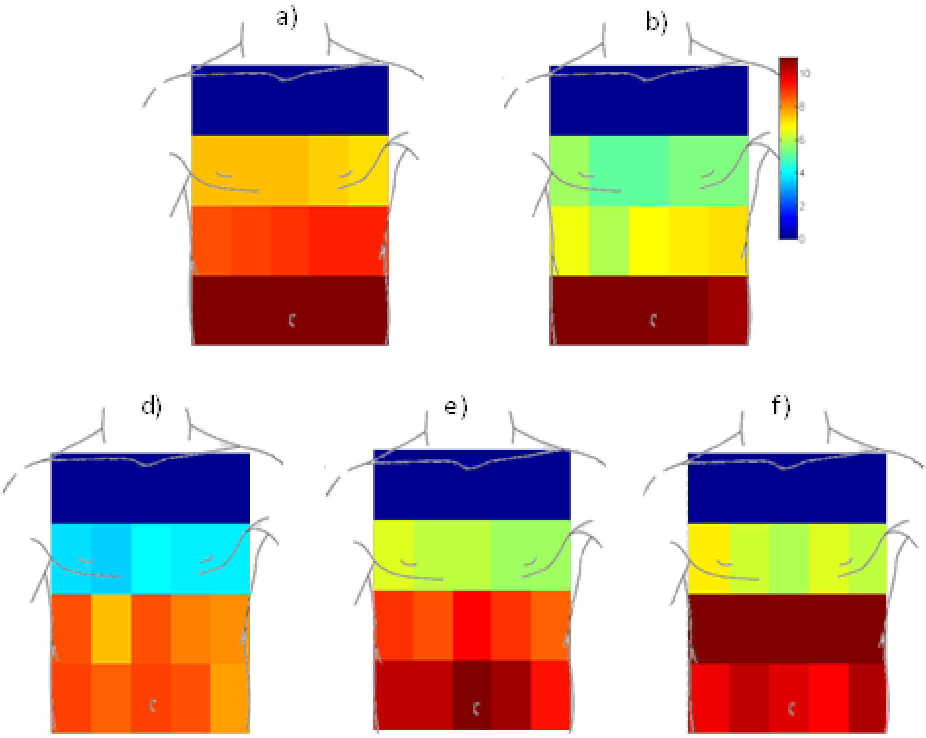

Figure 3.27: : Phase shift at 19 Hz during a) spontaneous breathing, b) sedation, c) paralysis at ZEEP, d) paralysis at PEEP 5 before RM, e)paralysis PEEP 5 after RM

As the frequency stimulus increases, also the phase increase, in fact the maximum shift we get at 5 Hz is 5.22±1.33 rad, at 11 Hz is 8.00+1.23 rad and at 19Hz it is 11.97+2.45. When the phase delay is more than π, it means that the two reasons are mowing in counter-phase, this happen for the ribcage and the abdomen at 5 Hz.

The main goal of this study is to prove the feasibility of measurement with interferometer and to validate the use of this kind of system in a clinical environment.

From this very preliminary study we can assess that the system is suitable for the clinical environment and easy to use, furthermore we have acquired only 20 points but it is easy to customize in order to increase the spatial resolution in the cranial-caudal direction if the patient's pathology suggest the presence of heterogeneity in the lung.

By comparing the results along the same line we can see very reproducible data, since the five interferometers are system completely independent, we can interpret this results as an issue to stand the interferometer ability to detect displacement and to estimate phase shift.

Although the very limited number of subjects and albeit the aim of the measurement was not to extrapolate physiological data, it is possible to hypothesis some preliminary results which need a higher number of subjects to be confirmed.

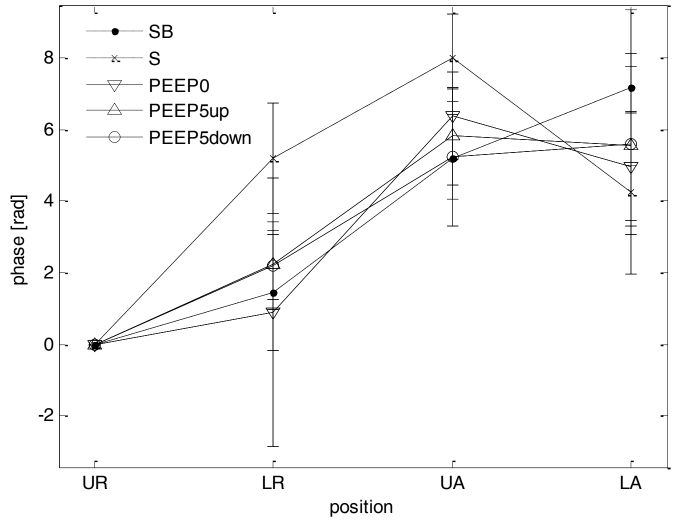

Figure 3.28: Phase shift at 11 Hz during a) spontaneous breathing, b) sedation, c) paralysis at ZEEP, d) paralysis at PEEP 5 before RM, e)paralysis PEEP 5 after RM

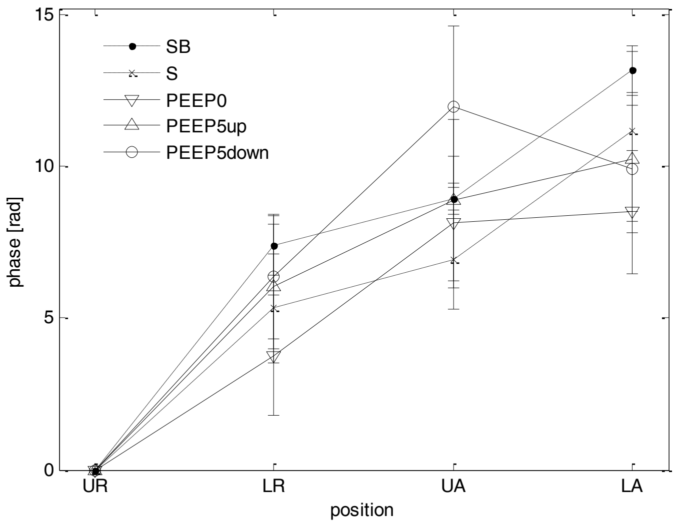

Figure 3.29: Phase shift at 19 Hz during a) spontaneous breathing, b) sedation, c) paralysis at ZEEP, d) paralysis at PEEP 5 before RM, e)paralysis PEEP 5 after RM

By looking the behavior of the phase shift along the chest-wall it is possible to note that it doesn't act as it is homogenous, in particular at 5 Hz it is possible to identify clearly the region of the rib cage, where the pressure stimulus moves fast, and the abdomen where the pressure wave is slowed down by the high inertive component, in accord with the theory of the two compartment model. This trend tends to be less marked as the frequency increased, indeed at 19 Hz, we can still see heterogeneity, but the phase shift tends to get similar to a line.

The line at 5 Hz shows that the maximum changes is associated with sedation, that is more evident in the LR, then this change can be traced also for paralysis at ZEEP, where there an increasing both in the absolute values but also in the shape, which can be associated with variation in the subdivision of the chest-wall.

At 11 Hz the variation induces by sedation are more evident on the lower rib cage which may be related to the reduction in FRC.

By increasing frequency, the behavior is more homogenous but the trends are more similar to the one at 5 Hz with predominance of the effect of variation in the configuration of the chest-wall.

Another useful analysis may be performed by plotting the three frequencies along the chest-wall for each condition.

From Figure 3.30 we can get that the frequencies of stimulus shows a similarity in the behavior at each anesthesia stage.

The recruitment maneuver seems to involve more the 11 Hz, maybe because its main changes are due to the FRC. The reduction in FRC seems to suggest de-rectruitment but the trend of Z_{in} contracted these hypotheses and this issue agrees with the chest-wall mechanics. In particular if some atelectasis and consolidation are present in the lung parenchyma, we may aspect at 11Hz and 19 Hz an increase in the propagation velocity but the lack for increasing velocity confirms the absence also of de-rectruitment.

In conclusion we may affirm that although during induction of anesthesia no atelectasis has been found, the impedance map shows some slightly variation during the different stages, which is an encouraging results about the sensitivity of this system. In fact if it is able to detect little variation in healthy subject, which are not so evident also to Z_{in}, we can aspect high sensitivity also in pathological conditions.

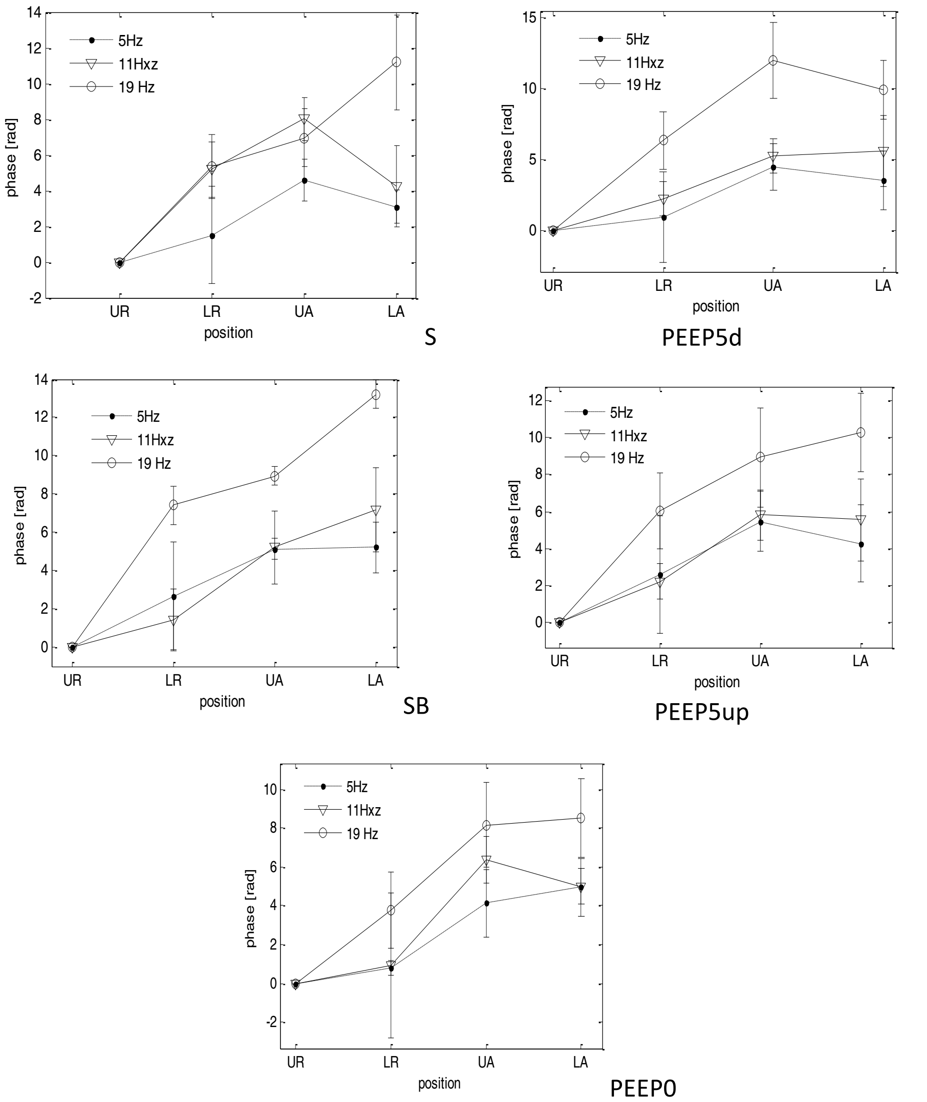

Figure 3.30: For each condition the phase at 5,11, 19 Hz plotted versus the position of the chest-wall

D. DISTAZIOMETER VALIDATION FOR IN VIVO MEASUREMENTS

Just some brief notes about a test performed on a patient to test the feasibility of the measurement with proximity sensor to find angles and positions.

To validate in vivo the ability of proximity sensors in measuring angle and distances, we acquire the external lines of the chest-wall during spontaneous breathing and sedation.

The scanning system will acquire four transversal lines on the rib cage and on the abdomen. Around each line, the motor will be rotate of just two angular steps (1.8°) to allow a better reconstruction of the chest-wall morphology (Figure 3.31).

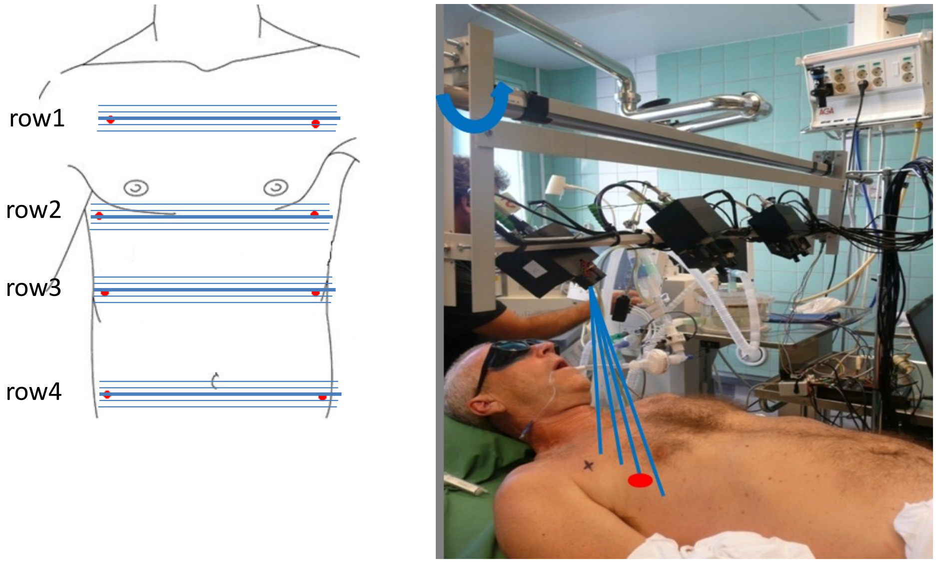

Figure 3.31: scanning system path of measurements for angular estimation

As an example, the four angle estimated around the first raw are reported.

As can be seen, although the distances measured show high similarity, the estimated angle may vary dramatically, according to the chest-wall configuration.

Table 3.3 First line's distance and angle computed on the awaken patient.

	angles (degrees)				distances (cm)				
distantiometer 1	81.53	89.90	88.86	80.36	33.04	33.21	33.23	33.22	33.42
distantiometer 2	74.22	40.13	19.96	69.93	57.24	56.77	58.99	64.61	63.91

In order to have a better comprehension of the phenomenon, the polar graphs have been plotted.

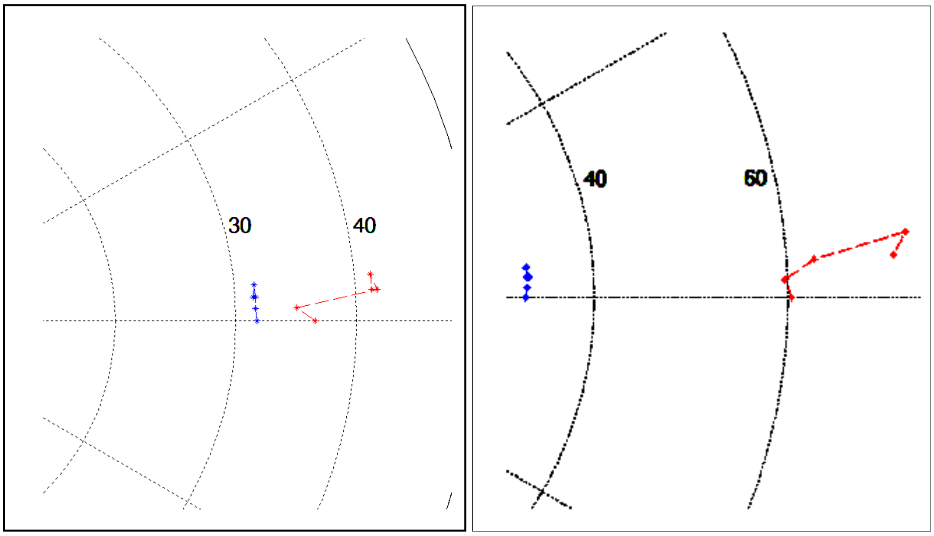

Figure 3.32 Distances of the points around the first row, on the left, and the second computed every step. The left side is represented in blue and shows a little changing from point to point than the other one, in red; they're both calculated on the awaken patient.

In the Figure 3.32 there are represented the different values of distances computed at every step of the motor for both the distantiometers (in blue the values obtained from the first, in red the other ones) at each line in the spontaneous breathing situation. In both the lines indeed we can see that the values plotted in blue follow a curvilinear path as the distances are quite similar around 33 cm, which is a sort of ray centered at the origin of the plane and it justify the high angular values founded. The regularity of this path covered by the distantiometer with 1.8° steps is confirmed by the fact that the last backward step gives a value which coincides with the other one previously computed in the specific position. The other path covered by the opposite optical device shows a visible direction change with a corner shape, which is effectively underlined by the 30 ° shifts between the first two consecutives angles, while the following two differs of 10°, as we can see from the less sharp straight line. The computation of the distance values after the backward step shows a sort of hysteresis, indeed there's another big difference with previous calculated angle.

Comparing these positions with the following ones, we can see a similar pattern concerning the first distantiometer, with then many distances that are similar within the successive movements performed by the stepper motor, also the curvilinear shape is slightly modified towards a more vertical line and the values computed are around 31 cm. The other path is much different from the corresponding previous one, as the there's the same corner-like shape but with different tilting and then the surface tends to the vertical direction; a little hysteresis is also seen at the last value. So we can deduce that the distantiometers cover the many steps in completely different districts, in particular the blue lines are related to a region which may be more close to a side of the chest wall without irregularities in the surface presenting a quite homogeneous tilting, whereas the opposite condition occurs on the opposite edge, showing a more complex superficial pattern.

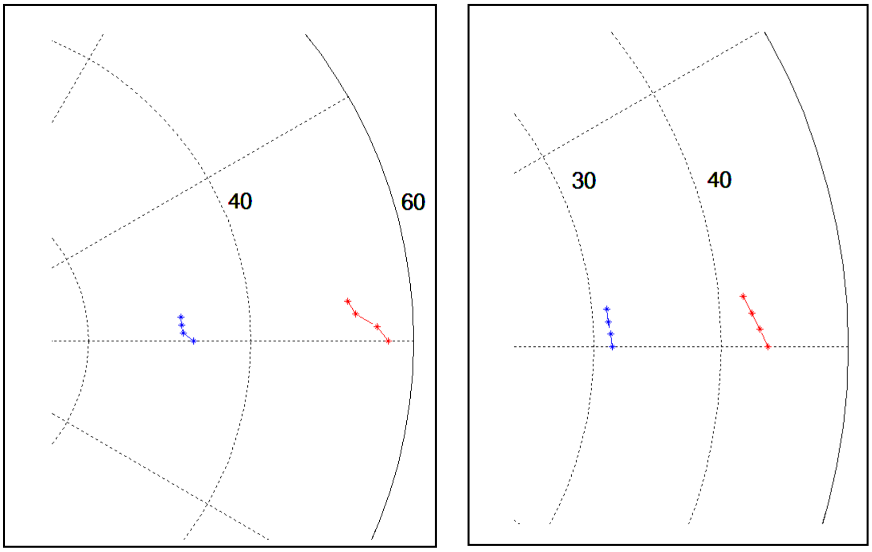

Figure 3.33 Distances of the points around the first row, on the left, and the second computed at every step. The left side is represented in blue and shows a little changing from point to point than the other, in red; they're both calculated on the sedated patient

In the Figure 3.33 on the left the movements of the distantiometers till the reaching of the first line in which the interferometer stop for 30 s, on the right the distance computed still the second one. Comparing them with the previous two positions computed during normal breathing we can see that the blue line is positioned at distance values very close to the ones calculate before, 32-32 cm instead of 32-31 and the two paths of respective second acquisitions shows an almost identical pattern with very little hysteresis. The path of the second distantiometer is very different from the one described before, as there aren't any corners, only a slight bending in the tracing of Fig. on the left, whereas the other points can be fitted by a linear trend.

This macroscopic difference may be a mismatch in the starting positions between the different conditions, but, as we will see that the other distances computed by the first distantiometer can be considered comparable and they're strictly fixed, a possible explanation may be that the motion of the chest wall changes as the respiration of the patient depends on the mechanical ventilator, in particular it causes a more regular contraction of the analyzed region.

Comparing now the two patterns tracing during the sedation we can see that, as it happens during spontaneous breathing, the first distantiometer doesn't compute huge distance differences, about 1 cm, so the path remains almost the same, avoiding the initial angular differences; in these positions the displacement velocity can be interpolated from the point in which the signal interferometer is computed, as the surface in both the side paths displays the same tilting with its beam.

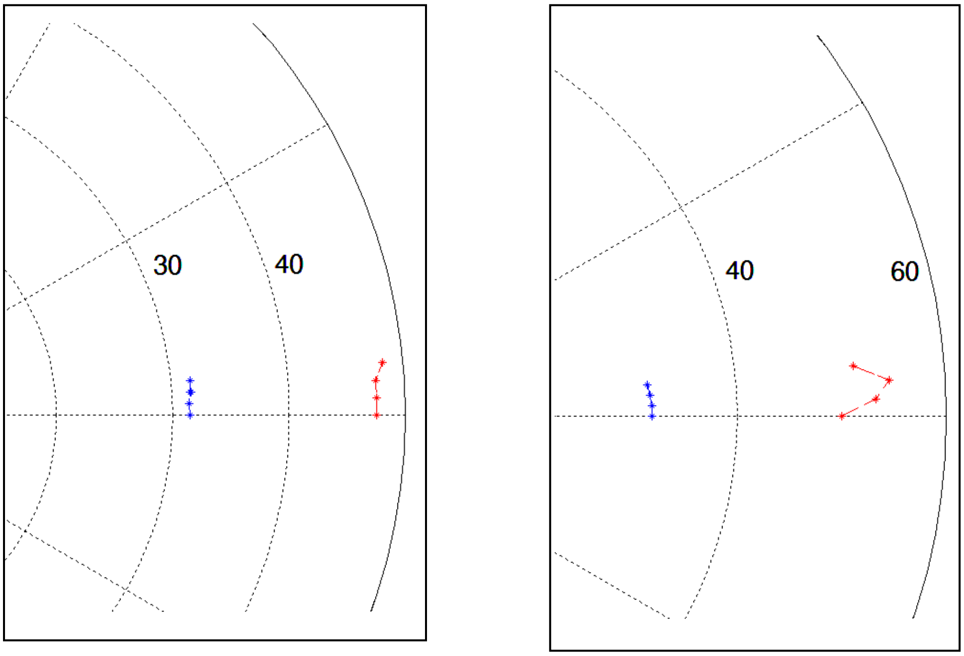

Figure 3.34 Distances of the points around the third row, on the left, and the fourth computed at every step. The left side is represented in blue and shows a little changing from point to point than the other one, in red; they're both calculated on the awaken patient.

Finally, Figure 3.34 represents the last two paths covered by the distantiometers before stopping in the positions in which the interferometers records the signals, the third line on the left and the fourth on the right. Starting from the blue line we can see that there isn't a great difference both comparing to the previous and the next position, also if the distance shift is about 1 cm, but in both the tracing there isn't any hysteresis displayed, symptom of the accuracy and repeatability of the measure that we're performing.

Dealing with the positions computed with the second distantiometer, we can noticed some differences both in the distances, differing 4 cm in respect to the previous position and 6 to the next one, and in the tracing of involving the different points and it' s related to the different orientation of the districts of the thoracic-abdominal surface. Indeed it changed to the almost linear trend of the third position (Fig. left) to a corner-shape path, situated more far from the other, as all the distances are comprised between 50 and 55 cm. It means that the path covered presents shape variations, as we actually expect as they're passing the end of the rig cage and coming to the beginning of the abdominal region, so it's important to determine the correct directions in all these points and in particular in the one in which the interferometer stops.

We report then the relative distances between the rows calculated both on the awake and the sedated patient; even if the linear path assumption standing between the different point involving in the computation isn't verified, this data are suitable to determine the reciprocal positions of the different rows scanned on the chest wall surface, starting from the top of it, so to reconstruct the differences in the local transfer impedances performing a map of them.

	distance between row 1 - row 2
distantiometer 1	7.34
distantiometer 2	31.96

		distances	
	row 1 - row 2	**row 2 - row 3**	**row 3 - row 4**
distantiometer 1	6.90	6.91	6.95
distantiometer 2	14.77	11.07	13.25

Table 3.4 Reciprocal distances between consecutives rows in which the punctual displacement is recorded starting from the top of the chest wall.

These data confirms the preceding conclusions deduced from the data, that the left side of the chest wall has a more limited range of motion in both the wake and sedated conditions, as the reciprocal distance between the consecutive rows stands between 6.9 and 7.3 cm, actually only in the second one it' s comprises between 6.9 and 7 cm. They are the same calculated in the formula for the angles computation and reflect in this case the regularity of the disposition of these points, which is symmetrical to the almost constant angular orientation between the same and different rows.

The right side shows otherwise some changing in the reciprocal distances among the rows, as we can see dealing with the ones calculated on the sedated patient, displaying a range of 15-11 cm, which isn't even so wide if compared with the differential surface orientations that can be assessed also around the single line of interest. This is probably due to the regular scan performed by the stepper motor, but otherwise, if the compared these differential measures with the one of the other side, it gets clear the fact that the range of motion involving these rows is significantly wider.

All these data then point out the difference standing between the two sides of the chest wall analyzed, with differences in the punctual orientation standing within the row itself or among different ones, suggesting that the different parts of the chest wall ay display a differently oriented motion that can get then to inhomogeneities in the local transfer impedances assessment.

The aim of these measurements is to check the feasibility of measurement with distantiometer. It gave promising results in particular:

1) Determination of angles and distances: these are the variables of interests and their computation was demonstrated to be accurate and repeatable using the distantiometers. The system was suitable for the use in rough surface, as the skin, and their behavior doesn't change within light intensity or temperature, and was stable in all the experimental conditions faced in this study. The response to the tilting of the surface was found to be better at lower values, but it can extended to angular inclinations till 90°, which is the maximal value which could be of interest for our work.

Integration with the FOT measurements: these laser devices were suitable to be used with the equipment needed to perform the forced oscillation technique (FOT), by which it's possible to get the non-invasive measurements of the input and transfer impedance.

2) Assessment of the different orientations of the chest wall surface in the different functional conditions of the patient: analyzing the two sides (right and left) of the chest wall, we were able to assess the different directions within the points around the rows in which the interferometers recorded the displacement.

Thanks to these results, it' s feasible to get the displacement component in the effective direction of motion of the single points on the chest wall surface, allowing the assessment of inhomogeneities of the local transfer impedances by comparing different regions, such as the upper and lower part of the thoraco-abdominal surface.

In conclusion, the combination of laser interferometers with optical distantiometers is feasible and provides an accurate method to assess the chest wall displacement during FOT. This new approach to measure the mechanical properties of the chest wall and their regional distribution might provide important insights for the comprehension of the whole respiratory system’s mechanics in health and disease.

3.3. REFERENCE

1. Lundquist H, Hedenstierna G, Strandberg Å, Tokics L, Brismar B. CT-assessment of dependent lung densities in man during general anaesthesia. Acta Radiol. 1995;36(6):626-32.

2. MedScape: Atelectasis [Internet].; Nov 19, 2010. Available from: http://emedicine.medscape.com/article/296468-overview#a0104.

3. Hedenstierna G, Rothen HU. Atelectasis formation during anesthesia: Causes and measures to prevent it. J Clin Monit Comput. 2000;16(5):329-35.

4. Rahn H, Otis AB, Chadwick LE, Fenn WO. The pressure-volume diagram of the thorax and lung. American Journal of Physiology--Legacy Content. 1946;146(2):161.

5. Hedenstierna G, Tokics L, Lundquist H, Andersson T, Strandberg Å, Brismar B. Phrenic nerve stimulation during halothane anesthesia. effects of atelectasis. Anesthesiology. 1994;80(4):751.

6. Burger E, Macklem P. In: The effect on lungs of breathing 100% oxygen near residual volume. Fed. proc; ; 1966. p. 566.

7. Otis Jr D, Johnson M, Pedley T, Kamm R. Role of pulmonary surfactant in airway closure: A computational study. J Appl Physiol. 1993;75(3):1323-33.

8. Oyarzun M, Iturriaga R, Donoso P, Dussaubat N, Santos M, Schiappacasse M, et al. Factors affecting distribution of alveolar surfactant during resting ventilation. American Journal of Physiology-Lung Cellular and Molecular Physiology. 1991;261(2):L210-7.

9. Wollmer P, Schairer W, Bos J, Barker W, Krenning E, Lachmann B. Pulmonary clearance of 99mTc-DTPA during halothane anaesthesia. Acta Anaesthesiol Scand. 1990;34(7):572-5.

10. Gunnarsson L, Tokics L, Gustavsson H, Hedenstierna G. Influence of age on atelectasis formation and gas exchange impairment during general anaesthesia. Br J Anaesth. 1991;66(4):423.

11. Strandberg Å, Tokics L, Brismar B, Lundquist H, Hedenstierna G. Atelectasis during anaesthesia and in the postoperative period. Acta Anaesthesiol Scand. 1986;30(2):154-8.

12. Strandberg Å, Tokics L, Brismar B, Lundquist H, Hedenstierna G. Constitutional factors promoting development of atelectasis during anaesthesia. Acta Anaesthesiol Scand. 1987;31(1):21-4.

13. Pelosi P, Croci M, Ravagnan I, Tredici S, Pedoto A, Lissoni A, et al. The effects of body mass on lung volumes, respiratory mechanics, and gas exchange during general anesthesia. Anesthesia & Analgesia. 1998;87(3):654.

14. Gunnarsson L, Tokics L, Lundquist H, Brismar B, Strandberg A, Berg B, et al. Chronic obstructive pulmonary disease and anaesthesia: Formation of atelectasis and gas exchange impairment. European Respiratory Journal. 1991;4(9):1106-16.

15. Hachenberg T, Lundquist H, Tokics L, Brismar B, Hedenstierna G. Analysis of lung density by computed tomography before and during general anaesthesia. Acta Anaesthesiol Scand. 1993;37(6):549-55.

16. West J, Dollery C, Naimark A. Distribution of blood flow in isolated lung; relation to vascular and alveolar pressures. J Appl Physiol. 1964;19(4):713.

17. Neumann P, Rothen H, Berglund J, Valtysson J, Magnusson A, Hedenstierna G. Positive end-expiratory pressure prevents atelectasisduring general anaesthesia even in the presence of a high inspired oxygen concentration. Acta Anaesthesiol Scand. 1999;43(3):295-301.

18. Reinius H, Jonsson L, Gustafsson S, Sundbom M, Duvernoy O, Pelosi P, et al. Prevention of atelectasis in morbidly obese patients during general anesthesia and paralysis: A computerized tomography study. Anesthesiology. 2009;111(5):979.

19. Tokics L, Strandberg A, Brismar B, Lundqwist H, Hedenstierna G. Computerized tomography of the chest and gas exchange measurements during ketamine anaesthesia. Acta Anaesthesiol Scand. 1987;31(8):684-92.

20. Rothen H, Sporre B, Engberg G, Wegenius G, Hedenstierna G. Reexpansion of atelectasis during general anaesthesia may have a prolonged effect. Acta Anaesthesiol Scand. 1995;39(1):118-25.

21. Rothen HU, Sporre B, Engberg G, Wegenius G, Hogman M, Hedenstierna G. Influence of gas composition on recurrence of atelectasis after a reexpansion maneuver during general anesthesia. Anesthesiology. 1995;82(4):832.

22. DREYFUSS D, SAUMON G. Ventilator-induced lung injury. lessons from experimental studies. American journal of respiratory and critical care medicine. 1998;157(1):294.

23. PARKER JC, HERNANDEZ LA, PEEVY KJ. Mechanisms of ventilator-induced lung injury. Crit Care Med. 1993;21(1):131.

24. Slutsky AS, Ranieri VM. Mechanical ventilation: Lessons from the ARDSNet trial. Respiratory research. 2000;1(2):73.

25. Mercat A, Richard JCM, Vielle B, Jaber S, Osman D, Diehl JL, et al. Positive end-expiratory pressure setting in adults with acute lung injury and acute respiratory distress syndrome. JAMA: the journal of the American Medical Association. 2008;299(6):646.

26. Amato MBP, Barbas CSV, Medeiros DM, Magaldi RB, Schettino GP, Lorenzi-Filho G, et al. Effect of a protective-ventilation strategy on mortality in the acute respiratory distress syndrome. N Engl J Med. 1998;338(6):347-54.

27. Acute lung injury, the open lung approach [Internet].; 2002. Available from: http://www.ccmtutorials.com/rs/ali/05_aliopen.htm.

28. Takeuchi M, Goddon S, Dolhnikoff M, Shimaoka M, Hess D, Amato MBP, et al. Set positive end-expiratory pressure during protective ventilation affects lung injury. Anesthesiology. 2002;97(3):682.

29. Suarez-Sipmann F, Böhm SH, Tusman G, Pesch T, Thamm O, Reissmann H, et al. Use of dynamic compliance for open lung positive end-expiratory pressure titration in an experimental study. Crit Care Med. 2007;35(1):214.

30. Bellardine Black CL, Hoffman AM, Tsai LW, Ingenito EP, Suki B, Kaczka DW, et al. Relationship between dynamic respiratory mechanics and disease heterogeneity in sheep lavage injury*. Crit Care Med. 2007;35(3):870.

31. Berggren P, Lachmann B, Curstedt T, Grossmann G, Robertson B. Gas exchange and lung morphology after surfactant replacement in experimental adult respiratory distress syndrome induced by repeated lung lavage. Acta Anaesthesiol Scand. 1986;30(4):321-8.

32. Carvalho ARS, Jandre FC, Pino AV, Bozza FA, Salluh JI, Rodrigues RS, et al. Effects of descending positive end-expiratory pressure on lung mechanics and aeration in healthy anaesthetized piglets. Critical Care. 2006;10(4):R122.

33. Gattinoni L, Caironi P, PELOSI P, Goodman LR. What has computed tomography taught us about the acute respiratory distress syndrome? American journal of respiratory and critical care medicine. 2001;164(9):1701.

34. Vieira SRR, Puybasset L, Richecoeur J, LU Q, Cluzel P, Gusman PB, et al. A lung computed tomographic assessment of positive end-expiratory pressure-induced lung overdistension. American journal of respiratory and critical care medicine. 1998;158(5):1571.

35. Dellacà RL, Zannin E, Kostic P, Andersson Olerud M, Pompilio PP, Hedenstierna G, et al. Optimisation of positive end-expiratory pressure by forced oscillation technique in a lavage model of acute lung injury. Intensive Care Med. 2011:1-10.

4. CONCLUSION

The respiratory system is a very complex system which is fundamental for life. Non physiological condition, such as anesthesia or pathological one may produce great variations in its behavior, in particular in its mechanics due to the presence of atelectasis.

The conventional approach to find atelectasis is the CT since it is able to distinguish the different density region, but it has evident disadvantages such as to be invasive (a dose of ionizing radiation is given to the patient at each measurement), not suitable for the bedside of the patients and very expensive.

For these regions other methods and approaches that allow the detection of de-recruited lung may represent useful tool in clinics to aid the physicians in the diagnose, treatment and monitoring.

A good candidate is FOT, that allows studying the mechanical of the respiratory system which is deeply influenced by variation in recruited lung; in particular input impedance is easy to be measured and has been proven very sensitive to alteration in the percentage of open lung. The major limits associated to Z_{in} is intrinsic and is the fact that information that it provides is an average of all the respiratory system, and it doesn't allow to detect where the variation observed taken place. Another parameter which is more sensitive to the position may be local transfer impedance, which estimate how the pressure wave travels inside the chest wall which involved the different structure found by the pressure wave along its pathway.

Anyway up to know little is known about the impedance of the chest-wall since there are some technical difficulties that limit its detection such as the lack for instrument to measure displacement in an accurate way.

In this work of thesis a new device and a new system has been presented and validate that allow to measure the mechanical properties of the chest-wall in a not invasive way and without requiring patient cooperation thanks to optical devices such as laser self-mixing interferometer pointing on the chest wall of the subjects.

To reach this aim, several intermediate steps have been done.

In particular the first stage has been a feasibility study to verify if laser self-mixing interferometer allows to measure displacement of low diffusive target such as the human skin. As reported in chapter two, to get displacement measurements from these kind of noisy signal has been necessary to design a new processing algorithm more reliable to speckle. Then we validate the algorithm in vitro by measuring a known displacement and comparing the measured space with the true one.

As a second stage, we realized a primitive but working set-up that allow to measure chest-wall displacement in patient in supine position during the administration of pressure stimulus. The main limitation of this set-up consists in the long time required to acquire multiple points on the chest-wall since the laser has to be managed by hand by the operator. Although this system was not user friendly, it gave very promising results, in fact the data acquired on healthy subjects looked very reliable and reproducible, confirming and validating the algorithm of reconstruction.

Inspired by the previous set up, but with the consciousness of its limitation a new scanning system more compact and easy to use, which can be also used in clinical environment has been design and tested.

The main improvement respects to the first set-up has been the introduction of a system to scan in a fast way the chest-wall acquiring simultaneously multiple points. This aim was reached by means of five interferometer fixed on a bar rotated by a stepper motor in order to perform a scan in the cranial-caudal direction. To overcome also limitation related to the lack of information about the absolute position of the patient and of the different spots on its chest-wall and the absence of information about the incidence angle, the system may be integrated with distantiometer.

Therefore a an algorithm to estimate angle of incidence and position from the signal of distantiometer has design and tested in vitro and in vivo on two patients with accurate results, if the device is properly calibrated and the measured surface doesn’t present too elevate incidence angle which reduces the backscattered light.

Finally this system has been proven at the Uppsala Hospital University on five patients which undergoes anesthesia to verify the feasibility of this kind of measurement and to assess the sensitive of this system.

The results are very promising, in fact the data seems very reliable and reproducible, moreover, although patients don’t present any atelectasis, as confirmed by the contemporary measurement of the input impedance, the phase reconstructed shift map shows some interesting features,

In more details, although five patients are not enough to have a statistical analysis, it is possible to state that these data are comparable with results obtained by Dellacà et al, the maps allows to separate the ribcage compartment from the abdomen one and to detect a slightly little differences according to the frequency and the condition at whom the patient is undergone. In particular all the trends seem to show that the behavior of the chest-wall is more uniform as the frequency increase, while at low frequency, such as 5 Hz, the abdomens and the ribcage are very heterogeneous.

In conclusion with this thesis we reach the aim of proposing a new approach to measure local transfer impedance based on interferometer and we validate both the reconstructive algorithm both the scanning system realized; in this way the first stone in order to study how mechanical chest-wall is influenced by patho-physiological alteration has been set.

Although we reached our goal future developments are needed, at least in two directions: to completely integrate and validate the system by performing measurement with all the distantiometer, to acquire more patients of several typologies to verify which kind of parameter may be extrapolated by the chest-wall mechanics to identify the respiratory system status.